Durham University

Durham E-Theses

Realisation of a cold mixture of rubidium and caesium

Margaret L. Harris

How to cite:

Harris, Margaret L. (2008) Realisation of a cold mixture of rubidium and caesium. Doctoral thesis, Durham University.

Use policy

The full-text may be used and/or reproduced, and given to third parties in any format or medium, without prior permission or charge, for personal research or study, educational, or not-for-profit purposes provided that:

- a full bibliographic reference is made to the original source
- a https://etheses.durham.ac.uk/id/eprint/2300/ is made to the metadata record in Durham E-Theses
- the full-text is not changed in any way

The full-text must not be sold in any format or medium without the formal permission of the copyright holders.

Please consult the full Durham E-Theses policy for further details.

Academic Support Office, The Palatine Centre, Durham University, Stockton Road, Durham, DH1 3LE
e-mail: e-theses.admin@durham.ac.uk Tel: +44 0191 334 6107
https://etheses.durham.ac.uk

Realisation of a Cold Mixture of Rubidium and Caesium

Margaret L. Harris

A thesis submitted in partial fulfilment
of the requirements for the degree of
Doctor of Philosophy

The copyright of this thesis rests with the author or the university to which it was submitted. No quotation from it, or information derived from it may be published without the prior written consent of the author or university, and any information derived from it should be acknowledged.

Department of Physics
Durham University

July 7, 2008

0 7 OCT 2008

Realisation of a Cold Mixture of Rubidium and Caesium

Margaret L. Harris

Abstract

This thesis describes a new apparatus designed to study cold, ultracold, and quantum degenerate mixtures of rubidium and caesium atoms. The Rb-Cs mixture is prepared using a double magneto-optical trap (MOT) system in which a two-species pyramid MOT acts as a source of cold atoms for a 'science' MOT. The first results of experiments on the magneto-optically trapped mixture are presented, including measurements of trap loss rates due to single-species and interspecies inelastic collisions. A technique for reducing interspecies loss by spatially separating the MOTs during loading is described. This technique allows 50-50 mixtures of Rb and Cs atoms to be loaded into a magnetic trap at close to their respective maximum single-species atom numbers. Alternatively, one species can be loaded with arbitrarily small amounts of the other. The displaced MOT technique is thus an excellent starting point for investigations of interspecies Feshbach resonances and sympathetic cooling of Rb-Cs mixtures in magnetic and optical traps.

In addition, a model of polarisation spectroscopy based on numerical integration of population rate equations is described. Theoretical polarisation spectra generated by the model are shown to agree with experimental spectra for the $F = \mathcal{I} + 1/2 \rightarrow F'$ transitions in Rb and Cs. An investigation of the sub-Doppler dichroic atomic vapour laser locking (DAVLL) technique demonstrates how locking signals can be optimised for the Rb $D2$ transitions. The role of polarisation purity in generating the spectra is discussed, and impurities are modeled using a Jones matrix approach. Comparisons with polarisation spectroscopy and DAVLL are used to enhance understanding of atom-light interactions in spectroscopic systems, and indicate methods for optimising locking signals for use in cold atom experiments.

Declaration

I confirm that no part of the material offered has previously been submitted by myself for a degree in this or any other University. Where material has been generated through joint work, the work of others has been indicated.

Margaret L. Harris
Durham, July 7, 2008

The copyright of this thesis rests with the author. No quotation from it should be published without their prior written consent and information derived from it should be acknowledged.

Let the words of my mouth, and the meditation of my heart, be acceptable in thy sight, O LORD, my strength, and my redeemer.

Psalm 19:14

Acknowledgements

My first thanks go to the two people who worked with me most on the Rb-Cs mixture experiment: my supervisor Simon Cornish, and my colleague Patrick Tierney. Simon's scientific and organisational skills have contributed tremendously to the mixture project. He has also helped me become a more effective communicator of scientific ideas. Patrick's hard work and dedication helped make the project possible, and his sense of humour and eclectic taste in lab music made it more fun. If his unicycling and juggling talents have failed to rub off on me, this is surely not his fault.

Ifan Hughes has taught me some of the finer points of atom-light interactions as co-supervisor of the spectroscopy work in this thesis and via his graduate lectures. I have enjoyed hearing Ifan's opinions on education, sport, and the superiority of all things Welsh at tea breaks over the past few years. I thank him both for his enthusiasm and for his dedication to teaching. I have also benefited from the guidance and insights of Charles Adams, particularly during the first year of my PhD. In addition to his role in examining this thesis, Simon Gardiner has helped me find answers to various pastoral, mathematical and computational questions. All of these contributions are greatly appreciated.

The past four years have witnessed a tremendous expansion in the Durham Atmol group. I have been fortunate to work with many talented people during my PhD, including Mike Brockley, Paul Foulkes, Sylvi Händel, Jean-Christophe Karam, Zhao-Yuan Ma, Danny McCarron, Isobel McLeod, Fred Millett-Sikking, Malcolm Parks, Sam Pollock, Ben Sheard, Ajay Tripathi and Faye Tuddenham. Beyond the Cornish corner of the Atmol hall, I appreciate the example set by the 'first wave' of Atmol experimentalists: Paul Griffin, Simon MacLeod, Graham Purves, Dave Smith and Kev Weatherill. Kev, in particular, has been here throughout my PhD, and his calm competence and willingness to lend me odd bits of kit have been very helpful. More recent arrivals have also brought expertise and friendship; I thank Richard Abel, Meltem Akyilmaz, David Carty, Paul Halkyard, Matt Jones (for helpful advice and helpful pints), James Millen, Ashok Mohapatra (for loaned equipment and South Indian restaurant recommendations), Jonathan Pritchard, Matt Pritchard, Paul Siddons and Steve 'Boris does Boulder' Wrathmall (for general zaniness and cricketing insights). I would especially like to thank Mark Bason, Andy Martin and Mark Saunders, who along with Patrick

Tierney helped make the 2007 Young Atom Opticians conference the most enjoyable (and most manic!) week of my PhD. I have known other members less well, but all have contributed to the knowledge base and collaborative spirit which made me glad to be part of the Durham Atmol community.

Several non-Atmol members of the Durham Physics department also deserve thanks. Phil Armstrong, Steve Lishman, John Scott, Lee Bainbridge, Chris Cavagin, Andrew Crosby, Malcolm Robertshaw, George Teasdale, Kevin Tindale, Jess Wathen, Paul White and the rest of the mechanical and electronics workshop staff constructed many of the building blocks of the mixture apparatus, and their patience and expertise have helped us put together many more. I would also like to thank Ian Manfren, Wayne Dobby, and John Dobson for loaned equipment and quick fixes. Special thanks go to Mike Pennington for support during my teaching fellowship.

Within the wider Atmol community, I thank Chris Foot both for serving as my external examiner and for welcoming me on a visit to the Clarendon Labs in the summer of 2007. I visited Kai Dieckman and Stephan Dürr on a QUDEDIS-sponsored trip in February of that same year; I thank both of them for showing me around and answering my questions. I have also appreciated Stephan's dry humour at various conferences. Finally, I thank Carl Wieman and John Thomas — the first for sparking my interest in atomic physics and giving me the opportunity to do research for the first time, and the second for his friendship and advice over the past several years.

On a more personal note, I would like to thank the teachers and students at Greenfield School (particularly Bob Hough and Nicholas Portwood) for their friendship during the year I worked with them. I also thank my own inspiring science teachers: Al Lee, Elizabeth Parks, John Holloway, Lynn Martens and Jan Sifers.

Several friends have been very supportive and understanding during my PhD. These include 'The Helens' (Armstrong and Vaughan); my housemates Dan Kolb, Kim Crabbe, Andy Cramman, and Malc Parks; John and Jane Allison, Venetia Appelbe, Emily Ballou, Anna Bohuszewicz, Haley DeKorne, Harry Gibson, Andi Feit, the King family, Namita Koppa, the Lovelace family, Marguerite Mauritz, Sarah Meyer, Rob Poole and the New Year Gang. I would also like to thank, collectively, the Durham University Hill-Walking Society. There is nothing quite like being halfway up a mountain in a Force 9 gale and a pissing rain for making lab problems seem remote, and nothing quite like good friends in a warm pub afterwards for making it all worthwhile.

Finally, I thank my family, who have provided long-distance love and support through good times and bad, and Matt King, who has done the same on this side of the Atlantic. I could not have done it without you.

Contents

List of Figures

List of Tables

Part I

Background

Chapter 1

Introduction

In the years since the first observations of Bose-Einstein condensation in ^{87}Rb and ^{23}Na in the summer of 1995 [1, 2], a number of other atomic species have been added to the quantum degenerate 'zoo.' These include all of the stable, abundant isotopes of the alkali metal atoms, including both bosonic and fermionic isotopes of lithium [3, 4] and potassium [5–7]. Degeneracy has also been reported in non-alkali species such as atomic hydrogen [8], metastable helium [9], bosonic and fermionic isotopes of ytterbium [10, 11], and chromium [12]. This proliferation of degenerate species has paralleled an explosion in studies of condensate properties and behaviour. Landmark demonstrations of atom lasers [13], condensates with tuneable interactions [14], molecules in condensates [15, 16], bright matter-wave solitons [17, 18] and many other discoveries have all contributed to our understanding of how matter behaves at temperatures near absolute zero. In awarding the 2001 physics prize 'for the achievement of Bose-Einstein condensation in dilute gases of alkali atoms, and for early fundamental studies of the properties of the condensates,' the Nobel committee recognised the importance of these experiments, which have also sparked many theoretical investigations. Cold-atom physics is therefore a near textbook example of how the interplay of experiment and theory can advance knowledge of the physical world.

One of the most promising directions of research in this field is the production and study of cold and ultracold mixtures of two or more atomic species. Such mixtures exhibit a wide range of fascinating phenomena not present in single-species systems. The balance between interspecies and in-

traspecies atomic interactions can lead to phase separation of a quantum degenerate mixture [19] and can trigger a collapse even when the two species are separately stable [20]. When confined in an optical lattice potential, binary atomic mixtures display a rich spectrum of quantum phases [21]. Such mixtures offer a means of forming ultracold heteronuclear molecules via photoassociation [22] or Feshbach resonances [23]. This in turn will facilitate the creation of dipolar quantum gases [24] and may aid the development of a scalable quantum information processing system [25].

On the technical side, mixtures allow species with unfavourable elastic to inelastic collision ratios to be cooled via elastic collisions with a second evaporatively cooled species. This sympathetic cooling technique has proved essential for cooling fermionic quantum gases to degeneracy [3]. Following the successes in fermionic systems, binary bosonic mixtures of ^{85}Rb-^{87}Rb [26, 27], ^{87}Rb-Cs [28–30], and ^{87}Rb-^{41}K [31] have also attracted experimental attention.

This thesis describes the development of a new experimental apparatus designed to study cold and ultracold mixtures of rubidium and caesium. The first results of experiments on magneto-optically trapped Rb-Cs mixtures are presented, including measurements of loss from the trap due to interspecies inelastic collisions, and the implementation of a new technique which minimises such loss by spatially separating the two species. These studies form the foundation for ongoing and future work on evaporative and sympathetic cooling of Rb-Cs mixtures in magnetic and optical traps.

1.1 Cool things to do with mixtures

Within the rich and dense list of mixture phenomena, a few common threads can be discerned. Broadly speaking, research programmes on cold, ultracold and quantum degenerate mixtures over the past decade have followed three paths: treating mixtures as a means to an end, studying the rich spectrum of mixture interactions, and using mixtures to open up new possibilities in quantum computation and control. There is considerable overlap both chronologically and thematically between these categories. However, the division provides a useful framework for summarising many important

developments in mixture research.

1.1.1 Sympathetic cooling: a means to an end

Experiments on sympathetic cooling have proved very successful at using mixtures to achieve degeneracy in species for which 'standard' evaporative cooling is not sufficient. Because s-wave collisions are suppressed in single-species Fermi gases, fermionic systems were a prime early target for sympathetic cooling studies. Adding a second species (including a different spin-state of the same element) lifts the restriction on s-wave collisions imposed by the Pauli exclusion principle, allowing atoms in the mixture to rethermalise via s-wave collisions as one or more components are evaporatively cooled.

The first degenerate Fermi gas was produced by evaporatively cooling a mixture of different spin states of ^{40}K (specifically, the $|F = 9/2, m_F = 9/2, 7/2\rangle$ states) [3]. A similar approach was later used to reach degeneracy in optically-trapped ^{6}Li [32]. An alternative method is to use bosons to sympathetically cool fermions [5, 33–35]. The resulting Bose-Fermi degenerate gases permit the study of mixtures in which the component species obey different quantum statistics. Very recently, a quantum degenerate *fermionic* mixture of ^{6}Li-^{40}K has been created via sympathetic cooling with bosonic ^{87}Rb [36]. In this three-species quantum degenerate mixture, the presence of K was found to enhance the sympathetic cooling of Li by Rb. This phenomenon was dubbed 'catalytic cooling'.

The usefulness of sympathetic cooling is by no means limited to fermions. Some bosonic species also exhibit low ratios of 'good' (elastic) collisions to 'bad' (inelastic) collisions. For example, ^{41}K and ^{85}Rb have both been cooled to degeneracy using ^{87}Rb as the coolant species [37, 38]. Sympathetic cooling has been studied in many other bosonic mixtures, including ^{39}K-^{87}Rb [39] and ^{7}Li-Cs [40] in addition to those already mentioned.

Because sympathetic cooling relies on interspecies collisions, measurements of a mixture's elastic collision rate are an important step towards understanding the cooling process and how it can be optimised. The interspecies collision rate Γ_{12} is proportional to the average interspecies number density and the

mean relative velocity of the colliding particles,

$$\Gamma_{12} = \sigma_{12}\langle n_{12} v_{\mathrm{rel}} \rangle. \tag{1.1}$$

The constant of proportionality σ_{12} is the interspecies scattering cross section. Interspecies scattering lengths[1] have been measured for all of the mixtures discussed so far, although at this writing detailed knowledge is limited to particular spin states for some mixtures, including Rb-Cs [41]. The importance of this scattering data extends well beyond its usefulness for optimising sympathetic cooling, as the next section should make clear.

1.1.2 Interactions: a rich playground

The collisional dynamics of a mixture depend on both intraspecies and interspecies interactions. As an example of how single-species interactions[2] can affect mixture characteristics, consider the Fermi-Bose mixture ^{6}Li-^{7}Li. The scattering length of ^{7}Li in the $|F = 2, m_F = 2\rangle$ state is negative, and the resulting attractive interactions limited the number of bosons in the first ^{6}Li-^{7}Li quantum degenerate mixture to around 1000 [33]. By contrast, the $|F = 1, m_F = -1\rangle$ state has a small positive scattering length, and experiments using this state produced condensates with an order of magnitude more atoms [34]. In this case, the two components of the mixture were able to coexist.

Conversely, another Fermi-Bose mixture, ^{40}K-^{87}Rb, has been observed to be unstable unless the number of degenerate atoms of *both* species is limited to below 2×10^4 [20]. This instability occurs even though the single-species scattering lengths of both ^{40}K and ^{87}Rb are positive, making them separately stable. The negative *interspecies* scattering length in the K-Rb mixture causes the Fermi gas to collapse when the number of bosons rises above a threshold value. The phenomenon of condensate collapse is familiar from single-species experiments [42], but interspecies interactions add another layer of complexity to the system.

[1] The relationship between scattering cross section and scattering length is discussed in Chapter 2.

[2] The terms 'single-species' and 'intraspecies' are used interchangeably in this work, as are 'two-species' and 'interspecies.'

Besides collapse and coexistence, degenerate mixtures can also exhibit phase separation. One form of phase separation occurs when the coupling between atoms in *e.g.* the fermionic component is stronger than the coupling between bosons. In this case, the fermions will experience a potential minimum in the center of the trap, and a fermionic 'island' will exist inside a Bose-condensed 'sea'. If the coupling strengths are reversed, the fermions will be localised near the edge of the condensate, forming a 'shell' around the condensate. Conditions for each of these regimes in Bose-Fermi mixtures were first discussed by K. Mølmer [43], with a more complete treatment provided in a later work by Lewenstein *et al.* [21]. Similar conditions for phase separation, collapse and coexistence have been derived for Bose-Bose mixtures [19, 44, 45].

The presence of either single-species (see *e.g.* Ref. [23] and references therein) or interspecies [27, 46–49] Feshbach resonances allows the scattering lengths in the mixture to be tuned by varying the magnetic field. Changing the scattering lengths changes the balance between interspecies and intraspecies interactions. Feshbach resonances can therefore be used to tune mixtures between different interaction regimes. The possibilities of this tuneability have only recently begun to be investigated experimentally [50], and much remains to be done in this promising area of research.

1.1.3 Ultracold polar molecules: a new era

In addition to their use in studies of mixture interactions, Feshbach resonances have been used to make cold molecules in a number of different systems [23]. Molecules formed directly from Feshbach resonances are, however, in highly excited vibrational levels. Such molecules have very small permanent dipole moments [51] and short lifetimes due to collisions [52]. Collisions can be suppressed by confining the molecules in an optical lattice [53, 54], but to increase their polarity the component atoms must be tightly bound. Molecules in their vibrational ground state are both stable and strongly polarised; hence, the formation of such molecules is highly desirable.

Molecules are, of course, formed almost continuously in a MOT via photoassociation, even when only the trapping beams are present. Some of the molecules created in this fashion will spontaneously decay to the ground

state, and techniques like time-of-flight mass spectroscopy have been used to detect them [55]. The problem is that this process is not controllable — in fact, it is often described more prosaically as MOT loss! *Controlled* photoassociation uses a separate photoassociation laser tuned to excite the atoms to a particular molecular level. The molecules can then be pumped towards lower vibrational levels of the ground state using a sequence of pulses. Figure 1.1 shows the details of a scheme presented by Sage *et al.* [56] for creating RbCs molecules. In their experiment, five separate pulses are required: one to excite the atoms into weakly bound excited-state molecules, another to excite the metastable molecules created after decay by spontaneous emission, a third to stimulate them down to the ground state, and two to detect the ground-state molecules. Variants of this method have been demonstrated for several other heteronuclear alkali metal dimers; see *e.g.* Ref. [22] and references therein.

The drawback of this method — in addition to its incredible complexity! — is that the initial photoassociation step is inefficient, and the pumping to lower vibrational levels tends to leave the atoms in a distribution of final states [27]. Shaped photoassociation pulses using a femtosecond laser offer a promising means of correcting the first problem [57]. Experiments which apply this technology to cold atom research are currently underway at Durham, Newcastle, and Oxford. Another alternative is to form molecules via Feshbach resonances and then transfer them to their vibronic ground state via stimulated Raman transitions [51]. This stimulated Raman adiabatic passage (STIRAP) process has been predicted to increase the atom-to-molecule conversion efficiency to near unity [58, 59].

Why is there so much interest in creating ultracold polar molecules? The answer is in their name. Polar molecules interact via dipole-dipole interactions, for which the magnitude depends on the orientation of the dipoles. At ultralow temperatures, the energy of these interactions exceeds the thermal energy of the molecules. Polar molecules at such temperatures can therefore be manipulated in a controlled and targeted fashion using applied electric fields. This idea is at the heart of one proposal for a scalable quantum computer, in which the orientation of molecular dipoles (relative to an external electric field) serve as qubits [25]. The ability to manipulate processes like

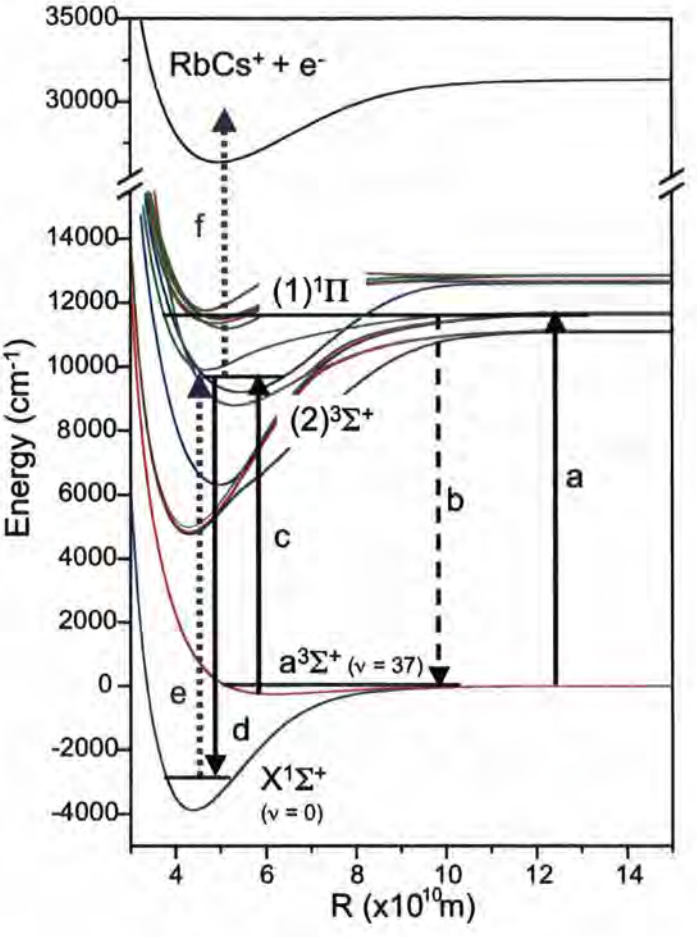

Figure 1.1: Scheme for creating and detecting ultracold ground-state RbCs as used in Ref. [56]. Molecular potentials for $^1\Sigma$, $^3\Sigma$, and Π states are indicated with blue, red and green lines (respectively). In a five-pulse sequence, Rb and Cs atoms are (a) excited into weakly bound RbCs* molecules, which then decay (b) to the $a^3\Sigma^+$ state. The resulting metastable molecules (v=37) are then excited to the $(2)^3\Sigma^+$ level, then stimulated down into the ground state. Detection (purple lines) is either performed directly, by driving molecules back to the excited level and then ionising them (pulses e and f), or indirectly by detecting the depletion of the $(2)^3\Sigma^+$ level (pulse f only).

elastic and inelastic collisions also raises the possibility of performing ultracold chemistry [60]. Other, even more exotic possibilities such as searches for parity violation and new forms of many-body quantum states have also been discussed [61, 62]. The great challenge for experimentalists is, as Jones *et al.* describe it, 'to produce an interesting number of molecules in the desired rovibrational level(s) of the ground state,' and then to keep them there long enough to perform experiments [22].

1.2 Why rubidium and caesium?

We now turn away from discussing the present and future of cold atomic mixtures to consider the state of mixture research in 2003, when the experiments described in this thesis began.

It is no accident that many of the examples in the previous section involved Bose-Fermi mixtures. Following the pioneering experiments on two-component ^{87}Rb and ^{23}Na spinor condensates [63, 64], years passed before the first two atomic species superfluid, a mixture of ^{41}K and ^{87}Rb, was created [6]. The second, which combined ^{39}K with the ever-popular ^{87}Rb, was demonstrated several years later [7]; the third, a mixture of ^{85}Rb and ^{87}Rb, appeared during the writing of this thesis [38]. The lack of experimental advances in this area does not, however, indicate a lack of interest in Bose-Bose mixtures. In addition to the theoretical studies on interaction regimes noted in the previous section, numerous studies of cold (*i.e.* non-degenerate) bosonic mixtures have been performed. Studies of two-species MOTs are of particular relevance to this work. By the end of 2003, magneto-optically trapped mixtures of most stable alkali species had been realised [65], as had a MOT containing bosonic ^{52}Cr and ^{87}Rb [66]. The question was not so much whether to study Bose-Bose mixtures, but which mixture to choose.

The combination of ^{87}Rb and ^{133}Cs offers particularly interesting prospects for experiments on quantum degenerate mixtures[3]. ^{87}Rb is the most commonly condensed alkali species due to its favourable ratio of elastic to inelastic collisions. In contrast, strong inelastic losses in Cs make it difficult

[3]Unless otherwise specified, any mention of Rb or Cs in this thesis always refers to these isotopes.

to condense in a magnetic trap [67, 68], and use of the $|F = 3, m_F = +3\rangle$ state in combination with several stages of optical trapping were required to achieve quantum degeneracy [69]. The Rb scattering length is essentially independent of magnetic field, with only narrow Feshbach resonances being present at accessible magnetic fields [70]. For Cs, a rich Feshbach structure containing both narrow and broad resonances has already been exploited to produce cold molecular samples of dimers [71] and Efimov trimers [72] and to precisely tune the scattering length around a broad zero-crossing [73]. Figure 1.2 illustrates the scattering lengths for fields of up to 200 G for Cs and Rb in their $|F=3, m_F=\pm 3\rangle$ (blue lines) and $|F=1, m_F=\pm 1\rangle$ states (red line), respectively.

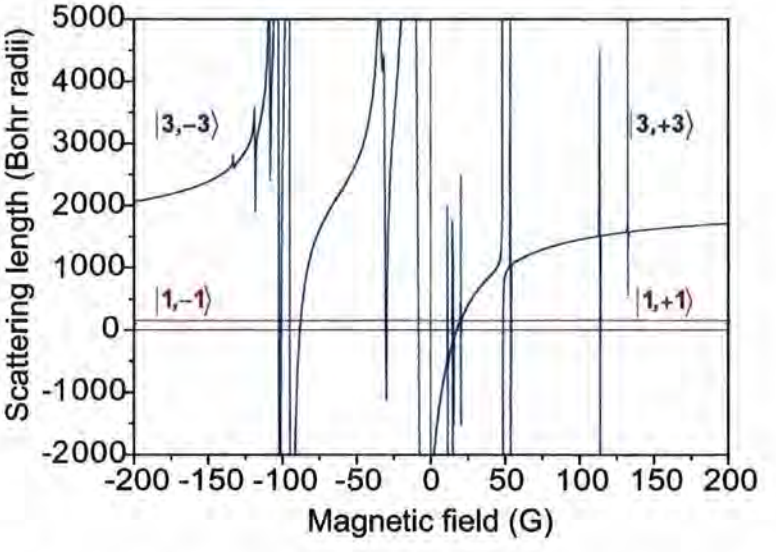

Figure 1.2: Scattering length as a function of magnetic field for Cs (blue lines) and Rb (red line) in the indicated states. The scattering length of Rb is essentially independent of field, while Cs exhibits a rich structure of broad and narrow Feshbach resonances. Figure based on data in Ref. [74].

Unlike some mixtures of alkali metals (particularly those containing Li [75]), the magnetic moment-to-mass ratios for Cs and Rb atoms in these states are very similar, differing by less than 2% for magnetic fields below $\sim$ 86 Gauss and by less than 10% for fields below 231 G. This ratio determines the acceleration of an atom due to a spatially varying applied magnetic field.

Hence, the very similar ratios for Rb and Cs mean that their oscillation frequencies in a harmonic magnetic trap differ by just 1% over this field range. The displacements of the Rb and Cs clouds due to gravity ('gravitational sag') are thus nearly identical. This leads to good spatial overlap of the clouds even at sub-microkelvin temperatures in a weak magnetic trap, making Rb an attractive species with which to sympathetically cool Cs. Figure 1.3 shows the ratio of collision rates with and without gravity — essentially a measure of the two species' spatial overlap — as a function of temperature for the Rb-Cs and ^{85}Rb-^{87}Rb systems. For the isotopic Rb mixture, the ratio begins to deviate from unity (complete overlap) by more than 10% for temperatures below $\sim$ 10 μK. The Rb-Cs mixture does not reach the same deviation until the temperature of the sample has been reduced by an additional two orders of magnitude.

Intriguingly, sympathetic cooling of Cs with Rb may offer a route to quantum degeneracy in magnetically-trapped Cs, particularly if the magnetic trap is combined with an optical 'dimple' potential [77]. Using a magnetic trap as the reservoir for loading this dimple rather than a large volume optical dipole trap [69] would greatly simplify the necessary experimental apparatus and would also give access to the equally rich Feshbach structure in the $|F=3, m_F=-3\rangle$ state of Cs.

When work on this project began, very little was known about the interspecies scattering properties of Rb-Cs, let alone the prospects for sympathetic cooling. Before these and other mixture phenomena could be studied, it was first necessary to create a cold mixture. The measurements on cold, magneto-optically trapped Rb-Cs mixtures described in this thesis are the initial results of the first UK-based experimental project on cold mixtures. This work therefore represents an important first step in exploring the rich physics discussed in the previous section.

Since 2003, several other groups have also carried out experiments on Rb-Cs mixtures. The Pisa group led by E. Arimondo has studied magnetically-trapped Rb and Cs in the $|F=2, m_F=2\rangle$ and $|F=4, m_F=4\rangle$ states, respectively. Rethermalisation measurements carried out by this group found that the elastic scattering cross-section for Rb-Cs in these states was consistent with a theoretically predicted value of $595a_0$ [28, 78]. Sympathetic cooling

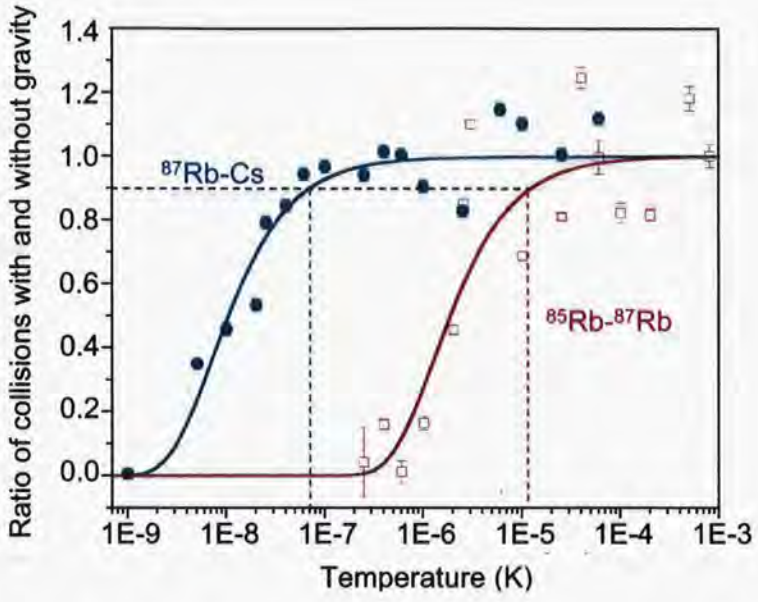

Figure 1.3: Ratio of collision rates with and without gravity for Rb-Cs and isotopic Rb mixtures. Results from Monte-Carlo simulations (dots, [76]) and theoretical calculations (lines, [41]) indicate that magnetically trapped clouds of Rb and Cs atoms will remain well overlapped at temperatures more that two orders of magnitude colder than clouds of ^{85}Rb and ^{87}Rb atoms. The excellent spatial overlap of the Rb-Cs system makes Rb an attractive species with which to sympathetically cool Cs.

of Cs with Rb was also observed, but the relatively small size of their initial trapped sample ($N_{\mathrm{Rb}} \approx 2 \times 10^6$, $N_{\mathrm{Cs}} \approx 10^5$ atoms) prevented its extension below a few μK. Monte Carlo simulations (described in Refs. [41, 79, 80]) of lower temperatures suggested that it would not be possible to cool Cs to quantum degeneracy using this spin-state mixture, even if N_{Rb} were increased by an order of magnitude. Intriguingly, simulations of Cs and Rb in the $|F=3, m_F=-3\rangle$ and $|F=1, m_F=-1\rangle$ states indicated a more favourable outcome to the sympathetic cooling process, with Cs condensates containing up to 5×10^4 atoms predicted for similarly large ($> 300a_0$) interspecies scattering lengths.

A more recent set of experiments carried out by the group of D. Meschede in Bonn demonstrated sub-μK sympathetic cooling of Cs by Rb, using the

same spin states as the Pisa group but a much higher initial $N_{\mathrm{Rb}}/N_{\mathrm{Cs}}$ ratio [29]. This greater sensitivity allowed them to derive a lower limit of 200 a_0 for the interspecies s-wave scattering length. A major goal of this group is to study quantum degenerate mixtures composed of large numbers of Rb atoms and a small Cs 'impurity' of 1-1000 atoms. The strong non-exponential losses of Cs in the presence of Rb which they observe for temperatures below 5 μK may therefore prove less of a problem for them than for groups wishing to create two-species superfluids containing roughly equal numbers of Rb and Cs atoms.

Very recently, a group led by R. Grimm at Innsbruck has also begun to study Rb-Cs mixtures. Building on expertise gained during their experiments on the first Cs condensates [69], they have employed Raman sideband cooling [81] and optical trapping to cool and trap mixtures of Rb and Cs in the high-field-seeking $|F=1, m_F=+1\rangle$ and $|F=3, m_F=+3\rangle$ states [82]. More information on this experiment, including data on interspecies Rb-Cs Feshbach resonances, is expected to be published later this year [83].

1.3 Overview of thesis

The main body of this thesis is devoted to experiments on cold mixtures of ^{87}Rb and ^{133}Cs atoms. Part I describes the theoretical concepts which underpin how the experimental apparatus operates, and which are needed to understand what a Bose-Einstein condensate is and how it can be realised experimentally. Part II describes the apparatus itself, and contains results of the first experiments performed on the Rb-Cs mixture. The last part of this thesis describes two investigations of alkali metal spectroscopy. The two chapters in this section are presented as more or less self-contained works. However, both types of spectroscopy were considered as potential methods for laser frequency stabilisation on the Rb-Cs mixture experiment, and the physical processes which drive them (*e.g.* optical pumping and the Zeeman shift) are also relevant for understanding the two-species magneto-optical trap.

The full breakdown of the chapters is as follows:

- Chapter 2 outlines the theory of Bose-Einstein condensation in an in-

teracting gas. It also covers aspects of scattering theory which are relevant to the Rb-Cs mixture, and contains a brief description of Feshbach resonances and how they can be used to explore different interaction regimes in a two-species quantum degenerate mixture.

- Chapter 3 describes the physics of atom cooling and trapping, including a discussion of collisions and loss mechanisms in a two-species magneto-optical trap.
- Chapter 4 describes the experimental apparatus used in studies of the Rb-Cs mixture.
- Chapter 5 contains the results of experiments which measured loss rate coefficients and demonstrated a new technique for minimising inter-species loss in the two-species magneto-optically trapped mixture.
- Chapter 6 presents a theoretical and experimental study of polarisation spectroscopy in rubidium and caesium.
- Chapter 7 contains spectra obtained for sub-Doppler dichroic atomic vapour laser locking, and discusses how the locking signals can be optimised for the Rb $D2$ transitions.
- Chapter 8 presents conclusions drawn from the work in this thesis, and looks ahead to future experiments with the next-generation Rb-Cs mixture apparatus currently being developed.

1.4 Contributions of others

The Rb-Cs mixture apparatus was constructed in collaboration with one other PhD student, Patrick Tierney, under the supervision and guidance of Dr. Simon L. Cornish. Figure 1.4 provides a summary of contributions made to the experiment by each student up to the end of the MOT measurements described in Chapter 5 (October 2007). More recent work on this experiment, including much more extensive magnetic trapping experiments and studies of evaporative cooling, may be found in Ref. [84].

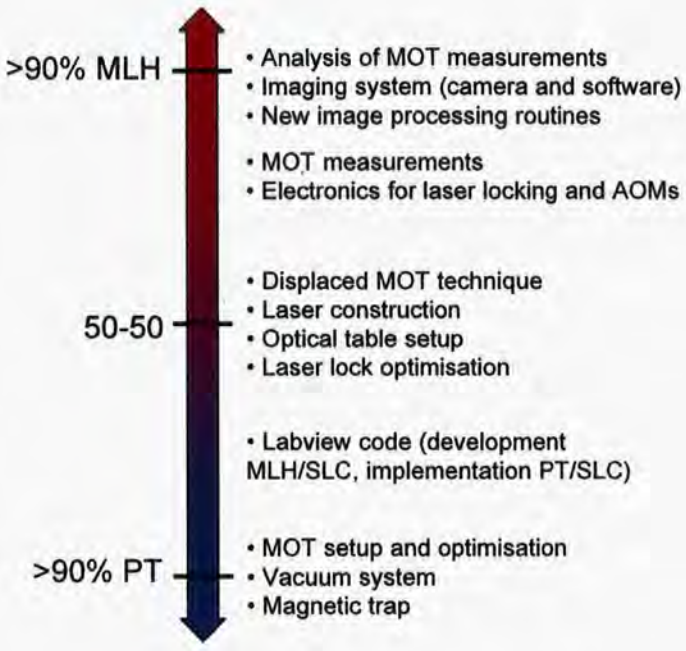

Figure 1.4: Summary of contributions made to Rb-Cs mixture experiment by the author (MLH) and Patrick Tierney (PT), under the supervision of Simon Cornish (SLC).

The original Mathematica code for modeling polarisation spectra of the cooling transitions in ^{85}Rb was written by Edmund Tarleton as part of his undergraduate M.Sci. project. It was subsequently modified to account for other Rb transitions and for Cs by a summer student, Isobel MacLeod. Later modifications of the code, studies of population dynamics, and measurements of experimental spectra were all performed by the author of this thesis. The project was supervised by Dr. Ifan Hughes and Professor Charles Adams as well as Dr. Cornish.

Finally, studies of sub-Doppler DAVLL spectra in Rb were begun by Dr. Ajay Tripathi. However, all spectra and analysis presented in this work are those of the author. The project was supervised by Dr. Hughes and Dr. Cornish.

1.5 Publications arising from this work

Substantial portions of Chapters 6 and 7 have been published in Refs. [85] and [86], respectively. The versions presented in this work contain additional data and more extensive descriptions of some theoretical concepts, *e.g.* the origins of the polarisation spectroscopy signal and the Jones matrix approach to polarisation impurities. Also, some material in Chapters 4 and 5 appears in Ref. [30] in a condensed form.

Chapter 2

Bose-Einstein condensation

Bose-Einstein condensation (BEC) has proved an astonishingly rich research topic, with many exciting developments including atom lasers [13, 87], vortices [88, 89] and vortex lattices [90], condensate collapse [14], and the observation of degeneracy in a Fermi gas [3]. Quantum degenerate mixtures of two or more atomic species exhibit a still wider range of phenomena, some of which have already been mentioned in the introduction to this thesis. However, the experimental potential of such systems is still largely unexplored. This chapter is intended to give an overview of the physics of Bose-Einstein condensation and low-temperature scattering theory, with an emphasis on how these may be applied to the study of mixtures of two different bosonic species.

2.1 What is a BEC?

Let us consider a system of N identical bosons with a temperature T and chemical potential μ. For the moment, we will ignore interactions between the bosons. The Bose-Einstein energy distribution function is:

$$f(\varepsilon) = \frac{1}{e^{(\varepsilon-\mu)/k_B T} - 1}. \tag{2.1}$$

At high temperatures, both this expression and its fermionic counterpart (identical except for a sign change in the denominator) reduce to the Boltzmann distribution. For bosons, as T approaches zero, the occupation of the lowest energy level of the system ($\varepsilon = 0$) can become macroscopically

large. When this happens, the sample undergoes a phase transition: a Bose-Einstein condensate forms. Because the particles in the BEC are all in a single quantum state (*i.e.* the ground state), they can be described by a single wavefunction. The constituent particles in a BEC can thus be likened to a 'superatom,' a system in which thousands or even millions of atoms behave like a single particle.

The phase transition can be understood in terms of the particles' thermal de Broglie wavelength, λ_{dB}:

$$\lambda_{\mathrm{dB}} = \sqrt{\frac{2\pi\hbar^2}{mk_BT}}, \tag{2.2}$$

where m is the mass of a particle. At high temperatures, the Heisenberg uncertainty principle dictates that the particles are well localised. As the temperature is reduced, the position uncertainty increases and the wave nature of the particles becomes more apparent. At sufficiently low temperatures, the de Broglie wavelength is long enough that the individual atomic wavefunctions overlap, and a condensate forms (Figure 2.1). The volume occupied by the atomic wave packets is multiplied by the peak number density of the sample to give the phase-space density, $PSD = n_{\mathrm{pk}}\lambda_{\mathrm{dB}}^3$. The transition to Bose-Einstein condensation occurs at a phase-space density of approximately 1.

To calculate the critical temperature T_c for the onset of BEC, we start by noting that it must occur when all N particles in the system can be 'just barely' accommodated in excited states, such that a further reduction in the temperature (kinetic energy) of the system leads to multiple occupation of the ground state. Under these conditions, the chemical potential is zero: any additional particles added to the system must go into the ground state, and the energy of the system does not change as a result of the addition[1]. The total number of particles in the excited states N_{ex} can thus be written as

$$N_{\mathrm{ex}}(T_c, \mu = 0) = N = \int_0^\infty g(\varepsilon)\frac{1}{e^{\varepsilon/k_BT_c} - 1}d\varepsilon, \tag{2.3}$$

where $g(\varepsilon)$ is the density of states. The form of $g(\varepsilon)$ depends on the potential (if any) in which the particles are confined. For our purposes, the most useful

[1]We have assumed that N is large enough that we can neglect the zero-point energy.

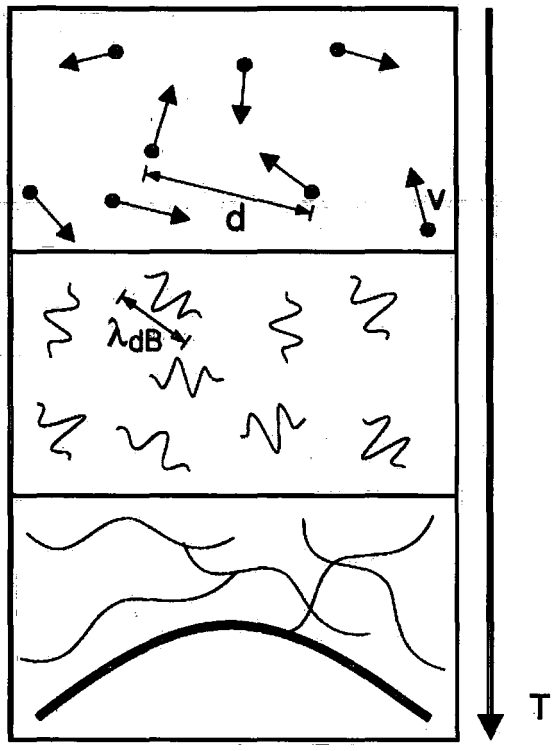

Figure 2.1: De Broglie wavelength and the transition to BEC. At temperatures $\gg T_c$ (top), the separation d between particles is much greater than their size, and atoms can be treated as point particles. As the sample is cooled (middle), the wave nature of the particles becomes more apparent. At $T \simeq T_c$, the individual atomic wavefunctions overlap, and a condensate forms (bottom). Figure adapted from [91].

potential to consider is that of a three-dimensional harmonic oscillator with cylindrical symmetry,

$$V(r) = \frac{1}{2} m\omega_r^2 \rho^2, \tag{2.4}$$

which is approximately the potential generated by our magnetic trap. Here $\rho^2 = x^2 + y^2 + \lambda^2 z^2$ and $\lambda = \omega_z/\omega_r$ is the ratio between the axial and radial trap frequencies. The solution to Eq. 2.3 for this potential is [92]:

$$k_B T_c = \frac{\hbar\overline{\omega} N^{1/3}}{\zeta(3)^{1/3}} \simeq 0.94\hbar\overline{\omega} N^{1/3}, \tag{2.5}$$

where $\zeta(3)$ is the Riemann zeta function and $\overline{\omega} = (\omega_r^2\omega_z)^{1/3}$ is the average harmonic oscillator frequency. The transition temperature is thus higher

for large numbers of atoms confined in a tight trap, in accordance with the qualitative picture of wave packet overlap provided by our discussion of the particles' de Broglie wavelengths. For example, in the mixture experiment described in Chapters 4 and 5, we load Rb atoms into a trap for which $\omega_r/2\pi \simeq 11$ Hz and $\omega_z/2\pi \simeq 4$ Hz. At these trap frequencies, a sample of 10,000 atoms will reach degeneracy at a temperature of 7 nK. The same number of atoms in a trap with frequencies an order of magnitude higher would condense at 70 nK. Unfortunately, at higher densities, atoms are also more likely to be lost from the trap due to inelastic processes, *e.g.* three-body collisions. This is important, because as we shall see in the next section, the very diluteness of alkali condensates is an advantage in formulating theoretical descriptions of their behaviour.

2.2 An interacting gas

In the previous section, we considered Bose-Einstein condensation in purely thermodynamic terms as a quantum-statistical phase transition which occurs in the absence of interactions between particles. What happens if we want to include interactions? The usual method is to make the *mean-field approximation*, which allows interactions between all N particles in the gas to be described by a single interaction term $\mathrm{H_{int}}$ in the Hamiltonian [89]. For an interacting gas in an external potential V_{ext}, the mean-field Hamiltonian takes the form

$$\mathrm{H} = \mathrm{H_0} + \mathrm{V_{ext}} + \mathrm{H_{int}}. \tag{2.6}$$

The mean-field approximation is often described alongside (and is sometimes equated with) the *Hartree approximation* [92], which allows us to write the wave function of an N-body system as the product of N single-particle wave functions. For a fully condensed sample, all bosons will be in the same single-particle state $\phi(\mathbf{r})$; hence we can write the condensate wave function Φ as

$$\Phi(\mathbf{r}_1, \mathbf{r}_2, \ldots, \mathbf{r}_N) = \prod_{i=1}^{N} \phi(\mathbf{r}_i), \tag{2.7}$$

where the $\phi(\mathbf{r}_i)$ are *e.g.* the ground state wave functions of a harmonic oscillator, and are normalised to one. The *Bogoliubov approximation* assumes

that the non-condensate fraction of the system can be treated as a perturbation. This approach is used in more technical explanations of mean-field theory [89], where the Hamiltonian is initially written in terms of second-quantised field operators $\hat{\Psi}(\mathbf{r})$ and $\hat{\Psi}^{\dagger}(\mathbf{r})$, and then approximated to a form which includes only the condensate wave function Φ.

For some condensed systems, the mean-field treatment is a very bad approximation indeed, and breaks down on one or more of the conditions listed above. Interactions between superfluid helium atoms, for example, prevent more than ~10% of atoms from being the ground state even at temperatures very close to absolute zero [93]. The liquid nature of the helium system means that multi-body interactions and non-condensed fractions cannot be ignored or treated as perturbations, making helium condensates very difficult to describe theoretically.

In alkali gases like the mixtures of rubidium and caesium atoms which are the primary focus of this work, the interparticle separation is much greater than for He atoms in a superfluid. This does not mean that interparticle interactions in alkali gases are negligible. Indeed, some of the most fascinating phenomena in cold and ultracold atomic physics arise from interactions between particles. It is, however, often sufficient to consider only two-body interactions, for which theoretical treatments are comparatively tractable. For a low-energy, dilute gas, the interaction Hamiltonian $\mathrm{H_{int}}$ can be approximated by a contact potential (delta function) because the interparticle separation is usually much greater than the range of the attractive or repulsive forces between atoms [92]. At very low temperatures, the interactions between two identical bosons can be characterised by a single parameter: the s-wave scattering length a. This quantity is discussed in more detail in the next section. For the moment, we simply use it to write an expression for the Hamiltonian at low energies:

$$H = \sum_{i=1}^{N} \left(\frac{\hat{\mathbf{p}}_i^2}{2m} + V_{\mathrm{ext}}(\hat{\mathbf{r}}_i) \right) + g \sum_{i<j} \delta(\hat{\mathbf{r}}_i - \hat{\mathbf{r}}_j), \tag{2.8}$$

where the coefficient of the interaction term g is defined as [92]

$$g = \frac{4\pi\hbar^2 a}{m}. \tag{2.9}$$

Using this Hamiltonian, we can write the well-known Gross-Pitaevskii equa-

tion (GPE) which describes the time-evolution of the trapped condensate:

$$i\hbar\frac{\partial}{\partial t}\Phi(\mathbf{r},t) = \left(\frac{-\hbar^2}{2m}\nabla^2 + V_{\text{ext}}(\mathbf{r}) + g|\Phi(\mathbf{r},t)|^2\right)\Phi(\mathbf{r},t), \tag{2.10}$$

where the number density $n(\mathbf{r}) = |\Phi(\mathbf{r},t)|^2$. Again using the mean-field approximation, the condensate wave function $\Phi(\mathbf{r},t)$ can be expressed as the product of a real part $\phi(\mathbf{r})$ and a time-dependent exponential $e^{-i\mu t/\hbar}$, where ϕ is normalised to the total number of atoms N. After minimising the energy of the system [92], we find the time-independent form of the GPE:

$$-\frac{\hbar^2}{2m}\nabla^2\phi(\mathbf{r}) + V(\mathbf{r})\phi(\mathbf{r}) + g|\phi(\mathbf{r})|^2\phi(\mathbf{r}) = \mu\phi(\mathbf{r}), \tag{2.11}$$

where μ is the chemical potential. These equations have the form of a non-linear Schrödinger equation, with the nonlinear term proportional to the number density and the scattering length. In the absence of interactions, Eq. 2.11 reduces to a linear Schrödinger equation. By contrast, the *Thomas-Fermi approximation* eliminates the kinetic energy term and concentrates on condensate behaviour due to the interactions (and external potential) alone. The conditions under which this approximation is valid are discussed in the next section.

2.3 Scattering theory

Quantum scattering theory is a well-established field with applications to a wide variety of physical systems. The purpose of this section is not to review scattering theory, but to define terms and introduce equations which are most necessary for understanding the role of scattering in cold and ultracold mixtures of rubidium and caesium. Detailed discussions of the aspects of scattering theory with greatest relevance for cold atomic gases may be found in numerous textbooks [92, 94–97] and theses [98–101].

The main scattering process of relevance for cold, dilute gases is two-body elastic scattering. Both evaporative and sympathetic cooling rely on elastic collisions between atoms to reduce the temperature of a sample. An unfavourable ratio of elastic ('good') collisions to inelastic ('bad') collisions has proved a serious stumbling block in efforts to cool some species of atoms,

notably caesium, to quantum degeneracy [68, 69]. The experimental apparatus described in this thesis was designed to study the collisional properties of a mixture of ^{87}Rb and ^{133}Cs, with an eye towards potentially overcoming the difficulties presented by cooling caesium alone. An understanding of the basic principles of elastic collisions is therefore essential.

2.3.1 Elastic scattering cross section

The Hamiltonian for the relative motion of two colliding atoms of mass m_1 and m_2 is

$$\mathrm{H} = \frac{\mathbf{p}^2}{2\mathrm{M}} + \mathrm{V}(\mathbf{r}), \tag{2.12}$$

where $\mathbf{r} = \mathbf{r_1} - \mathbf{r_2}$ and $\mathbf{p} = \mathbf{p_1} - \mathbf{p_2}$, with $M = m_1 m_2/(m_1 + m_2)$ being the reduced mass of the system. The eigenstates of this Hamiltonian with energy $E_k = \hbar^2 k^2/2M$ are the scattering states of the relative motion $\psi_k(\mathbf{r})$. The solutions to the Schrödinger equation for this Hamiltonian take the form

$$\psi_k(r) = e^{ikz} + f(\mathbf{k})\frac{e^{ikr}}{r}, \tag{2.13}$$

where $\mathbf{k}$ is the wave vector of the scattered wave, $f(\mathbf{k})$ is the scattering amplitude, and we have assumed that the potential vanishes as $r \to \infty$. The first term in Eq. 2.13 is an incoming plane wave, while the second is the scattered wave.

The scattering amplitude is related to the scattering cross section $\sigma(\mathbf{k})$ according to

$$\sigma(\mathbf{k}) = \int |f(\mathbf{k})|^2 d\Omega. \tag{2.14}$$

If we assume that the interaction between the atoms is spherically symmetric, we can write the scattering amplitude in terms of the scattering angle θ:

$$f(\theta) = \frac{1}{2ik}\sum_{l=0}^{\infty}(2l+1)(e^{i2\delta_l} - 1)P_l(\cos\theta). \tag{2.15}$$

Here, $l = 0, 1, 2, \ldots$ denotes the contribution of $s, p, d, \ldots$ partial waves to the total scattering amplitude, δ_l are the phase shifts associated with each partial wave, and $P_l(\cos\theta)$ are Legendre polynomials. The full derivation of Eq. 2.15 can be found in Refs. [92] and [95]. Substituting this expression

into 2.14 and performing the integral over the full solid angle $0 \leq \theta \leq \pi$, $0 \leq \phi \leq 2\pi$ (ϕ being the azimuthal angle) yields

$$\sigma(k, \delta_l) = \frac{4\pi}{k^2} \sum_{l=0}^{\infty} (2l+1) \sin^2 \delta_l. \tag{2.16}$$

Up to this point, we have said very little about the properties of the particles being scattered, and have in fact assumed implicitly that they are distinguishable. If the particles are indistinguishable bosons (fermions), the ψ_k must be (anti)symmetric under interchange of the coordinates of the two particles, *i.e.* $\mathbf{r} \rightarrow -\mathbf{r}$, $\theta \rightarrow \pi - \theta$, $\phi \rightarrow \pi + \phi$. Taking into account the symmetries of the particles and the potential, Eq. 2.13 becomes

$$\psi_k = e^{ikz} \pm e^{-ikz} + (f(\theta) \pm f(\pi - \theta)) \frac{e^{ikr}}{r}, \tag{2.17}$$

where the plus sign applies to bosons and the minus sign to fermions. To find the scattering cross section for indistinguishable particles, we must change the limits of the integral in 2.14 to half the full solid angle to avoid double-counting. The result is a cross-section with *twice* the amplitude for classical particles,

$$\sigma(k, \delta_l) = \frac{8\pi}{k^2} \sum_{l=0}^{\infty} (2l+1) \sin^2 \delta_l. \tag{2.18}$$

Finally, it is worth noting that due to the $(-1)^l$ parity of the Legendre polynomials, the requirement that ψ_k be symmetric for identical bosons means that only even-l partial waves can contribute to the total scattering cross section. For fermions the reverse is true, and the suppression of s-wave scattering makes it impossible to achieve quantum degeneracy in single-species fermi gases. As discussed in the introduction, adding a second species reintroduces s-wave collisions to the system, and degeneracy of the target species is reached via sympathetic cooling with the second. A similar line of reasoning shows that although p-wave scattering is suppressed for single-species bosonic gases, this is not true for mixtures of two different bosonic species except at low temperatures. The next two subsections examine scattering in the limits of interest for our Rb-Cs system.

2.3.2 Low-energy elastic scattering

At low energies, the scattering cross section for bosons is dominated by the $l = 0$ term. This is because particles with nonzero angular momentum experience a centrifugal barrier in addition to the bare atom-atom interaction potential $V(r)$ [95]. If their relative kinetic energy is less than the barrier they never achieve interparticle separations where $V(r)$ is non-negligible, and scattering does not take place. For simplicity we will continue to approximate $V(r)$ as the contact interaction; for a discussion of scattering from other potentials, see *e.g.* Ref. [101]. In the $l = 0$ limit, Eq. 2.18 reduces to

$$\sigma = \frac{8\pi}{k^2} \sin^2 \delta. \tag{2.19}$$

It is often useful to express the phase shift in terms of an s-wave scattering length a. The relation between the two is [94]:

$$k \cot \delta = -\frac{1}{a} + \frac{1}{2} r_{\text{eff}} k^2 + O(k^4), \tag{2.20}$$

where the first-order correction term r_{eff} is known as the effective range. Setting this to zero for the moment, we can combine Eqs. 2.19 and 2.20 to write the scattering cross-section in terms of a:

$$\sigma = \frac{8\pi a^2}{1 + k^2 a^2}. \tag{2.21}$$

This relation has two important limits. For $ka \ll 1$, the scattering cross-section is $8\pi a^2$, equivalent to scattering from a hard sphere of radius a, and is independent of energy. When the modulus of the scattering length is much larger than the de Broglie wavelength of the scattered particles, *i.e.* $ka \gg 1$, the scattering cross-section reaches the *unitarity limit*, where

$$\sigma = \frac{8\pi}{k^2}. \tag{2.22}$$

In this regime, the scattering cross-section is independent of the scattering length. This state of affairs is associated with a phenomenon known as a *zero-energy resonance*. These resonances occur when the inter-atomic potential $V(r)$ is deep enough to support bound molecular states, and the energy of the last molecular bound state is close to the energy of the scattering state. When the depth of the potential is just less than the threshold for a new

bound state to appear, the scattering length is large and negative. If the potential depth is just higher than the threshold, the scattering length is large and positive [102]. The resonance occurs at the threshold, where a diverges.

The sign of the scattering length has important implications for the stability of Bose-Einstein condensates. For $a < 0$, the interaction between atoms is attractive, while for $a > 0$ it is repulsive. Attractive interactions lead to an increase in density at the centre of the condensed cloud, and for atom numbers above a critical value $N_{\rm cr}$ the kinetic energy of the atoms is no longer sufficient to prevent the condensate from collapsing [42]. In the case of repulsive interactions, the condensate is stable. In the limit that $Na/a_{\rm ho} \gg 1$ ($a_{\rm ho}$ is the harmonic oscillator length $(\hbar/m\omega)^{1/2}$), we can make the Thomas-Fermi approximation, under which the interaction term in the GPE is assumed to dominate the condensate behaviour and the kinetic energy term is neglected. This greatly simplifies the form of the solutions to the GPE, which is especially important for mixed-species BECs [44, 45]. The implications of positive and negative scattering lengths for a mixture will be discussed later in this chapter.

What happens if we include the effective range correction? If we substitute Eq. 2.20 into Eq. 2.19, we find

$$\sigma = \frac{8\pi a^2}{k^2a^2 + \left(\frac{1}{2}k^2 r_e a - 1\right)^2}. \tag{2.23}$$

The value of this approximation is that it is accurate even for large magnitudes of the scattering length, as discussed in Ref. [103] and shown graphically in Ref. [98]. This is particularly important for Cs, which in the $F = 3, m_F = \pm 3$ state has a scattering length with a magnitude of almost 3000 times the Bohr radius a_0 at zero magnetic field [74].

2.3.3 Higher partial waves

If the scattered atoms have a relative kinetic energy higher than the centrifugal potential barrier, the approximation that only s-wave collisions contribute to the total scattering cross-section is no longer valid. The form of

the centrifugal potential is [41, 94]

$$V_{\text{rep}} = \frac{\hbar^2 l\,(l+1)}{2Mr^2}. \tag{2.24}$$

Hence, the minimum energy required for higher-l partial waves to contribute is given by

$$E_l = \frac{\hbar^2 l\,(l+1)}{2M(R_{\text{min}})^2} - \frac{C_6}{(R_{\text{min}})^6}, \tag{2.25}$$

where C_6 is the van der Waals coefficient[2], M is the reduced mass and R_{min} is the radius at which the effective potential $\hbar^2 l(l+1)/(2Mr) - C_6/r^6$ reaches its maximum value, given by

$$(R_{\text{min}})^2 = \left(\frac{6MC_6}{\hbar^2 l(l+1)}\right)^{1/2}. \tag{2.26}$$

Figure 2.2 shows the van der Waals potential $-C_6/r^6$ and V_{rep} for $l = 1$ (solid blue line) and $l = 2$ (solid red line). The physical meaning of E_l and R_{min} is apparent from the sums of the two potentials (dashed lines).

For Rb-Rb and Cs-Cs scattering, the next allowed partial wave in the expansion is $l = 2$. Using the C_6 values found in Ref. [104], we see from Eq. 2.25 that the energy threshold at which d-wave scattering begins to contribute is approximately 420 μK for ^{87}Rb and 180 μK for Cs. To put these values into an experimental context, typical temperatures for Rb and Cs atoms in a well-optimised magneto-optical trap (MOT) are below 100 μK, while T_c for the alkali metals is typically measured in tens of nK. We will therefore treat the d-wave contribution to the scattering cross-section as negligible.

The threshold for p-wave scattering is lower, and for mixtures of two different bosonic species we have already noted that p-wave collisions are not suppressed as they are for a pure sample of Rb or Cs. Taking the value of the Rb-Cs C_6 from Ref. [105], we find that the threshold for p-wave scattering is approximately 56 μK — still well above the threshold for condensation, but cold enough to contribute in the MOT and during evaporative cooling in the magnetic trap. Table 2.1 contains a list of C_6 coefficients and scattering thresholds relevant to the Rb-Cs system.

[2]Literature values of the van der Waals coefficient are often given in atomic units. To convert into units appropriate for Eq. 2.25, one must multiply by a_0^6 and the Hartree energy $E_h = \hbar^2/(m_e a_0^2)$, where m_e is the electron rest mass and a_0 is the Bohr radius.

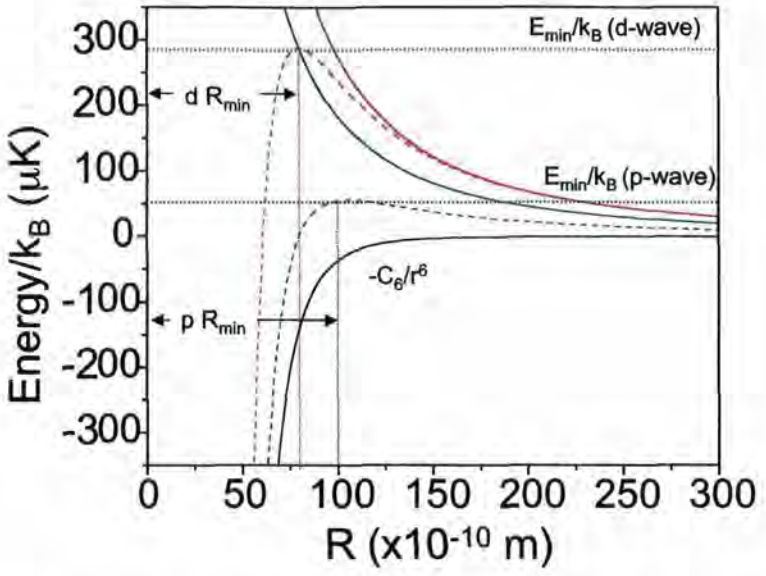

Figure 2.2: Scattering potentials for Rb-Cs. The solid black line indicates the van der Waals potential $-C_6/r^6$. Solid blue (red) lines show the potential barriers for p-wave (d-wave) scattering. Dashed lines indicate the sum of repulsive and attractive terms for p-wave (blue) and d-wave (red) scattering. The height of the potential barriers indicate that d-wave scattering will only occur at temperatures $\geq 290\mu$K, while the threshold for p-wave scattering is approximately 56 μK.

From Eq. 2.16, we find that the cross-section for s and p waves is:

$$\sigma_{s,p} = \frac{4\pi}{k^2}\left(\sin^2\delta_0 + 3\sin^2\delta_1\right). \tag{2.27}$$

We can generalise our expression in Eq. 2.20 to account for higher partial waves, with the result that the scattering length for the lth partial wave is related to the scattering cross-section by

$$k^{2l+1}\cot\delta_l = -\frac{1}{a_l} + \frac{1}{2}r_l k^2 + O(k^4) \tag{2.28}$$

where we have substituted an l-dependent effective range for the earlier $l = 0$ value. Combining equations as before, we find that the cross-section for p-wave scattering is

$$\sigma_p = \frac{12\pi a_1^2 k^4}{1 + a_1^2 k^6}. \tag{2.29}$$

Note that this cross-section vanishes as $k \to 0$, as required.

	Rb-Rb	Cs-Cs	Rb-Cs
C_6	4691	6851	5284
p-wave	N/A	N/A	56 μK
d-wave	410 μK	180 μK	290 μK

Table 2.1: C_6 values (in atomic units) and scattering thresholds for the Rb-Cs system. Single-species C_6 values are taken from Ref. [104]; the Rb-Cs value is from Ref. [105].

2.4 Feshbach resonances

So far, we have treated atoms as structureless particles, for which only elastic collisions are possible. Inelastic collisions are more complicated, because the scattered atoms can be in different internal states – or, in the language of scattering theory, the incident and outgoing scattering channels are no longer the same, and multiple channels may contribute to the total scattering potential. Chapters 3 and 5 discuss inelastic collisions in the context of a two-species MOT, but for the moment, we will consider only one phenomenon associated with inelastic scattering: Feshbach resonances[3].

As with zero-energy resonances, the change in scattering length near a Feshbach resonance occurs due to a coupling between the scattering state and the last bound state of the potential. For inelastic Feshbach resonances, the coupling occurs between the last bound state and *different* incoming and outgoing channels. For ground state atoms, these two channels are provided by different atomic hyperfine states. The energy of these states exhibits a magnetic field dependence via the Zeeman effect. By changing the magnetic field, a bound state supported by one scattering channel (closed channel) can be shifted into degeneracy with the scattering state of a second (lower energy) channel. This is illustrated in Figure 2.3. The result is that in the vicinity of a Feshbach resonance, the magnitude (and the sign) of the atoms' scattering length can be tuned over a wide range simply by changing the external magnetic field. The behaviour of the scattering length as a function

[3]Elastic Feshbach resonances are also possible, *e.g.* in the $|F = 3, m_F = +3\rangle$ state of Cs. For the purposes of this thesis and the related work described in Ref [84], we are primarily interested in inelastic resonances.

of the magnetic field B is given by

$$a(B) = a_{\text{bkgd}} \left(1 - \frac{\Delta B}{B - B_{\text{res}}}\right), \tag{2.30}$$

where a_{bkgd} is the scattering length far from resonance, ΔB is the width of the resonance and B_{res} is its position. The width of the resonance depends on the magnetic moment of the bound state and the coupling strength between the bound and scattering states.

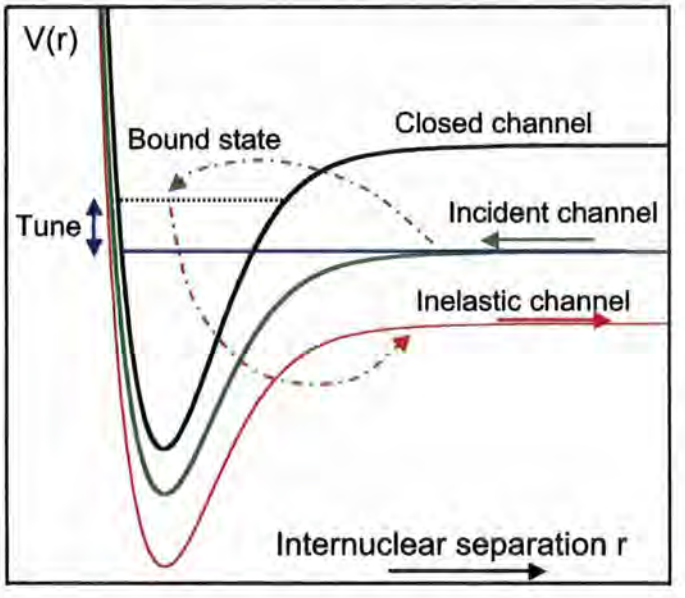

Figure 2.3: Illustration of scattering near an inelastic Feshbach resonance. Changing the magnetic field tunes the bound state supported by the closed channel into resonance with the incident channel, inducing a coupling to a lower-energy inelastic channel. Figure adapted from [98] and [106].

As the Gross-Pitaevskii equation (2.11) shows, changing the scattering length changes the strength of the interactions between the atoms. The importance of this tunability can hardly be overstated; indeed, Feshbach resonances have been compared to a 'magic dial' which would allow experimenters to alter the force of gravity at will! The tuneability of atomic interactions in the vicinity of a Feshbach resonance has been exploited experimentally for a number of purposes, including the creation of cold molecules [23] and solitons

[17, 18], the study of collapsing Bose-Einstein condensates [42], and investigations of the BEC-BCS crossover in fermionic systems [107–110]. They are also the subject of a rich theoretical literature (see, for example, Refs. [111–113]). The next section discusses their potential uses in a two-species mixture.

2.5 Two-species quantum degeneracy

To describe the behaviour of a two-species quantum degenerate gas using the mean-field approach, a second nonlinear term must be added to the Gross-Pitaevskii equations for the ground state of each species. The new term is proportional to the *interspecies* scattering length a_{12}, and represents interactions between the two species. The coupled equations are [44, 114]:

$$\begin{aligned}\left[-\frac{\hbar^2}{2m_1}+V_1(\mathbf{r})+g_{11}|\psi_1|^2+g_{12}|\psi_2|^2\right]\psi_1 &= \mu_1\psi_1 \\ \left[-\frac{\hbar^2}{2m_2}+V_2(\mathbf{r})+g_{12}|\psi_1|^2+g_{22}|\psi_2|^2\right]\psi_2 &= \mu_2\psi_2,\end{aligned} \tag{2.31}$$

where the coupling constants are defined as

$$\begin{aligned}g_{11} &= \frac{4\pi\hbar^2 a_{11}}{m_1} > 0 \\ g_{22} &= \frac{4\pi\hbar^2 a_{22}}{m_1} > 0 \\ g_{12} &= 2\pi\hbar^2 a_{12}\left(\frac{m_1+m_2}{m_1 m_2}\right).\end{aligned} \tag{2.32}$$

The solutions to these coupled equations are discussed in many theoretical works; see, for example, Refs. [19, 44, 45, 114–116] and references therein. A number of factors dictate the form of the solutions. Firstly, there is the question of the relative separation of the two species, which is proportional to their trap frequencies and the gravitational acceleration g. If the two species have different masses (and, for magnetically-trapped mixtures, different magnetic moments), it is possible for the two condensates not to overlap at all, in which case the equations in 2.32 are no longer coupled.

Less trivial interaction regimes can be studied by examining the effects of different magnitudes and signs of each of the coupling constants on the

solutions. A useful parameter is the relative strength of the interactions Δ, which we define here as

$$\Delta = \frac{g_{12}}{\sqrt{g_{11}g_{22}}} \simeq \frac{a_{12}}{\sqrt{a_{11}a_{22}}}. \tag{2.33}$$

Note that a_{11} and a_{22} are assumed to be positive, for convenience [44].

2.5.1 Interaction regimes

The behaviour of the two-species quantum degenerate mixture for different values of Δ is illustrated in Figure 2.4. There are three distinct regimes of interest.

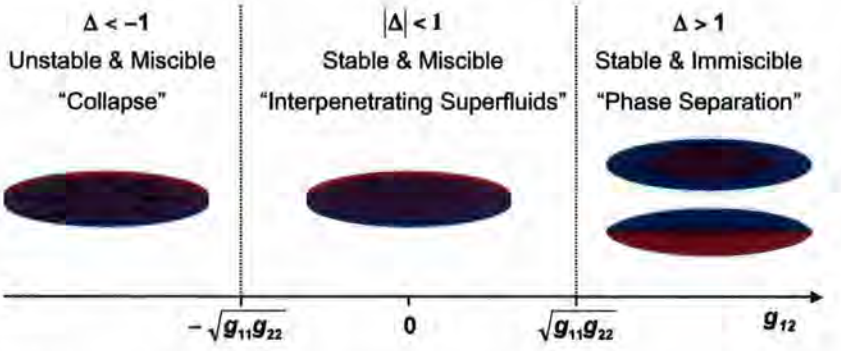

Figure 2.4: Behaviour of a two-species quantum degenerate gas at different relative interaction strengths.

Collapse

For $\Delta < -1$, the interspecies scattering length a_{12} is both negative and greater in magnitude than the geometric mean of the two single-species scattering lengths. In this case, the attractive interspecies interactions will dominate condensate behaviour, and lead to a collapse [19, 114]. Mathematically, the two BECs will only 'overlap' if there is a 'hole' in the condensate where both single-species wavefunctions vanish. This is not overlap in any physically meaningful sense.

Interpenetrating superfluids

For $|\Delta| < 1$, the interspecies scattering length may be either positive or negative, but its magnitude smaller than $\sqrt{a_{11}a_{22}}$. In this regime, the two condensates will be both stable and miscible. This is true even if the interspecies scattering length is negative, provided the restriction on the magnitude of $|\Delta|$ is not violated.

Phase separation

A final scenario occurs if $\Delta > 1$. In this case, a strong mutual repulsion leads to a phase separation between the two condensates. The ^{41}K-^{87}Rb condensate first reported in Ref. [6] fell into this category.

2.5.2 Towards a tuneable mixture

In the previous section, we saw that Feshbach resonances allow the scattering length of a single-species cold gas to be tuned to a range of values simply by changing the magnetic field. For mixtures, one can perform experiments in which Feshbach resonances in one or both components of the two-species quantum degenerate gas allow Δ to be tuned between two or more regimes, facilitating the creation of heteronuclear cold molecules [23]. Interspecies Feshbach resonances, such as those described in Refs. [46–50] should allow even greater flexibility in tuning the value of Δ.

Chapter 3

Colder, slower, denser: atom cooling and trapping

Laser cooling of atoms is an extremely useful technique with a distinguished pedigree, having been either directly [117–119] or indirectly [87, 120] the subject of six Nobel prizes in less than five years. It has led not only to useful tools such as the magneto-optical trap [121] and atomic clocks [122] but to a redefinition within the atomic physics community of what it means to be 'cold': with temperatures as low as a few μK readily achievable in magneto-optical traps, the use of few-kelvin cryogenic techniques has become unnecessary for cooling alkali metal atoms.

Laser cooling does have limits, however, and although the limiting temperature is colder than was first thought (Section 3.2), the magneto-optical trap (MOT) alone is not capable of producing a quantum degenerate sample. For cooling beyond the MOT, atoms must be transferred into traps which confine atoms using either magnetic or optical fields alone. Degeneracy is achieved in such traps after a period of evaporative cooling.

This chapter is intended to provide an overview of the theory behind the atom cooling and trapping techniques which were used in the Rb-Cs mixture experiment (Chapters 4–5). Optical trapping, which features prominently in future plans for this experiment (see Chapter 8) is also discussed briefly.

3.1 Laser cooling

This section begins with an informal description of laser cooling which is aimed chiefly at novice readers, and is intended to illuminate the ideas behind laser cooling in a qualitative way. The physics of laser cooling have been reviewed extensively in the literature; see *e.g.* Refs. [97, 123–125]. Here we will concentrate on the most prominent and important features needed to understand the operation of a magneto-optical trap.

3.1.1 A (mostly) qualitative description

Suppose a bowling ball is flying through the air towards you. Fortunately, you are armed with a gun which uses ping-pong balls as ammunition, and you begin to fire these at the bowling ball. Although the momentum of each ping-pong ball is very small, the *total* momentum of *all* the balls is enough to slow and even (hopefully!) stop the bowling ball before it hits you in the face.

If we replace the bowling ball with a heavy atom (such as rubidium or caesium) and the ping-pong ball gun with a laser 'firing' photons, we begin to understand the basic idea behind laser cooling. Atoms in a laser beam experience a momentum kick of $\hbar\mathbf{k}$, with the wavevector $\mathbf{k}$ directed along the axis of beam propagation, every time they absorb a laser photon. When the photon is spontaneously emitted, the direction of the emission is random. The net change of momentum due to spontaneous emission is therefore zero, but the stream of laser photons reduces the atom's velocity in the $-\mathbf{k}$ direction by $\hbar k/m$ for every photon absorbed (Figure 3.1). After several thousand absorption-emission cycles, an alkali metal atom which was initially at room temperature, with a velocity of hundreds of meters per second, will have been slowed down to just a few meters per second. If the slowed atomic sample is allowed to rethermalise, its temperature will also be reduced.

Although the mechanical effect of light on atoms was first observed in 1933 using a sodium lamp [126], light from a laser has the advantages of being intense, monochromatic, and tuneable. The effects of intensity are discussed in the next section, but the need for a tuneable and monochromatic light source can be explained qualitatively. In order for an atom to absorb

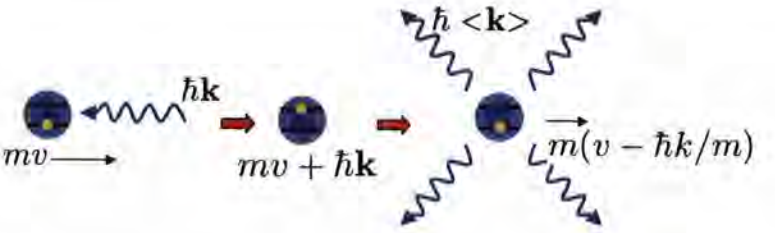

Figure 3.1: Laser cooling schematic. An atom with momentum mv absorbs a photon with momentum $\hbar\mathbf{k}$ traveling in the opposite direction. The atom is now in an excited state, with momentum equal to the sum of the initial atom and photon momenta. After spontaneously emitting a photon in a random direction, the atom is again in the ground state, with a new velocity $v' = v - \hbar k/m$.

a photon, the frequency of that photon cannot be either 'too hot' (high frequency) or 'too cold' (low frequency): it must be 'just right.'[1] Naively, one might assume that the 'just right' frequency would correspond to the resonant frequency ω_0 of an atomic transition. In fact, for laser cooling to work the frequency of the light must be lower than ω_0. This is due to the Doppler effect. In the atom's reference frame, an atom moving towards the photon source will see a photon which appears to have a higher frequency (blue detuned) than it would if the relative atom-photon velocity were zero, $\omega' = \omega + kv$. For red-detuned light, photons with wavevectors opposite the atoms' direction of motion will be Doppler shifted onto resonance. These photons will therefore be absorbed preferentially, leading to the atom being slowed in the direction of the beam.

This 1-D cooling effect can be generalised to three dimensions by adding more beams. Atoms located at the intersection of three mutually orthogonal counterpropagating beam pairs are literally slammed six ways from Sunday by the laser photons, producing three-dimensional cooling. This phenomenon is called *optical molasses*, and was first demonstrated by Chu *et al.* in 1985 [127]. The terminology is apt, as it brings to mind the image of an atom struggling through a viscous sea which retards its motion in all directions.

[1] Attempts by the author to introduce the term 'optical Goldilocks effect' for this behaviour have so far met with little success.

3.1.2 Mathematical description

The force on an atom due to scattering light from a laser field is given by

$$\mathbf{F} \equiv \hbar \mathbf{k} R, \tag{3.1}$$

where the scattering rate R for a two-level atom is

$$R = \frac{\Gamma}{2} \frac{I/I_{\text{sat}}}{1 + I/I_{\text{sat}} + 4(\Delta/\Gamma)^2}, \tag{3.2}$$

with $\Delta = \omega_{\text{L}} - \omega_0$ the detuning from resonance and I the intensity of the field. We have chosen the convention that the linewidth $\Gamma = 1/\tau$, where τ is the natural lifetime of the excited state[2]; under this definition of Γ the saturation intensity is defined as

$$I_{\text{sat}} \equiv \frac{2\pi^2 \hbar \Gamma c}{3\lambda^3}. \tag{3.3}$$

The intensity dependence of the scattering rate arises from the population dynamics of the two-level atom, which are described by the optical Bloch equations presented in Chapter 6. For the moment we simply note that the scattering rate is proportional to the probability of the excited state being occupied, ρ_{bb}, with Γ as the constant of proportionality. This makes physical sense: as the intensity of the light increases, the atom spends a larger fraction of its time in the excited state. In the limit that $I \gg I_{\text{sat}}$, $\rho_{bb} \to 1/2$; hence, the maximum deceleration due to the scattering or spontaneous force for a single beam is

$$a_{\text{max}} = \frac{\Gamma}{2} \frac{\hbar k}{m}. \tag{3.4}$$

For a pair of counterpropagating beams, the net force on the atoms is

$$F = \frac{\Gamma}{2} \hbar k \frac{I/I_{\text{sat}}}{1 + I/I_{\text{sat}} + 4\left(\frac{\Delta - kv}{\Gamma}\right)^2} - \frac{\Gamma}{2} \hbar k \frac{I/I_{\text{sat}}}{1 + I/I_{\text{sat}} + 4\left(\frac{\Delta + kv}{\Gamma}\right)^2}, \tag{3.5}$$

where $\Delta' = \Delta \pm kv$ has been substituted for Δ to account for the Doppler shift. Note that atoms at rest experience no net force, but for near-zero velocities the force depends linearly on the atomic velocity (Figure 3.2):

$$F \simeq \frac{8\hbar k^2 \frac{\Delta}{\Gamma} I/I_{\text{sat}}}{\left(1 + I/I_{\text{sat}} + 4(\Delta/\Gamma)^2\right)^2} v = -\alpha v. \tag{3.6}$$

[2]Note that we have expressed Γ in angular units. This means that Γ for e.g. Rb is $\sim 6 \times 2\pi$ MHz, corresponding to a lifetime of $\sim$27 ns. This convention is used throughout this work.

The negative velocity dependence indicates that the force is frictional, opposing the motion of an atom. This is the origin of the viscous optical molasses described in the previous section.

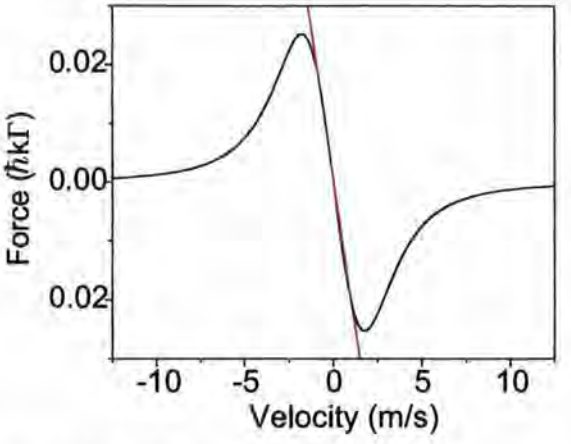

Figure 3.2: A plot of Eq. 3.5 shows that for velocities near zero, the spontaneous force due to two counterpropagating beams depends linearly on $-v$. The red line shows a linear fit to Eq. 3.5 for $|v| < 1$. The viscous medium this force creates is known as optical molasses.

3.2 Limits of laser cooling

Based on the analysis which produced Eqs. 3.5 and 3.6, there does not seem to be any reason why optical molasses alone cannot cool a sample of atoms to zero velocity and zero temperature. In fact, there are several processes which limit the degree of cooling possible, although some limits are more limiting than others.

3.2.1 Doppler limit

The Doppler limit is derived by balancing the effects of the cooling processes discussed so far with heating due to spontaneous emission. The limiting Doppler temperature is [124, 125]

$$T_D = \frac{\hbar\Gamma}{2k_B}. \tag{3.7}$$

For alkali metal atoms, $\Gamma/2\pi$ is on the order of several MHz, yielding T_D values of a few hundred μK. Spontaneous emission heats the atoms because at very low temperatures, the momentum kick due to a single absorption-emission cycle produces a significant change in the atom's velocity, even though the mean velocity change from all momentum kicks is zero. The preferential absorption of 'incoming' red-detuned photons due to the Doppler effect vanishes for atoms with zero mean velocity, so the atoms are equally likely to absorb photons from any of the counterpropagating beams. The result is a random walk, which acts as heating.

3.2.2 Sub-Doppler cooling

Soon after optical molasses was demonstrated in three dimensions, an unusual inversion of Murphy's Law for experimental physics occurred: cooling in an optical molasses was found to work *better* than expected, with temperatures many times less than T_D being observed in laser-cooled sodium [128]. The heating due to spontaneous emission is unavoidable, so the low temperatures had to be the result of some unexpectedly effective cooling mechanisms outside the Doppler model.

The Doppler model breaks down on two points. Firstly, the counterpropagating laser beams cannot be treated independently, as their interference produces gradients in the polarisation of the light field. Secondly, alkali metal atoms are not ideal two-level systems. The omission of these factors means that the model ignores optical pumping, the process by which beams of light with different polarisations drive different transitions between the Zeeman sub-levels of the hyperfine states. The theory behind sub-Doppler cooling is discussed extensively in Ref. [129] and reviewed in [124]; a less technical account may be found in Ref. [130]. The following brief overview is included as an introduction.

Sisyphus cooling

An atom placed in a light field experiences a shift in the energy of its magnetic sublevels due to the presence of the field. The strength of these light shifts (also called AC Stark shifts) is proportional to the atom-light coupling, which

in turn depends on the polarisation of the laser field and the orientation of the atomic dipole. Now let us consider two counterpropagating laser beams of orthogonal linear polarisation, the so-called 'lin ⊥ lin' configuration. The polarisation of this combined light field varies in space along the axis of beam propagation, changing from linearly polarised at 45°, to circularly polarised driving σ^- transitions ($\Delta m_F = -1$), to a perpendicular linear polarisation, to circularly polarised driving σ^+ transitions ($\Delta m_F = +1$), and back to 45° again after a distance of $\lambda/2$ (Figure 3.3). Hence, the light shifts will also vary in space, and an atom moving through the field will experience different light shift potentials at different times.

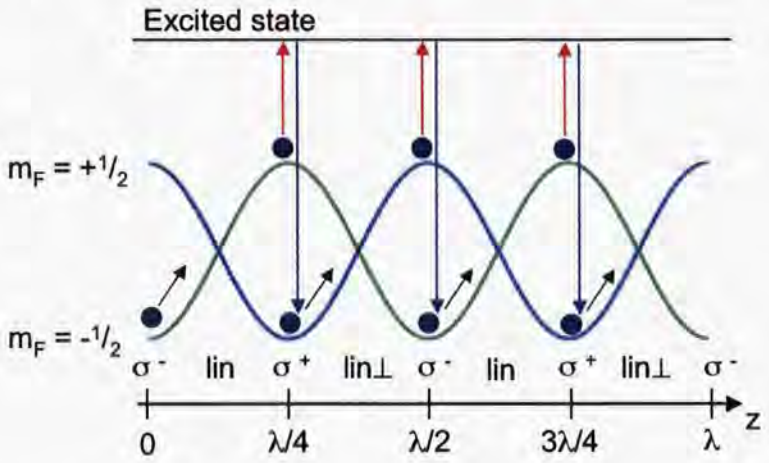

Figure 3.3: Illustration of Sisyphus cooling. A pair of laser beams in the lin ⊥ lin configuration generates a spatially varying light shift potential for atoms in different magnetic sublevels. An atom located at the top of a potential absorbs a photon and can then decay to a different magnetic sublevel, losing energy via the emitted photon.

Suppose an atom in a particular magnetic sublevel absorbs a photon whilst located at the top of a potential. It can then decay by spontaneous emission either to the original level or to a different one. If it decays to a different sublevel, the spontaneously emitted photon will have a higher frequency than the absorbed photon, and the atom will lose energy. Optical pumping processes due to spatial variations in the polarisation ensure that atoms will on average spend more time at the top of the potential 'hills' than at the bot-

tom, and will thus be more likely to scatter photons at the top, losing energy in the process. This is known as *Sisyphus cooling*, because of the analogy with Greek mythology — atoms reach to the top of a potential 'hill' only to decay, after which they must 'roll' back up again.

$\sigma^+ - \sigma^-$ polarisation gradient cooling

The second sub-Doppler cooling mechanism relies on counterpropagating laser beams with opposite circular polarisations. The polarisation of the total field is therefore everywhere linear, driving π transitions ($\Delta m_F = 0$) between the different magnetic sublevels. Atoms at rest will therefore be optically pumped into the $m_F = 0$ state, with lesser fractions of the population in the $m_F = \pm 1$ states.

Moving atoms, however, will experience a rotation of the quantisation axis as they move along the beam. This is because the direction of linear polarisation rotates along the axis of beam propagation, passing through 2π for every wavelength λ it travels. Because the optical pumping process takes a finite amount of time, as the atom moves the population of the $m_F = 0$ states lags behind the polarisation direction. It can be shown that atoms traveling towards the beam driving σ^+ transitions are more likely to have the $m_F = +1$ state populated, with the reverse being true for atoms traveling towards the σ^- beam [129]. In other words, the atoms scatter more photons from the beam towards which they are moving. The result is a viscous force which opposes the direction of motion, slowing and cooling the atoms.

The recoil limit and beyond

As the atoms are cooled via one or both of these sub-Doppler mechanisms, the energy gained from a photon recoil will eventually become equal to or greater than the depth of the spatial potential wells. This is the *recoil limit*, characterised by a temperature T_{rec}

$$k_B T_{\text{rec}} = \frac{\hbar^2 k^2}{2m}, \tag{3.8}$$

which is the temperature at which an atom's r.m.s. velocity is equal to the recoil velocity $v_{\text{rec}} = \hbar k/m$ in each direction. For most alkali metal atoms,

T_{rec} is below 1 μK[3]. At such low temperatures, the atomic de Broglie wavelength (though still shorter than is required for the BEC phase transition) is comparable to the cooling laser wavelength and hence to the extent of the potential wells. It is therefore no longer possible to localise the atomic wavepacket in the potential wells, even if they were deeper than the photon recoil energy.

Because the recoil limit is set by the energy of a single spontaneously emitted photon, it is possible to circumvent it by ensuring that the final state of the atoms is one for which spontaneous emission is not possible. However, for the purposes of this work the recoil limit may be considered fundamental; indeed, the minimum experimentally realised temperature obtained without recourse to sub-recoil methods is approximately $10T_{\text{rec}}$ [125].

3.3 The magneto-optical trap

Even in three dimensions, optical molasses is not a trap. Atoms which drift out of the beam intersection region are then free of the viscous force of the molasses. The magneto-optical trap, or MOT, addresses this problem by adding a magnetic field gradient configured such that an atom moving away from the centre of the trap is Zeeman shifted onto resonance with a laser beam pushing it back.

Like many concepts presented in this chapter, the MOT is best understood by creating a one-dimensional model and then generalising to three dimensions. For simplicity, let us consider an atom with a strongly allowed $F = 0 \rightarrow F' \equiv 1$ transition[4]. We require a field which is linear along the direction z of beam propagation, $B = |\mathbf{B}| = \beta|z|$, where β is the gradient. The Zeeman energy shift is given by [131]

$$\Delta E = \mu_B g_F m_F B, \tag{3.9}$$

where μ_B is the Bohr magneton and g_F is the Landé g-factor. With the zero of the field located at $z = 0$, we obtain the energy level shifts illustrated in

[3]The exception is Li, for which $T_{\text{rec}} \approx 3$ μK.

[4]The technique is applicable to any transition of the form $F \rightarrow F' = F + 1$, *e.g.* the ^{87}Rb $F = 2 \rightarrow F' = 3$ and Cs $F = 4 \rightarrow F' = 5$ cooling transitions used in this work.

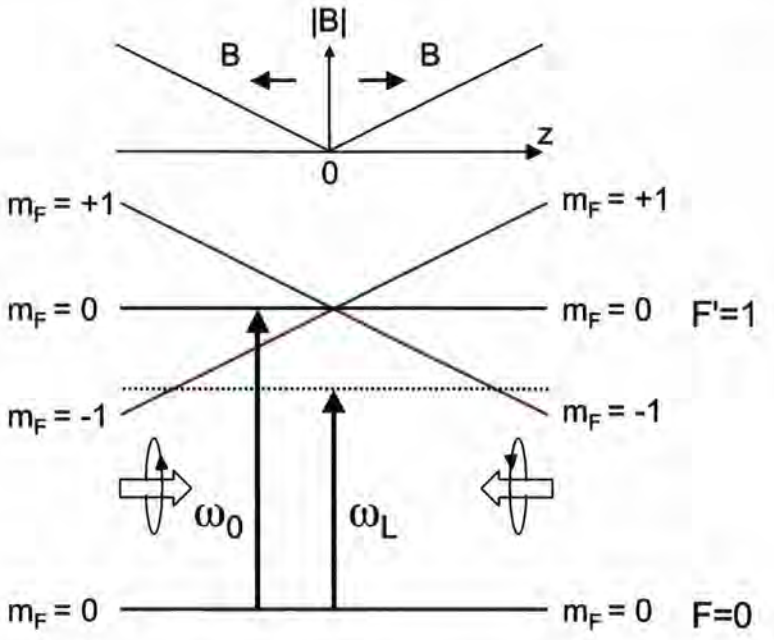

Figure 3.4: Schematic diagram of a 1-D magneto-optical trap on an $F = 0 \rightarrow F'$ transition. The magnetic field B changes direction at the centre. Note that because the polarisation of a beam is defined relative the the magnetic field, both beams will drive σ^- transitions on their way into the trap centre.

Figure 3.4. The figure also shows a pair of counter-propagating laser beams with a frequency ω_L red-detuned from the transition frequency ω_0. Both beams are right-hand circularly polarised, but they drive σ^- (σ^+) transitions when they are propagating against (along) the quantisation axis, which is set by the direction of the magnetic field. The combination of the Zeeman shift and the red-detuning of the beams mean that the $m_F = -1$ level is always closest to resonance with the laser light. Consequently, atoms are more likely to scatter light from the 'incoming' beams, and are therefore pushed towards the centre of the trap, $z = 0$.

A three dimensional MOT can be created by using three orthogonal pairs of counter-propagating beams and a quadrupole field produced by two coils in the anti-Helmholtz configuration, $\mathbf{B} = b(x, y, -2z)$. For alkali metal atoms, a second laser frequency is also needed in addition to the 'cooling' frequency ω_L. We generally think of the cooling light as being red-detuned by a few

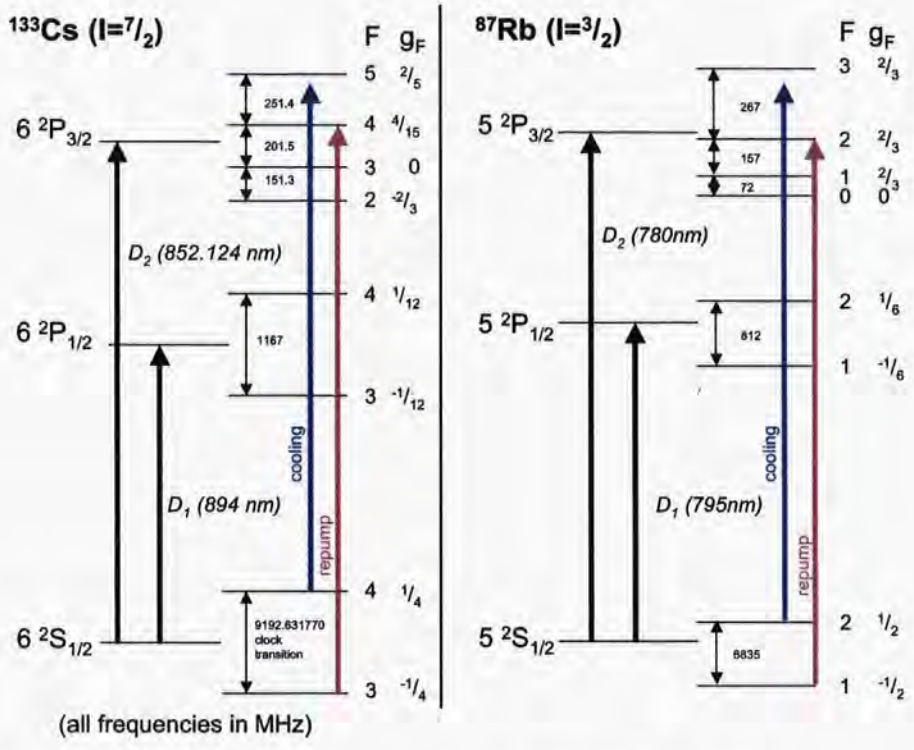

Figure 3.5: Energy level diagrams for ^{133}Cs and ^{87}Rb.

natural linewidths from the $F \rightarrow F' = F + 1$ transition, but this is the same as being very blue-detuned from the $F \rightarrow F' = F$ transition. Consequently, the cooling light will also drive this transition. Atoms in the $F' = F$ excited state can then decay back to the lower hyperfine level of the ground state, which is dark to the cooling light. Hence, a second 'repumping' frequency is needed to pump atoms out of this state and back into the MOT cycle. The level diagrams of Cs and ^{87}Rb in Figure 3.5 show the cooling and repumping frequencies schematically.

3.3.1 Pyramid MOT

In a pyramid MOT, a single beam with polarisation set to drive σ^- transitions is incident on a set of four mirrors in the shape of an inverted pyramid[5]. A

[5]The original pyramid MOT [132] used a conical hollow mirror. The four-mirror configuration is consistent with our realisation of a pyramid MOT (Chapter 4).

series of reflections from these mirrors produces a radiation field with the same configuration of light polarisations as a standard six-beam MOT (Figure 3.6). The first reflection produces a pair of counter-propagating beams with the opposite circular polarisation; the second produces a retro-reflected beam which drives σ^+ transitions. If the mirror assembly is constructed with a small hole at the vertex, aligning the magnetic field zero of the MOT over the hole allows the pyramid MOT to be used as a cold atom source [133].

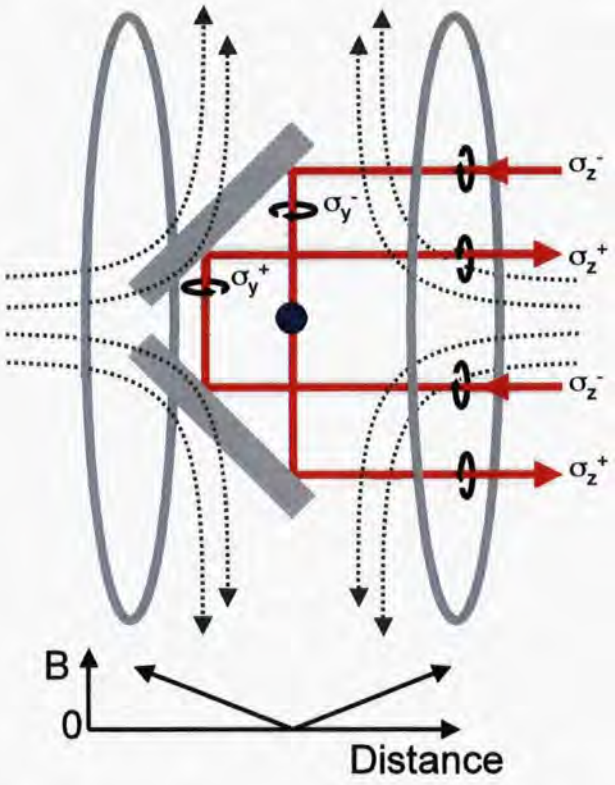

Figure 3.6: Cross-section of a pyramid MOT showing the polarisation configuration resulting from a single input beam propagating along the z axis with σ^- polarisation. The σ labels indicate which transition is being driven by the beam in the vicinity of the label. Dashed lines indicate the direction and shape of the quadrupole field.

3.3.2 Sub-Doppler cooling in a MOT

In our system, the MOT acts as a source of cold atoms for loading into a magnetic trap. Ideally, we would like atoms in the MOT to be as cold, densely packed, and numerous as possible before loading. In practice, there are trade-offs to be made between these criteria. The limits on density will be discussed in the next section; for the moment, we will concentrate on understanding the connection between temperature and atom number.

As the MOT beams are circularly polarised, one might assume that only $\sigma^+ - \sigma^-$ polarisation gradient sub-Doppler cooling would be possible for atoms trapped in a MOT. In fact, Sisyphus (lin $\perp$ lin) cooling is also possible for all atoms not moving directly along one of the beam axes, as the off-axis position dependence of the polarisation is quite complex for a 3D MOT [99]. A more interesting question is whether sub-Doppler cooling processes are actually present in a real MOT. We have seen in our discussion of the MOT field gradient that the direction of polarisation can only be given in terms of the magnetic field. Given their sensitivity to polarisation, does the presence of a magnetic field disrupt sub-Doppler cooling processes?

The short answer is 'yes, but.' Sub-Doppler cooling *can* occur in a MOT, as Steane and Foot demonstrated [134] by measuring sub-Doppler temperatures in their Cs MOT. The problem is that it does not occur everywhere. Earlier studies on sodium had shown that a molasses temperature of half the Doppler-limited value could be obtained in the presence of a 1 G magnetic field. At this field, the Zeeman shift was of the same order as the light shift for the ground state [135]. For higher fields, sub-Doppler cooling can no longer operate. The spatial magnetic field gradient in a MOT means there is a characteristic radius beyond which sub-Doppler cooling will not occur. MOTs which exceed this radius will therefore have a central region characterised by colder temperatures, and an outer region where only Doppler cooling is possible. This separation is not stable, and sub-Doppler temperatures will eventually disappear as the cloud rethermalises [136].

Let us return now to our optimum criteria for loading atoms into a magnetic trap: colder, denser, (numerically) bigger. Due to the spatial limits of sub-Doppler cooling, there is clearly a trade-off to be made between 'very cold' and 'very large' MOTs. One way around this problem is to turn off the MOT

field gradient for a brief (few 10's of ms) period before loading the magnetic trap. In this optical molasses phase, polarisation gradient cooling occurs throughout the atom cloud, producing colder temperatures - at the cost of reduced density as the no-longer-trapped cloud expands in free space.

3.3.3 MOT density

The most important density-limiting process for large MOTs is that in dense atomic clouds, the mean free path of a photon is short, with multiple absorption and emission cycles taking place before photons can escape the atom cloud. The re-radiated light (fluorescence) has a different frequency distribution and polarisation than the incident light; hence, its average absorption cross section $\langle\sigma_F\rangle$ differs from that of the cooling light $\langle\sigma_L\rangle$. The repulsive force between a pair of atoms due to light scattering is of the order [137]

$$F_R = \frac{\langle\sigma_F\rangle\langle\sigma_L\rangle I}{4\pi c r^2}, \tag{3.10}$$

where r is the distance between atoms and c is the speed of light. This force is counteracted by an attractive force between the atoms due to the attenuation of laser light as photons are absorbed. Although more recent research has questioned the physicality of this attraction under some conditions [138], the general idea of a maximum density set by the relative sizes of $\langle\sigma_F\rangle$ and $\langle\sigma_L\rangle$ makes intuitive sense. Methods of calculating these cross sections are discussed in the literature (see *e.g.* Refs. [136, 137, 139]). For present purposes we simply note that the average absorption cross section for re-radiated light is greater than for incident light, leading to a repulsion between the atoms which determines a maximum cloud density. For Cs atoms, the maximum density is of order 10^{11}cm^{-3} [136].

The magnitude of the limiting density is increased for high field gradients and high detunings, as the attractive force is proportional to the gradient and falls off with detuning more slowly than the repulsive force due to re-radiation [139]. Unfortunately, it is not practicable simply to operate the MOT in a steady state under these conditions. This is because increasing the density of the sample leads to an increase in the inelastic collision rate. As we shall see in the next section, such collisions heat the sample and can cause atoms to be lost from the trap. It is, however, possible to compress the MOT via

changes in detuning and gradient for a brief period prior to loading atoms into the magnetic trap, and thus obtain a more dense sample [136, 140]. The experimental operation of this compressed MOT (CMOT) phase for the Rb-Cs mixture experiment is discussed in Chapter 4. The amount of time the atoms spend in the CMOT and optical molasses phases is a balancing act, and the optimum durations are determined by experimental conditions.

3.4 MOT loss mechanisms

Having discussed limits on the temperature and density of atoms in a MOT, we now turn to limits on the *number* of atoms in a MOT. The diameter of the trapping beams is of course one limiting factor, but a more physically interesting constraint is the presence of inelastic collisions in the MOT. If sufficiently energetic, such collisions result in one or more of the colliding atoms gaining enough energy to exit the trap.

Several theoretical models [141] have been developed to account for the collisional processes taking place in the MOT. Calculations based on these models have often been used to explain experimental results. However, in their landmark review of cold collisions, Weiner *et al.* [141] described many instances of agreement as 'fortuitous' and concluded that 'the accord between experiment and theory must be considered unsatisfactory.'

In the absence of a full theoretical model which accurately predicts loss rates for a wide range of trap parameters and atomic species, a more phenomenological approach is often used. In this approach, a simple rate equation is used to model how the number of atoms in a MOT evolves in time. The next two subsections discuss this rate equation for single and two-species MOTs.

3.4.1 Single-species MOTs

The time evolution of a single-species MOT is modeled according to the rate equation

$$\frac{dN_i}{dt} = L - \gamma N_i - \beta_i \int n_i^2 d^3r, \tag{3.11}$$

where N_i is the number of atoms in the MOT, n_i is their density profile, L is the loading rate (*e.g.* from the pyramid MOT), γ represents the loss rate due to collisions with the background gas, and β_i is the loss rate coefficient for light assisted inelastic collisions between cold atoms of the same species. At high densities, collisions with the background gas contribute relatively little to the total loss rate in a UHV environment. The situation is reversed for very low-density MOTs, where cold collisions become less likely and background collisions are the dominant loss process. For the moment we will focus on cold collisions only.

The single-species loss rate coefficient β_i is a 'catch-all' term which encompasses several loss mechanisms. Atoms can be ejected from the trap as a result of inelastic collisions between two atoms in the ground state, or through collisions in which one atom has been excited by the trapping light.

Ground-excited collisions

For ground-excited collisions, two mechanisms have been identified as major contributors to MOT loss. After one of the atoms has been excited by the trapping light, a collision can occur in which a red-detuned (relative to the atomic resonance) photon is spontaneously emitted. This process is called radiative escape (RE), and is described by

$$\mathrm{A} + \mathrm{A} + \hbar\omega \rightarrow \mathrm{A}_2(\mathrm{S}_{1/2}\mathrm{P}_{3/2}) \rightarrow \mathrm{A} + \mathrm{A} + \hbar\omega', \tag{3.12}$$

where ω is the resonant frequency of the transition from ground to excited states and $\omega > \omega'$. Figure 3.7(a) illustrates the loss channel for radiative escape. In the single-species case, an energy $\Delta E_{RE}/2 = \hbar(\omega - \omega')$ will be transferred to each atom. The loss rate due to radiative escape depends on the trap depth, which depends on the magnetic field gradient and on the detuning and intensity of the MOT beams. Typical MOT trap depths are of order 100 mK, so radiative escape will cause loss in single-species MOTs only when $\Delta = \omega - \omega'$ is above approximately $2\pi \times 1$ GHz.

If spontaneous emission does not occur, the atom in the excited state can undergo fine structure change (FSC). This process is shown in Figure 3.7 (b), and described by

$$\mathrm{A} + \mathrm{A} + \hbar\omega \rightarrow \mathrm{A}_2(\mathrm{S}_{1/2}\mathrm{P}_{3/2}) \rightarrow \mathrm{A}(\mathrm{P}_{1/2}) + \mathrm{A} + \Delta E_{FSC}. \tag{3.13}$$

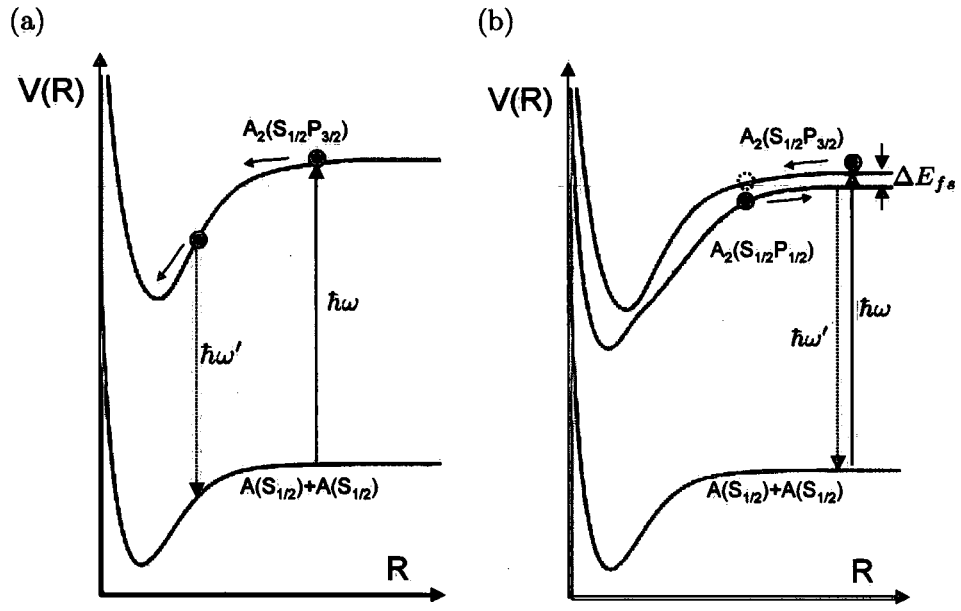

Figure 3.7: Schematic diagrams illustrating the loss channels for (a) radiative escape and (b) fine-structure change (FSC). The trapping laser excites one of the atoms and a ground-excited state quasimolecule is formed. During radiative escape, spontaneous emission (dashed line) of a red-shifted photon transfers energy to both atoms. The atom in the excited $P_{3/2}$ state can also undergo fine-structure change to the $P_{1/2}$ state, transferring an energy of $\Delta E_{fs}/2$ to each atom.

In this case, the atom pair gains an energy equal to the difference between the energy of the absorbed photon and the energy of the lower ($P_{1/2}$) excited state. For Li, this energy is roughly equal to the trap depth of a MOT, and hence FSC will not necessarily lead to loss. However, the fine-structure splitting for Cs is 16611.8 GHz, so a collision of this type will lead to both Cs atoms acquiring energies of $E/k_B = 400$ K. For Rb, the smaller fine-structure splitting of 7123 GHz means that two Rb atoms which undergo a FSC collision will acquire 'only' $E/k_B = 170$ K, which is still far greater than the trap depth. Hence, for Rb and Cs, FSC always leads to both colliding atoms being lost from the trap.

Ground-ground collisions

The main loss mechanism for ground-ground collisions is hyperfine structure change (HFC). While the interaction potential for collisions between atoms of the same species in the ground and excited states has a relatively long-range nature (proportional to $1/R^3$), the interaction potential energy for two ground-state atoms is given by the van der Waals expression $W_{gg} \propto \pm 1/R^6$. Hence, HFC will occur at a smaller interatomic distance than collisions between ground and excited state atoms. Atoms which change from the upper to the lower hyperfine level of the ground state (for ^{87}Rb, $5S_{1/2}F = 2 \rightarrow F = 1$; for Cs, $6S_{1/2}F = 4 \rightarrow F = 3$) gain kinetic energy equal to the hyperfine splitting ΔE_{hfs}. The ground-state hyperfine splittings for Cs and ^{87}Rb are 9192 MHz and 6835 MHz respectively [142]. Hence the per-atom energy gain for Cs is about 220 mK, while for Rb it is ~160 mK. If this energy is greater than the MOT trap depth, the atoms will escape. The physical processes which drive HFC, spin exchange and spin dipole-dipole interaction, are reviewed in Ref. [141]. For our purposes, we simply note that these processes do not depend on the trapping light.

3.4.2 Two-species MOTs

For the two-species MOT, Eq. 3.11 becomes

$$\frac{dN_i}{dt} = L - \gamma N_i - \beta_i \int n_i^2 d^3r - \beta_{ij} \int n_i n_j d^3r, \qquad (3.14)$$

where $n_{i,j}$ are density profiles of each species in the MOT, and β_{ij} is the rate constant for the loss of species i due to collisions with species j.

All of the loss mechanisms — radiative escape, fine-structure changing collisions, and hyperfine-changing collisions — which we discussed for single-species MOTs are also present in two-species MOTs. Note, however, that the kinetic energy produced in such collisions will not be shared equally between atoms of different mass. Conservation of momentum dictates that the lighter atom will have a higher velocity after the collision, and is thus more likely to be lost from the trap. Also, the shape of the excited- and ground-state quasimolecular potentials depends on which species is excited, which will alter the energy spectrum for radiative escape compared to the single-species case.

There are two additional loss channels for two-species MOTs which can in principle contribute to the total loss rate. Firstly, collisions between atoms of species A in the excited state and ground-state atoms of species B can result in an energy exchange (EE) reaction:

$$A^* + B \rightarrow A + B^* + \hbar(\omega_A - \omega_B). \tag{3.15}$$

The energy released by EE in the Rb-Cs system is very large ($E/k_B = 2 \times 10^5$ K) relative to the other mechanisms. However, the cross-section for EE collisions in other alkali metal systems, *e.g.* Na-Cs and Rb-K, has been found to be small (see Ref. [143] and references therein). Indeed, given the energy involved, the fact that mixed-alkali MOTs even exist indicates that reactions of this type are likely to have a negligible influence on the value of β_{ij}.

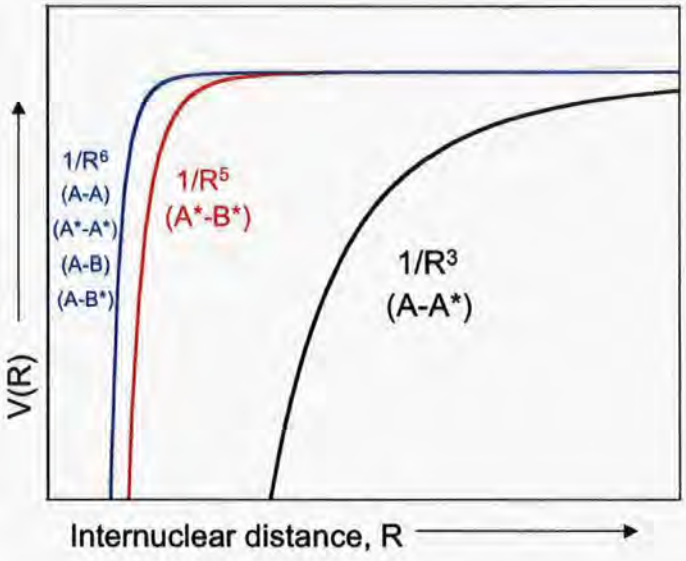

Figure 3.8: Approximate form of interatomic potentials. For single-species MOTs, the long-range $1/R^3$ potential dominates interactions, and both ground-ground (A-A) and excited-excited (A*-A*) collisions are suppressed. For two-species collisions, the mid-range $1/R^5$ potential can contribute if a sufficiently large number of atoms are in the excited state.

The second two-species loss channel involves an excited state-excited state colliding pair. In the single-species MOT, the potential for such collisions

exhibits a $-1/R^6$ dependence, while the potential for ground-excited collisions depends on $-1/R^3$. Hence the ground-excited $-1/R^3$ potential will dominate interactions, preventing atoms from approaching internuclear separations where shorter-range potentials begin to make a non-negligible contribution to the total potential. By contrast, in the two-species MOT the excited-excited potential is proportional to $-1/R^5$ and thus actually more attractive than the ground-ground and ground-excited potentials, which both exhibit a $-1/R^6$ dependence in the two-species case (Figure 3.8). Losses due to excited state-excited state collisions have been observed in a Na-Rb MOT [144], but only in the presence of a 'catalysis' laser beam used to pump more atoms into excited states.

3.4.3 Differentiating loss channels

The relative contributions of RE, FSC and HFC on the single-species and two-species loss rates depend on the trap parameters and the properties of the trapped species. A common picture suggests that HFC constitutes the main loss channel at low trap intensities because relatively few atoms are in the excited state [75]. At higher intensities, the trap depth is high enough that atoms undergoing HFC are not lost, but RE and FSC are both more probable and energetic enough to eject atoms from the MOT.

This qualitative description is appealing in its simplicity, but the true picture is more complicated. Telles *et al.* note that at low intensities, the intensity dependence of the total trap loss rate for a Cr MOT is similar to that of the alkalis. Chromium, however, has no hyperfine structure. Hence, although the hyperfine states are probably involved in low-intensity loss for the alkalis [145], factors like the low escape velocity at such intensities may contribute more to the overall pattern of loss [146]. The presence of repumping light has also been shown to modify the loss due to HFC [147].

As an illustration of the complicated nature of real MOTs, Figure 3.9 shows potential energy curves for RbCs dimers, based on calculations in Ref [148]. The figure contains only the five lowest potentials for molecules in the $^1\Sigma^+$ and $^3\Sigma^+$ states, and only the lowest six for $^{1,3}\Pi$ molecules. It is already clear even from this limited set of potentials that the nature of possible Rb-Cs interactions in a MOT is very complex due to the large range of

available molecular states. The relatively simple list of mechanisms presented here and in much of the literature is obviously only an approximate picture. Disentangling the effects of different mechanisms, either experimentally or theoretically, is not a trivial task. Overall, the safest conclusion to draw about the nature of the loss process in MOTs is probably that of Mudrich *et al.*, who describe it as 'uncertain' [145].

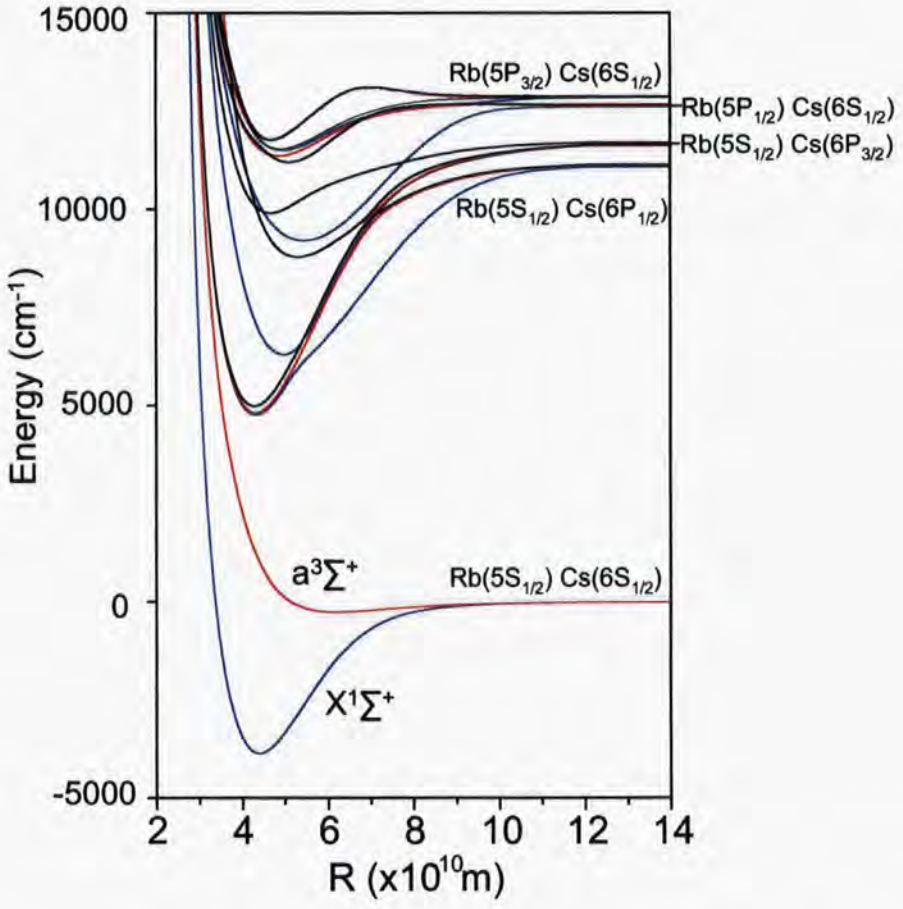

Figure 3.9: Potential energy curves showing the lowest $^1\Sigma^+$ (blue), $^3\Sigma^+$ (red) and $^{1,3}\Pi$ (black) states of RbCs molecules. Figure based on data in [148].

3.5 Magnetic trapping

Earlier in this chapter (Eq. 3.9), we noted that an atom in a magnetic field experiences a Zeeman shift of its energy levels, $\Delta E = \mu_B g_F m_F B$. Atoms with $m_F g_F > 0$ are said to be *weak-field seeking*, and can be trapped at a local minimum of the magnetic potential. There are several possible ways of realising a magnetic trap experimentally; the following sections describe those of greatest relevance for this work.

3.5.1 Quadrupole trap

The simplest magnetic trap for atoms is variously called a Paul trap (for its inventor W. Paul [149]) or a quadrupole trap for the shape of the field. It consists of two coils in an anti-Helmholtz configuration, which each provide an on-axis field of

$$B_z = \frac{\mu_0}{2} \frac{nIR^2}{((d-z)^2 + R^2)^{3/2}}, \tag{3.16}$$

where I is the magnitude of the current flowing in the coil, R is the coil radius, n the number of turns, and d is the distance from the coils to trap centre along the axis of the coils (z axis) to the trap centre. The field gradient for an identical pair of coils with separation $2d$ is

$$\left.\frac{\partial B}{\partial z}\right|_{z=0} = \frac{3\mu_0 nIR^2 d}{(d^2 + R^2)^{5/2}}. \tag{3.17}$$

This type of trap is relatively easy to construct, and as the configuration of the coils is the same as for the MOT, it is possible to realise both a MOT and a magnetic trap with the same set of coils. It has one major disadvantage, however: the field is zero at the trap centre (Figure 3.6), and hence the coldest atoms in the sample can undergo Majorana 'spin flip' transitions to an untrapped state and be lost from the trap. This was a major problem in early attempts at producing a quantum degenerate gas, and led to innovative new trapping techniques being developed [1, 150] which either 'plugged' the hole at the trap centre with a laser beam or moved the location of the trap centre at a rate lower than the frequencies of spin-flip transitions, ensuring that atoms always remained in the same state relative to the magnetic field (time-orbiting potential, or TOP, trap).

3.5.2 Ioffe-Pritchard traps

An alternative to either the laser-plugged quadrupole or TOP traps is to use a trap geometry for which the field minimum is not zero. An Ioffe-Pritchard (IP) trap [151] combines a linear quadrupole field formed by four straight current-carrying bars with an axial field formed by a pair of 'pinch' coils. The currents flowing through the coils are in the same direction, and have equal magnitudes, but are separated by more than the Helmholtz condition, *i.e.* $2d > R$. Figure 3.10 illustrates the geometry of the field. The full Ioffe expansion for the magnetic field $\mathbf{B}$ due to this configuration is given in several theses [84, 99, 101, 152]. The field magnitude can be approximated near the trap centre by

$$|\mathbf{B}| \simeq B_0 + \frac{1}{2}\gamma z^2 + \left(\frac{\beta^2}{2B_0} - \frac{\gamma}{4}\right) r^2. \tag{3.18}$$

The bias field B_0, gradient β and curvature γ can all be measured experimentally. This trap combines a restoring force in the radial direction (provided by the bars) with a confining potential along the z axis provided by the coils.

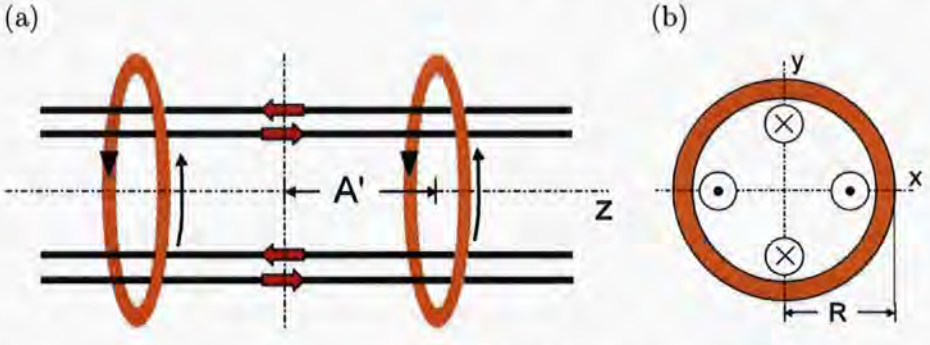

Figure 3.10: Schematic diagram of an Ioffe-Pritchard trap. (a) Orientation of bars and coils. Arrows indicate the direction of current flow. The separation between the coils is $2A'$, where $A' > R$. (b) Top view of IP trap showing the direction of current flow in the Ioffe bars.

One variant of the coils and bars IP trap is the baseball trap [153], so called because it consists of a single coil shaped like the seams on a baseball (Figure 3.11). This geometry combines the functions of the parallel bars and pinch coils into a single coil, and is simpler to operate because only one

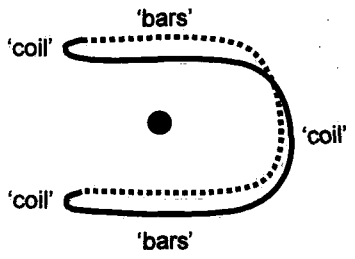

Figure 3.11: Illustration of a baseball coil. Labels indicate which parts of the coil correspond to the anti-Helmholtz coils and Ioffe bars of a standard IP trap. The circle shows the position of the magnetic field minimum, where atoms are trapped.

current needs to be regulated and optimised. The field produced by this configuration is qualitatively similar to that of a classic IP trap.

3.6 Optical trapping

A major limitation on the utility of magnetic traps is that only atoms in weak-field seeking states can be confined in the magnetic potential. *Optical* traps, by contrast, operate independently of atoms' magnetic spin state, and can thus be used to trap and study a wider range of atomic species. The optical trapping force arises from the interaction between a light field and the field-induced electric dipole moment of an atom in the field. The field $\mathbf{E}(\mathbf{r},t) = \hat{\mathbf{e}}\tilde{E}(\mathbf{r})\exp(-i\omega t) + c.c.$ and dipole moment $\mathbf{d}(\mathbf{r},t) = \hat{\mathbf{e}}\tilde{d}(\mathbf{r})\exp(-i\omega t) + c.c.$ are related via the equation

$$\tilde{d} = \alpha(\omega)\tilde{E}, \tag{3.19}$$

where α is the complex polarisability of the atomic medium. The potential $U_{\rm dip}$ arising from this relation is given in terms of the field intensity $I = 2\epsilon_0 c|\tilde{E}|^2$ by

$$U_{\rm dip} = -\frac{1}{2\epsilon_0 c}\mathrm{Re}(\alpha)I. \tag{3.20}$$

For a real multi-level atom, α is difficult to calculate [154, 155], so an approximation is often made which considers the atom as a two-level system which interacts with a classical radiation field. This approximation is valid

for light at a frequency ω far detuned from the resonant frequency ω_0, and in the limit of negligible saturation. Under these circumstances, the potential becomes [156]

$$U_{\mathrm{dip}}(\mathbf{r}) = -\frac{3\pi c^2}{2\omega_0^3}\left(\frac{\Gamma}{\omega_0-\omega}+\frac{\Gamma}{\omega_0+\omega}\right)I(\mathbf{r}). \tag{3.21}$$

We can see from this equation that for red-detuned light ($\omega < \omega_0$), the potential is attractive, and atoms will be trapped in regions of high intensity. Traps with blue-detuned light are realised at intensity minima.

Unlike the scattering force discussed in Section 3.1.2, the optical dipole force is conservative: the work done by F_{dip} on an atom does not depend on the atom's path. We can therefore write F_{dip} as the gradient of U_{dip}, hence

$$F_{\mathrm{dip}}(\mathbf{r}) = -\nabla U_{\mathrm{dip}}(\mathbf{r}) = \frac{1}{2\epsilon_0 c}\mathrm{Re}(\alpha)\nabla I(\mathbf{r}). \tag{3.22}$$

As this equation shows, the conservative nature of the dipole force is more than just a mathematical technicality - it indicates that the trapping force depends on intensity gradients in the light field. There are many ways to realise such gradients experimentally, but the simplest uses a single, red-detuned, focused laser beam. Such a configuration was proposed by Ashkin in 1970 [157] and experimentally realised by Chu *et al.* in 1986 [158]. The beam has a Gaussian intensity profile, given by

$$I(r,z) = \frac{2P}{\pi w^2}\frac{1}{1+(z/z_R)^2}\exp\left(\frac{-2r^2/w^2}{1+(z/z_R)^2}\right), \tag{3.23}$$

where w is the beam's $1/e^2$ radius, $z_R = \pi w^2/\lambda$ is the Rayleigh range, and P is the beam power. As the beam is red-detuned, atoms will be trapped in the region where the intensity reaches its maximum value of $I_{\mathrm{pk}} = 2P/\pi w^2$, *i.e.* at the focus.

Many other trapping geometries have been realised experimentally, including standing-wave traps formed by two counterpropagating beams [159, 160], two crossed beams [161], and three-dimensional lattices [162]. Some possible uses for more complex geometries in studies of Rb-Cs mixture are discussed in the last chapter of this thesis; Ref. [156] contains a very useful (although now somewhat out of date) brief review of experiments using other types of traps.

The geometry of the focused-beam optical dipole trap is far easier to realise than a six-beam MOT. However, the much shallower depth of the optical trap relative to the MOT makes the former a poor first step for most cold-atom experiments. For example, Rb atoms in a trap created by a 1064 nm Nd:YAG laser with a power of 2 W and a waist of 60 μm will experience a potential corresponding to $U/k_B = 52$ μK, compared to many hundreds of mK for a MOT. It is therefore customary to first cool atoms in a MOT, then load them into either an optical trap or a magnetic trap. If the aim of the experiment is to achieve quantum degeneracy, the next step is to cool the sample even further via evaporative cooling.

3.7 Evaporative cooling

For over ten years, evaporative cooling has been the final experimental step on the road to quantum degeneracy [120]. As such, the basic idea behind evaporative cooling is now well-known. Briefly, an atomic sample in thermal equilibrium will have a small fraction of atoms with energies many times higher than the mean energy of the sample (Figure 3.12). If these energetic atoms can be removed from the cloud preferentially, the mean energy of the sample will be reduced. Once the sample has rethermalised via elastic collisions, the temperature of the cloud will be reduced as well.

For alkali metal atoms in a magnetic trap, the most commonly used technique for preferentially removing energetic atoms is radio-frequency evaporation[6]. In this method, an rf field is applied to the sample which drives atomic transitions from a trapped to an untrapped state. Higher-energy atoms have larger orbits around the trap, and will therefore encounter a larger range of magnetic fields in a single circuit. By selecting an rf frequency which drives transitions only at an 'atypical' magnetic field (*i.e.* one which corresponds to an energy several times the mean energy of the sample), only higher-energy atoms will be forced out of the trap by the rf field. This method is often described as an rf 'knife' which cuts away atoms with an energy greater than $\eta k_B T$, where η is the ratio of the desired cut-off energy to the mean energy of the sample (Figure 3.13).

[6]Evaporation using microwave frequencies is also used; see *e.g.* Refs. [29] and [163].

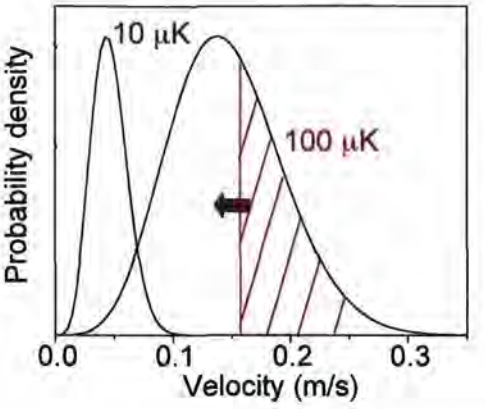

Figure 3.12: Velocity distributions of ^{87}Rb atoms in thermal equilibrium at 10 and 100 μK. Evaporative cooling removes the hottest atoms from the sample (red lines). After the sample has rethermalised, atoms will be in a new distribution at a lower temperature.

In optical traps, the most common (and first-demonstrated) evaporative cooling technique is to reduce the intensity of the trapping beams, whereupon more-energetic atoms will leave the trap [161]. Unlike rf evaporation in the magnetic trap, however, this form of evaporation changes the shape of the potential, reducing the confinement and therefore also reducing the density and elastic collision rate of the now weakly-trapped sample. 'Runaway' evaporation, in which the collision rate increases during evaporative cooling [164], is therefore more difficult to achieve with this method. In spite of this fact, several groups have achieved quantum degeneracy by all-optical means since it was first demonstrated for ^{87}Rb in 2001 [165]. Also, radio-frequency evaporation has been used on optically-trapped atoms in experiments where the presence of an additional magnetic levitation field results in different potentials for different magnetic substates (see *e.g.* Refs. [106, 166]).

The key to making evaporative cooling work is the high ratio of 'good' (elastic) to 'bad' (inelastic) collisions noted in Chapter 2. Essentially, rethermalisation must proceed sufficiently quickly that loss processes (and evaporation itself) do not drain all the atoms from the trap before the sample achieves a phase-space density greater than 1. The limits on evaporative cooling posed by atomic species with 'bad' scattering properties has led to sympathetic

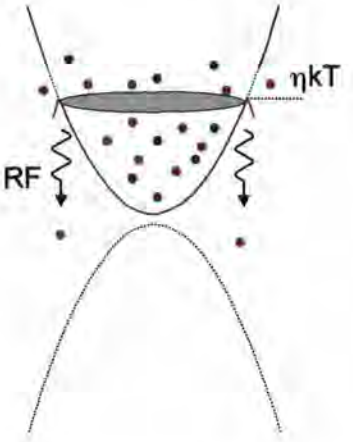

Figure 3.13: Illustration of evaporative cooling via radio-frequency transitions. An applied rf field drives transitions in the atomic sample from a trapped (top curve) to an anti-trapped state (bottom curve). The rf field is only resonant with these transitions at a particular value of the magnetic potential (indicated by the grey surface), so only atoms with energy greater than the cut-off value $E_{\max} = \eta k_B T$ will be removed.

cooling being used to achieve degeneracy in both bosonic [6, 26, 63] and Bose-Fermi mixtures, as described in the introduction to this thesis.

Part II

Rb-Cs mixtures

Chapter 4

Rb-Cs mixture apparatus

This chapter describes an experimental apparatus designed to study an ultracold gaseous atomic mixture of ^{133}Cs and ^{87}Rb. The apparatus was used in the studies described in Chapter 5 of this work, and continues to be used in experiments on evaporatively cooled Rb-Cs mixtures and the search for interspecies Feshbach resonances. The greatest emphasis is placed on the parts of the apparatus which are new to the Durham group, and those which I was directly involved in developing. Briefer descriptions of other components are included for completeness.

4.1 Overview

The Rb-Cs mixture is prepared using a double magneto-optical trap (MOT) system in which a two-species pyramid MOT acts as a source of cold atoms for a 'science' MOT. After the initial MOT phase, atoms in the mixture are optically pumped into the magnetically trappable $|F=3, m_F=-3\rangle$ and $|F=1, m_F=-1\rangle$ states of Cs and Rb (respectively) and loaded into an Ioffe-Pritchard magnetic trap. Light for the MOTs, imaging and optical pumping is generated by a system of six frequency-stabilised diode lasers, three for each species. Optical fibres transmit the light from the laser table to a second optical bench containing the vacuum system and MOT optics. Information about the cold mixture is obtained via absorption imaging and fluorescence detection. The following sections describe each of these systems in greater detail.

4.2 Vacuum system

The vacuum apparatus for the mixture experiment consists of a two-chamber system connected by a differential pumping tube. In the first chamber, a pyramid MOT serves to initially collect and cool the atoms from a background vapour. A gap at the apex of the pyramid leads to a flux of cold atoms into the UHV chamber, where they are captured in the science MOT. The pyramid MOT chamber is pumped by a single $40\,\mathrm{ls}^{-1}$ ion pump (Varian) and houses commercial dispensers (SAES) for Rb and Cs. In total six dispensers, three for each species, are spot-welded to two separate electrical feedthroughs. The vapour pressure of each species is controlled independently by running separate currents through the Rb and Cs dispensers. Figure 4.1 shows the arrangement of the vacuum system components.

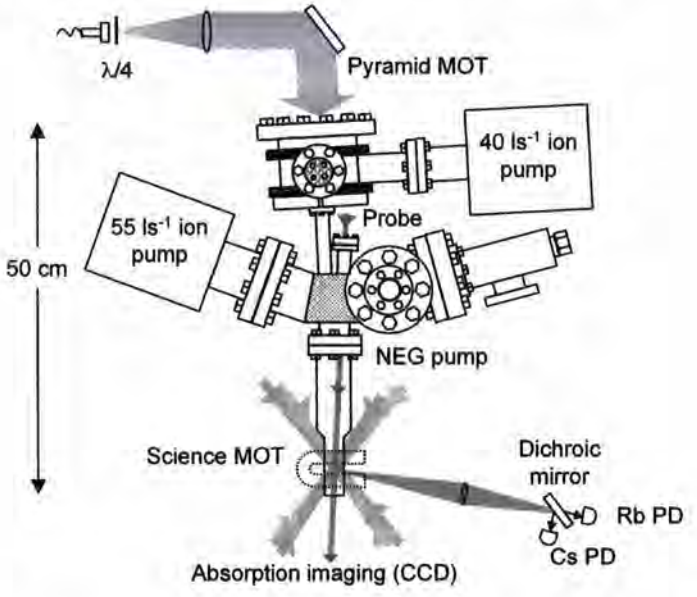

Figure 4.1: Vacuum system 'footprint' showing arrangement of vacuum chambers relative to other experimental systems.

The differential pumping tube comprises two sections: a 1.7 cm tube with an inner diameter of 5 mm, followed by a 8.7 cm tube with an inner diameter of 16 mm. The combined conductance is approximately $0.7\,\mathrm{ls}^{-1}$. The tube is aligned at a $\sim 3^{\circ}$ angle relative to the axis of the science cell in order to

create space for a 34 mm outer diameter viewport at a similar angle in the opposite direction. This provides optical access for absorption imaging along the axis of the cell.

The rectangular science cell is made from 2 mm thick fused silica and has internal dimensions of 20 × 20 × 83 mm. A cylindrical graded index section increases the overall length of the cell from the flange to ∼ 21 cm. The cell is pumped by a 55 ls^{-1} ion pump (Varian) and a non-evaporable getter (NEG) pump (SAES).

4.3 Lasers

A system of six diode lasers (three for each species) provides the light required for the experiment. Two commercial 'master' lasers (Sacher Lasertechnik Lynx TEC-120) provide ∼150 mW of light at 780 nm and 852 nm for cooling in the pyramid MOT, imaging, and injecting two homebuilt 'slave' lasers. The slave lasers provide cooling light for the science MOT. Other homebuilt extended cavity diode lasers supply repumping light for both MOTs, and light for optical pumping.

The design of the repumping lasers was modified only slightly from the design developed by K. J. Weatherill and described in [155]. The laser is in a Littrow configuration [167], with the diode mounted in an aluminium block and the beam incident on a diffraction grating. A thermo-electric cooler (TEC) is attached to the laser block, and the temperature is controlled and stabilised by a commercial servo circuit (Wavelength Electronics MPT-2500). This laser design is very compact and has worked well in a number of experiments at Durham [155, 168, 169]. The Cs repumping laser uses a 50 mW SDL-5401-G1 diode, and the Rb repumper uses a 120 mW Sharp GH0781 diode. The Cs slave laser has a maximum power of 100 mW (SDL-5411 diode), while the Rb slave produces 80 mW (Sanyo DL-7145-201S). Both slave lasers are frequency stabilised by being injected with ∼ 1 mW of light derived from the master lasers.

The commercial master lasers use a modified version of the Littrow configuration in which the beam is incident upon a grating and then reflected back through the diode and coupled out the diode's rear face [170]. We en-

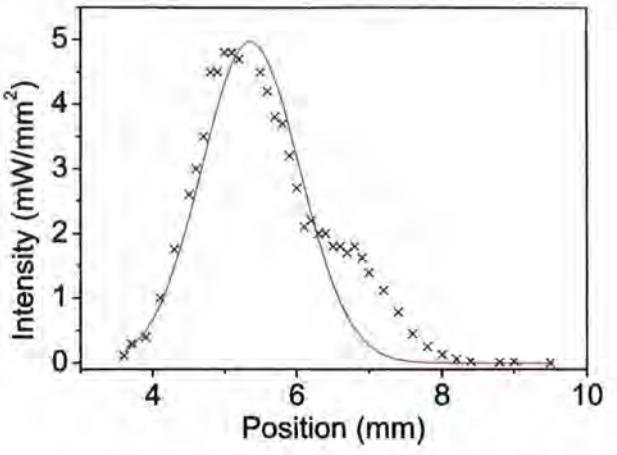

Figure 4.2: Intensity profile of Rb Sacher laser beam along the horizontal axis. The red line shows a Gaussian fit to the data points (black crosses) obtained from knife-edge measurements. Approximately 20% of the total laser power is not in the main beam but in a side 'lobe.'

countered a number of problems with these lasers, especially the Rb Sacher. The power output of both lasers was on the low end of their specifications, and the initially excellent (> 7 GHz) scan range of the Rb laser deteriorated during its lifetime. Another problem with the Rb Sacher laser was the presence of structure in its nominally Gaussian beam profile. Knife-edge measurements [171] showed that approximately 20% of laser power was not in the main TEM_{00} mode, but in a 'lobe' which appeared on one side of the beam profile. The lobe is clearly visible in Figure 4.2, which shows a plot of laser intensity as a function of position. Successive realignments of the laser grating reduced and eventually removed the lobe, but for a period of roughly six months during the setup of this experiment it was not possible to have the laser on transition without the lobe present.

The most serious problem with the Rb Sacher laser was its poor frequency stability. Even after improvements to the locking setup (described in the next section), the laser was prone to frequency 'jumps' of a few MHz. We speculate that this is due to a combination of poor-quality diodes and poor temperature stability in the laser design. The mixture Rb Sacher was replaced by a

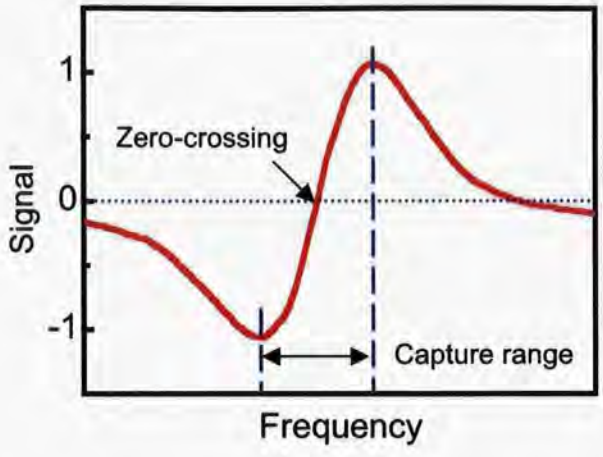

Figure 4.3: Example of an error signal used for laser locking. The lock point, or zero-crossing, is indicated, and is located at the frequency of an atomic transition. The capture range over which locking is possible is also defined as the region near the zero-crossing where the slope of the error signal is positive. This definition is appropriate because the servo electronics we use for laser locking (Oxford Central Electronics: EW1303, EW1225) require a positive slope.

different commercial laser (Toptica DL100) shortly after the work described in Chapter 5 was completed.

4.4 Frequency stabilisation

As we have seen in Chapter 3, the process of cooling and slowing atoms with laser light [124] requires control of the laser frequency to a fraction of the linewidth of the atomic transition. This generally means implementing some type of active frequency stabilisation, or 'locking,' to keep the laser light at the desired frequency. To accomplish this, one generates a signal (the 'error signal') which is derived from an atomic reference. Figure 4.3 shows a typical error signal and defines the terminology used in this section.

There are as many methods of generating an error signal for laser locking as there are ways to skin cats. A partial list of methods includes 'dithering'

the laser frequency [172], Sagnac interferometry [173, 174], prismatic deflection [175, 176], using acousto-optic modulators [177, 178], low-field Faraday polarimetry [179], velocity-selective saturated absorption spectroscopy [180], bi-polarization spectroscopy [181, 182], polarization spectroscopy [183–185], dichroic atomic vapor laser locking (DAVLL) [178, 186, 187], a combination of saturated absorption and DAVLL [188, 189], frequency-modulation spectroscopy using an external phase modulator driven at radio frequencies [190], and modulation transfer spectroscopy [191].

The performance and capabilities of these locking techniques differ. There are tradeoffs between simplicity, cost, ease of operation, location of zero-crossings with respect to the atomic reference, sensitivity to external perturbations, and the frequency deviation the system can tolerate and still return to the desired lock-point (the 'capture range' illustrated in Figure 4.3). In our case, a large capture range was essential, as we wanted to obtain light for optical pumping and depumping by changing the frequency detuning of the repump and master lasers, instead of setting up separate lasers with a fixed detuning. Stability was also a priority. With six lasers to keep on transition, we could not afford to use a high-maintenance locking system. Based on these requirements, we chose to lock all four master lasers in the Rb-Cs mixture experiment using the dichroic atomic vapour laser locking (DAVLL) technique [187], with saturated absorption/hyperfine pumping spectra [192, 193] used as a frequency reference.

4.4.1 DAVLL basics

In a typical DAVLL setup (Figure 4.4a), a linearly polarised probe beam is incident on an atomic vapour with the wavevector of the light parallel to the axis of an applied magnetic field. After interacting with the atoms, the probe passes through a quarter wave plate before impinging on a polarising beamsplitter (PBS). The linearly polarised beam can be decomposed into two orthogonal circularly polarised beams of equal amplitude. The signals measured by detectors placed in the output arms of the PBS are proportional to the intensity of the right and left circularly polarised beams. In the absence of a magnetic field, different m_F states are degenerate and the σ^+ and σ^- transitions overlap. When a finite magnetic field is applied, the degeneracy

is lifted and the medium becomes dichroic: the centre frequencies of the σ^+ and σ^- absorption lines are displaced in different directions. The magnetic field magnitude is chosen such that the frequency displacement of the absorption lines is similar to their Doppler-broadened widths. Consequently, the difference signal has a dispersion-like shape, with a zero-crossing at line centre and a wide capture range of typically a few hundred MHz for Rb and Cs (Figure 4.4b).

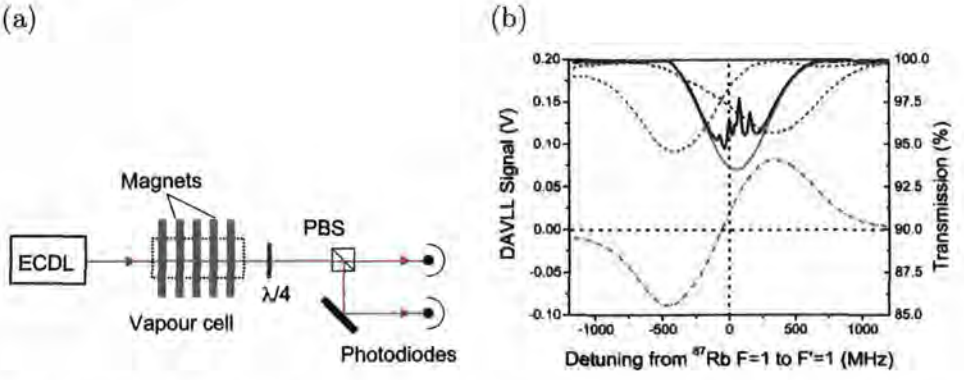

Figure 4.4: (a) Basic setup for dichroic atomic vapour laser locking. Light from an extended cavity diode laser (ECDL) is incident on the atomic vapour in the cell, and interacts with the atoms in the presence of an axial magnetic field. The beam then passes through a quarter wave plate before impinging on the PBS, which splits the light into vertically and horizontally polarised components. (b) The intensities in each arm of the PBS (green and blue curves) are recorded by photodiodes and subtracted electronically, producing the signal (red curve). Saturated absorption spectra with and without the pump beam (black and grey lines) are also shown. Figure (b) taken from Ref. [194].

Several studies have been made of various aspects of DAVLL, including the effects of temperature [194–197], the suppression of stray magnetic fields [198], and variations which use a Doppler-free system [86, 189] or very thin vapour cells [199]. The abundance of such studies is a testament both to the popularity of DAVLL as a locking method and to the complicated dependence of the DAVLL signal on a number of factors. DAVLL is popular for several reasons. Firstly, a basic DAVLL cell can be constructed very easily

and inexpensively with permanent 'refrigerator'-type magnets. Secondly, the error signal has a number of attractive features, notably the large capture range mentioned before, which allows the lock frequency to be changed over a large range. Finally, a well-optimised DAVLL lock can be remarkably stable. Drift magnitudes of as little as 350 kHz over 16 hours have been reported [195], and in their seminal paper Corwin *et al.* [187] described trying and failing to unlock their laser by banging on the table with a hammer.

These are very considerable advantages. However, there are also some drawbacks associated with the DAVLL method. The birefringence of the polarisation optics used in a DAVLL setup can be highly temperature-dependent, making the lock point prone to long-term drifts due to changes in the ambient temperature. Fluctuations in the intensity or polarisation purity of the beam entering the DAVLL cell will also shift the lock point [155]. The next section gives a brief overview of modifications to the basic DAVLL apparatus which have improved the lock performance of the lasers.

4.4.2 Durham DAVLL developments

The first DAVLL cells used on the Rb-Cs mixture experiment were all of the basic 'refrigerator' magnet design. In this design, the vapour cell rests inside a set of permanent magnets, each approximately 5 mm thick. The magnets are separated by 2 mm thick copper rings. The optimum number of magnets and copper rings was found by measuring the gradient and capture range of the DAVLL signal for different configurations. There is a trade-off between these two quantities, as Figure 4.5 shows. From these plots of gradient and capture range for the $F = 3 \rightarrow F'$ transition in Cs, we can see that an inter-magnet spacing of 4–6 mm offers a good compromise.

We can see from Figure 4.6 that the magnetic field produced by a permanent magnet cell is far from uniform. The mean field of this cell, which consisted of five magnets separated by 4 mm, is 165 G, with a standard deviation of 31 G. The shape of the DAVLL signal is quite robust with respect to such variations, however. Millett-Sikking *et al.* [194] observed differences of only a few percent in the amplitude and line-centre gradient for error signals generated by a permanent magnet cell compared to a cell inside a solenoid with field uniformity greater than 0.2%. At this writing, both Cs lasers in

the mixture experiment are locked using permanent magnet DAVLL cells.

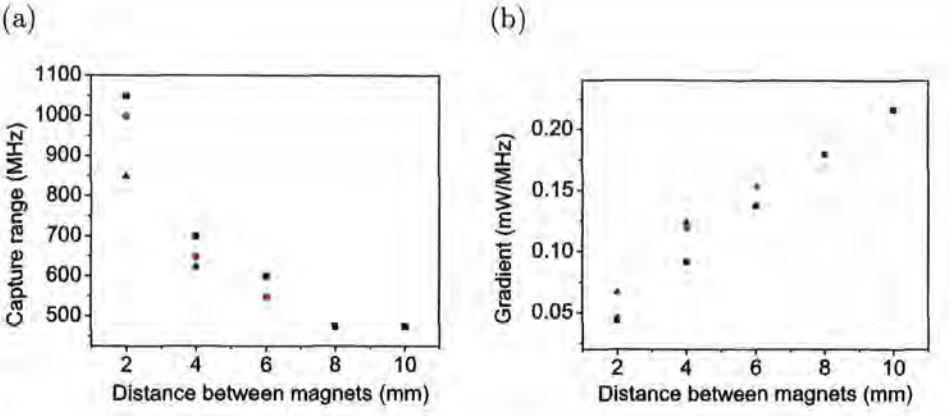

Figure 4.5: (a) Capture range and (b) gradient of the error signal generated by a permanent magnet DAVLL cell. Black squares represent data from a cell with six magnets, whilst red circles and blue squares represent seven- and eight-magnet cells, respectively.

A more serious problem with the permanent magnet cell is the small error signal amplitude generated for the $F = 1 \rightarrow F'$ repumping transitions in ^{87}Rb. At room temperature, the Rb vapour in a 5 cm long cell absorbs less than 10% of light tuned to this resonance, and the DAVLL signal amplitude is approximately half that of the ^{87}Rb cooling transition. In our first attempt to improve the signal by increasing absorption, a mount was designed for the vapour cell in which the ends of the cell were surrounded (and supported) by brass blocks [194]. These blocks were mounted on thermoelectric controllers and could be heated to 50 degrees. Figure 4.7 shows the effects of heating the end blocks on the DAVLL signal amplitude At room temperature, the signal amplitude was approximately 700 mV, so heating the blocks to 42 degrees produces a fourfold increase in signal.

In this design, only the ends of the vapour cell were in contact with the heated blocks. This prevented the Rb vapour from condensing on the cell windows. However, it also meant that the system was prone to temperature drifts. Besides affecting the absorption in a time-dependent way, these drifts may also have caused the permanent magnets to expand and contract, making the field time-dependent as well. As a result, the locking stability of the

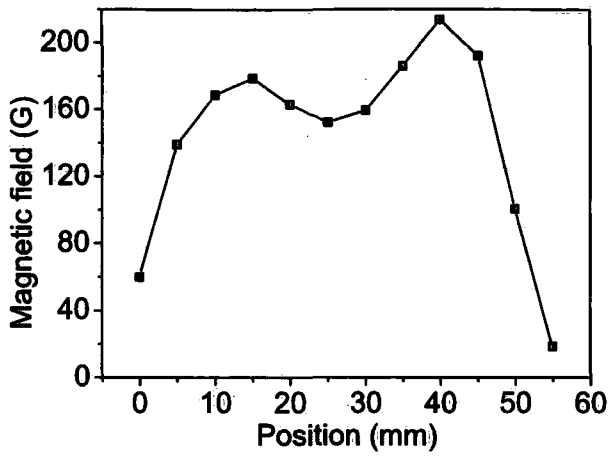

Figure 4.6: Field generated by a DAVLL cell using five magnets separated by 4mm. The cell is 50 mm long and centred at x =25 mm.

laser was not significantly improved with this design despite the increased signal amplitude.

The next version of DAVLL cell used a solenoid to generate the magnetic field. Ohmic heating from the solenoid leads to an increase in the signal amplitude. The design and optimisation of this cell are described in detail in [197], and only the results will be quoted here. For the weak $F = 1 \rightarrow F'$ transitions in ^{87}Rb, the optimum gradient is achieved by setting the magnetic field to ~120 gauss [194]. The solenoid cell was designed to produce this field whilst also heating the Rb vapour until the line-centre absorption reaches ~75%, the value which was found to optimise the gradient for a given field. Under these conditions, the solenoid cell produces signal amplitudes up to 12 times greater and gradients up to 7.5 times steeper for this transition than a cell in a water-cooled solenoid generating the same magnetic field. At this writing, the solenoid DAVLL cell is still in use for the Rb repumping lasers in the Rb-Cs mixture experiment.

The large capture range of the DAVLL signal allowed us to change the lock point of our master lasers by up to ~100 MHz, *e.g.* during the depumping phase of the experiment, simply by applying a voltage offset to the laser locking servo. However, this large capture range is a bug as well as a feature.

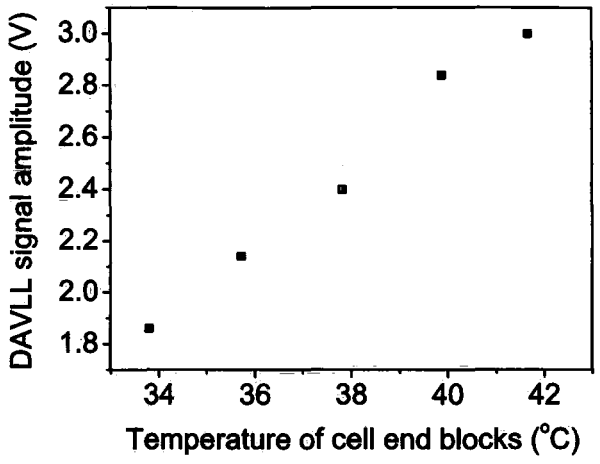

Figure 4.7: Temperature dependence of DAVLL signal amplitude for ^{87}Rb $F = 1 \rightarrow F'$ transitions. Heating the end blocks of the TEC-mounted permanent magnet cell increases the amount of resonant light absorbed by the Rb vapour, thus increasing the amplitude of the error signal.

Because the laser can be locked to any point in the DAVLL signal's capture range, it is impossible to determine the frequency of the lock point from the DAVLL signal alone. Consequently, an independent frequency reference is needed. This reference was provided by saturated absorption/hyperfine pumping spectroscopy.

4.4.3 Saturated absorption/hyperfine pumping spectroscopy

In saturated absorption/hyperfine pumping spectroscopy, a pump beam is counterpropagated with a weak probe beam through an alkali vapour cell (Figure 4.8a). The frequency of both beams is tuned onto resonance with the desired atomic transition. The presence of the pump beam reduces the number of ground-state atoms with which the probe can interact via the processes of saturated absorption and hyperfine pumping [192, 193]. Sub-Doppler resolution is achieved because only atoms with a small longitudinal velocity (those with a Doppler shift comparable to or less than the natural

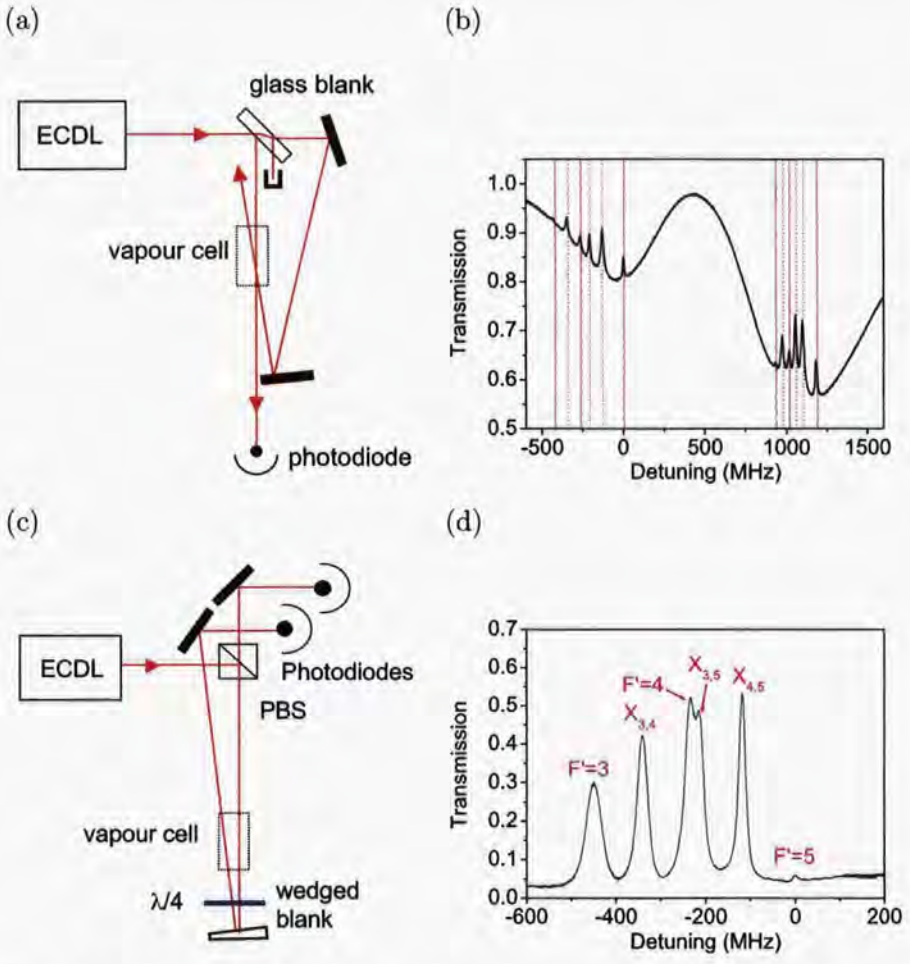

Figure 4.8: (a) Light from an extended cavity diode laser (ECDL) reflects off the surface of a glass blank and probes the atomic vapour inside the cell. The more powerful pump beam is counterpropagated with the probe beam. (b) Saturated absorption spectra for the $F = 2 \rightarrow F'$ transitions in ^{87}Rb (left) and $F = 3 \rightarrow F'$ transitions in ^{85}Rb (right). Solid lines indicate the frequencies of the three hyperfine transitions per isotope. Dotted lines show crossover frequencies. (c) Optical setup used to generate Doppler-free spectra. A polarising beamsplitter (PBS) sends light through the vapour cell. After the cell, the probe beam passes through a quarter wave plate and hits a wedged blank. One of the reflected beams is counterpropagated with the probe beam, and a signal similar to (a) is recorded by the upper photodiode. The signal from the other reflected beam is simply the Doppler-broadened absorption profile. (d) Saturated absorption spectra of the Cs $F = 4 \rightarrow F'$ transitions after subtracting the Doppler background.

linewidth) interact with both pump and probe beams. Figure 4.8(b) shows spectra obtained for the $F = 2 \rightarrow F'$ transitions in ^{87}Rb and the $F = 3 \rightarrow F'$ transition in ^{85}Rb. Naively, one might expect three resonances for each isotope owing to the $\Delta F = 0, \pm 1$ selection rule; however, crossover resonances are also observed at frequencies halfway between conventional resonances [192]. At these frequencies, a moving atom 'sees' one beam's frequency as being Doppler shifted onto resonance with one transition, and the other beam's frequency shifted onto resonance with another. The pump and probe beams are thus driving different transitions for atoms in the same velocity class.

In more elaborate optical setups, the signal from an additional probe beam can be subtracted from the pumped probe signal to produce spectra in which the hyperfine peaks appear without the Doppler background. Figure 4.8(c) shows one setup for generating these 'Doppler-free' spectra. Here, the probe beam reflects off a PBS, passes through the vapour cell and quarter wave plate, and hits a wedged glass blank. One of the reflected beams is counterpropagated with the probe beam, and the upper photodiode records a signal similar to that in Figure 4.8(b). The signal from the other reflected beam is simply the Doppler-broadened absorption profile. This background signal is subtracted electronically from the saturated absorption signal. Figure 4.8(d) shows the saturated absorption/hyperfine pumping signal for the $F = 4 \rightarrow F'$ transitions in caesium after the Doppler background has been subtracted.

4.5 Setting frequency detunings

In principle, any of the hyperfine peaks in Figure 4.8 can be used as reference features for laser locking. In practice, the choice of feature is determined by two factors: the frequency of light required and, to a lesser extent, the preference for a strong peak easily distinguished from neighbouring features. For Rb (Cs), the saturated absorption/hyperfine pumping peak which best satisfies the latter criterion is the $F = 2 \rightarrow X_{2,3}$ ($F = 4 \rightarrow X_{4,5}$) crossover peak. However, this peak is located 133.5 (125.7) MHz below the cooling transition, approximately an order of magnitude more red-detuned than is

typically required for the MOT.

In order to stabilise the Rb master laser at the optimum detuning for the pyramid MOT using this crossover resonance as a reference, the frequency of the pump beam in the reference spectra is shifted by −231.3(1) MHz relative to the probe beam using an accousto-optic modulator (AOM) in a double-passed configuration. The crossover feature occurs at a frequency $(\nu_{\text{pump}}+\nu_{\text{probe}})/2$. With $\nu_{\text{probe}} = \nu_{\text{laser}}$ equal to the frequency of the $F = 2 \rightarrow F' = 3$ transition minus the pyramid MOT detuning, using the $X_{2,3}$ crossover peak as a reference with this AOM shift yields a detuning for the pyramid MOT of approximately 17 MHz. The principles behind AOMs are discussed in Ref. [200]. Figure 4.9(a) shows the optics used to derive probe and pump beams for the reference spectra, as well as the DAVLL beam which provides the error signal for locking. The probe, DAVLL, and pyramid beams are all at the optimum detuned frequency for the pyramid MOT. Light for the pump beam is double-passed through the spectroscopy AOM, and the pump beam itself is derived from the zeroth-order (un)diffracted light of the probe AOM. The frequency of the spectroscopy AOM was set by comparing shifted and unshifted saturated absorption/hyperfine pumping spectra, as shown for Rb in Figure 4.9(b).

Besides the spectroscopy AOM, additional double-passed AOMs are used to diffract some light from the spectroscopy AOM back to the detunings required for the science MOT and absorption imaging. A single-passed AOM is used for fast shuttering of the optical pumping light, which is derived from the repumping laser. Larger frequency shifts required for optical pumping (depumping) are obtained by additionally applying a dc voltage offset to the DAVLL signal used for locking the repump (master) laser, thereby offsetting the laser lock point. Figure 4.10 contains a schematic diagram of the optical setup for Rb; the Cs layout is similar. The complete optical layout is found in Appendix D.

4.6 Optical fibres

Light from the optical table is transmitted to the experiment via a total of five polarisation maintaining fibres. For the pyramid MOT, cooling and re-

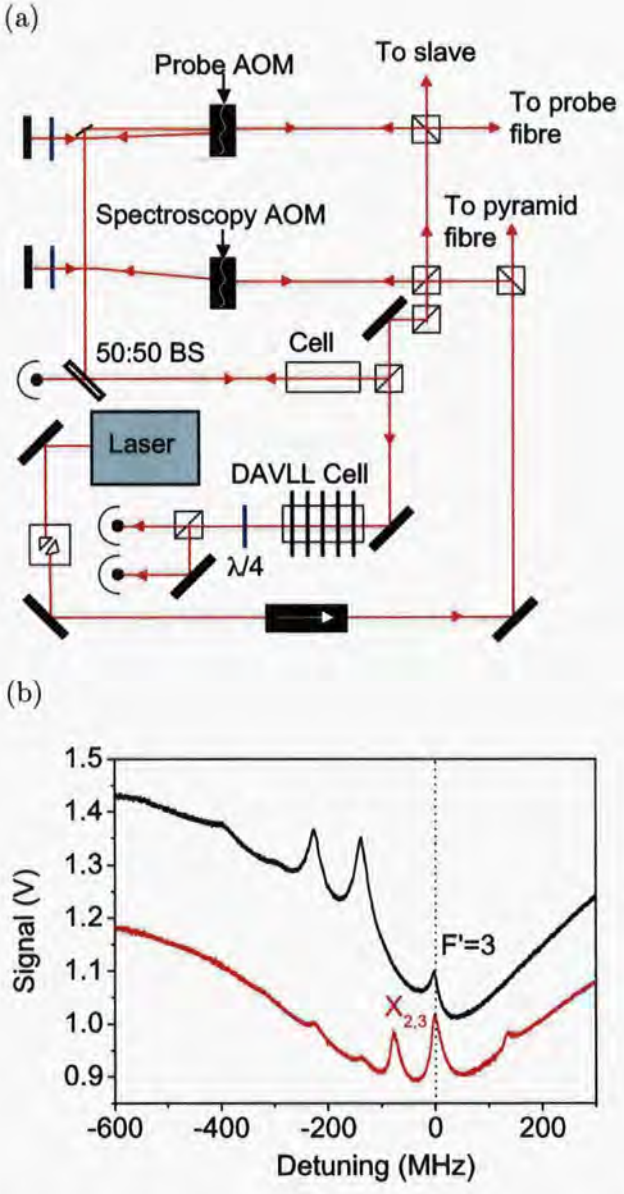

Figure 4.9: Setting the cooling laser lock point. (a) Optical setup used to derive probe and pump beams for the reference spectra, and the DAVLL beam for the error signal. (b) Shifted (red) and unshifted (black) saturated absorption spectra for Rb. The spectroscopy AOM was set to the frequency at which the unshifted $F' = 3$ and shifted $X_{2,3}$ peaks coincided. A similar system was used for Cs.

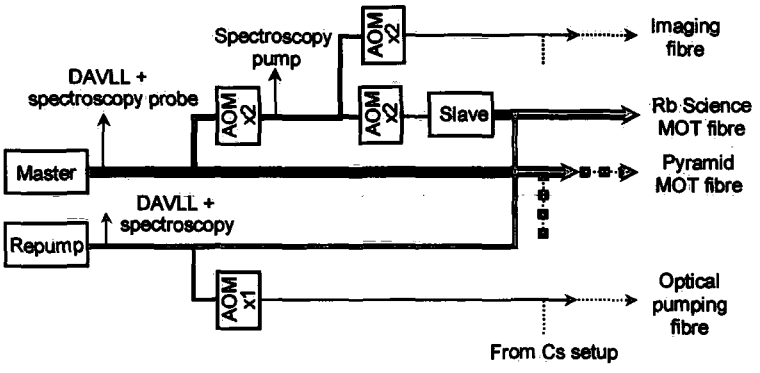

Figure 4.10: Schematic diagram of the optical layout for Rb. Three lasers provide light for cooling, repumping, imaging and optical pumping in the double-MOT system. The Cs layout is similar. Line thickness indicates relative beam power. Acousto-optic modulators (AOMs) in double pass (×2) and single pass (×1) configurations allow independent control of all frequency detunings. Larger shifts in frequency required for optical pumping and depumping stages are obtained by additionally applying a dc voltage offset to the dichroic atomic vapour laser lock (DAVLL) signal in order to offset the laser lock point. All light is transferred from the laser table to the experiment via optical fibres. For the pyramid MOT, optical pumping, and imaging light, dichroic optics are used to combine 780 nm and 852 nm beams before transmitting both wavelengths down single fibres.

pumping light are combined into a single beam using a PBS. The 780 nm and 852 nm beams are then overlapped using a dichroic mirror from LaserOptik which transmits (reflects) light at 780 nm (852 nm). The resulting four-frequency beam is coupled into a single fibre, with the polarisations of the cooling and repumping beams aligned to the two orthogonal axes of the fibre. Dichroic mirrors are also used to couple both wavelengths into the fibres which transmit light for imaging and optical pumping. Light for the Rb and Cs science MOTs is coupled into separate fibres for each wavelength.

Great care must be taken when aligning the polarisation angle of the beams with the fibre axes. Poor alignment will produce an output beam with a polarisation which oscillates between circular and linear over periods of between several minutes to a few tens of seconds. In aligning the fibre, it is helpful

to quantify the polarisation purity of the output beam by measuring the powers of light with the desired and undesired linear polarisations. This is usually done by sending the light through a PBS in a rotatable mount, such that at 0° (90°) of rotation the transmitted beam is horizontally (vertically) polarised relative to the optical bench. The ratio of these powers is known as the *extinction ratio*, and is our standard measurement of polarisation purity. Figure 4.11(a) shows the time-averaged extinction ratios of the output beam as a function of the angle of a half wave plate placed at the fibre input. Note that the extinction ratio increases sharply at waveplate angles of $\sim 45n$ degrees ($n = 1 \ldots 3$ here), indicating that the input beam's polarisation angle would be roughly aligned with a fibre axis if the wave plate were removed.

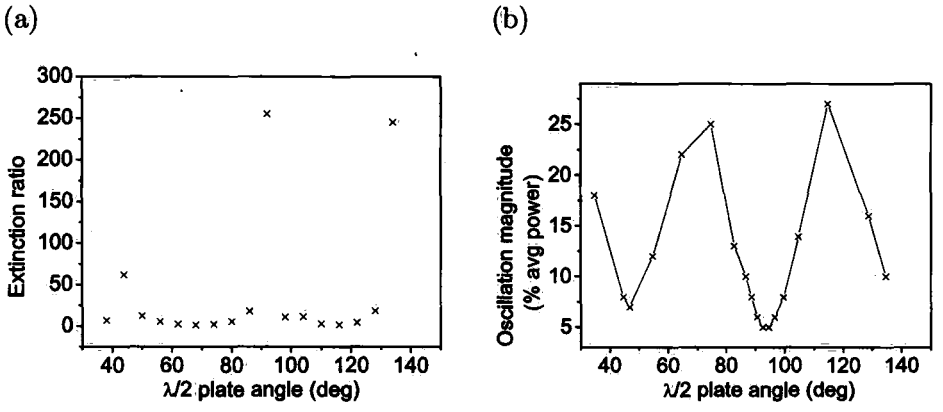

Figure 4.11: (a) Extinction ratio of the fibre output beam as a function of input polarisation angle. Higher extinction ratios indicate greater polarisation purity, and hence better alignment. (b) The magnitude of the oscillations in the output beam illustrates how polarisation impurities affect the power transmitted through a PBS cube. Oscillations of below 5% are achievable, but we have found that anything below 10% is acceptable.

An alternative method of quantifying the alignment is illustrated in Figure 4.11(b). In this case, we have measured the polarisation oscillations directly by recording the maximum and minimum powers transmitted through a fixed PBS over several oscillation cycles. The oscillation amplitude is then divided by the average transmitted power to give the oscillation magnitude. This gives us a useful illustration of how polarisation impurities in the output

beam will translate into power fluctuations after the beam passes through PBS cubes, *e.g.* to produce beams for the MOT. The oscillation data are broadly consistent with the data shown in the extinction ratio graph, with minima at approximately every $45n$ degrees. All of the fibre output beams in this experiment have oscillation magnitudes of less than 10% of the average power.

An additional complication for fibre polarisation alignment is that the dichroic mirrors used in this experiment exhibit pressure-dependent birefringence when mounted in standard mirror mounts (Thorlabs KCM1). Mounts of this type exert pressure on the optic at three points along the optic's edge, and the pressure is increased by tightening a grub screw. Tests showed that for dichroic mirrors held in this type of mount, the polarisation purity of the 780 nm transmitted beam dropped from an incident extinction ratio of >200:1 to as little as 6:1 as a result of passing through the dichroic. The ellipticity of the transmitted beam increased as the optic was tightened, and was also dependent on the angle of incidence (red line in Figure 4.12). Poor polarisation purity at the fibre input causes the polarisation angle of the output light to oscillate; at one point our Rb pyramid MOT was appearing and disappearing in synch with the polarisation oscillations. The problem was solved by mounting the dichroic mirrors in non-stressing mounts (black line in Figure 4.12).

4.7 Double-MOT system

This next section is intended to provide a general description of the double-MOT apparatus used in the Rb-Cs mixture experiment. A more detailed explanation of *e.g.* how the alignment of the science MOT beams was fine-tuned and how the MOT gradient and detunings were optimised may be found in Ref. [84].

4.7.1 Pyramid MOT

The pyramid MOT provides a compact, robust two species atom source. The pyramid is formed by mounting two high reflection coated 45 degree prisms in

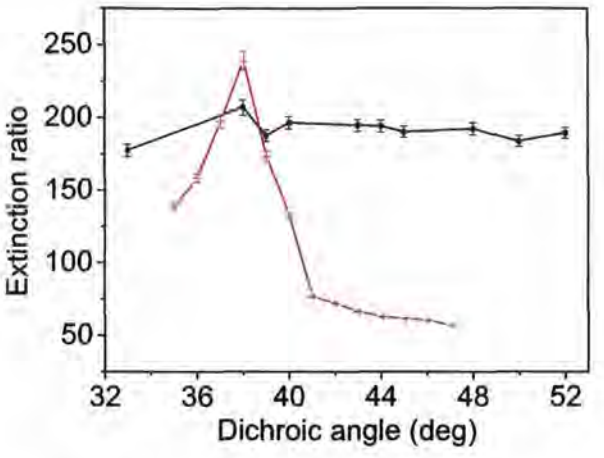

Figure 4.12: Pressure-dependent birefringence in the dichroic mirrors. When the dichroic optic is held in a mount which exerts pressure on its sides, the polarisation purity, or extinction ratio, of the transmitted 780 nm light shows a strong dependence on the angle of incidence (red crosses). Mounting the optic in a non-stressing fashion virtually eliminates this dependence (black squares). The polarisation purity of the incident light was >200:1.

a 90 degree 'V' formed by two rectangular mirrors held perpendicular to each other within the vacuum chamber. The base of the pyramid is 60×60 mm. The apex of the pyramid is truncated, producing a gap of $\sim 2.4 \times 3.0$ mm which is aligned with the differential pumping tube leading into the UHV region of the vacuum system. Figure 4.13 contains a close-up view of the pyramid optics. The arrangement of the dispensers can also be seen.

Light from the pyramid MOT fibre ($\sim$ 50 mW of cooling and $\sim$ 2 mW of repumping power at both wavelengths) passes through a single achromatic $\lambda/4$ plate and is collimated ($1/e^2$ radius = 20.4(4) mm) before entering the vacuum chamber. A 10 cm diameter mirror allows us to adjust the angle of the pyramid beam as it enters the chamber. An initial rough alignment was performed by copropagating light from a laser pointer (which was intense enough to be detectable at the far end of the science cell) with the lower-intensity pyramid beam. Aligning the circularly polarised pyramid MOT beam onto the mirror assembly produces three orthogonal pairs of beams

Figure 4.13: Close-up view of pyramid optics. The gap in the apex of the pyramid allows the cold atoms to stream into the UHV chamber via a differential pumping tube. Metal clips hold the optics in place. The design of the pyramid MOT chamber is based on one developed at Oxford by C. J. Foot and D. Cassettari.

with the polarisations of a standard six-beam MOT, as described in [133] and discussed in Chapter 3.

The magnetic field gradient required for the pyramid MOT is produced by a pair of water-cooled circular coils (24 turns each, coil diameter $\sim$ 140 mm), operated in the anti-Helmholtz configuration and wound directly onto the vacuum system. The current through these coils is controlled via a servo circuit, parts of which are also water-cooled. More details of the current servo circuit may be found in Ref. [101]. Additional 'shim' coils provide a bias field, allowing the position of the magnetic field zero to be adjusted. When the zero-field point is located directly in front of the pyramid apex, the pyramid MOT acts as a cold atom source for the science MOT.

The gradient and detunings of the single-species pyramid MOTs were optimised by maximising the loading rate of the science MOT. This was done by monitoring the fluorescence of atoms captured in the science MOT during the first 10 s of loading. For Cs, the maximum science MOT loading rate of $1.3(3)\times10^7$ atoms s^{-1} was achieved for a pyramid magnetic field gradient of 8.5(1) Gcm^{-1} and a pyramid MOT laser detuning of $\Gamma/\Delta = -3.06(4)$.

The maximum loading rate for Rb was 1.8(3) $\times 10^7$ atoms s^{-1}, at the same gradient and a detuning of $\Gamma/\Delta = -2.80(3)$ (see Table 4.1). These optimum settings showed only a weak dependence on the second MOT parameters in the vicinity of *their* optimum settings.

The atomic flux and therefore the science MOT loading rate are strongly dependent on the dispenser current which sets the vapour pressure in the pyramid chamber. Increasing the dispenser current above its usual operating value of 3 A led to a much increased atomic flux, but would potentially degrade the vacuum in the UHV region over time. At 4 A, for example, the science MOT loading rate is increased by more than an order of magnitude and is then comparable to the rates demonstrated previously for a similar Rb-Cs cold atomic beam source [201].

4.7.2 Science MOT

Atoms in the cold atomic beam generated by the pyramid MOT are captured in two six-beam science MOTs. Light from the Rb and Cs science MOT fibres is collimated to a $1/e^2$ radius of 10.9(1) mm. The beams are subsequently truncated by passing through the 20 mm square polarising beamsplitter cubes which split the light into six beams per species. In the horizontal plane there are eight beams (four per species), the intensity, alignment and polarisation of which can all be independently adjusted. The 780 nm and 852 nm beams in this plane are separated by $\sim 7°$. In the vertical direction the 780 nm and 852 nm light is aligned along a common beam path. All of the beams contain both cooling and repumping light. Having independent adjustment in the horizontal plane means that each single-species MOT can be independently optimised without affecting the performance of the MOT for the other species.

Figure 4.14 (a) shows the layout of the MOT optics in the horizontal plane. Red (blue) lines indicate 852 nm (780 nm) beams; the purple square at the centre of the science cell indicates the position of the overlapped 780 nm-852 nm vertical beam. The footprint of the vacuum system and the breadboards are drawn on the same scale. Figure 4.14 (b) contains a photograph of the completed optical setup.

(a)

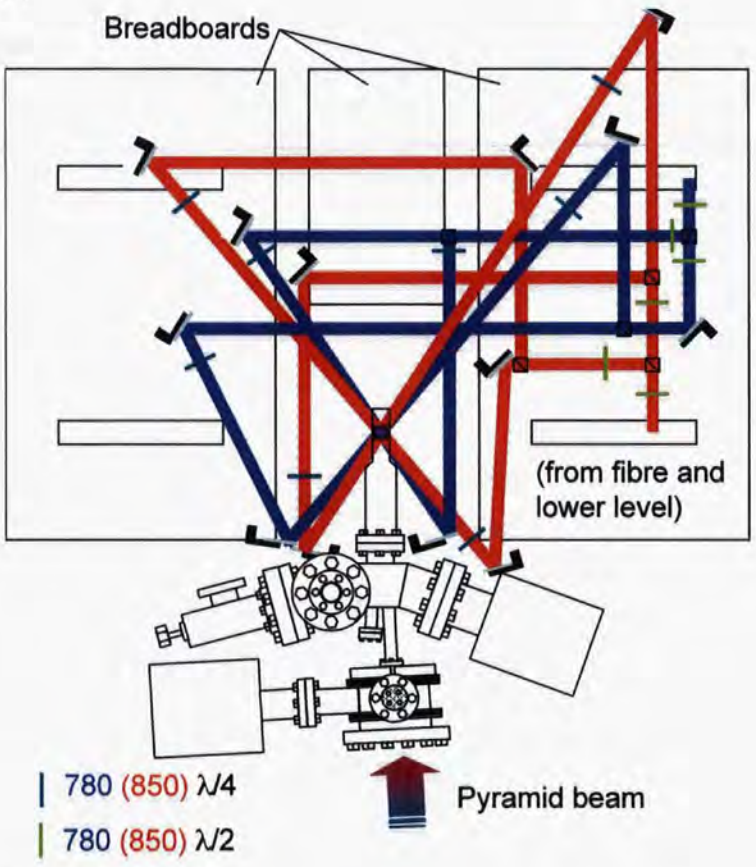

(b)

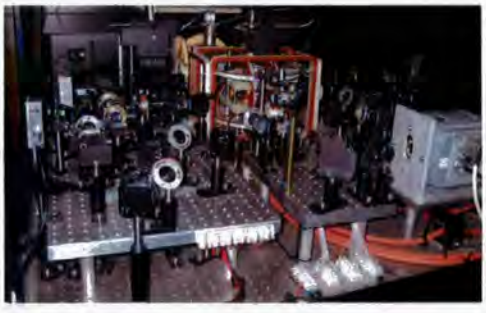

Figure 4.14: (a) Schematic diagram of science MOT optical layout. Red (blue) lines indicate 852 nm (780 nm) beams. The breadboards are drawn on the same scale; the two larger boards measure 70×40 cm each. The distance between the pyramid MOT chamber and the science cell is 30 cm. The positions of half and quarter wave plates are indicated with light and dark green lines. (b) Photograph of completed optical setup.

	^{87}Rb	^{133}Cs
Cooling transition	$F = 2 \rightarrow F' = 3$	$F = 4 \rightarrow F' = 5$
Repumping transition	$F = 1 \rightarrow F' = 2$	$F = 3 \rightarrow F' = 4$
Pyramid MOT detuning (Δ/Γ)	-2.80(3)	-3.06(4)
Science MOT detuning (Δ/Γ)	-1.99(3)	-1.97(4)
I_{Pyramid} (mW cm^{-2})	49.2(6)	49.8(8)
I_{Science} (mW cm^{-2})	11.0(3)	11.8(3)
MOT gradient (G cm^{-1})	10.1(1)	10.1(1)

Table 4.1: Summary of experimental parameters. The natural linewidth Γ is $2\pi\times6.06$ MHz ($2\pi\times5.22$ MHz) for Rb (Cs). The MOT intensities represent values due to all the beams combined.

A pair of anti-Helmholtz coils mounted on a framework outside the science cell provide the magnetic field gradient. The current through the coils is generated by a power supply capable of producing up to 67 A at 7.5 V (Xantrex XPD 7.5-67), with current noise and drift rated at less than 150 mA rms and less than 34 mA over 8 hours (respectively). Like the pyramid coils, the science MOT coils are water-cooled. As in the pyramid MOT, three pairs of 'shim' coils provide a tuneable bias field, allowing the position of the science MOT to be adjusted.

The alignment, detuning, and magnetic field gradient of the Rb and Cs science MOTs were optimised in order to maximize the trapped atom numbers of each species without the other species present. For Rb, a magnetic field gradient of 10.1(1) G cm^{-1} and a laser detuning of $\Delta/\Gamma = -1.99(3)$ produced a MOT containing $9(1)\times10^8$ atoms. For Cs, $4(1)\times10^8$ atoms were trapped in the MOT at the same optimised gradient and a detuning of $\Delta/\Gamma = -1.97(4)$. Table 4.1 summarises the optimum operating parameters of the pyramid and science MOTs.

4.8 Magnetic trap

The experiment uses an Ioffe-Pritchard type 'baseball' trap to generate 3D confinement with a controllable, non-zero bias field, as described in Chapter 3. The baseball consists of nine windings of Kapton-coated square copper

tubing (outer diameter 3.175 mm with a 2.00 mm round hole down the centre). This coil alone produces a radial gradient of 1.087(4) $Gcm^{-1}A^{-1}$, an axial curvature of 0.154(2) $Gcm^{-2}A^{-1}$, and a bias field of 0.3410(3) GA^{-1}. Additional bias and cancellation coils (nine and three turns, respectively, of tubing with an outer diameter of 4 mm and an inner diameter of 2.75 mm) in the Helmholtz configuration are used to either enhance or cancel the bias field produced by the baseball. Vertical bias coils will be used in future experiments on optically trapped atoms in combination with a levitation field gradient produced by the MOT coils. Figures 4.15(a) and 4.15(b) show the arrangement of the coils.

The currents in these coils are controlled by a circuit similar to that used in Ref. [101]; Ref. [84] contains detailed information about how this design was modified to meet the needs of the Rb-Cs mixture experiment, and how the new circuit was tested and optimised. The magnetic trap controller (EW1285) and servo electronics (EW1282) were constructed to designs from Oxford's Central Electronics workshop.

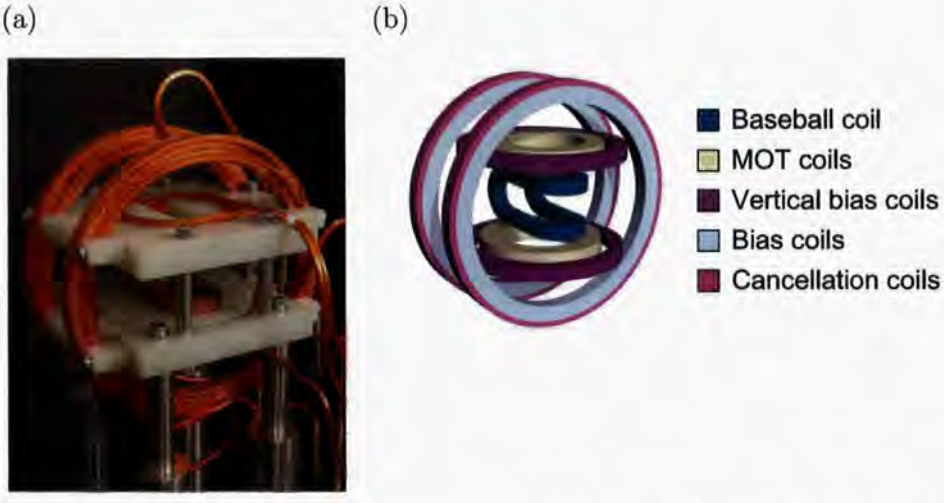

Figure 4.15: Arrangement of coils in magnetic trap. (a) Photograph of completed trap. (b) Schematic diagram of the magnetic trap identifying position and function of different coils. The labels are in order of increasing distance from trap centre.

4.9 From MOT to magnetic trap

It is possible to load atoms into the magnetic trap directly from the science MOT. However, atoms in the MOT are a) occupying a relatively large volume at relatively low density, b) not necessarily located at the magnetic trap centre and c) not all in the same magnetic sublevels of the hyperfine state (m_F states). Left uncorrected, these conditions will lead to lower atom numbers in the magnetic trap and increased heating of the atoms which do get trapped. This section describes procedures which address these problems.

4.9.1 CMOT

The purpose of the compressed MOT (CMOT) phase of the experiment is to produce a dense cloud of atoms located at the magnetic trap centre. To increase the density of the trapped atoms, the detuning of the cooling laser is increased for both Rb and Cs. Increasing the detuning decreases the scattering of photons from the cooling laser. Such scattering limits the density of the MOT as photons are absorbed and re-radiated by the trapped atoms, as discussed in Chapter 3. The magnetic field gradient provided by the MOT coils is also increased, to 20.8(2) G cm^{-1}. This increases the effective spring constant confining the atoms to the centre of the MOT. Note, however, that increasing the gradient also decreases the maximum radius at which sub-Doppler cooling can occur.

During the CMOT phase, the settings of the science MOT shim coils are adjusted such that the centre of the MOT is shifted from the optimum science MOT loading position to the centre of the magnetic trap. If the centres of the MOT and magnetic trap are not well aligned, the atom cloud will 'slosh' around the magnetic trap (Figure 4.16). Anharmonicities in the trapping potential will lead to heating as collisions between the sloshing atoms convert the potential energy of the sample into kinetic energy. The amplitude of the slosh is measured by taking a series of absorption images of the magnetically trapped cloud and plotting the position of the cloud centres as a function of time. Optimum settings for the shim coils during the CMOT phase are found by minimising the slosh amplitude.

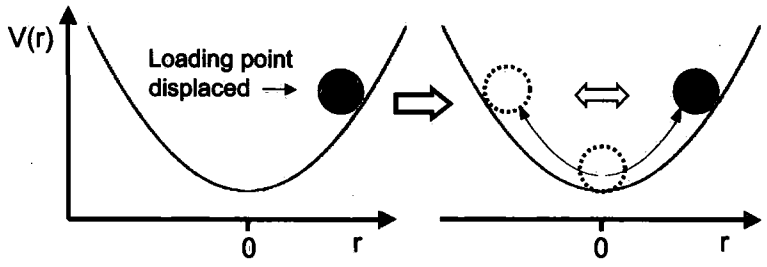

Figure 4.16: Illustration of slosh in one dimension. Atoms loaded into the magnetic trap from a MOT displaced from the magnetic trap centre will gain more potential energy during trap turn-on than atoms loaded at the centre. This potential energy will be converted into kinetic energy via collisions between atoms as they 'slosh' around the trap.

4.9.2 Optical molasses

The CMOT phase increases the density of the atom cloud at the cost of increasing its temperature (kinetic energy). The optical molasses phase counteracts this effect by switching off the quadrupole field, allowing sub-Doppler polarisation gradient cooling to take place throughout the cloud. While the field is off, the cloud expands. The expanded cloud is, of course, less dense than it was initially, and naively one might conclude that the benefits of the CMOT and molasses phases cancel each other out. In fact this is not the case, as the following example illustrates.

Suppose that a dense atom cloud with high kinetic energy (corresponding to the end of the CMOT phase) is loaded into the centre of the magnetic trap. If the kinetic energy of the cloud is higher than the potential energy due to the trapping potential, the cloud will expand and contract in a 'breathing' motion. Eventually, the cloud will reach thermal equilibrium — but at a density which has been determined by its kinetic energy, not by the density at which it was loaded. By cooling the cloud beforehand, we reduce the kinetic energy and eliminate one cause of breathing[1]. Hence, the CMOT and molasses phases together allow us to tune the position, density and kinetic energy of the atom clouds to match the parameters of the magnetic trap.

[1]A mismatch in the *shape* of the laser-cooled cloud relative to the trapping potential can also produce breathing.

Getting the laser cooled cloud to match the thermal equilibrium distribution in the magnetic trap allows us to maximise the phase space density of the trapped cloud, a process known as mode-matching.

The magnetic trap is loaded at field of 158 G (selected because there are no Cs Feshbach resonances nearby), and the radial and axial trap frequencies at this field are $\nu_r = 10.82(1)$ and $\nu_{ax} = 3.878(3)$ ($\nu_r = 11.29(4)$ and $\nu_{ax} = 4.027(2)$) for Rb (Cs). The durations of the CMOT and molasses phases which produced the best mode-matching were found to be 30 ms and 15 ms, respectively, although at this writing the CMOT stage is being reexamined and the optimisation process is ongoing [84].

4.9.3 Optical pumping

The last phase in the MOT $\rightarrow$ magnetic trap transition addresses the fact that the MOT traps atoms in all m_F states. Some of these states are high-field seeking and thus cannot be magnetically trapped, but both Cs and ^{87}Rb have multiple weak-field seeking states. Inelastic collisions between atoms in these m_F states will lead to a loss of atoms from the magnetic trap. Before loading the trap, it is therefore necessary to purify the atomic sample by optically pumping both Rb and Cs atoms into stretched states.

In our case, these are the $|F = 3, m_F = -3\rangle$ and $|F = 1, m_F = -1\rangle$ states of Cs and Rb respectively. The optical pumping scheme for Rb is illustrated in Figure 4.17. A pulse of optical pumping light is provided by detuning the repumping lasers to frequencies which drive $F = 3 \rightarrow F' = 3$ ($F = 1 \rightarrow F' = 1$) transitions in Cs (Rb). The cooling lasers are also detuned to the Cs (Rb) $F = 4 \rightarrow F' = 4$ ($F = 2 \rightarrow F' = 2$) transitions. This 'depumping' light ensures that no atoms remain in the upper hyperfine states ($F = 4$ and $F = 2$ for Cs and Rb). The MOT shim coils settings are changed during the optical pumping phase to provide a quantisation field, ensuring that the light drives σ^- transitions. The magnitude of the quantisation field and the duration and detunings of the optical pumping pulses were set by maximising the percentage of atoms recaptured in the MOT after the magnetic trap is switched on for a few seconds, and then the MOT coils and beams are turned back on.

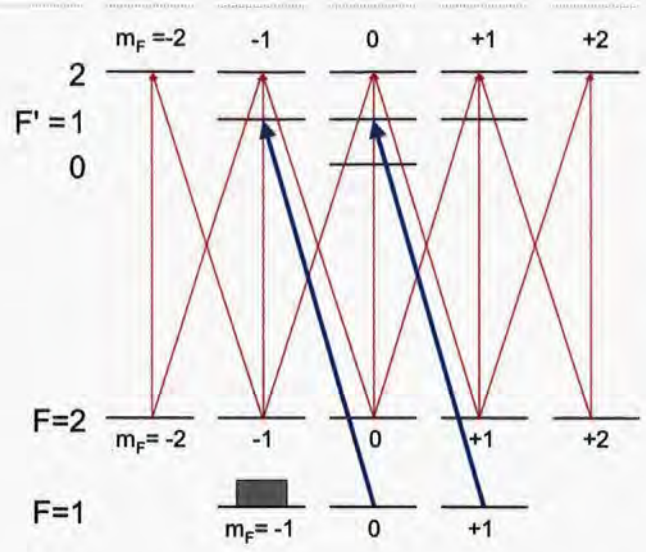

Figure 4.17: Optical pumping scheme for Rb. Optical pumping light (blue lines) tuned to the $F = 1 \rightarrow F' = 1$ transition drives σ^- transitions between the atomic sublevels. Atoms accumulate in the $|F = 1, m_F = -1\rangle$ state, which is dark to the OP light. A separate pulse of"depumping' light (red lines) depopulates the upper hyperfine states.

4.10 Diagnostics

Both fluorescence detection and absorption imaging are used to probe the atomic mixture. This section provides an overview of the principles behind both methods, then discusses their implementation in this experiment. Technical details of what happens during each imaging sequence are also provided.

4.10.1 Fluorescence detection

Fluorescence from the MOT is focused using a single lens and directed onto separate photodiodes for Rb and Cs light using a dichroic mirror (Figure 4.1). This dichroic, like the ones described earlier in this chapter, reflects 852 nm light and transmits 780 nm light. A small amount (1.2(2)%) of 780 nm light is also reflected, and contributes to the signal recorded by the photodiode monitoring the Cs fluorescence. This residual Rb fluorescence signal is sub-

tracted from the Cs signal; Chapter 5 contains details of how the subtraction was optimised for measurements of the two-species MOT.

The fluorescence signal of the photodiode can be converted into atom number using the equations found in Appendix C of Ref. [101]. Briefly, the conversion factor depends on properties of the atom (transition lifetime, saturation intensity), properties of the MOT light (detuning and frequency), and properties of the experiment (solid angle subtended by the collection lens, responsivity and gain resistance in the photodiode). The conversion factors for our experiment were 1.6×10^6 atoms/mV (3.6×10^6 atoms/mV) for Rb (Cs). Monitoring the fluorescence signal of the MOT thus gives a useful real-time picture of MOT performance for diagnostic purposes. Fluorescence detection was also used in measurements of atom numbers for the MOT studies in Chapter 5. A final application is the well-known 'MOT recapture' technique, in which the MOT light is switched back on after the atoms have been held in a purely magnetic trap. This technique allows us to measure the number of atoms captured in the magnetic trap *relative* to the number in the MOT, and is thus particularly useful for optimising optical pumping.

4.10.2 Absorption imaging

In absorption imaging a cloud of atoms is illuminated with a short ($\sim$10 μs) pulse of resonant light derived from a frequency locked, single mode laser. As this light passes through the cloud, the atoms absorb and scatter photons, resulting in a 'shadow' image which is recorded by a CCD camera (Figure 4.18). The amount of light absorbed is related to the column density of atoms in the cloud, from which we can determine the number of atoms in the cloud. We can also measure the cloud's spatial distribution after a short expansion time, and thereby gain information about its temperature and density - information which cannot be obtained via fluorescence detection.

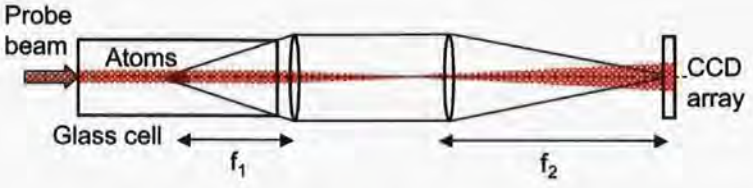

Figure 4.18: Schematic diagram of absorption imaging. The magnification of the image is the ratio of the two focal lengths, f_2/f_1.

Optical depth

We recall from Chapter 3 that a two-level atom in a laser field scatters light at a rate R, where

$$R = \frac{\Gamma}{2}\frac{I/I_{\text{sat}}}{1 + I/I_{\text{sat}} + 4\left(\Delta/\Gamma\right)^2}. \tag{4.1}$$

For N atoms confined in a volume d^3x, the amount of scattered power per unit volume is $n\hbar\omega R$, where $n = N/d^3x$ is the density. The fractional change in beam intensity due to scattering from the atoms is then

$$\frac{dI}{dy} = -n\hbar\omega R, \tag{4.2}$$

where we have taken the direction of beam travel to be along the y-axis.

This relation is often written in terms of the scattering cross section $\sigma = \hbar\omega R/I$. Note that we are concerned here with atom-light scattering, not the atom-atom scattering discussed in Chapter 2. In the limit that $I \ll I_{\text{sat}}$, $\sigma_0 = 3\lambda^2/2\pi$ for a two-level atom. Hence, we find after substitution that in terms of I_{sat},

$$\sigma_0 = \frac{\Gamma}{2}\frac{\hbar\omega}{I_{\text{sat}}}. \tag{4.3}$$

If we substitute this into Eq. 4.2, we obtain the following relation

$$\frac{dI}{dy} = -n\sigma_0\frac{I}{1 + I/I_{\text{sat}} + 4\left(\Delta/\Gamma\right)^2}. \tag{4.4}$$

To find the light absorbed, we integrate this equation along y, taking I_0 as the intensity of the light before it enters the atom cloud. If we describe the cloud density by a normalised Gaussian

$$n(x,y,z) = n(x,z)\frac{1}{\sigma_y\sqrt{2\pi}}\exp\left(-y^2/2\sigma_y^2\right), \tag{4.5}$$

we find

$$\int_{I_0}^{I} \frac{1 + I/I_{\text{sat}} + 4(\Delta/\Gamma)^2}{I} dI = -\sigma_0 \int_{-\infty}^{\infty} n(x,z) \frac{1}{\sigma_y \sqrt{2\pi}} \exp\left(-y^2/2\sigma_y^2\right) dy, \tag{4.6}$$

where the σ_i denote $1/e^2$ radii of the atom cloud. The right-hand side contains a standard Gaussian integral which is unity, so the final equation is

$$\left(1 + \frac{4\Delta^2}{\Gamma^2}\right) \ln\left(\frac{I}{I_0}\right) + \left(\frac{I - I_0}{I_{\text{sat}}}\right) = -\sigma_0 n(x,z) = -OD(x,z) \tag{4.7}$$

where

$$n(x,z) = \frac{N \exp\left(\frac{-x^2}{2\sigma_x^2} - \frac{z^2}{2\sigma_z^2}\right)}{2\pi\sigma_x\sigma_z} \tag{4.8}$$

and $OD(x,z)$ represents the optical depth at (x,z).

In the limit of low laser intensity and no detuning, Eq.4.7 becomes

$$I = I_0 \exp\left(-OD(x,z)\right). \tag{4.9}$$

It is instructive to compare this expression with the standard differential form of Beer's law, which is

$$\frac{I}{I_0} = \exp(-\alpha l c), \tag{4.10}$$

where α is the substance's absorption coefficient, l is the path length, and c is the concentration. By analogy we can see that the optical depth is proportional to the atom cloud's column density.

To determine the optical depth of the cloud experimentally, three separate camera images are taken. First, the atom shadow produced when the probe beam passes through the cloud is recorded (I_{atoms}). Second, an image is taken with the probe beam on, but no atoms present (I_{light}). The third image, I_{bkgd}, is a background image, taken with neither probe nor atoms present; this provides a calibration of stray (i.e. non-probe) light and of the CCD camera's dark current. These three images combine to give a measured optical depth in the limit of small detuning and low intensity of

$$OD_{\text{meas}} = \ln\left(\frac{I_{\text{light}} - I_{\text{bkgd}}}{I_{\text{atoms}} - I_{\text{bkgd}}}\right), \tag{4.11}$$

where the calculation is repeated for each pixel of the CCD camera.

There are some important systematic effects affecting this measured optical depth. One is that any off-resonant or incorrectly-polarised light that reaches the camera will cause the measured optical depth to be lower than its true value for an individual cloud, in essence because the cloud never had a chance to absorb such light. Shielding the probing region from outside light sources (*e.g.* room lights) removes a trivial source of unwanted light; a bigger problem is off-resonant or incorrectly-polarised light leaking into the probe fibre. Another effect occurs in clouds with high optical depths, where photons may be absorbed and scattered by several atoms. Such rescattering causes the atom cloud to saturate at lower values of I_0, decreasing the effective saturation intensity.

Measuring atom number from optical depth

To obtain the number of atoms in the cloud, a Gaussian function is fit to the data from the absorption images. The fitted values are used to calculate N. Rearranging Eqs. 4.7 and 4.8, we obtain

$$N = \frac{2\pi OD(x,z)\sigma_x\sigma_z}{\sigma_0} \exp\left(\frac{(x-x_c)^2}{2\sigma_x^2} + \frac{(z-z_c)^2}{2\sigma_z^2}\right), \tag{4.12}$$

where the coordinates of the cloud centre (x_c, z_c) and the cloud radii are found by the fit. The fitting and other image analysis processes are performed by a Matlab programme, details of which may be found in Appendix A. At the cloud centre, the expression for atom number reduces to

$$N_{fit} = \frac{2\pi OD_{\mathrm{pk}}\sigma_x\sigma_z}{\sigma_0}. \tag{4.13}$$

Temperature and density

For the study of MOT collisions and loss presented in the next chapter, the only pieces of information we require from our images are the atom number, cloud radii, and position of the Rb and Cs clouds. For magnetically trapped atoms, however, knowing the clouds' density and temperature is often necessary as well. Expressions for these quantities can be derived from the energy distribution of a thermal atom cloud, which is given by the Maxwell-Boltzmann distribution:

$$f(E) = f_0 \exp\left(-E/k_B T\right). \tag{4.14}$$

For an atom cloud in an harmonic potential,

$$E = \frac{1}{2}m\sum_j v_j^2 + \omega_j^2 j^2, \tag{4.15}$$

where $j = x, r$ and the ω_j are trap frequencies. We can then write

$$f(\mathbf{x},\mathbf{v}) = f_0 \prod_j \exp\left(-\frac{m}{2k_BT}\left(v_j^2 + \omega_j^2 j^2\right)\right). \tag{4.16}$$

To calculate f_0, we use the fact that the total number of atoms in all states must be N; after performing the integral over phase space, we find that

$$f(\mathbf{x},\mathbf{v}) = \frac{Nm^3\omega_x\omega_r^2}{8\pi^3 k_B^3 T^3}\prod_j \exp\left(-\frac{m}{2k_BT}\left(v_j^2 + \omega_j^2 j^2\right)\right). \tag{4.17}$$

Finally, we can write this as a density $n(\mathbf{x})$ by integrating over all velocities:

$$n(\mathbf{x}) = N\omega_x\omega_r^2\left(\frac{m}{2\pi k_BT}\right)^{3/2}\prod_j \exp\left(-\frac{m\omega_j^2 j^2}{2k_BT}\right). \tag{4.18}$$

The prefactors in the exponential term of Eq. 4.18 have dimensions of $1/\text{length}^2$, allowing us to write the density as

$$n(\mathbf{x}) = \frac{N}{(2\pi)^{3/2}\sigma_x\sigma_r^2}\exp\left(-\frac{x^2}{2\sigma_x^2} - \frac{r^2}{\sigma_r^2}\right);\ \sigma_i = \frac{1}{\omega_i}\sqrt{\frac{k_BT}{m}}, \tag{4.19}$$

where the σ_i are again cloud radii found from the fit. The peak density, found at $n(x_c, z_c)$, is

$$n_{pk} = \frac{N}{(2\pi)^{3/2}\sigma_x\sigma_r^2}, \tag{4.20}$$

with the average density

$$\langle n\rangle = \frac{1}{N}\int n(\mathbf{x})^2 d^3x = \frac{N}{8\pi^{3/2}\sigma_x\sigma_r^2}. \tag{4.21}$$

In terms of the cloud radii, the (radial) temperature of the atom cloud is

$$T_r = \frac{m\omega_r^2\sigma_r^2}{k_B}. \tag{4.22}$$

If the magnetic trap is switched off and the cloud allowed to expand in free space, after an expansion time τ_{exp} Eq. 4.17 will become

$$f(\mathbf{x},\mathbf{v}) = \frac{Nm^3\omega_x\omega_r^2}{8\pi^3 k_B^3 T^3}\prod_j \exp\left(-\frac{m}{2k_BT}\left(v_j^2 + \omega_j^2(j - \tau_{\text{exp}}v_j)^2\right)\right). \tag{4.23}$$

The expansion in each spatial direction will be, via simple kinematics,

$$\sigma_j(t) = \sqrt{\sigma_j^2(0) + \omega_j^2 \tau_{\rm exp}^2 \sigma_j^2(0)} = \sigma_j(0)\sqrt{1 + \omega_j^2 \tau_{\rm exp}^2}, \qquad (4.24)$$

where the $\sigma_j(0)$ represent the widths of the trapped cloud. To calculate the density and temperature of the trapped cloud from those of the expanded cloud, we simply substitute the new expressions for $\sigma_j(0)$ into Eqs. 4.19, 4.20 and 4.21.

Magnification

The magnification of the imaging system is found by taking a series of absorption images of the atom cloud after the trap has been turned off. By varying the delay between $t_{\rm off}$ and the imaging time, we can calculate the magnification by relating the position of the cloud centre to how far the cloud has fallen under gravity. Figure 4.19 shows the magnification measurement performed for the two-species MOT studies described in Chapter 5. In terms of the image variables, the acceleration due to gravity is

$$g = \frac{\text{binning} \times \text{pixel size} \times g'}{M}, \qquad (4.25)$$

where g' (c_3 in the figure) is the coefficient of the quadratic term in the fit and M is the magnification. In this case, the binning was 2×2, the Andor camera has a pixel size of 8 μm, and $g' = 0.28(3)$ pixels/ms^2, so the magnification is 0.46(5).

4.11 Experimental control

Atom cooling and trapping experiments depend very critically on our ability to control the sequence and timing of experimental events. If, for example, we wish to load atoms from the pyramid into the science MOT, transfer them to the magnetic trap, and then take an absorption image of them there, we must wait until the science MOT has loaded, then change the settings for the MOT and shim coils to compress the MOT, change them again for a period of optical molasses, optically pump the atoms into the correct state for imaging, turn the light off and the trap on, and finally fire the camera. Of these steps, only loading the science MOT takes place on what

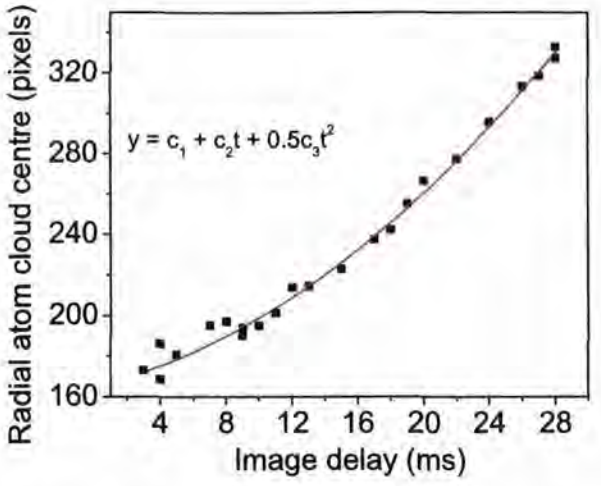

Figure 4.19: Magnification of the imaging system. Plotting the position of the cloud centre as the cloud falls under gravity allows us to calculate the magnification of the absorption images.

may be termed a 'human' time scale (typically a few tens of seconds) and with 'human' precision (a second either way will not make much difference). All of the other operations require 'machine' timing and precision. To achieve this, we use the popular Labview graphical programming software package, in conjunction with a National Instruments PCI-DIO32 32-channel digital input-output controller.

4.11.1 Control systems

The basic structure of our experimental control system and Labview code are similar to those described in [101]. Devices like shutters and the camera are assigned to one of the 32 channels on the digital input-output controller and connected to one of 32 ports on an output board. Labview represents these 32 channels as a two-dimensional array[2] of four rows by eight columns. Each element in the array has two possible states, variously referred to as 'high' and 'low' (*i.e.* in terms of the TTL signal produced by the output board), in

[2]This is referred to as a 'vector' within Labview; however, 'array' is a more accurate term.

boolean form as 'T' and 'F,' or in binary terms as 1 and 0. One can think of the array as being like a snapshot of the experiment: it contains a complete description of what the experiment is doing (*i.e.* which devices are receiving high and low TTL signals) at a single instant in time.

To incorporate the passage of time, the array must be expanded into a pattern. This may be thought of as a stack of snapshots. In the course of an experimental sequence, one or more subroutines within the main Labview programme modify the pattern and pass the modified pattern onto the next subroutine. Once the software has completed the pattern for a particular routine, the pattern is loaded into the buffer on the board and then written to the output channels. The virtual sequence of events represented by the pattern then becomes an actual sequence of events in the experiment.

Some devices, such as the MOT coils and AOMs, require 2-4 different voltages to set their operating parameters during different phases of the experiment. These devices are controlled by a multiplexer (Oxford Central Electronics, Voltage Level Multiplexer), which takes in a binary TTL signal from two ports on the output board (*i.e.* 00, 01, 10, or 11) and supplies different voltages for each binary pair to a single output. The experiment also uses two analog channels to control the magnetic trap current.

The system for controlling the CCD camera used in absorption imaging involves the camera's own software as well as Labview. The camera and Labview communicate via a homemade input/output box whose input and output ports are connected to the auxiliary input (AUXIN1–4) and output (AUXOUT1–4) pins on the camera PCB card. The sequence of events is:

1. The user selects a programme script for the camera software to run.
2. After 190±2 ms the camera is ready to acquire an image.
3. At any time afterwards, Labview can send a TTL 'high' pulse to the external trigger input on the camera.
4. The camera takes either an image or series of images, according to the script being run.
5. When the image-taking process is finished (including time required to save the data), the camera software produces a 'finished' TTL pulse by

setting the AUXOUT1 port to 'high' for 3 ms.

6. Labview receives the 'finished pulse' via one of the board's four digital input ports and moves on to the next part of the pattern.

To take an absorption image, steps 3–6 are repeated three times (representing the atoms, probe-only, and background shots). Figure 4.20 illustrates the timing of the listed steps for single-species imaging. Note that unlike the imaging system described in Ref. [101], there is no need for a separate TTL pulse to 'arm' the camera prior to sending the pulse which triggers the actual image-taking. The next subsection describes how the absorption imaging system was optimised for single- and two-species imaging.

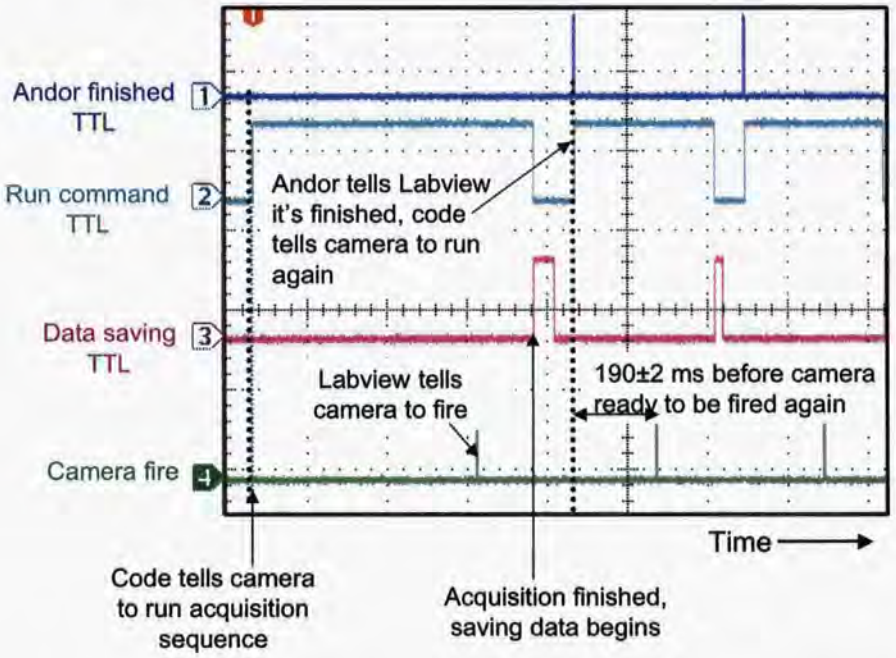

Figure 4.20: Diagram showing timings of events in Andor software/Labview interface.

4.11.2 Taking images with the Andor iXon camera

The frame transfer CCD camera (Andor iXon 885) used to record images of Rb and Cs clouds is relatively new and had not been used before in the

Durham group. Prior to integrating the camera into the Rb-Cs mixture experiment, we studied the images the camera produced in several operation modes and measured the timings of each imaging sequence. This information allowed us to select which operation modes should be used for single- and two-species imaging.

A key factor in our decision was the need to make the time between images as short as possible. This was particularly important for two-species imaging because we wanted to record separate images of the magnetically trapped Rb and Cs clouds in a single experimental sequence. Hence, we needed to minimise the time between Rb and Cs images in order to be sure the images were taken under the same experimental conditions, and to prevent the time of flight for the second image being so long that the atoms would hit the floor of the glass cell before they could be imaged.

Single-species imaging

We investigated two different modes of triggering the camera for single-species imaging. In fast external trigger mode, the camera begins to acquire an image after receiving a TTL 'camera fire' pulse from the Labview programme. The length of the camera exposure is set via a dialog box within the Andor software, and is independent of the Labview trigger length. In bulb mode, the length of the exposure is tied to the length of the trigger pulse. When the trigger TTL is high, the camera begins to record an image, and as soon as the trigger returns to zero the camera stops recording. The camera also has an internal trigger mode which is useful for troubleshooting the imaging system, but was not used to record data.

Figure 4.21 illustrates what the camera does in bulb mode. The illustrations at the top of the figure are images recorded by the camera when a 20 μs pulse of light was incident on the camera at the times indicated. Phase 1 shows what happens when light arrives at the camera before the trigger pulse (which coincides with the red 'fire monitor' line) begins. The blue 'arm monitor' line is high, indicating that the camera is ready to receive a trigger, but because no trigger has yet arrived, charge is drained away from the CCD array. Late in phase 1, the trailing edge of the light pulse hits the CCD during or after the fire pulse has started, and a 'ghost image' is recorded on

the camera. Phase 2 represents normal imaging. The light pulse arrives at the camera during the fire pulse, and the camera records an image. After the end of the trigger pulse, the camera begins shifting the image data up the active CCD array, row by row, and into the masked frame transfer CCD array. The duration of phase 3 depends on the camera shift speed, which was set to 1 row/ 1.963 μs when this data was taken. At the end of phase 3, the arm monitor is high again, and any light which falls on the camera is not recorded.

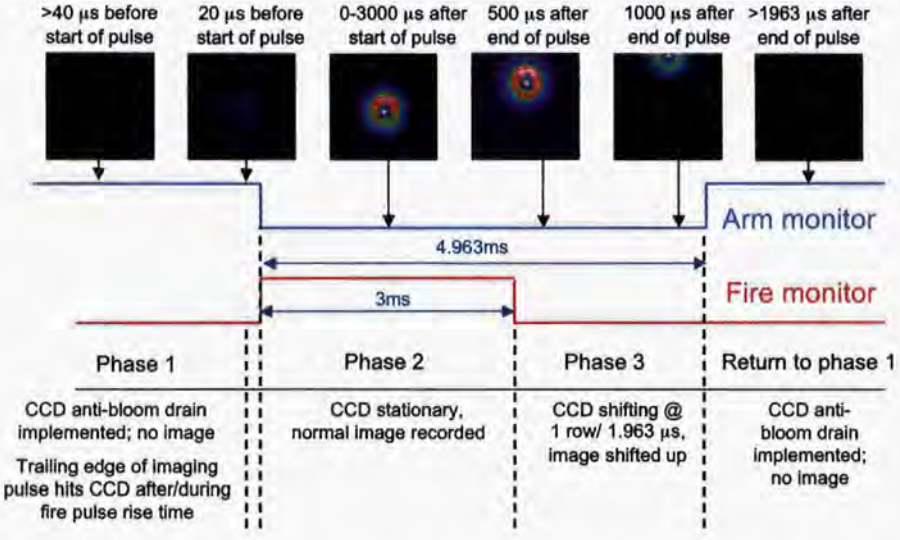

Figure 4.21: Timing diagram showing camera behaviour in bulb mode.

The diagram for fast external trigger mode is very similar to Figure 4.21. The difference is that the duration of the camera's 'fire pulse' (defined as the time when the CCD is stationary and a normal, unshifted image is recorded) can be different from the Labview trigger. The structure of the phases is the same: 1.963 ms after the end of the fire pulse, regardless of its duration, the CCD array is finished shifting and no image is recorded. As there was no need to set the camera's fire pulse and the Labview trigger time separately, we decided to use bulb mode for imaging single species in the MOT or magnetic trap.

Two-species imaging

In Figure 4.21, the camera's arm monitor goes high as soon as the image has been shifted into the frame transfer area of the CCD. However, a second Labview trigger sent at this point will not result in a second image because of the additional delay required for image processing, as discussed in Section 4.11.1. The camera's 'fast kinetics' mode allows us to take multiple images in a rapid-fire sequence, leaving the image processing stage to the end. In this mode, the charge accumulated in the active CCD during the imaging of the first species is subsequently shifted into a second masked CCD. The active CCD is then exposed again and an image of the second species is recorded. Both images are then read into a computer for processing. The total time required to perform the two-image fast kinetics sequence three times (for the absorption, probe only, and background images) is typically $\sim$ 2 s, limited by the readout speed of the camera.

We investigated three triggering modes for fast kinetics imaging. The fast kinetics versions of external trigger mode and bulb trigger mode are very similar to their single-shot counterparts. In both cases, the user sets both the number of images and the length of time between images. In bulb mode this is done by setting the length and time separation of the triggering pulses, while in external trigger mode these parameters are set in a dialog box within the camera software. The third mode, external start trigger, requires only one triggering pulse, and simply takes the second image as soon as the camera is ready — that is, as soon as the first image has been shifted into the masked CCD.

Figure 4.22 illustrates camera behaviour in external start trigger mode. The top (bottom) row of illustrations shows the first (second) image taken in the two-image sequence. Note that although two images were recorded at each point in the diagram, only one pulse of light was incident on the camera. Before the trigger pulse, light which hits the camera is not recorded as an image. For the first 1.921 ms after the trigger pulse, the camera performs a 'clean cycle,' shifting charge out of the active CCD in preparation for the first image. At the end of this cycle, the CCD stops shifting and remains stationary for the user-defined duration of exposure. At the end of the exposure period t_{exp}, the camera begins shifting the data up into the masked frame

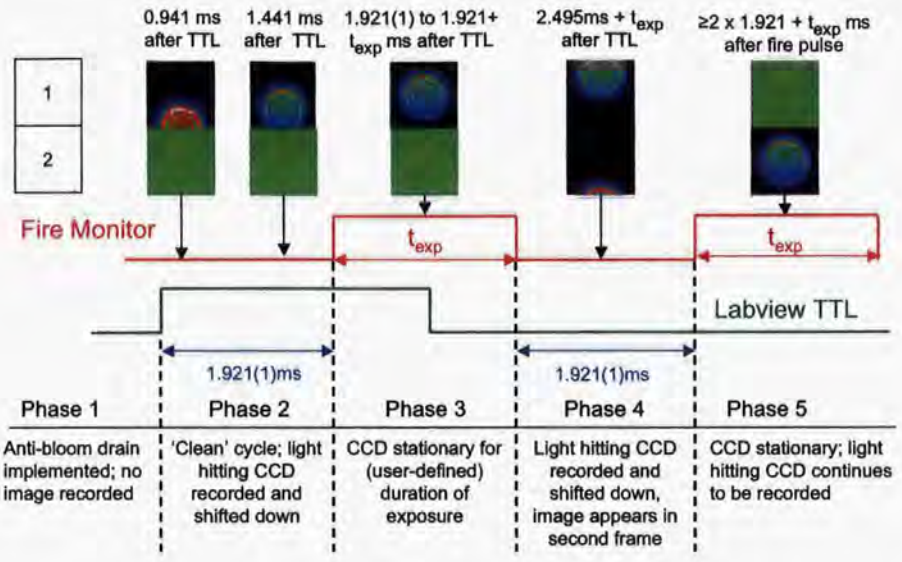

Figure 4.22: Timing diagram showing camera behaviour in external start trigger mode.

transfer arrays. Hence, any light which falls on the camera during this period is split between the two frames. Once all the rows of data have been shifted, the camera immediately starts to record the second image. Light which falls on the CCD during this time is recorded in the second frame - including any stray light incident on the camera during the period when both images are being read out. The background count level for the second image in each of the three pairs (atoms, probe-only and background) is therefore higher than for the first.

For our experiment, there was no need to set the delay between images of Rb and Cs to anything other than its minimum value of 1.921 ms, determined by the shift speed and the size of the array. The camera also had a software bug which prevented us from using 2×2 binning in fast kinetics bulb or fast kinetics external trigger modes. We therefore used external start triggering when imaging Rb and Cs in the magnetic trap. Further details of the imaging process, including the specific programme settings needed to run an imaging sequence in the Durham mixture experiment, are found in Appendix B.

4.12 Summary and look ahead

The Rb-Cs mixture apparatus — vacuum system, lasers, MOTs, magnetic trap, and diagnostic systems — was described in this chapter as it was during the studies of the Rb-Cs double-MOT system, with only a few notes on modifications made since those measurements were completed. The next chapter focuses on studies of the Rb-Cs science MOT.

Chapter 5

Collisions and loss in a Rb-Cs MOT

The MOT has been described as the 'workhorse' of atomic physics [202]. As such, achieving a MOT is frequently regarded as a step on the road to quantum degeneracy or more complex experiments rather than as an end in itself. The experimental apparatus described in the previous chapter, for example, is currently being used to study Rb-Cs mixtures at temperatures much colder than the $\sim$100 μK achievable in the two-species science MOT. Yet this picture of a MOT as a means to an end ignores two important facts. Firstly, despite almost two decades of experimental and theoretical work (see *e.g.* Refs. [96, 141] and references therein), the atom-light and atom-atom interactions taking place in a 3D MOT are still not fully understood. Secondly, the flip side of being an unglamorous workhorse is that a good MOT is the *sine qua non* of many experiments: having fewer atoms in the MOT means fewer atoms available for transfer into magnetic or optical traps, making it more difficult to reach quantum degeneracy via evaporative cooling.

Part of Chapter 3 was devoted to a discussion of the cold collisions which lead to a loss of atoms from one- and two-species MOTs. Such information is needed to understand the measurement methods used in our studies of the Rb-Cs MOT, the dependence of loss on MOT parameters like intensity, gradient and detuning, and the special challenges of two-species MOTs. Experimentally, however, our primary focus was not on the specific loss processes but on how we could reduce or suppress them and thus increase the

number of cold Rb and Cs atoms available for loading into the magnetic trap. The bulk of this chapter is therefore devoted to experimental measurements of MOT loss.

5.1 Introduction

Since the first demonstration of a two-species MOT of ^{87}Rb and ^{85}Rb in 1994 [203], a number of different mixture MOTs have been studied experimentally. These include MOTs containing various combinations of alkali metal atoms (see *e.g.* Ref. [65] and references therein), rubidium and metastable argon [204], and rubidium and chromium atoms [66]. Recently, a three-species MOT of rubidium and fermionic isotopes of lithium and potassium has also been demonstrated [205].

Several topics appear repeatedly in the experimental literature on two-species MOTs. The most common experiments study the loss of one species from the MOT in the presence and absence of a second trapped species. This allows the relative contributions of single-species and two-species inelastic collisions to the total loss rate to be determined. We present the results of such loss measurements on our Rb-Cs MOT in Section 5.2. A common extension is to examine how the loss rates vary with the intensity [206] or detuning [207] of the trapping beams. We saw in Chapter 3 that many of the MOT loss mechanisms depend on intensity, detuning, or both. Hence, information on intensity or detuning dependence of loss can indicate which loss mechanisms are most important for a particular species or set of experimental conditions. Numerous studies of single-species MOTs [141] have found that relatively small alterations in trap parameters, *e.g.* a factor of two change in intensity, can produce changes of several orders of magnitude in the loss rate coefficients.

A less common type of experiment attempts to separate the contributions of different loss channels to the total loss rate. This was done for lithium and caesium by chopping the Li trapping light, thereby altering the average excitation of the Li atoms [75]. It is also possible to gain information about different loss channels by measuring the rate at which atom-ion molecules are produced in the MOT, using a time-of-flight spectrometer [208]. Such

measurements were beyond the scope of this work, and are mentioned chiefly to provide some idea of experiments which can be performed to understand the MOT loss mechanisms discussed theoretically in Chapter 3.

5.2 Measurement methods

We now turn away from a general discussion of two-species MOTs to examine how the single-species and two-species loss rate coefficients can be measured. It is helpful to recall from Chapter 3 that the time-evolution of a single-species MOT is described by the rate equation

$$\frac{dN_i}{dt} = L - \gamma N_i - \beta_i \int n_i^2 d^3r, \tag{5.1}$$

while the two-species equation is

$$\frac{dN_i}{dt} = L - \gamma N_i - \beta_i \int n_i^2 d^3r - \beta_{ij} \int n_i n_j d^3r. \tag{5.2}$$

Three methods have been used to measure values of β and thereby characterise MOT loss. The first of these examines the MOT as it is being loaded and is included here for completeness as it was not used in our studies. The other two methods were used, and are described in more detail.

5.2.1 Loading method

Assuming the MOT loads at a constant density [209], the one-species equation reduces to

$$\frac{dN_i}{dt} = L - (\gamma + \beta_i \langle n_i \rangle) N_i, \tag{5.3}$$

where $\langle n_i \rangle$ is the mean number density and we have considered only one-species MOTs for simplicity. The factor $\gamma + \beta_i$ is determined by measuring the number of trapped atoms as a function of time, *e.g.* by recording the fluorescence with a photodetector. Solutions to Eq. 5.3 are then fit to the data. Figure 5.1 shows the loading of the Cs MOT after the repumping beam is unblocked at $t = 0$. In order to extract β_i, a separate experiment must be performed in which the MOT is operated at very low atom numbers. In this regime, cold collisions play little role in the total loss rate, and the equation reduces further to

$$\frac{dN_i}{dt} = L - \gamma N_i. \tag{5.4}$$

This allows γ to be measured independently. If we assume that $\gamma \approx 0$ for the data in Figure 5.1, and take the cloud density to be 4.29×10^9 cm^{-1} (the average value for all Cs clouds, measured from absorption images), a fit to the loading curve for $t = 0 - 40$ s gives $\beta_{Cs} = 4.65(9) \times 10^{-11}$, where the error is calculated from the fit.

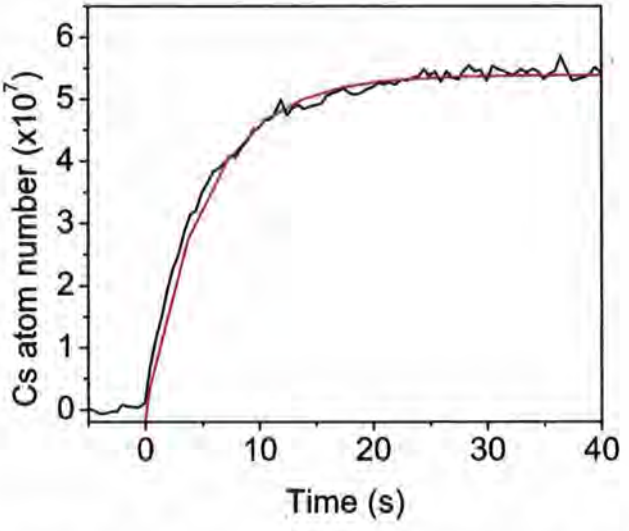

Figure 5.1: Loading of the single-species Cs MOT. Unblocking the repumping beam at $t = 0$ allows Cs atoms to be trapped in the science MOT. The loss rate coefficient β_{Cs} can be determined by fitting Eq. 5.3 to the data.

5.2.2 Decay method

A second technique allows the values for β_i and γ to be measured in a single experimental run. In this method, the loading is turned off ($L = 0$ in Eqs. 5.1 and 5.2) and the fluorescence observed as the MOT decays. Initially, the decay occurs in a constant density regime, where the MOT loses atoms and decreases in size without any change in density. Later, the density begins to decrease. Eventually, the density is so low that collisions with the background gas are the dominant loss mechanism. As the decay of one species can be recorded either in the presence or absence of a second species, this method can be used to measure both single-species and two-species loss rate coefficients.

For decays of two-species MOTs, the two-species rate equation becomes

$$\frac{\mathrm{d}N_i}{\mathrm{d}t} = -\left(\gamma + \beta_i\langle n_i\rangle + \beta_{ij}\langle n_j\rangle F_{ij}\right) N_i, \tag{5.5}$$

where the factor F_{ij} represents the (normalised) density of species j weighted by the probability distribution of species i. F_{ij} approaches zero as the two clouds become spatially separated, while two clouds of equal size centred at the same position will have an F_{ij} of unity. F_{ij} may therefore be thought of as a measure of the relative overlap of the two trapped atom clouds.

5.2.3 Steady-state method

The third method is specific to two-species MOTs. In the so-called 'steady-state' method, the interspecies rate coefficients are determined by comparing equilibrium values of atom number and the size of trapped clouds in the single-species MOT to the corresponding equilibrium values with another species present. In this method, Eq. 5.2 is solved for β_{ij} in the presence and absence of a second species. To do this, we recall that the average densities for single and two-species atom clouds are defined as

$$\begin{aligned}\langle n_i\rangle &= \frac{1}{N_i}\int n_i^2 d^3r \\ \langle n_{ij}\rangle &= \frac{1}{N_i}\int n_i n_j d^3r.\end{aligned} \tag{5.6}$$

Using these definitions, the rate equation becomes

$$\frac{dN_i}{dt} = L - \gamma N_i - \beta_i\langle n_i\rangle N_i - \beta_{ij}\langle n_{ij}\rangle N_i. \tag{5.7}$$

These definitions also allow us to formally define the 'overlap' factor F_{ij} as

$$F_{ij} = \frac{\int n_j n_i/N_i d^3r}{\int n_i n_i/N_i d^3r} = \frac{\langle n_{ij}\rangle}{\langle n_i\rangle}. \tag{5.8}$$

To obtain an expression for β_{ij}, steady-state solutions to the rate equation are found in the presence and absence of a second species. In the single-species MOT, this gives

$$L = \gamma\tilde{N}_i + \beta_i\langle\tilde{n}_i\rangle\tilde{N}_i, \tag{5.9}$$

where the $\tilde{}$ denotes quantities in the single-species MOT. Adding a second species changes the equation to

$$L = \gamma N_i + \beta_i\langle n_i\rangle N_i + \beta_{ij}\langle n_{ij}\rangle N_i. \tag{5.10}$$

Solving for β_{ij} gives the result:

$$\beta_{ij} = \frac{1}{\langle n_{ij} \rangle N_i} \left[\gamma \left(\tilde{N}_i - N_i \right) + \beta_i \left(\langle \tilde{n}_i \rangle \tilde{N}_i - \langle n_i \rangle N_i \right) \right]. \tag{5.11}$$

5.3 Modifications to experimental setup

All of the methods for measuring β_i and β_{ij} require knowledge of the number of atoms in the MOT and their density profile to calculate the loss rate coefficients. Fluorescence detection allows changes in atom number to be observed in real time, and is thus essential for decay or loading measurements. The steady-state atom number can be obtained either from fluorescence detection or via absorption images. Absorption images provide information about the atoms' location (important for calculating the overlap between trapped Rb and Cs atoms) and the cloud density. This section describes modifications to the diagnostic systems and to the optimum MOT parameters which were made specifically for the MOT measurements.

5.3.1 Fluorescence measurements

In order to monitor MOT decay, we needed to record the evolution of the atom number for longer than the 100 s maximum period for a single oscilloscope scan. The fluorescence detection system used for the MOT measurements was therefore modified from the standard setup used for routine diagnostics. The signals from the two fluorescence photodiodes were first sent to a pair of current-to-voltage converter circuits (Figure 5.2). The circuits allowed us to monitor the photodiode signal on the oscilloscope and a GPIB-enabled volt meter at the same time, without any change of signal due to problems with impedance matching the two devices. The circuit also featured four gain settings, which are summarised in Table 5.1. The gain factors were calibrated using a constant light source and are within 10% of their expected values based on the resistors used. Both battery-powered and mains-powered circuits were constructed; however, only the mains-powered circuits were used in these experiments.

In the description of the fluorescence detection apparatus in Chapter 4, it was noted that the dichroic mirror reflects a small percentage of the Rb

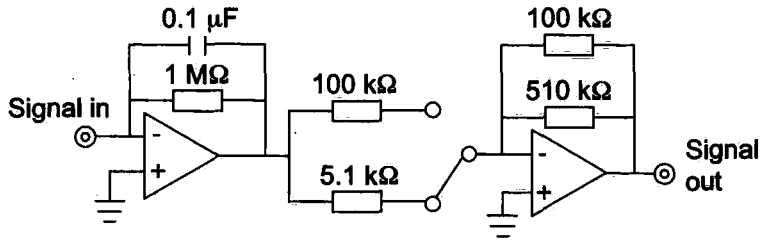

Figure 5.2: Current-to-voltage converter circuit. The signal from the fluorescence photodiode is sent through this circuit before being recorded on an oscilloscope and a digital voltmeter. AD648 op-amps were used for the battery powered circuit, while a mains-powered version used TL082s.

Resistor 1	Resistor 2	Expected gain	Measured gain
100 kΩ	100 kΩ	× 1	× 0.944(8)
100 kΩ	510 kΩ	5.1	4.9(2)
5.1 kΩ	100 kΩ	19.6	18.8(8)
5.1 kΩ	510 kΩ	100	95(7)

Table 5.1: Predicted and measured gain settings for current-to-voltage converter circuit.

light onto the photodiode monitoring Cs fluorescence. The effect of this on the Cs fluorescence signal is shown in Figure 5.3. The red (black) curve is the Rb (raw Cs) fluorescence signal. At $t = 25$ s, the Rb repumping light was unblocked and the Rb MOT began to fill. The signal recorded by the photodiode monitoring Cs light increased proportionally to the Rb signal until $t = 200$ s, when the Cs repumping light was unblocked. The sharp jump in the black curve represents the presence of actual Cs fluorescence. This problem was solved by subtracting a percentage of the Rb signal from the raw Cs signal. The amount of the correction was empirically set to 1.2(2)%, the value which gave a flat Cs signal in the absence of a Cs MOT. This is shown in the blue curve in Figure 5.3.

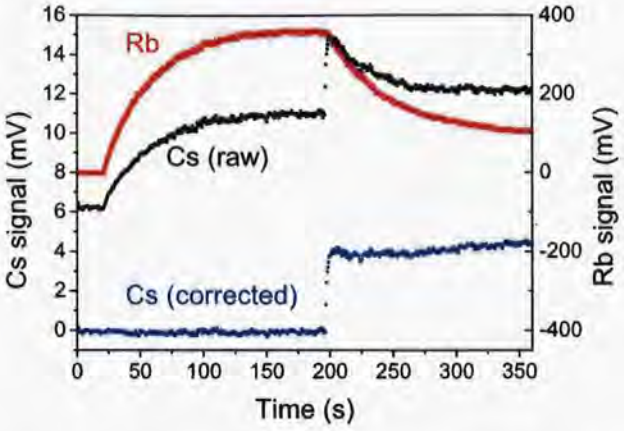

Figure 5.3: Effect of leaked Rb light on Cs fluorescence signal. The red curve shows Rb fluorescence as the MOT loads, starting at $t = 25$ s. The black curve shows the raw Cs fluorescence signal, which mirrors the Rb curve until $t = 200$ s, when the Cs MOT was turned on. The blue curve shows the Cs signal after 1.2% of the Rb signal was subtracted from the raw Cs signal.

5.3.2 Absorption imaging in the MOT

Imaging in the MOT was performed with the CCD camera in bulb mode. In this mode charge is being continuously drained away from the CCD whenever the camera is not firing. In theory this means that any light which falls on the camera before the image is taken will not affect the image. In practice the time required to remove charge depends on the amount of light which has fallen on the camera. For our system, images taken less than ~30 ms after the MOT light has been switched off contain images of MOT fluorescence in addition to the intended absorption image. This leads to the optical depths being underestimated, because the probe and background images do not contain residual MOT fluorescence. This is not a problem for imaging in the magnetic trap, because the atoms are typically held in the trap for $\gg 100$ ms before the images are taken. For MOT imaging *in situ* it was necessary to modify the standard imaging sequence to allow the unwanted fluorescence to be subtracted. The new imaging sequence is:

1. Image a: absorption + probe + fluorescence + background

2. Image b: probe + background
3. Image c: background only
4. Image f: fluorescence + background.

Image f is obtained during a separate data run, during which the probe beam is blocked during the imaging cycle. The new, corrected Image A which is imported by the Matlab code for analysis is

$$A = a - f + c. \tag{5.12}$$

Figure 5.4 contains absorption and fluorescence images of the MOT. As discussed in Chapter 4, the images show an array of optical depths, with higher depths shown in red. Note that the fluorescence appears as a negative optical depth; hence, optical depths in the corrected Image A will be higher than in the uncorrected version.

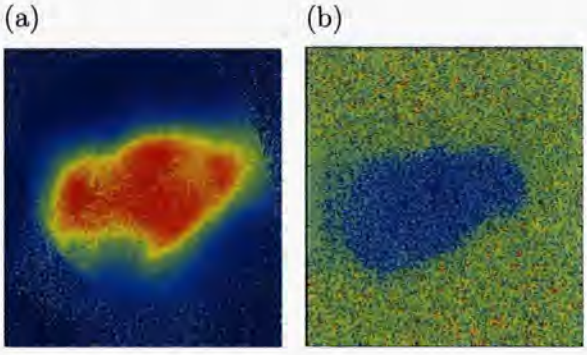

Figure 5.4: (a) Absorption+probe+fluorescence+background and (b) fluorescence+background images of the Rb science MOT. The fluorescence image is subtracted from the absorption image during image processing.

5.3.3 MOT parameters

Very large MOTs presented a challenge for absorption imaging. The largest Rb MOTs we measured nearly filled the camera's field of view along the radial direction, even after we reduced the magnification of the imaging system from ~1 to 0.46(5). Our solution to this (happy!) problem was to increase the

	^{87}Rb	^{133}Cs
Pyramid MOT detuning (Δ/Γ)	-2.80(3)	-3.06(4)
Science MOT detuning (Δ/Γ)	-1.99(3)	-3.49(4)
I_{Pyramid} (mW cm^{-2})	49.2(6)	49.8(8)
I_{Science} (mW cm^{-2})	11.0(3)	11.8(3)
MOT gradient (G cm^{-1})	20.8(2)	20.8(2)

Table 5.2: Summary of experimental parameters during the MOT measurements. The natural linewidth Γ is $2\pi\times6.06$ MHz ($2\pi\times5.22$ MHz) for Rb (Cs). The MOT intensities represent values due to all the beams combined.

magnetic field gradient to 20.8(2) Gcm^{-1}. This compressed both MOTs, and also ensured that the Cs MOT was located entirely within a larger Rb MOT — an effect desirable in its own right. The detuning of the Cs MOT was also changed to $\Delta/\Gamma = -3.49(4)$ to increase the number of trapped Cs atoms at the higher gradient. All other MOT parameters remained at their optimum values given in Chapter 4; Table 5.2 provides a full list of parameters.

At the new gradient and Cs MOT detuning, the increased density of the clouds meant that the measured optical depths for all but the smallest Cs clouds were very high (> 3.5). At such high optical depths, a very small increase in the absorption produces a disproportionately large increase in the optical depth. Taken at face value, such measurements would lead us to overestimate the number of atoms in the MOT. To avoid this, we performed all of our absorption imaging with the Cs probe beam detuned from resonance. The densities derived from the optical depth were then corrected for the detuning. Studies of detuned and resonant imaging in both species showed very similar results for the cloud radii regardless of the probe detuning.

5.4 Single-species loss measurements

We used the decay method to measure the single-species loss rate coefficients β_{Rb} and β_{Cs}. Figure 5.5 shows the fluorescence of the Rb MOT after the Rb pyramid MOT beam was blocked with a shutter. The decay is plotted on a logarithmic scale, so that periods of exponential decay are indicated by straight lines in the data. Initially, the decay occurs at a constant density

and the rate is exponential. As the number of atoms decreases, the radiation absorption effect of the MOT weakens enough that further loss of atoms results in a decrease in density, and the rate of loss increases. The density distribution of the cloud becomes Gaussian during this period. Eventually, the cloud enters the regime where cold collisions are no longer a major loss mechanism, as discussed in Chapter 3. The loss rate is again exponential, but with a reduced time constant γ determined by background gas collisions. Measurements of both species' lifetime in the magnetic trap showed that $\gamma = 1.5(3) \times 10^2$ s.

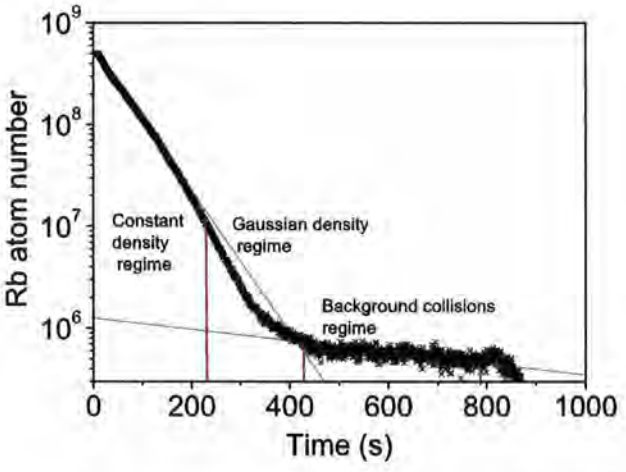

Figure 5.5: Fluorescence signal recorded during decay of Rb MOT. Initially, the density of the atom cloud remains constant and the MOT decays exponentially (first region). At some point, the density begins to decrease, and the decay is no longer exponential (second region). Eventually, so few atoms are left in the MOT that cold collisions play little role, and the decay is again exponential (third region).

We want to extract our values for β_{Rb} and β_{Cs} from the period in which the density is constant and limited by the re-radiation of photons discussed in Chapter 3. The precise boundaries of this period are not clear from the decay curves alone. To clarify the extent of the constant-density regime, a series of absorption images was taken for several different numbers of trapped atoms. The densities derived from these images showed considerable variation for MOTs containing less than $\sim 10^6$ atoms, and we have already noted that

very large MOTs ($> 5 \times 10^8$ atoms) are difficult to image. At intermediate values, the densities were relatively constant. This is illustrated in Figure 5.6 (a). Note that the magnitudes of the densities in this figure are lower than for most MOTs we studied by approximately a factor of 1.7; this is because these data were taken during preliminary experiments at the lower (optimised) gradient of 10.8 Gcm^{-1}. Later experiments at the higher gradient of 20.8 Gcm^{-1} focused on imaging only Rb MOTs in the constant-density regime, as shown in Figure 5.6 (b).

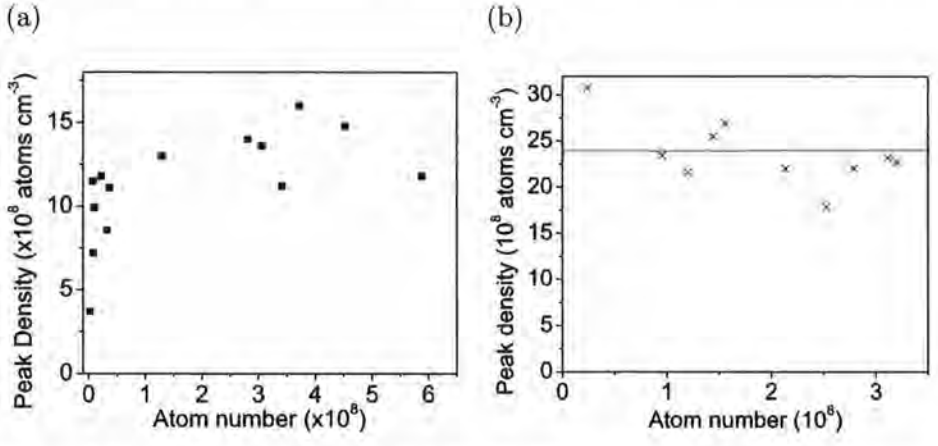

Figure 5.6: (a) Peak density of the Rb MOT as a function of atom number at a magnetic field gradient of 10.8 Gcm^{-1}. For MOTs containing more than $\sim 10^8$ atoms, the density is relatively constant. (b) Similar data taken at the higher gradient of 20.8 Gcm^{-1}, this time focusing only on the constant-density regime. The red line shows the mean value for the data set of $2.4(1) \times 10^9$ atoms cm^{-3}. The intensity and detuning of the MOT light was the same for both figures, with values given in Table 5.2.

Further evidence that the MOT is decaying exponentially for this atom number range was obtained by performing a series of fits to the decay curve in Figure 5.5. Each point in Figure 5.7 represents the value of $\tau = 1/(\beta_{\mathrm{Rb}} n_{\mathrm{Rb}})$ measured by fitting an exponential to 20 s of decay. Between 20-280 s, corresponding to $\sim 56 - 0.56 \times 10^7$ Rb atoms, τ is constant to within 15%. The sharp increase in τ after 300 s indicates a change in the MOT behaviour, and the increase in the size of the error bars indicates that the decay is not well approximated as exponential. We conclude that at this point, the MOT

has entered the non-constant density regime. Similar data for Cs showed that the decay of the Cs MOT is exponential for the first 20 s, corresponding to $\sim 0.36 - 7 \times 10^7$ Cs atoms.

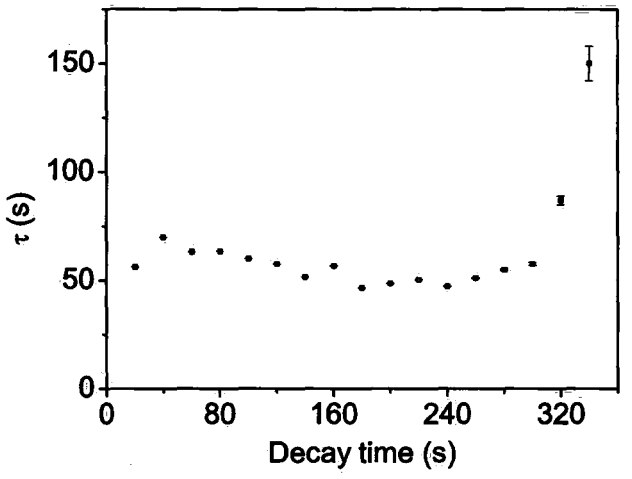

Figure 5.7: A series of fits to the decay curve in Figure 5.5 shows that the time constant $\tau = 1/(\beta_{\mathrm{Rb}} n_{\mathrm{Rb}})$ of the decay varies little for the first 300 s. The sharp increase near that time indicates a change in decay behaviour; larger error bars indicate that the decay is no longer exponential.

Single exponential fits to the Cs and Rb decay data over these time periods yielded $\beta_{\mathrm{Rb}} = 1.5(2) \times 10^{-11}\mathrm{cm}^3\mathrm{s}^{-1}$ and $\beta_{\mathrm{Cs}} = 2.1(1) \times 10^{-11}$ cm $^3\mathrm{s}^{-1}$, where the errors represent statistical variation over four decay measurements per species. Additional systematic uncertainties of up to 30% arise primarily from measurements of atomic cloud sizes. These values are in good agreement with the available published data [210, 211].

5.5 Two-species loss measurements

We first measured the two-species rate constants β_{RbCs} and β_{CsRb} by comparing the decay rates of Rb and Cs (in the constant-density regime) in the presence and absence of a second species. The MOTs were initially loaded to their two-species equilibrium values. The Cs pyramid MOT beam was then switched off, and the Cs MOT allowed to decay in the presence of cold Rb.

Although the number of Rb atoms increased during this decay, the position of the Cs MOT near the centre of the much larger Rb cloud meant that the overlap factor F_{CsRb} remained constant, and the Cs decay curve could be described by a single exponential throughout the density-limited regime. As Figure 5.8(a) shows, the Cs MOT lifetime is reduced by a factor of five from the single-species value in the presence of Rb. Averaging over three decay curves yielded $\beta_{\mathrm{CsRb}} = 1.0(6) \times 10^{-10}\mathrm{cm}^3\mathrm{s}^{-1}$.

To measure β_{RbCs} using the decay method, we restricted our fit to the first 10 s. Shortly after this period, the Cs atom number started to increase, and the Rb decay accelerated as a larger fraction of the Rb cloud was in contact with cold Cs. Figure 5.8(b) illustrates this. Measurements of initial Rb decay in the presence of Cs yielded $\beta_{\mathrm{RbCs}} = 1.6(4) \times 10^{-10}\mathrm{cm}^3\mathrm{s}^{-1}$.

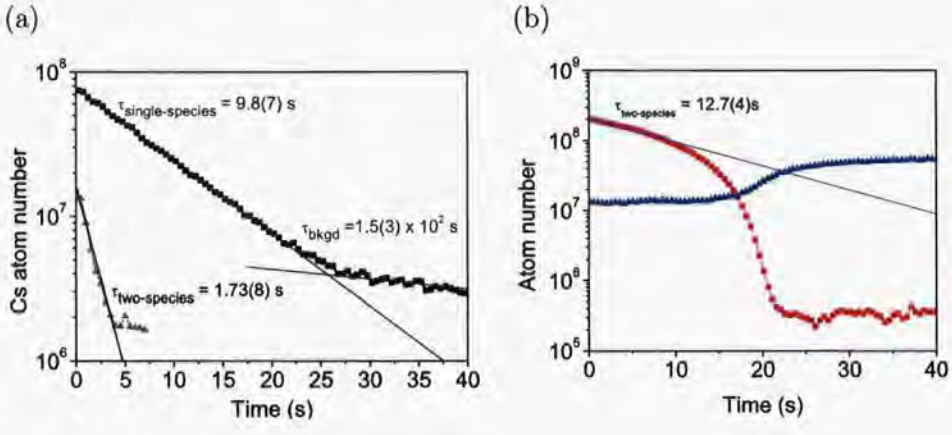

Figure 5.8: (a) Decay of the Cs MOT in the presence (grey) and absence (black) of cold Rb. The presence of the Rb MOT reduces the Cs MOT lifetime by a factor of five due to light-assisted interspecies inelastic collisions. (b) Decay of the Rb MOT (red) in the presence of the Cs MOT (blue). After ~10 s of exponential decay, during which time the number of Cs atoms is nearly constant, the recovery of the Cs MOT produces an acceleration in the Rb decay rate.

We also characterised the two-species loss rates using the steady-state method. Figure 5.9 shows a typical loading sequence used to extract the number of atoms present in the single-species and two-species equilibria. Initially, no repumping light is present, preventing the MOTs from forming. At

$t = 0$ s, the Cs repumping beam is unblocked, and the Cs MOT loads to its single-species equilibrium level. At $t = 45$ s the Rb repumping beam is unblocked, and collisions with cold Rb atoms cause rapid losses of $\sim 75\%$ of the trapped Cs atoms. The loading sequence is then reversed. Absorption images were taken of the Cs and Rb MOTs at their single-species and two-species equilibrium levels and values for the cloud radii obtained from Gaussian fits to these images. Figure 5.10 shows typical images of the single-species and two-species Rb and Cs MOTs. Note that in the two-species MOT, the Cs atom cloud is located entirely inside the Rb cloud. Hence, the Cs MOT decays very rapidly in the presence of Rb, whereas the Cs MOT simply acts like a small 'hole' in the Rb MOT, and its presence causes less rapid loss of Rb.

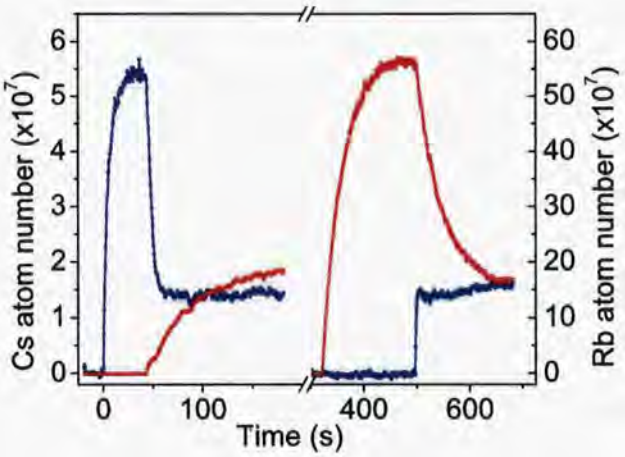

Figure 5.9: Sample sequence for steady-state measurements showing loading and loss in the Rb-Cs MOT. Initially, only Cs (blue line) is trapped. Unblocking the Rb repumping beam after 45 s leads to rapid losses of $\sim$75% in the Cs cloud. At $t = 300$ s the loading sequence is reversed. Note that the Cs MOT reaches its two-species equilibrium value within 10 s after the Cs repumping beam is unblocked, while the Rb cloud decays much more slowly due to the reduced overlap with the Cs cloud.

Based on these steady-state measurements, we found $\beta_{\mathrm{RbCs}} = 2.1(3) \times 10^{-10}$ cm^{3}s^{-1} and $\beta_{\mathrm{CsRb}} = 9(2) \times 10^{-11}$ cm^{3}s^{-1}, where the errors represent statistical variation over 3 (4) data sets for β_{RbCs} (β_{CsRb}). Additional systematic

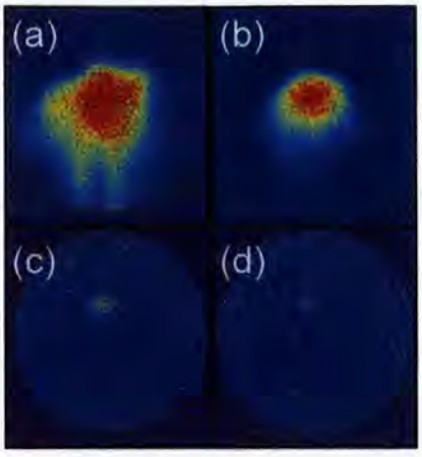

Figure 5.10: Absorption images of Rb and Cs in the single-species and two-species MOTs. Images of the Rb cloud without (a) and with (b) Cs present show a sharp reduction in cloud size due to interspecies inelastic collisions. Similar images of the Cs MOT without (c) and with (d) Rb present also show equilibrium numbers much reduced in the two-species MOT.

uncertainties of up to 30% arise primarily from measurements of atomic cloud sizes. These values are in good agreement with the values from the decay measurements.

5.6 Minimising interspecies loss

The very strong interspecies loss evident from both measurements presents a challenge for optimising the two-species Rb-Cs MOT. One possible optimisation strategy would be to alter the alignment and intensity balance of the MOT beams from their single-species optimised values in order to reduce the overlap of the two clouds. This realignment can be time-consuming, and ultimately one wants the two clouds well overlapped in order to load both into the centre of the magnetic trap. Additionally, changing the detunings and intensity of the MOT beams can in some cases be beneficial. Gensemer *et al.* demonstrated that for Rb, shifting the laser detuning by just one natural linewidth can change β_{Rb} by up to three orders of magnitude [210]. However, as Weiner *et al.* have discussed, the relationship between detuning, intensity,

and trap loss rate is quite complex even for single-species MOTs [141]. The parameter space is thus very large, and it is difficult to know *a priori* what effect changes will have on the loss rate.

We have developed an alternative method for reducing the interspecies loss which does not require any deviation from the optimum single-species MOT parameters. In this technique, a beam of light (with a $1/e^2$ radius of 7(1) mm and a peak intensity of 0.48(2) $\mathrm{mWcm^{-2}}$) close to resonance with the Rb cooling transition is aligned through the MOT centre during loading. The effect is to shift the centre of the Rb MOT by several mm, spatially separating the trapped Rb and Cs clouds. This 'push' beam is simply the beam used for absorption imaging at a higher intensity. Implementing the displaced MOT thus requires no additional optics or alignment. Optimum conditions for single-species trapping can be recovered by turning off the push beam, with no need for complex and time-consuming adjustments.

Figure 5.11(a) shows the fluorescence of the Rb and Cs MOTs during loading with and without the Rb MOT displaced. The Rb MOT is allowed to load to approximately 50% of its maximum single-species level before the Cs MOT loading is turned on at $t = 40$ s. With the push beam off, the Cs MOT loading is strongly suppressed, and the Rb MOT begins to decay. When the experiment is repeated with the push beam on, the Rb MOT loading proceeds unimpeded, and the Cs MOT reaches $\sim$ 70% of its single-species level before the Rb and Cs clouds begin to overlap, and interspecies inelastic collisions prevent further increase in the Cs atom number. If necessary, the overlap could be reduced further by displacing the Cs MOT as well. Using the displaced MOT technique, we have created two-species Rb-Cs MOTs containing a total of more than 10^9 atoms.

The effect of the displaced MOT technique on the magnetic trap loading is also pronounced. At the end of the MOT loading phase, a standard sequence of CMOT, optical molasses and optical pumping is used to load the atoms into the magnetic trap, as described in Chapter 4. The push beam is switched off immediately before the start of the CMOT phase, so that the two trapped atomic clouds become well overlapped prior to loading the magnetic trap. The short duration of the loading phase, however, means that there are no detectable losses due to interspecies light assisted collisions even though the

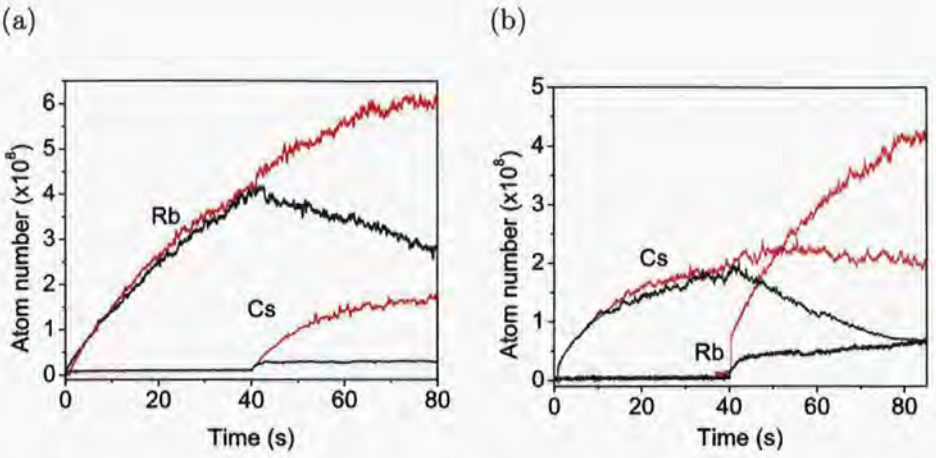

Figure 5.11: Performance of the displaced double MOT. (a) The Cs MOT is switched on after 40 s of loading Rb alone. Without the push beam (black line), atoms are lost from the Rb MOT due to light assisted interspecies inelastic collisions, and loading of the Cs MOT is greatly impaired. Turning the push beam on (red line) displaces the Rb MOT from the Cs MOT loading region, limiting losses due to interspecies collisions. (b) A similar sequence, but with Cs loaded first. With the push beam on (red lines), the Cs MOT reaches $\sim$ 70% of its single-species level before being limited by the presence of the Rb MOT. The Rb MOT loading proceeds unimpeded with the push beam on, but is greatly impeded in the non-displaced MOT (black line).

clouds are well overlapped at this stage.

Figures 5.12(a)–(c) contain images of magnetically trapped clouds taken with and without the push beam on during the MOT phase. The figures also contains vertical cross-sections of the atom clouds, showing the increase in optical depth for magnetically-trapped atoms loaded from the displaced MOT. The flexibility of the displaced MOT technique allows us to vary the composition of the trapped mixture over a wide range by adjusting the load duration of each species. We can load mixtures containing an equal amount of each species at close to their respective maximum single-species atom numbers. At the other extreme, we can load one species to its single-species maximum together with an arbitrarily small amount of the second species.

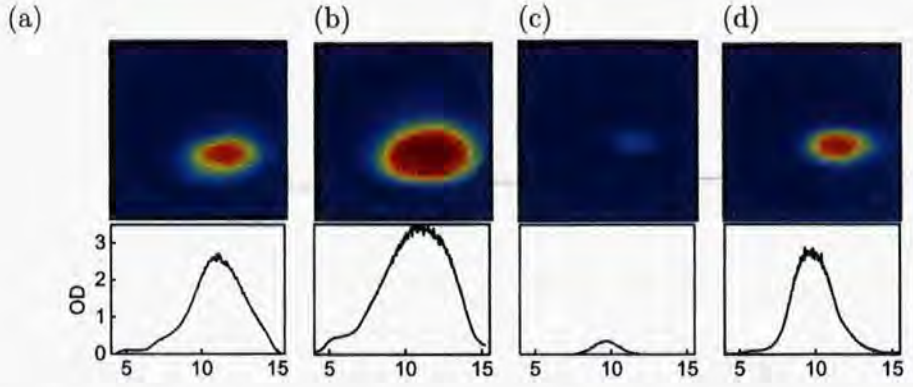

Figure 5.12: Absorption images of magnetically trapped Rb clouds loaded from unperturbed (a) and displaced (b) MOTs. Cross sections of the clouds in the vertical direction show increases in optical depth and size with the push beam present. Similar images of Cs clouds without (c) and with (d) the Rb MOT displaced show even more significant improvement. All images are displayed on an optical depth scale of 0-3 except the unperturbed Cs cloud, which is on a 0-1 scale. The cross sections are on a common 0-3.5 scale.

5.7 Conclusions

In summary, measurements on the Rb-Cs science MOT showed strong losses due to light-assisted inelastic collisions between the two species. For our MOT parameters, the rate coefficients β_{RbCs} and β_{CsRb} for two-species loss are approximately one order of magnitude larger than the single-species loss coefficients. This indicated that reducing two-species loss would lead to significant improvements in MOT performance. A simple but effective technique was developed to suppress two-species collisions by spatially separating the Rb and Cs MOTs during loading. This method is not specific to the Rb-Cs mixture, and should prove useful in reducing loss in other two-species MOTs.

The work on MOT losses described in this chapter was essential to the future progress of the Rb-Cs mixture experiment. The knowledge gained about the MOT has given us a better understanding of optimum loading conditions for the two-species MOT. In particular, the displaced MOT technique has proved a reliable and consistent method of preparing atoms for loading into

the magnetic trap. A particular advantage is that the push beam technique allows considerable flexibility in the ratio of Rb to Cs atoms available for loading into the magnetic trap. The two-species MOT we have developed thus represents an advantageous starting point for a range of experiments on cold Rb-Cs mixtures, including a search for interspecies Feshbach resonances and studies of sympathetic cooling.

Part III

Spectroscopy

Chapter 6

Polarisation spectroscopy of rubidium and caesium

Although the spectra of alkali metal atoms have been studied for decades [212], both spectroscopic techniques and their underlying theory remain active research topics. The atom-light interactions taking place in spectroscopic systems can be quite complex, yet in many cases simple theoretical models can be constructed which reproduce observed phenomena.

This chapter presents an experimental and theoretical study of one spectroscopic technique, polarisation spectroscopy. The study grew out of work by Edmund Tarleton, a Durham undergraduate who constructed a model of polarisation spectra for the $F = 3 \rightarrow F'$ transition in ^{85}Rb as part of his final-year project [213]. Details of the *Mathematica* code used to construct the model may be found in Appendix C and will not be discussed here. Instead, this chapter focuses on the physical processes involved in polarisation spectroscopy, how these were modeled theoretically, and the experimental studies performed to test the model's accuracy for rubidium and caesium.

6.1 Introduction

Like the saturated absorption/hyperfine pumping spectroscopy method described in Section 4.3, polarisation spectroscopy is a sub-Doppler technique which requires both pump and probe beams. In polarisation spectroscopy, the probe beam is linearly polarised, with the plane of polarisation set at 45°

with respect to a polarising beam splitter (PBS) which acts as an analyser (Figure 6.1). The quantity of interest is the difference between the signals in the reflected and transmitted arms of the PBS. When the circularly polarised pump beam is blocked, the two arms will have equal intensities, and the difference will be zero.

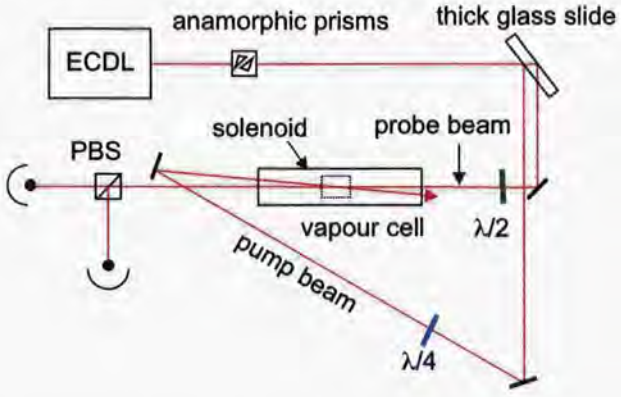

Figure 6.1: Experimental layout for polarisation spectroscopy. A thick glass slide picks off a fraction of the extended cavity diode laser (ECDL) light and splits it into two parallel beams. One beam acts as the probe, and the other as a (nearly) counterpropagating pump. The beams overlap inside a vapour cell, which rests inside a long solenoid and below a coil that cancels the ambient laboratory field. A half wave plate rotates the plane of polarisation of the probe beam with respect to the polarising beamsplitter (PBS) cube axis; a quarter wave plate makes the pump circularly polarised. Neutral density filters (not shown) are used to modify the pump and probe powers independently.

To understand the signal produced when the pump beam is turned on, a simple theoretical model of polarisation spectroscopy was developed based on a calculation of the rate equations for multi-level atoms. This chapter describes how these equations are used to generate theoretical polarisation spectra for the hyperfine transitions of the $D2$ lines of rubidium and caesium. These model spectra are then compared to experimental spectra, and reasons for agreement or disagreement between the model and the data are discussed.

6.2 Origins of the polarisation spectroscopy signal

A linearly polarised beam can be decomposed into two beams of equal amplitude and opposite circular polarisation. With the direction of propagation along the z axis, and the linear polarisation set at an angle ϕ relative to the x axis, the electric field of this beam can be written as

$$E = \begin{bmatrix} E_x \\ E_y \end{bmatrix} = E_0 \begin{bmatrix} \cos\phi \\ \sin\phi \end{bmatrix} = E_0 \left\{ \frac{e^{-i\phi}}{2} \begin{bmatrix} 1 \\ i \end{bmatrix} + \frac{e^{i\phi}}{2} \begin{bmatrix} 1 \\ -i \end{bmatrix} \right\} \tag{6.1}$$

where the last equality describes the field in terms of the circular polarisation basis vectors. In polarisation spectroscopy, a circularly polarised pump beam is counterpropagated with the linearly polarised probe beam as it passes through the vapour cell. Light from this pump beam drives σ^+ transitions in the alkali atoms, and the atoms are optically pumped into the higher m_F states. There is a difference in absorption coefficients, $\Delta\alpha$, for the optically pumped medium: $\Delta\alpha = \alpha_+ - \alpha_-$, with $\alpha_\pm$ being the absorption coefficients of the circular polarisation components driving $\sigma^\pm$ transitions. Hence, the electric field of the beam after a cell of length L is

$$E = E_0 \left\{ \frac{e^{-i\phi}}{2} \begin{bmatrix} 1 \\ i \end{bmatrix} e^{-ik_+ L} e^{-\alpha_+ L/2} + \frac{e^{i\phi}}{2} \begin{bmatrix} 1 \\ -i \end{bmatrix} e^{-ik_- L} e^{-\alpha_- L/2} \right\}, \tag{6.2}$$

where $k_\pm = n_\pm \omega/c$ and the $n_\pm$ are refractive indices corresponding to the different absorption coefficients. We have neglected the birefringence of the cell windows because the effects of the medium are expected to dominate.

Following the approach of Pearman *et al.* [184], and correcting for a sign error, we can rewrite this expression as

$$E = E_0 \exp\left(\frac{-iwnL}{c} - \frac{\alpha L}{2}\right) \left(\frac{e^{-i\phi}}{2} \begin{bmatrix} 1 \\ i \end{bmatrix} e^{-i\Omega} + \frac{e^{i\phi}}{2} \begin{bmatrix} 1 \\ -i \end{bmatrix} e^{i\Omega} \right). \tag{6.3}$$

Here,

$$\Omega = \frac{\omega \Delta n L}{2c} - i\frac{L}{4}\Delta\alpha, \tag{6.4}$$

and along with $\Delta\alpha = \alpha_+ - \alpha_-$, we have defined $\alpha = (\alpha_+ + \alpha_-)/2$, $n = (n_+ + n_-)/2$, and $\Delta n = n_+ - n_-$. The PBS splits the beam into its horizontally (x) and vertically (y) polarised components, and the intensity of each beam ($I \propto$

$|E|^2$) is recorded by a photodiode. The photodiode signals are subtracted electronically, giving a polarization spectroscopy signal of

$$\begin{aligned} I_{sig} &= I_y - I_x, \\ I_{sig} &= -I_0 e^{-\alpha L} \cos\left(2\phi + L\Delta n \frac{\omega}{c}\right), \end{aligned} \tag{6.5}$$

where I_0 is the intensity of the probe beam before it enters the cell. The difference in absorption has a Lorentzian profile of the form

$$\Delta\alpha = \frac{\Delta\alpha_0}{1+x^2} \tag{6.6}$$

where $\Delta\alpha_0$ is the difference in absorption of the atomic vapour at line centre and $x = (\omega_0 - \omega)\,/\,(\Gamma/2)$ is the detuning from line centre in units of the half linewidth $\Gamma/2$. The refractive index is related to the absorption coefficient by the Kramers-Kronig dispersion relation,

$$\Delta n = \frac{c}{\omega_0}\Delta\alpha_0 \frac{x}{1+x^2}. \tag{6.7}$$

Again following Pearman *et al.*, we assume that the laser profile is scanned across a single resonance. We also take the angular rotation induced by the atomic vapour to be small, such that the signal is maximised when $\phi = \pi/4$ and the small angle approximation $\sin(L\Delta n\omega/c) \approx L\Delta n\omega/c$ is valid. This yields the simplified expression

$$I_{sig} = I_0 e^{-\alpha L} L\Delta\alpha_0 \frac{x}{1+x^2}. \tag{6.8}$$

This signal has a dispersion-like shape, with a steep gradient through line centre and a zero-crossing at the frequency of the transition; it is therefore useful for laser locking. We can also see clearly from Eq. 6.5 that the incident linearly polarised probe beam exits the medium with a rotated elliptical polarisation, and both the ellipticity and the angle of rotation are proportional to $\Delta\alpha_0$. This differential absorption (*i.e.* dichroism) can be measured directly with only a small modification to the polarisation spectroscopy setup [184]. To make the measurement, a quarter wave plate is inserted before the analyser PBS, and its orientation is set such that the circular polarisation component of the probe which drives σ^+ (σ^-) transitions is converted into horizontally (vertically) polarised light. The photodiodes in the transmitted and reflected arms of the PBS then record the absorption of the two components directly.

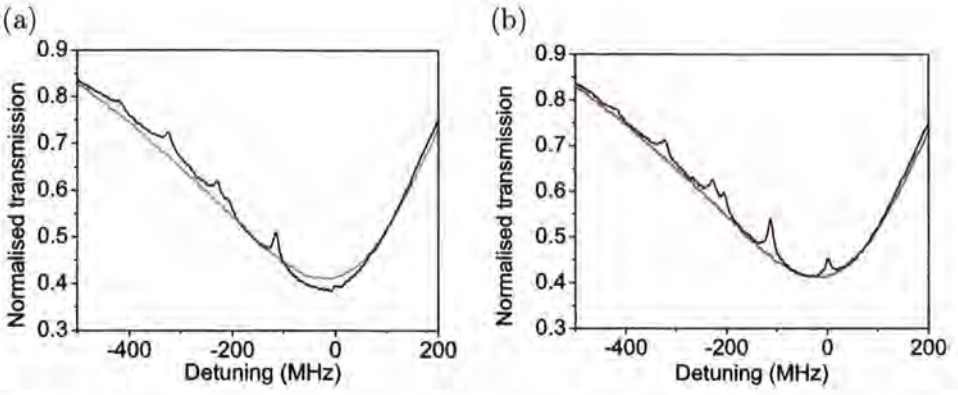

Figure 6.2: Differential absorption of light driving a) σ^+ and b) σ^- transitions in a caesium vapour. Red (black) traces show the absorption with the pump beam blocked (unblocked). The largest anisotropy is observed in the vicinity of the $F = 4 \rightarrow F' = 5$ laser cooling transition.

Figure 6.2 shows data obtained for the $F = 4 \rightarrow F'$ 'cooling' transitions in caesium. The red trace in each graph shows the absorption with the pump beam blocked, *i.e.* the conventional Doppler broadened absorption spectrum. With the pump beam present (black traces), the absorption is modified at the frequencies of the hyperfine transitions in Cs. A comparison of the horizontally and vertically polarised signals in Figures 6.2(a) and 6.2(b) shows that a large difference in absorption occurs in the vicinity of the $F = 4 \rightarrow F' = 5$ closed transition. The sign of the absorption also changes: while the component of probe light driving σ^+ transitions shows little, if any, enhanced absorption at this frequency, the absorption of the σ^- component is significantly reduced. Note that the difference in absorption for the Cs closed transition is not as striking as it is for the equivalent transition in Rb (see *e.g.* Fig. 5 in [184]). The discrepancy occurs because over 60% of resonant light has been absorbed by Cs vapour, whereas for Rb the absorption was less than 30%. There is therefore less scope for increased absorption in Cs. This difference between Rb and Cs has important implications for our theoretical model of polarisation spectroscopy, and will be discussed in greater detail later in this chapter.

Based on these measurements of the medium's anisotropy, we can predict

that the polarisation spectra of Rb and Cs should be dominated by the transitions which display the greatest anisotropy, *i.e.* the closed transitions. The next few sections describe how this prediction was expanded into a more complete theoretical model of polarisation spectroscopy.

6.3 Modeling population change

In the previous section, we derived the form of the polarisation spectroscopy signal in terms of 'laboratory' variables such as the input intensity of the probe beam and the difference $\Delta\alpha_0$ in the absorption of light driving $\sigma^{\pm}$ transitions when the laser is tuned to an atomic resonance. It must be emphasised that $\Delta\alpha_0$ is a property of the *medium*, that is, of the atomic vapour as a macroscopic system. In order to model polarisation spectroscopy theoretically, it is necessary to describe the anisotropy in a more fundamental way.

For this, we introduce the (time-dependent) *population* anisotropy of the medium, $\mathcal{A}(t)$. This is defined as a sum over all of the ground m_F states of the difference in the absorption coefficients for the components of the probe beam driving $\sigma^{\pm}$ transitions, taking into account the ground and excited state populations:

$$\mathcal{A}(t) = \sum_{m_F=-F}^{F} \alpha_{(F,m_F\rightarrow F',m_F+1)} \left(P_{F,m_F} - P'_{F',m_F+1}\right) - \alpha_{(F,m_F\rightarrow F',m_F-1)} \left(P_{F,m_F} - P'_{F,m_F-1}\right). \tag{6.9}$$

Here, the α's represent line strengths of each transition between states, and P_{F,m_F} (P'_{F,m_F}) represents the probability of each ground (excited) state in the atom being occupied at a particular time. The average value of $\mathcal{A}(t)$ over all transitions is proportional to $\Delta\alpha_0(t)$.

In order to calculate these quantities, we need to understand how the population of atomic states evolves in time. The rest of this section is intended to provide a very basic overview of the theoretical framework needed for this task. A much more detailed explanation may be found in Ref. [214]; Chapter 2 and Appendix C of Ref. [215] also contain some useful derivations.

6.3.1 Density matrix

To begin with, consider a two-level system of particles which are in a statistical mixture of a ground state $|a\rangle$ and an excited state $|b\rangle$. Such a system cannot be represented by a wavefunction. Instead, we use the density operator, which for a pure state is given by

$$\rho = |\psi\rangle\langle\psi| \tag{6.10}$$

where $|\psi\rangle = c_a|a\rangle + c_b|b\rangle$. This allows us to describe the system using the density matrix:

$$\begin{pmatrix} \rho_{bb} & \rho_{ba} \\ \rho_{ab} & \rho_{aa} \end{pmatrix} = \begin{pmatrix} c_b c_b^* & c_b c_a^* \\ c_a c_b^* & c_a c_a^* \end{pmatrix}.$$

Each term of the density matrix has a physical interpretation. We have met the diagonal terms already in the previous section: the P_{F,m_F} in Eq. 6.9 are equivalent to the diagonal density matrix elements ρ_{F,m_F,F,m_F}. Hence for our simple two-level system, ρ_{aa} and ρ_{bb} represent the probability of occupation of the ground and excited states. The off-diagonal terms represent the coherences between states. We can generalise this for non-pure mixed states by redefining the density operator as

$$\rho = \sum_i P_i |\psi_i\rangle\langle\psi_i|,$$

where P_i is the classical probability of being in a state $|\psi_i\rangle$.

The evolution of individual pure states is described by the Schrödinger equation, and in principle this applies to a population as well. However, as the number of particles increases, it becomes increasingly impractical to perform all of the necessary calculations. Instead, an equivalent formulation to the Schrödinger equation, known as Liouville's equation, is used to describe the evolution of the density matrix:

$$\dot{\rho} = \frac{i}{\hbar}[\rho, \mathcal{H}], \tag{6.11}$$

where the Hamiltonian for a two-level atom interacting with laser light is

$$\mathcal{H} = \mathcal{H}_A + V_{AL}. \tag{6.12}$$

$\mathcal{H}_A$ represents the atomic Hamiltonian, and V_{AL} is the atom-light interaction potential. We write V_{AL} in terms of the radiation field of a laser with

frequency ω_L and the atomic dipole:

$$V_{AL} = -\boldsymbol{d} \cdot \boldsymbol{E} \cos(\omega_L t). \tag{6.13}$$

We now have the tools necessary to write down equations for how the populations of each state evolve in time. The next section describes this process.

6.3.2 Optical Bloch equations

By substituting the Hamiltonian into Eq. 6.11, we obtain the relations

$$\begin{aligned}
\dot{\rho}_{aa} &= -\dot{\rho}_{bb} = -i\Omega_R \cos(\omega_L t)\left(\rho_{ba} - \rho_{ab}\right), \\
\dot{\rho}_{ab} &= i\omega_0 \rho_{ab} - i\Omega_R \cos(\omega_L t)\left(\rho_{bb} - \rho_{aa}\right), \\
\dot{\rho}_{ba} &= -i\omega_0 \rho_{ba} + i\Omega_R \cos(\omega_L t)\left(\rho_{bb} - \rho_{aa}\right),
\end{aligned} \tag{6.14}$$

where the Rabi frequency Ω_R is defined thus:

$$\hbar\Omega_R = -\boldsymbol{d}_{ab} \cdot \boldsymbol{E}. \tag{6.15}$$

These equations are *nearly* the well-known optical Bloch equations. However, the effects of spontaneous emission have so far been omitted from our analysis. To include them, we must add terms which depend on the linewidth Γ:

$$\begin{aligned}
(\dot{\rho}_{bb})_{\text{spont}} = -(\dot{\rho}_{aa})_{\text{spont}} &= -\Gamma\rho_{bb} \\
(\dot{\rho}_{ab})_{\text{spont}} &= -\frac{\Gamma}{2}\rho_{ab} \\
(\dot{\rho}_{ba})_{\text{spont}} &= -\frac{\Gamma}{2}\rho_{ba}.
\end{aligned} \tag{6.16}$$

This process of adding in the spontaneous emission terms 'after the fact' is known as the approximation of independent rates of variation. Its validity depends on being able to treat the coupling of the quantum field and the laser field separately, and a detailed justification is given in Ref. [214].

Another useful approximation involves discarding terms of the form $e^{\pm i(\omega_0+\omega)t}$ while keeping all $e^{\pm i(\omega_0-\omega)t}$ terms. This 'rotating wave approximation' allows us to replace the cosine terms in Eq. 6.14 with single exponential terms. With this done, we can suppress the time dependence in the

coefficients of Eq. 6.14 entirely by introducing 'slow' variables:

$$\begin{aligned}\tilde{\rho}_{ba} &= \rho_{ba}e^{i\omega_L t},\\ \tilde{\rho}_{ab} &= \rho_{ab}e^{-i\omega_L t},\\ \tilde{\rho}_{aa} &= \rho_{aa}, \qquad \tilde{\rho}_{bb} = \rho_{bb}.\end{aligned} \tag{6.17}$$

After substituting the relations in Eq. 6.17 into Eq. 6.14, and adding the spontaneous emission terms in Eq. 6.16, we arrive at the optical Bloch equations:

$$\begin{aligned}\dot{\rho}_{bb} &= -i\frac{\Omega_R}{2}(\tilde{\rho}_{ab} - \tilde{\rho}_{ba}) - \Gamma\rho_{bb},\\ \dot{\tilde{\rho}}_{ba} &= i\Delta\tilde{\rho}_{ba} + i\frac{\Omega_R}{2}(\rho_{bb} - \rho_{aa}) - \frac{\Gamma}{2}\tilde{\rho}_{ba},\\ \dot{\tilde{\rho}}_{ab} &= -i\Delta\tilde{\rho}_{ab} - i\frac{\Omega_R}{2}(\rho_{bb} - \rho_{aa}) - \frac{\Gamma}{2}\tilde{\rho}_{ab},\\ \dot{\rho}_{aa} &= i\frac{\Omega_R}{2}(\tilde{\rho}_{ab} - \tilde{\rho}_{ba}) + \Gamma\rho_{bb}\ .\end{aligned} \tag{6.18}$$

6.3.3 Eliminating the coherences

It becomes much easier to solve these equations if the coherences can be eliminated. To show that such an elimination is valid for our system, the optical Bloch equations containing the coherences and the population-only rate equations were solved for a few sample systems. For a short time the solutions differ; the rate equations are linear in time whereas the optical Bloch equations give a quadratic time dependence for the evolution of populations. However, the solutions become indistinguishable after a time of $\sim 7\tau$ [216], where $\tau = 1/\Gamma$=26.24(4) ns for rubidium [217] and 30.57(7) ns for cesium [218]. As the typical time of flight of an atom through the laser beams (discussed below) is roughly two orders of magnitude longer ($\simeq 10 \times 10^{-6}$ s) it is an excellent approximation to solve the equations for the rate of change of populations. We therefore assume that the coherences evolve sufficiently quickly that their steady state values can be used.

To eliminate the coherences, we set the time derivatives to zero in the second and third expressions of Eq. (6.18) and substitute into the first equation, obtaining

$$\dot{\rho}_{bb} = -\dot{\rho}_{aa} = -\frac{\Gamma}{2}\frac{I}{I_{sat}}\frac{(\rho_{bb} - \rho_{aa})}{1 + 4\Delta^2/\Gamma^2} - \Gamma\rho_{bb}. \tag{6.19}$$

This leaves rate equations for populations only. Recalling that the light intensity I is proportional to the square of the Rabi frequency, the saturation intensity $I_{\rm sat}$ is defined as $I/I_{\rm sat} = 2\Omega_{\rm R}^2/\Gamma^2$. The first term on the right-hand side of Eq. 6.19 represents stimulated emission out of the excited state, which is proportional to the light intensity. The second represents absorption into the excited state, which is also proportional to the light intensity. The third term, as we have already seen, encompasses spontaneous emission out of the excited state, which is independent of the light intensity. The intensity-dependent terms have a Lorentzian line-shape, with full width at half maximum of Γ. Note that the usual rate equations of laser physics for populations with Einstein A and B coefficients assume broad-band radiation, and use the intensity per bandwidth (evaluated at line center). In contrast, equation (6.19) is valid for narrow-band radiation and is a function of the detuning.

6.3.4 Multilevel systems

Generalising these equations for multilevel systems like Rb and Cs is a straightforward, if computationally intense, process. As there are three possible polarizations, and the $\Delta F = 0, \pm 1$ selection rule applies, each excited state can decay into up to nine different ground states. The pump beam drives σ^+ transitions, and the Rabi frequencies and saturation intensities are calculated from the known line-strength coefficients. The line strength for a transition between two states a and b is proportional to the square of the dipole matrix element, given [219] by

$$\begin{aligned} |d_{ab}|^2 &= |e\langle n_b L_b||r||n_a L_a\rangle|^2 \qquad (6.20)\\ &\times (2J_b+1)(2J_a+1)(2F_b+1)(2F_a+1)\\ &\times \left[\begin{Bmatrix} L_b & J_b & S \\ J_a & L_a & 1 \end{Bmatrix}\begin{Bmatrix} J_b & F_b & \mathcal{I} \\ F_a & J_a & 1 \end{Bmatrix}\begin{pmatrix} F_a & 1 & F_b \\ m_{F_a} & q & -m_{F_b}. \end{pmatrix}\right]^2, \end{aligned}$$

The quantities L and S are respectively the orbital and spin angular momenta of the electron, J is their sum, $F = \mathcal{I} + J$ where $\mathcal{I}$ is the nuclear spin, and m_F is the projection of F onto the z axis. The expressions in curly brackets are standard $6J$ symbols encountered when re-coupling angular momenta, and the term with large round brackets is a $3J$ symbol. These can be calculated

using *Mathematica* or other standard packages. The value of q denotes the change in z-component of the angular momentum in the transition between the two levels, with $q = 0$ for π transitions, and $q = \pm 1$ for $\sigma^{\pm}$ transitions.

6.3.5 An example: ^{87}Rb

To make this discussion more concrete, let us consider the simplest of our three species, ^{87}Rb ($\mathcal{I} = 3/2$), which has two hyperfine levels in the ground state, $F = 2, 1$. If the pump laser is tuned in the vicinity of the resonances $S_{1/2}(F = 2) \rightarrow P_{3/2}(F' = 3, 2, 1)$ with the detuning, Δ, defined relative to the closed transition $S_{1/2}(F = 2) \rightarrow P_{3/2}(F' = 3)$, the strongest transition will be $^2S_{1/2}(F = 2, m_F = 2) \rightarrow ^2P_{3/2}(F' = 3, m_{F'} = 3)$. For this transition, the saturation intensity $I_{\rm sat}$ has the value 1.6 mW/cm^2. The reduced matrix element for the transition $\langle 5S||r||5P\rangle = 5.14a_0$, where a_0 is the Bohr radius, is calculated from the excited state lifetime. The line-strength ratios, which we define as

$$R_{F,m_F\rightarrow F',m_{F'}} = \left(\frac{d_{F,m_F\rightarrow F',m_{F'}}}{d_{2,2\rightarrow 3,3}}\right)^2, \tag{6.21}$$

are always less than one as they are normalized relative to the strongest transition.

The five $F = 2, m_F$ ground states obey the rate equations

$$\frac{dP_{F,m_F}}{dt} = -\sum_{F'=F-1}^{F+1} R_{F,m_F\rightarrow F',m_F+1}\frac{\Gamma}{2}\frac{I}{I_{\rm sat}}\frac{(P_{F,m_F} - P_{F',m_{F+1}})}{1+4(\Delta'/\Gamma)^2}$$

$$+\sum_{m_{F'}=m_F-1}^{m_F+1}\sum_{F'=F-1}^{F+1} R_{F,m_F\rightarrow F',m_{F'}}\Gamma P_{F',m_{F'}}, \tag{6.22}$$

where $\Delta' = \Delta$ if $F' = F + 1$; $\Delta' = \Delta + \Delta_{32}$ if $F' = F$; and $\Delta' = \Delta + \Delta_{31}$ if $F' = F - 1$. Here $\hbar\Delta_{32}$ and $\hbar\Delta_{31}$ are the excited state hyperfine intervals. The first row of Eq. (6.22) contains the stimulated absorption and emission terms, the second row the spontaneous emission terms.

The three $F = 1, m_F$ ground states obey the rate equations

$$\frac{dP_{F,m_F}}{dt} = \sum_{m_{F'}=m_F-1}^{m_F+1}\sum_{F'=F-1}^{F+1} R_{F,m_F\rightarrow F',m_{F'}}\Gamma P_{F',m_{F'}}. \tag{6.23}$$

Note that there are no laser-dependent terms as the large ground state splitting means that these transitions very far off resonance. These states can only increase their population by spontaneous emission from the excited states.

Finally, the excited state population rate equations are

$$\frac{dP_{F',m_{F'}}}{dt} = \sum_{F=2} R_{F,m_{F'}-1\rightarrow F',m_{F'}} \frac{\Gamma}{2} \frac{I}{I_{\text{sat}}} \frac{(P_{F,m_{F'}-1} - P_{F',m_{F'}})}{1+4\left(\Delta'/\Gamma\right)^2}$$

$$- \sum_{m_F=m_{F'}-1}^{m_{F'}+1} \sum_{F=F'-1}^{F'+1} R_{F,m_F\rightarrow F',m_{F'}} \Gamma P_{F',m_{F'}}. \qquad (6.24)$$

A useful check before solving these equations is that the sum of all of the right-hand sides of these equations must be zero, because the total population in all states is constant. Note that there are 24, 36, and 48 Zeeman levels which have to be considered for the ^{87}Rb, ^{85}Rb, and ^{133}Cs systems, respectively; hence the simplification of the equations by eliminating the coherences is substantial.

6.4 Calculation of anisotropy

The calculation assumes that there is no excited state population initially, and that the ground state population is spread uniformly amongst the $2(2\mathcal{I}+1)$ different $|F, m_F\rangle$ levels. Equations similar to 6.19 were written down for each m_F level, and the set of coupled equations solved numerically.

As an interim step before calculating the anisotropy in Eq. 6.9, we can use the solutions to the rate equations to examine what happens to the population of each hyperfine state after the pump beam is turned on. Figure 6.3 shows the time evolution of the populations for a sample of ^{87}Rb atoms when $\Delta/2\pi$=0, -267 MHz, and -424 MHz, corresponding to a laser on resonance with the $F = 2 \rightarrow F' = 3, 2, 1$ transitions, respectively. When the laser is resonant with the closed $F = 2 \rightarrow F' = 3$ transition, atoms are rapidly pumped into the extreme $|2, 2\rangle$ state, with over 50% of atoms in this state after <10 μs. The population of the other states is either constant or decreasing after ~ 1 μs.

These figures clearly show the different optical pumping dynamics as a function of the laser detuning. A detuning Δ=0 (Figure 6.3a) is optimum

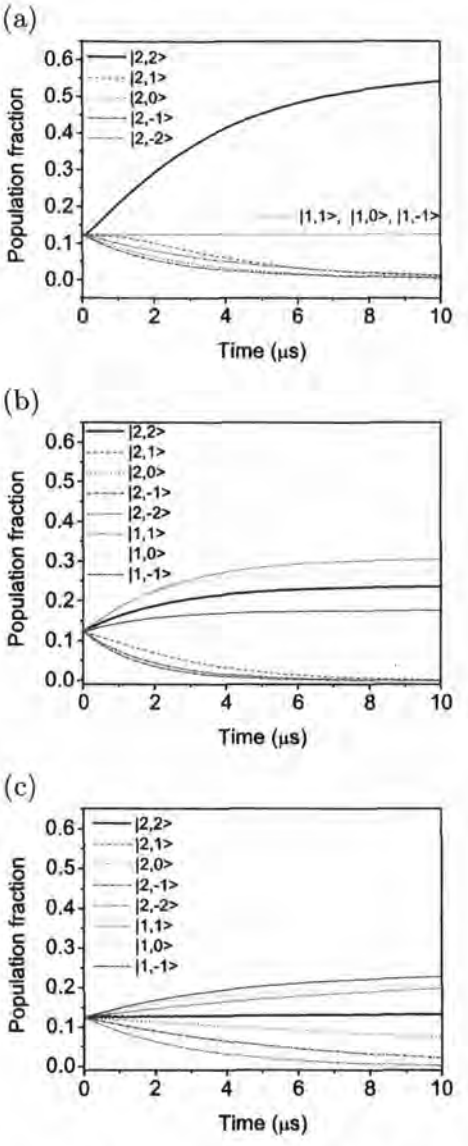

Figure 6.3: Populations of the eight ground state sub-levels of ^{87}Rb as a function of time after the pump beam is turned on. (a) Laser tuned to $F = 2 \rightarrow F' = 3$ transition. Within a few μs the initial isotropic population distribution becomes highly anisotropic, as atoms are optically pumped into the $|2, 2\rangle$ state. This transition is closed, so no change occurs in the population of the $F = 1$ manifold. (b) When the laser is tuned to the $F = 2 \rightarrow F' = 2$ transition the atoms are again optically pumped towards the $|2, 2\rangle$ state. As this is an open transition, a significant fraction of population accumulates in the $F = 1$ manifold. These states do not contribute to the medium's optical anisotropy. (c) For the laser tuned to the $F = 2 \rightarrow F' = 1$ transition even fewer atoms are pumped into the $|2, 2\rangle$ state.

for achieving the greatest population anisotropy. For $\Delta/2\pi = -267$ MHz (Figure 6.3b) the distribution becomes anisotropic, but to a lesser extent. This is due to the open nature of the transition, which allows atoms to accumulate in the $F = 1$ manifold, where they are too far from resonance to influence the medium's anisotropy. This effect is even more pronounced for $\Delta/2\pi = -424$ MHz (Figure 6.3c), and the anisotropy at this detuning is correspondingly reduced in comparison with the other detunings.

These population graphs allow us to predict that the polarisation spectroscopy signal should be dominated by the closed transitions, $S_{1/2}(F = \mathcal{I} + 1/2) \rightarrow P_{3/2}(F' = F + 1)$ and $S_{1/2}(F = \mathcal{I} - 1/2) \rightarrow P_{3/2}(F' = F - 1)$. For such transitions, selection rules forbid atoms in the excited state from falling into the other ground state; consequently, all of the ground state population ends up pumped into the extreme magnetic sublevels with $m_F = F$ (for $\mathcal{I} + 1/2$, as discussed in the example above) or $m_F = F$ and $m_F = F - 1$ (for $\mathcal{I} - 1/2$). The absorption coefficients $\alpha_\pm$ differ most for this extreme state; therefore, the anisotropy of the medium is maximized.

This prediction is in line with our results in section 4.3.1, where we measured the anisotropy of the medium directly. The more complex treatment we have developed for population anisotropy allows us to make additional predictions. Notably, the sign of the anisotropy generated by the $\mathcal{I} + 1/2$ transitions is expected to be opposite that of the lower hyperfine transitions, due to the lack of allowed σ^+ transitions from the ground $m_F = F = \mathcal{I} - 1/2$ states. Figure 6.4 illustrates the optical pumping process.

6.5 Generating theoretical spectra

For each isotope and each ground state F, the anisotropy in Eq. 6.9 is calculated for the three frequencies corresponding to the resonances $F \rightarrow (F' = F + 1, F, F - 1)$, *i.e.* Δ=0, $-\Delta_{32}$, and $-\Delta_{31}$. It is assumed that since the experiment uses counter propagating pump and probe beams only atoms with zero velocity along the axis of the beams (z axis) contribute significantly. The details of the transverse motion of the atoms is outlined in the next sub-section.

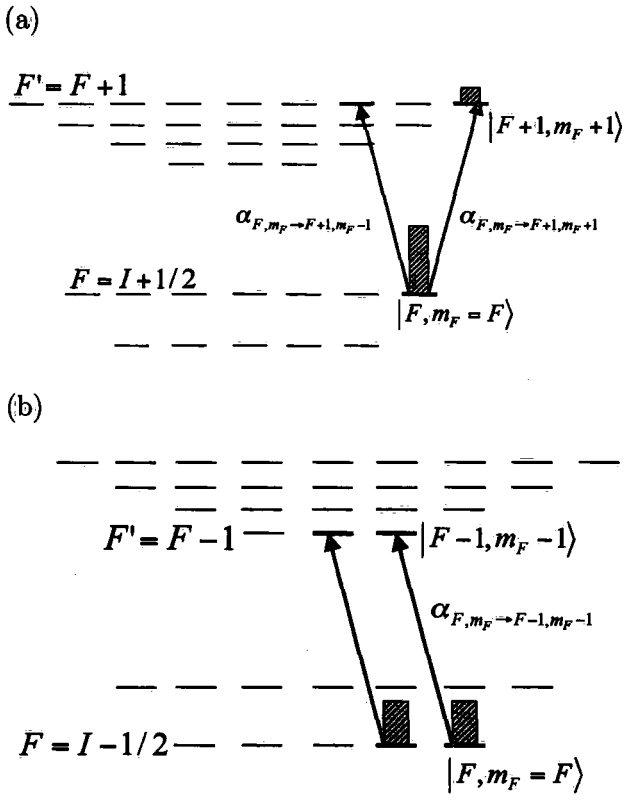

Figure 6.4: Sign of anisotropy for closed transitions. a) For the closed $F = \mathcal{I} + 1/2 \rightarrow F' = F + 1$ transition the population is optically pumped into the $|F, m_F = F\rangle$ state, with a small fraction in the excited state. The line strength $\alpha_{F,m_F \rightarrow F+1,m_F+1}$ is significantly larger than $\alpha_{F,m_F \rightarrow F+1,m_F-1}$. b) For the closed $F = \mathcal{I} - 1/2 \rightarrow F' = F - 1$ transition the population is optically pumped into the $|F, m_F = F\rangle$ and $|F, m_F = F - 1\rangle$ states. There are no allowed σ^+ transitions for these states, whereas the line strength for the σ^- transitions are finite. Consequently, the anisotropy of the medium has opposite sign relative to a). All levels are drawn as for an atom with $\mathcal{I} = 5/2$; the structure of the other alkali atoms is similar.

6.5.1 Transverse motion of atoms

The experiment measures the average anisotropy of the medium. To simulate this, we average the time-dependent anisotropy, $\mathcal{A}(t)$, with a weighting function, $\mathcal{H}(t)$, which gives the distribution of times of flight transverse to the beam. The weighting function has two components: $\mathcal{F}(\ell)$, the probability distribution of having a path length ℓ through a beam for a uniform gas, and $\mathcal{G}(t,\ell)$, the probability distribution for having a transit time t for a given ℓ.

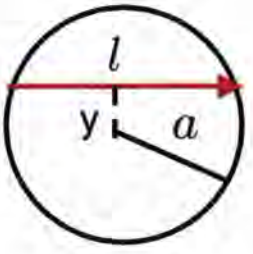

Figure 6.5: Transverse motion of atoms. An atom traverses a path of length ℓ through a laser beam of radius a. We have chosen ℓ parallel to the $x-$axis for convenience. The path is at a height y above the $x-$axis.

To calculate $\mathcal{F}(\ell)$, we consider an atom moving in the xy plane, with a path length ℓ through a circular laser beam of radius a. As Figure 6.5 indicates, we have arbitrarily chosen ℓ parallel to the $x-$axis for convenience. It is clear from the figure that $\left(\frac{\ell}{2}\right)^2 + y^2 = a^2$; hence,

$$\frac{dy}{d\ell} = \frac{-\ell}{4y}. \tag{6.25}$$

The normalised probability distribution as a function of y is

$$\int_{-a}^{a} \mathcal{F}(y)dy = 1; \quad \mathcal{F}(y) = \frac{1}{2a}, \tag{6.26}$$

and we can use the normalisation condition to equate this with the probability distribution as a function of ℓ:

$$\begin{aligned} \mathcal{F}(\ell)d\ell &= \mathcal{F}(y)dy \\ \mathcal{F}(\ell) &= \mathcal{F}y\left|\frac{dy}{d\ell}\right| \\ &= \frac{1}{2a}\frac{\ell}{4y}. \end{aligned} \tag{6.27}$$

After normalisation, this gives

$$\mathcal{F}(\ell) = \frac{\ell}{2a\sqrt{4a^2 - \ell^2}}. \tag{6.28}$$

We obtain the second component of $\mathcal{H}(t)$ from the Maxwell velocity distribution for a sample of atoms of mass m at temperature T:

$$k(v) = \frac{m}{k_B T} v \exp\left(-\frac{mv^2}{2k_B T}\right). \tag{6.29}$$

Transforming $k(v)$ into an expression in terms of position and time gives:

$$\mathcal{G}(t, \ell) = \frac{m\ell^2}{k_B T t^3} \exp\left(-\frac{m\ell^2}{2k_B T t^2}\right). \tag{6.30}$$

A graph of $\mathcal{G}(t, \ell)$ for ^{87}Rb at room temperature and ℓ equal to the diameter of the laser beam is shown in Figure 6.6. Note that a significant fraction of the atoms spend more than 10 μs interacting with the laser light. A quick comparison with Figure 6.3 shows that for these transit times, we can expect significant amounts of anisotropy to build up for the closed transitions.

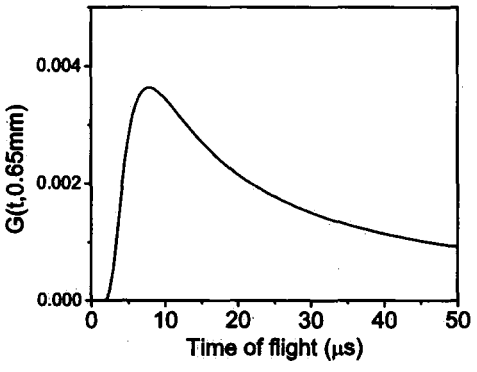

Figure 6.6: Distribution of times of flight through the laser beam for a sample of room-temperature ^{87}Rb atoms. By setting ℓ in Eq. 6.30 equal to the laser beam diameter, we see that the peak of the distribution lies between 5–10 μs, with a significant fraction of atoms spending several tens of μs interacting with the laser light.

The distribution function $\mathcal{H}(t)$ is:

$$\mathcal{H}(t) = \int_{\ell=0}^{2a} \mathcal{G}(t, \ell)\mathcal{F}(\ell) d\ell, \tag{6.31}$$

which can either be evaluated numerically or in closed form in terms of the complex error function. The average anisotropy $\overline{\mathcal{A}}$ is calculated by averaging the time-dependent anisotropy with the time of flight weighting function, which is:

$$\overline{\mathcal{A}} = \int \mathcal{A}(t)\mathcal{H}(t)dt. \tag{6.32}$$

This integral is calculated numerically at the three resonant frequencies of each $D2$ transition.

6.5.2 Incorporating lineshapes and broadening

To generate the predicted spectra, the three values of $\overline{\mathcal{A}}$ from (6.32) are multiplied by dispersion functions of the form $x/(1+x^2)$, where $x = 2\Delta/\Gamma$. As in the work of Yoshikawa *et al.* [220] the strength of cross-over features is assumed to be the average of the two associated resonances; hence cross-over features are calculated by multiplying this average by a dispersion function located halfway between each resonance.

To account for spectral broadening produced by saturation effects (power broadening), we substituted a broadened linewidth $\gamma = k\Gamma$ MHz for the natural linewidth Γ in the dispersion function. We found that for $1 \leq k \leq 2$, the experimental data do not provide a tight constraint on the value of γ. Doppler broadening is incorporated by convolving the resulting spectra with a Gaussian of FWHM $\leq 1 \times 2\pi$ MHz, consistent with residual Doppler broadening due to the finite crossing angle between the probe and pump beams. Magnitudes for both types of broadening were set by the experimental conditions, as were the values for temperature (293K for rubidium, 273K for caesium), beam radii, and I/I_{sat}.

6.6 Experimental setup

The experimental layouts for rubidium and caesium spectroscopy are both very similar to the generalised setup in Figure 6.1, differing only in the length of the alkali vapour cell, equipment used to control the magnetic field along the axis of the cell, and wave plate type. Table 1 contains information on the spot radii ($1/e^2$ intensities) of the beams after the light has passed through

Table 6.1: Specifications of lasers used in this work.

Atom	λ	Horizontal r $(1/e^2)$	Vertical r $(1/e^2)$
Rb	780 nm	0.65±0.01 mm	0.59±0.01 mm
Cs	852 nm	0.69±0.01 mm	0.70±0.01 mm

a pair of anamorphic prisms.

In both experiments the pump and probe beams were derived from the same extended cavity diode laser (ECDL). The diode for the rubidium (caesium) laser was a Sanyo DL-7140-201 (SDL-5401-G1). The crossing angle between probe and counterpropagating pump within the vapour cell was <3.0±0.2 mrad. Neutral density filters were used to vary pump and probe powers independently.

Since light of a given polarisation may drive σ^+, σ^- or π transitions depending on the external magnetic field, it is necessary to establish a 'preferred' magnetic field direction along the vapour cell axis. In the rubidium experiment this is done by placing a room-temperature cell containing ^{85}Rb and ^{87}Rb inside a 300-turn solenoid of length 280 mm and diameter 26 mm. Numerical simulations showed that the magnetic field inside the solenoid is uniform to within 0.2% over the length of the 70 mm cell.

In the caesium experiment the cell is partially submerged in an ice bath, and two 300 × 300 mm square coils in the Helmholtz configuration generate an axial magnetic field uniform to 1%. The ice bath is needed because our model assumes an optically thin medium, but at 23 °C absorption exceeds 90% for a 50 mm Cs vapor cell (compared to a maximum of 30% for Rb in a 70 mm cell). In the ice bath this is reduced to 60% (50%) for transitions from the upper (lower) hyperfine level of the ground state. In both experiments we also cancel the (primarily vertical) ambient laboratory magnetic field with a 245 mm diameter coil mounted above the cell. Any inhomogeneity due to the finite diameter of this coil makes a negligible contribution to the total field when added in quadrature with the axial field. The magnitude of the axial field is set to a value just below the point where Zeeman splitting of the hyperfine levels begins to distort the polarisation spectra, typically a few

gauss.

An alternative means of controlling the magnetic field is to surround the cell with a magnetic shield, leaving only small ($\sim$ few mm diameter) axial holes for the probe and pump beams. The result is very similar to that obtained with the coils and solenoid: a small but finite magnetic field along the axis of the cell, and essentially zero radial field. Members of the Durham group who employ polarisation spectra for laser locking have found that using a shield can increase the magnitude of spectral features by up to a factor of two, without the need for active control of the field, extra power supplies, etc. The shield method is therefore recommended if it is not deemed too costly or time-consuming to construct, and especially if the setup is intended to be permanent.

6.7 Comparing experimental and theoretical spectra

Figure 6.7 shows the data obtained with the layout described in the last section (thick line) and the theoretical spectra (thin line). All experimental spectra were taken with pump and probe beam intensities $\leq 0.1\ I_{\rm sat}$ to reduce saturation effects. The spectra shown are of transitions from the upper hyperfine level of the ground state, i.e. the $5^2S_{1/2}(F=2) \rightarrow 5^2P_{3/2}(F'=1,2,3)$ transitions in ^{87}Rb, $5\,^2S_{1/2}\ (F=3) \rightarrow 5\,^2P_{3/2}\ (F'=2,3,4)$ transitions in ^{85}Rb, and $6\,^2S_{1/2}\ (F=4) \rightarrow 6\,^2P_{3/2}\ (F'=3,4,5)$ transitions in ^{133}Cs. Zero detuning is relative to the highest-frequency transition, and we have used linear detunings, $\Delta/2\pi$. The magnitude of each feature is given in volts, and will depend on the gain resistance in the photodiode circuit (1 MΩ in our experiment). For Cs, two sets of data are shown; one taken with the vapour cell at room temperature (dashed line), the other with the cell in an ice bath as described in the previous section (solid line).

In these spectra, polarisation signals of closed transitions dominate, with magnitudes up to three times that of the next largest feature. This is true for all three species, and is in marked contrast with conventional saturated absorption/hyperfine pumping spectra [193]. As predicted, the $F \rightarrow F' = F$

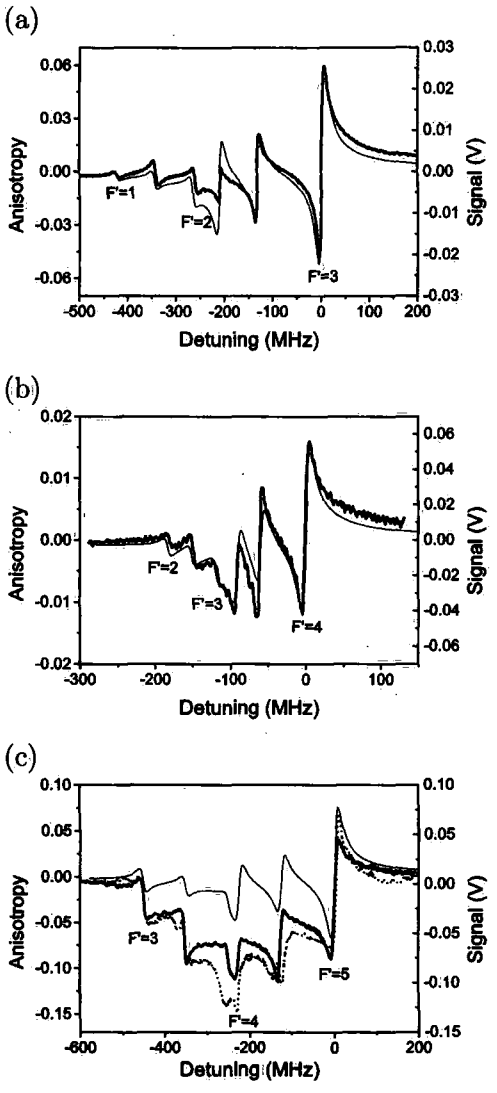

Figure 6.7: Experimental (thick line) and theoretical (fine line) polarization spectra of D2 line transitions in a) ^{87}Rb, b) ^{85}Rb, and c) ^{133}Cs. Spectra were obtained by tuning the laser frequency to drive transitions from the upper hyperfine level of the atom's ground state ('cooling transitions'). All three spectra are dominated by the strong dispersion features associated with the closed transition. For the Cs upper hyperfine spectra, solid (dashed) lines represent spectra taken with the vapor cell at 0° (23°) C.

transitions produce a moderate amount of anisotropy, and the lowest frequency open transitions give the smallest signal. We saw in Figure 6.6 that the most probable time of flight for rubidium atoms traveling through a beam with the experimental waist was between 5–10 μs, and a significant fraction of the atoms had times of flight longer than 20 μs. Therefore we do indeed see that the timescale needed to build up anisotropy is significantly longer than the spontaneous decay time, and comparable to transit times. The accumulation of anisotropy can be accelerated by using a more intense pump beam; however, this will not greatly increase the signal as most atoms are already pumped into the extreme state within the transit time. This is also what is observed experimentally.

Spectra taken of transitions from the lower hyperfine level of the ground state show a more complicated pattern. As Figure 6.8(b) and 6.8(c) show, the (low-frequency) closed transitions in Cs and ^{85}Rb show a characteristic strong dispersion feature, but in ^{87}Rb the largest feature arises from one of the cross-over peaks (Figure 6.8(a)). In ^{85}Rb closely-spaced transitions generate a polarisation spectrum in which individual peaks merge, making exact matching of features and transitions difficult.

By comparing theoretical and experimental traces, we see immediately that our model reproduces experimental features of upper hyperfine transition spectra with a high degree of accuracy. Fine spectral details like the 'horns' resulting from the closely-spaced $F = 2 \rightarrow F' = 2$ and $X_{3,1}$ cross-over peaks in ^{87}Rb arise automatically from the calculated population anisotropies. The magnitudes of theoretical spectral peaks relative to the large closed transition peaks also agree well with experimental data, especially in ^{85}Rb. The effect of reducing vapour pressure by cooling the Cs cell is readily apparent. Although the central peaks are still offset from theoretical spectra compared to their counterparts in the Rb spectra, the magnitude of the offset is significantly less at 0 °C than at room temperature, and the shapes of the spectra broadly agree.

For lower hyperfine spectra, we observe that the sign of the anisotropy for the closed-transition peak is reversed compared to corresponding peaks in upper hyperfine spectra, as predicted in our model. However, most other spectral features differ markedly from predictions. Crucially, though, the

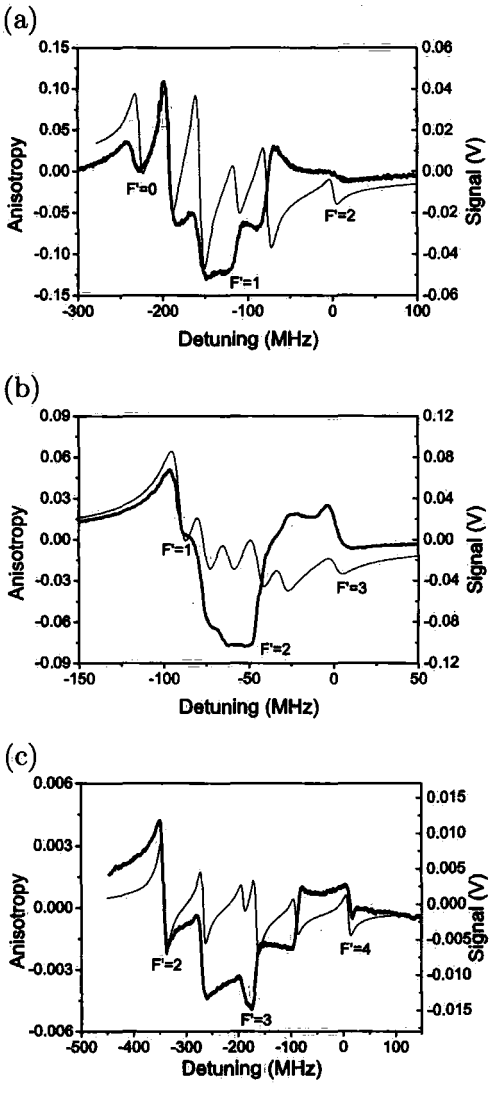

Figure 6.8: Experimental (thick line) and theoretical (fine line) polarization spectra of D2 line transitions in a) ^{87}Rb, b) ^{85}Rb, and c) ^{133}Cs. Spectra were obtained by tuning the laser frequency to drive transitions from the lower hyperfine level of the atom's ground state ('repump transitions'). The data indicate that the medium is strongly (and negatively) anisotropic in the vicinity of the crossover resonances, particularly for ^{85}Rb. This feature is not reflected in the theoretical model.

model spectra show similar discrepancies for each of the three species, indicating that the lack of agreement must be due to physical processes not included in our model which are specific to the lower hyperfine transitions. As a test, we ran our simulation again, this time allowing the position and magnitude of the three Lorentzians (representing three transitions) to float unconstrained by any input parameters. We found that no values of detuning or anisotropy could account for the observed spectra.

To gain insight into the anisotropies induced by lower hyperfine transitions (particularly 'open' transitions, *i.e.* those with a decay channel to the other ground state level), we repeated the anisotropy measurements described in Section 4.3.1, this time focusing on the 'repump' transitions in the three species. As noted before, for the upper hyperfine transitions the medium was found to be most anisotropic in the vicinity of the the closed transitions. This agrees with theoretical predictions and is reflected in our model. For lower hyperfine transitions, *e.g.* the ^{85}Rb 'repump' transitions shown in Figure 6.9, the medium is strongly negatively anisotropic at the crossover frequencies. These strongly negative anisotropies are reflected in our experimental polarisation spectra, but not in the model. This suggests that for such transitions, it is no longer valid to assume that the strength of crossover features is the average of the two associated resonances.

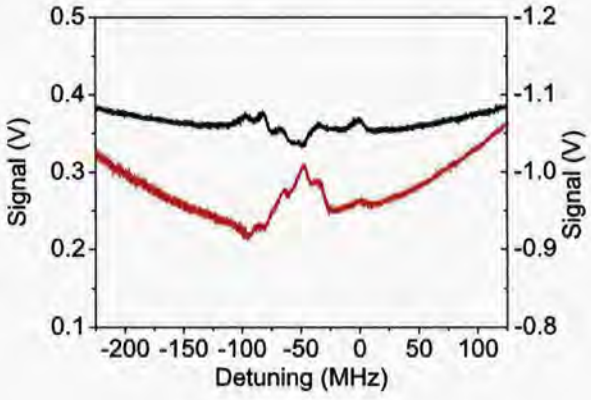

Figure 6.9: Anisotropy of the ^{85}Rb repump transition. The black (red) trace shows the absorption profile of the probe beam component driving σ^+ (σ^-) transitions. Unlike the cooling transitions, the greatest difference in the two signals is in the vicinity of the crossover resonances.

The present model assumes a uniformly distributed circular laser beam. The experimental beam has a Gaussian profile, which will lead to slight variations in the absolute height of the spectroscopic peaks. It will not, however, account for the difference between upper and lower hyperfine transitions. It is also possible that if the optical pumping is not complete for the lower hyperfine states, ignoring the coherences could have a large effect.

The most significant approximation that is likely to break down for lower hyperfine transitions is the assumption that only atoms with no axial velocity will contribute to the anisotropy. As was shown in [193], a full description of the spectrum, especially open transitions, must take into account a large velocity class of atoms moving along the beam, not just the 'stationary' ones. The contribution of these nonzero velocity classes will be more significant for $F = \mathcal{I} - 1/2$ because the line strength factors for the closed transition are weakest; for $F = \mathcal{I} + 1/2$, line strength factors are strongest for the closed transition, and the 'stationary atom' approximation is reasonable.

Expanding the model to include a large velocity class would be computationally intense, and is beyond the scope of this work. Walewski *et al.* have performed numerical simulations which included nonzero axial velocities, and successfully used their model to explain features of polarisation spectra in flames [221]. However, the organic molecules they studied have very different structures and properties from those of the alkali atoms examined here, and adapting their model to account for alkali spectra would be correspondingly nontrivial.

In comparing theoretical predictions with experimental signals, we have chiefly focused on the shape and relative magnitudes of spectral features. The absolute magnitude of the experimental polarisation spectroscopy signal depends not only on the gain resistor in the photodiode circuit, as discussed in the previous section, but also on the intensity of the probe beam in the absence of a vapour cell. This in turn depends on the optical thickness of the vapour, which is both temperature-dependent (as noted earlier in our discussion of caesium) and different for each species. Because of these factors, the species with the largest calculated anisotropy will not necessarily produce the largest experimental signal. Our decision to display theoretical and experimental spectra on separate scales reflects these considerations.

6.8 Conclusions and future work

This chapter has presented a model of polarisation spectroscopy based on numerical integration of population rate equations. This model can be used to simulate the optical pumping process that leads to an anisotropic population distribution, and thus to differential absorption in the medium. Theoretical polarisation spectra generated by this model account very well for $F = \mathcal{I} + 1/2 \rightarrow F'$ transitions in ^{87}Rb, ^{85}Rb, and ^{133}Cs, but not as well for $F = \mathcal{I} - 1/2 \rightarrow F'$ transitions.

During the writing of this thesis, Do *et al.* [222] have demonstrated a model for polarisation spectroscopy which accurately reproduces spectra for all of the transitions in rubidium. Their model is also based on a calculation of the rate equations, although the full details have not yet been published. In addition, work by other members of the Durham group has shed further light on reasons for disagreement between our model and experimental spectra for the lower hyperfine transitions [223]. In their investigation of absorption spectra on the Rb D lines, Siddons *et al.* found that for the upper hyperfine transitions, a probe beam intensity of $0.1I/I_{\text{sat}}$ was sufficiently low to prevent hyperfine pumping during an atom's transit through (or along) the beam. At this intensity, their experimental data on absorption agreed with their model — which, like the one presented here, did not include nonzero velocity classes.

For the lower hyperfine transitions, the relative weakness of the closed transition line strengths compared to those of neighbouring transitions meant that a lower probe intensity ($I \leq 0.01I/I_{\text{sat}}$) was needed to achieve the same effect. This work supports our conclusion that nonzero velocity classes are a more significant factor in polarisation spectra of the lower hyperfine transitions. Unfortunately, the low probe intensities used in the absorption spectra studies are not practical for polarisation spectroscopy, because eliminating pumping between hyperfine levels will also eliminate the optical pumping between Zeeman sublevels needed to generate the polarisation spectroscopy signal. Both polarisation and absorption spectroscopy continue to be an area of active experimental and theoretical interest.

Finally, note that for $F = \mathcal{I} + 1/2 \rightarrow F'$, the closed $F' = F + 1$ transition dominates the polarisation spectra, with a steep slope through line center

which makes an excellent frequency reference for laser locking. Polarisation spectroscopy as a laser locking technique is discussed further in the next chapter.

Chapter 7

Sub-Doppler DAVLL

In the sub-Doppler DAVLL technique [188, 189], a pump beam is used to produce sub-Doppler features in the DAVLL signal described in Chapter 4. The resulting set of six steep zero-crossings eliminates a major drawback of DAVLL, namely that the error signal is prone to long term drifts. We investigated this method as a possible alternative locking scheme for the next-generation Rb-Cs mixture experiment which is described in the last chapter of this thesis. This chapter contains a detailed study of sub-Doppler DAVLL spectra on the Rb $D2$ line.

7.1 Introduction

Sub-Doppler DAVLL can be thought of as a hybrid of saturated absorption/hyperfine pumping spectroscopy and 'conventional' DAVLL. As in conventional DAVLL, a linearly polarised probe beam interacts with an atomic vapour, passes through a quarter wave plate, and is split by a PBS into the components of the beam which have driven σ^+ and σ^- transitions. Sub-Doppler DAVLL adds a counterpropagating linearly polarised pump beam to the system. The presence of a magnetic field (which, as in ordinary DAVLL, is oriented in the direction of probe beam propagation) ensures that both the centre frequencies of the Doppler-broadened σ^+ and σ^- absorption lines and the frequencies of the sub-Doppler features are shifted in opposite directions. The resulting sub-Doppler DAVLL signal can be thought of as having two components: a broad, sloping 'background' signal which resem-

bles the DAVLL spectra discussed in Chapter 4, and narrow (~10 MHz) anti-symmetric, dispersion-like sub-Doppler features.

A complete theoretical description of sub-Doppler DAVLL would have to include the physical processes which give rise to both of these components. This might seem like a relatively simple task. Saturated absorption/hyperfine pumping spectra have been observed for decades, and adding a static magnetic field to the system is also not new [224]. However, the theory behind saturated absorption/hyperfine pumping spectra is still a topic of active study [225], and even models which incorporate the Zeeman effect for multi-level atoms have not been wholly successful in predicting experimental spectra [196]. This chapter therefore focuses on chiefly experimental studies of how sub-Doppler DAVLL spectra depend on magnetic field, pump beam power, and polarisation purity. Sub-Doppler DAVLL spectra are also compared to the polarisation spectra described in the previous chapter, and conclusions are drawn about the relative merits of the two techniques for laser locking.

7.2 Experimental details

The experimental setup (Fig. 7.1) uses a grating-stabilised diode laser (Toptica DL100) to provide light at 780 nm. After the laser, a low order half wave plate (Casix WPL1210) is used in conjunction with a polarising beamsplitter (Casix PBS0201) to transmit a fraction of the laser light (~5 mW) into the spectroscopy setup. An isolator prevents light from being reflected back into the laser. Neutral density filters are used to vary the pump and probe powers independently. At the vapour cell the probe beam has a $1/e^2$ radius of (0.84±0.05) mm horizontally and (0.81±0.02) mm vertically. The $1/e^2$ radii of the pump beam are similar to those of the probe beam.

The pump and probe beam are counterpropagated along a 7 cm long vapour cell, with a crossing angle of 9 mrad between the two beams. This small angle can be eliminated entirely by using a nonpolarising beamsplitter to overlap the beams. Note, however, that many inexpensive beamsplitters are highly birefringent; as we shall see later in this chapter, the error signal lineshapes are altered by polarisation impurities, so it is desirable to avoid introducing them. After the cell the probe beam passes through a low-

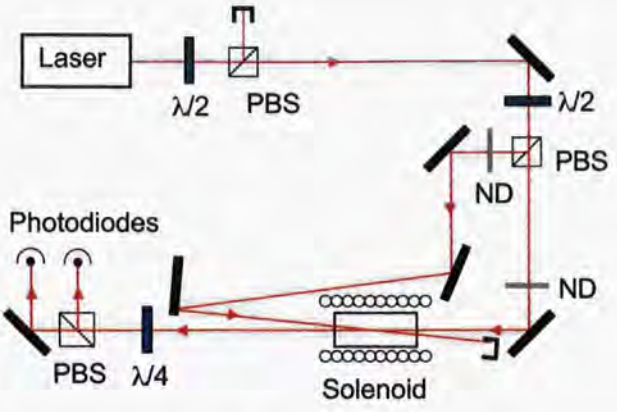

Figure 7.1: Optical layout used for sub-Doppler DAVLL spectroscopy. The pump and probe beams are separated by a polarising beamsplitter. Neutral density filters (ND) are used with PBSs and half wave plates to regulate the intensities of each beam independently. Additional PBSs and half wave plates (not shown) are placed in the pump and probe beams to 'clean up' the polarization. The cell containing room-temperature rubidium vapor is located inside a solenoid. The crossing angle between the pump and probe beams inside the cell has been exaggerated for clarity. Two photodiodes monitor the absorption of light which has driven σ^+ and σ^- transitions.

order quarter wave plate (Casix WPL1210) followed by another polarising beamsplitter. Simple amplified photodiode circuits in the output arms of the PBS are used to monitor the absorption of light which has driven σ^+ and σ^- transitions. Both detectors were calibrated and checked for linearity of response with respect to input power. The detectors have a measured responsivity of (0.45±0.04) AW^{-1}, and the amplifiers a transimpedence of 5.3 MΩ.

The vapour cell was placed in a 7 cm long solenoid with 22 turns per cm. This generated a longitudinal field of (23.15±0.08) GA^{-1}. Saturated absorption/hyperfine pumping spectroscopy was employed to calibrate the frequency of the sub-Doppler DAVLL spectra using the known Rb hyperfine splittings [142, 212].

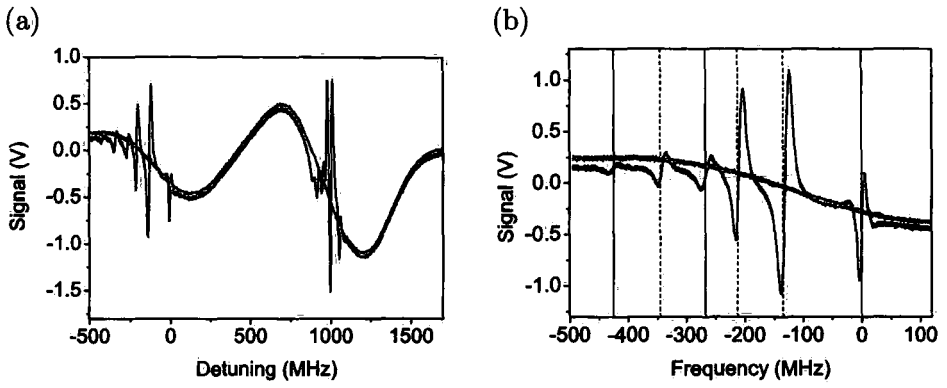

Figure 7.2: (a) Typical sub-Doppler DAVLL spectra recorded for the $F = 2 \rightarrow F'$ line in ^{87}Rb and $F = 3 \rightarrow F'$ ^{85}Rb (black line). The sub-Doppler features are superimposed on the conventional DAVLL signal (grey line) obtained by blocking the pump beam. (b) A zoomed-in section of (a) showing the sub-Doppler DAVLL signal for the $F = 2 \rightarrow F'$ transitions of ^{87}Rb. Vertical lines indicate the expected line centres of the three transitions (solid lines) and three crossovers (dashed lines). Small discrepancies in the location of spectral features relative to the line centres arise from the slightly non-linear laser scan. Spectra were taken at a magnetic field of 9.5 G, a pump power of 154 μW, and a probe power of 20 μW.

7.3 Results

Figure 7.2 (a) shows typical sub-Doppler spectra of the $F = 2 \rightarrow F'$ transitions in ^{87}Rb and $F = 3 \rightarrow F'$ transitions in ^{85}Rb recorded with a magnetic field of 9.5 G. The conventional DAVLL spectrum, with features of the order of $\sim$ 0.5 GHz wide, is seen as a background. As the widths of the sub-Doppler features are more than an order of magnitude narrower than the Doppler-broadened absorption lines, the field needed is correspondingly weaker than the field of $\sim$ 140 G which gives the optimal conventional DAVLL signal [194]. Figure 7.2 (b) shows the ^{87}Rb $F = 2 \rightarrow F'$ transitions in greater detail. The anti-symmetric dispersion-like nature of the sub-Doppler features is evident. Six features are seen, one for each sub-Doppler transmission peak. The steepest gradients of the sub-Doppler DAVLL peaks are approximately coincident with the centre frequencies of the Rb hyperfine transitions (crossover reso-

nances), as indicated by the solid (dashed) lines in Figure 7.2 (b). Note that the strongest locking signals are obtained for the transitions which show the largest sub-Doppler transmission features.

7.3.1 Dependence of spectra on power and field

Changing the magnetic field and the pump power produces marked differences in the sub-Doppler DAVLL lineshapes. The dependence of the properties of interest for locking (the peak to peak amplitude and the gradient of the signal at the zero crossing) were quantified for the $F = 2 \rightarrow F' = 2, 3$ crossover transition in ^{87}Rb. This feature was selected because it is among the strongest lines in all four Rb transitions, and is separated from other spectral features by many tens of MHz. Other transitions are discussed briefly in Section 7.3.3.

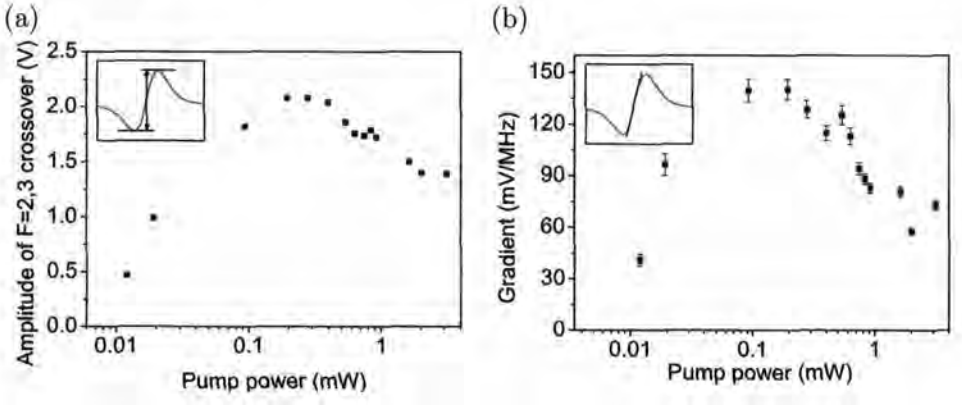

Figure 7.3: Dependence of (a) amplitude and (b) gradient on pump power for the ^{87}Rb $F = 2 \rightarrow F' = 2, 3$ crossover transition feature. The data were taken with a probe power of 20 μW and a magnetic field of 9.5 G. Error bars represent measurement uncertainties; the frequency calibration produces an additional systematic uncertainty of 3% in the magnitude of the gradient.

Figure 7.3 shows the evolution of (a) the amplitude and (b) the line-centre gradient of the $F = 2 \rightarrow F' = 2, 3$ crossover transition in ^{87}Rb as a function of pump power for a fixed magnetic field of 9.5 G. Both the amplitude and gradient are maximised for pump powers of $150 - 300$ μW, with the gradient reduced significantly due to power broadening above 700 μW. The probe

power was fixed at 20 μW. The choice of probe power is a trade-off between two effects. A higher probe power gives a better signal-to-noise ratio from the photodiode circuit. However, a low probe beam power ensures that one is in the weak-field limit, for which the absorption is largest [192, 193].

Figure 7.4 shows the effect of the solenoid's magnetic field on (a) the amplitude and (b) the gradient for three pump powers. The amplitude increases monotonically for all three pump powers up to a field of 20 G, at which point it begins to level off or decrease for the two lower pump powers. The gradient reaches its maximum value of 150 mV MHz^{-1} with an optimised pump power of 154 μW for magnetic fields between 10 – 15 G. A reduction in gradient is expected for larger fields because the Zeeman shift is such that the σ^+ and σ^- transitions differ in frequency by more than one natural linewidth. Above $\sim$ 30 G the smoothness of the sub-Doppler DAVLL lineshape is also compromised as Zeeman splitting begins to appear in the hyperfine structure.

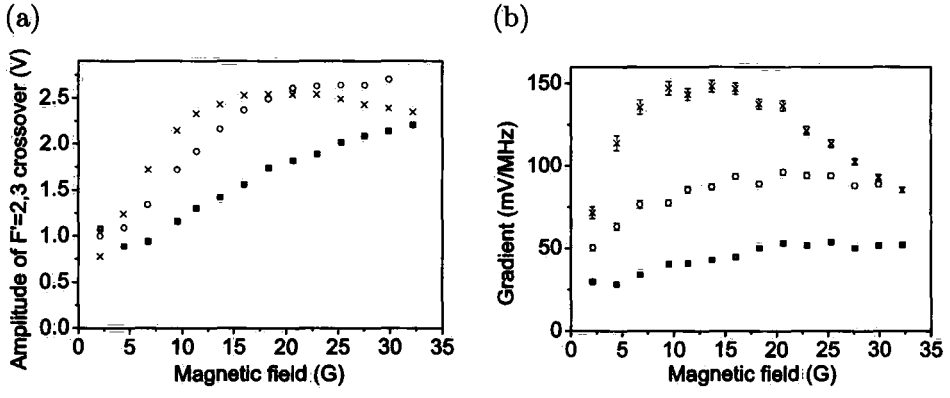

Figure 7.4: Dependence of (a) amplitude and (b) gradient of the $F = 2 \rightarrow F' = 2, 3$ crossover transition in ^{87}Rb on magnetic field. The data were taken with a probe power of 20 μW and pump powers of 154 μW (crosses), 784 μW (circles) and 3.04 mW (squares).

Figure 7.5 contains several examples of non-optimal spectra with the pump beam on (black traces) and blocked (red traces). In Figure 7.5 (a), the pump power has been set to 26 μW, barely stronger than the probe beam. The amplitudes of the sub-Doppler features are reduced by up to a factor of four. The spectra in Figure 7.5 (b) illustrate the opposite problem. At a pump

power of 3.04 mW, power broadening has increased the width of the features by almost a factor of two. Although the amplitude of the features has also increased, the gradient at line centre is still less than its optimum value. Figure 7.5 (c) shows the effect of reducing the magnetic field to 2 G, which (as in our study of polarisation spectroscopy) is just large enough to define a preferred direction for the magnetic field along the vapour cell axis. Changes in the magnetic field will, of course, affect the shape (magnitude and slope) of the background signal as well as the sub-Doppler features. Figure 7.5 (d) illustrates the effects of using a higher (30 G) magnetic field. This field is still almost factor of five lower than the optimum field for conventional DAVLL. However, it is high enough that the different m_F states of the ground state hyperfine levels are no longer degenerate. In the excited state, F and m_F are no longer good quantum numbers at these fields, leading to distortions in the spectra, *e.g.* the 'knee' between the two crossover features.

Another relevant quantity for locking a laser's frequency to an atomic transition is the magnitude of the difference between the transition frequency and the zero-crossing of the error signal. These zero-crossing shifts were measured by turning down the laser scan and comparing the zero-crossing frequency to the frequency of the associated saturated absorption peak. Measurements of the zero-crossing shift as a function of magnetic field showed that for fields between $5 - 20$ G, the magnetic field dependence of the zero crossing frequency is less than (70±20) $\mathrm{kHzG^{-1}}$. A field-independent frequency offset of between (0.6 ± 0.2) and (4.2 ± 0.2) MHz was observed for the different zero-crossing angles discussed in Section 7.3.4. These offsets are related to the slope of the background DAVLL signal, and can be set to any value within the capture range of the error signal by fine adjustments to the quarter wave plate angle.

The settings of magnetic field and pump power which maximise signal gradient and amplitude have clear trends. Empirically, one increases the pump power for a (low) fixed magnetic field until the gradient starts to decrease, then increases the field to produce the largest peak-to-peak amplitude without compromising the gradient. As these optimal field and power settings are largely uncorrelated, a few loops of the above procedure rapidly produces a reliable lock-point.

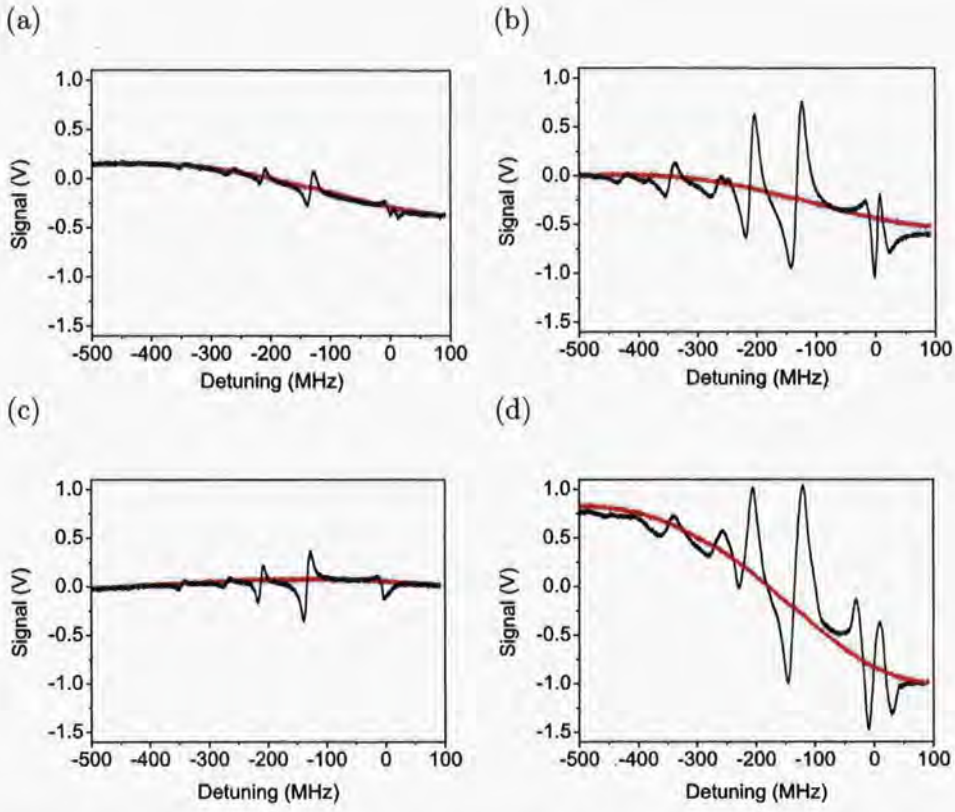

Figure 7.5: Sub-Doppler DAVLL spectra of the ^{87}Rb $F = 2 \rightarrow F'$ transitions for non-optimised values of pump power and magnetic field. Black (red) traces show spectra with the pump beam on (blocked). (a) Spectra taken at 9.5 G and a pump power of 26 μW. (b) Power-broadened spectra taken at 9.5 G and a pump power of 3.04 mW. (c) Spectra taken at the optimised pump power of 154 μW and a field of just 2 G. (d) At a field of 30 G, the presence of Zeeman substructure in the hyperfine levels distorts the lineshapes.

7.3.2 Comparison with polarisation spectroscopy

The optical setup required to generate sub-Doppler DAVLL spectra is very similar to that required for polarisation spectroscopy. In the latter, the quarter wave plate is moved from the probe to the pump beam to produce a circularly polarised pump beam. An additional half wave plate is placed in the probe beam before the vapour cell to set the error signal to zero with the pump beam blocked. Sub-Doppler DAVLL requires a solenoid, whereas

to maximise the polarisation spectroscopy signal a magnetic shield is often used. A shield was not used here because the ambient magnetic field was largely directed along the cell axis; consequently, spectra appeared very similar with and without a shield present. For other experiments in our group, the ambient magnetic field direction is at an angle relative to the cell, and as noted in Chapter 6, use of a shield can increase the magnitude of the polarisation spectra features by up to a factor of two.

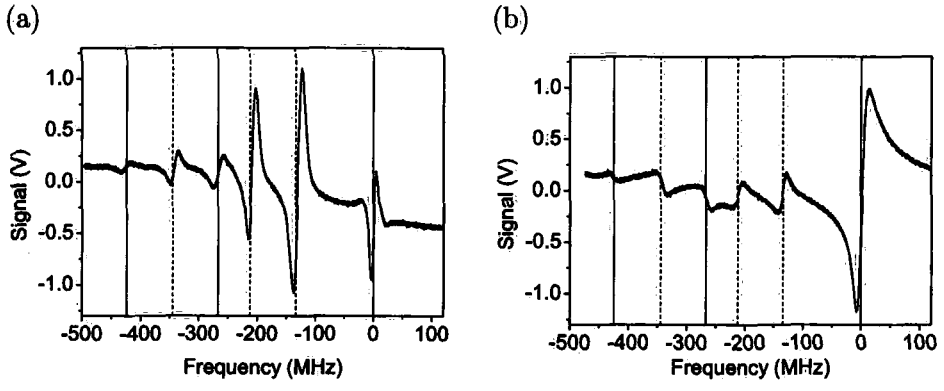

Figure 7.6: Comparison of (a) sub-Doppler DAVLL with (b) polarisation spectroscopy of the $F = 2 \rightarrow F'$ transitions in ^{87}Rb. The data were taken with the same photodiode detectors at a pump (probe) power of 154 μW (20 μW) The magnetic field was 9.5 G for the sub-Doppler DAVLL spectra and < 0.3 G for the polarisation spectra.

Figure 7.6 shows a comparison of polarisation and sub-Doppler DAVLL spectra for the ^{87}Rb $F = 2 \rightarrow F'$ transitions. The most noteworthy feature is the difference in amplitudes of spectral features arising from the same transitions. Polarisation spectroscopy relies on atoms in the medium absorbing many photons from the circularly polarised pump beam to drive the population towards a maximal m_F state, thus it is hampered by the process of hyperfine pumping. Consequently the closed transition $F = 2 \rightarrow F' = 3$ dominates [85]. In contrast, the crossover peaks involving open transitions are enhanced significantly by hyperfine pumping [192, 193], thus the sub-Doppler DAVLL spectra for these peaks are correspondingly larger. The choice of which technique to use essentially comes down to the question of whether an error signal centred on the closed transition, or one displaced

from the closed transition by an excited state hyperfine interval, is desired. This depends on the exact spectroscopic application, and the availability of acousto-optic modulators to modify the frequency of the beam used in an experiment with respect to the beam used in the spectroscopy setup. Note also that for certain atomic transitions, *e.g.* the $^1S_0 \rightarrow ^1P_1$ transition in ^{88}Sr, polarisation spectra do not exist, whereas sub-Doppler DAVLL spectra can still be generated.

7.3.3 Spectra of other Rb transitions

The sub-Doppler DAVLL spectra of other Rb transitions also provide useable error signals for laser locking. Figure 7.7 (a) shows the ^{85}Rb $F = 3 \rightarrow F'$ transitions. The $F' = 3, 4$ crossover feature appears particularly favourable for locking, with a well-defined zero crossing despite being separated from other features by only a few tens of MHz.

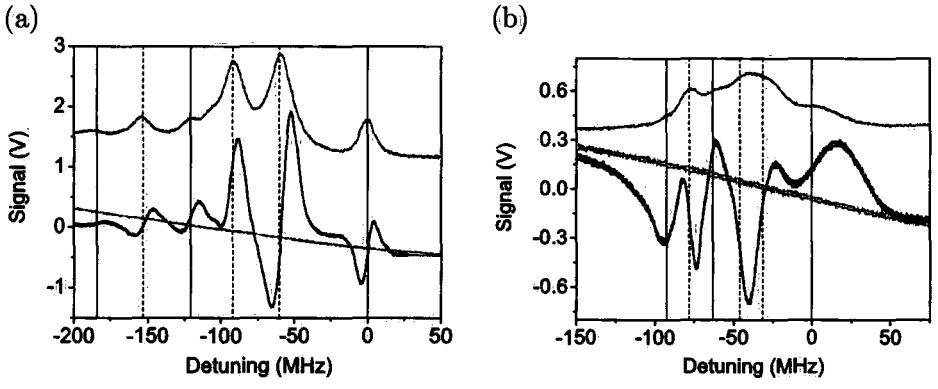

Figure 7.7: Sub-Doppler DAVLL signal for the (a) $F = 3 \rightarrow F'$ and (b) $F = 2 \rightarrow F'$ transitions of ^{85}Rb. The small hyperfine splitting of the latter transitions make it difficult to distinguish individual features. Light grey lines show the signal without the pump beam. Dark grey lines show the saturated absorption/hyperfine pumping spectra, which have been offset for clarity. The magnetic field and beam powers are the same as in Figure 7.6.

The sub-Doppler DAVLL spectra for the ^{85}Rb $F = 2 \rightarrow F'$ transitions (Figure 7.7b) share a feature with polarisation spectroscopy on the same transitions [85]: namely, the hyperfine splitting is so small that the six dis-

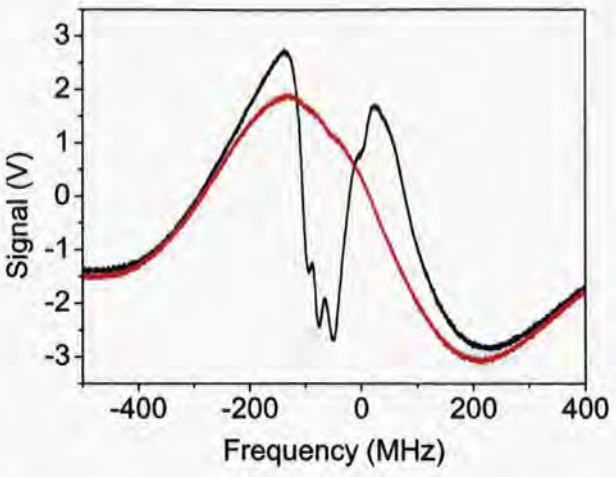

Figure 7.8: Power-broadened sub-Doppler DAVLL spectra of the ^{85}Rb $F = 2 \rightarrow F'$ transitions. Increasing the probe and pump powers to 134 μW and 3.57 mW respectively produces sub-Doppler DAVLL spectra (black trace) with zero-crossings which have steeper gradients than the 'background' DAVLL signal (red trace). The field was also increased to 17.87 G.

tinct spectral features seen on the other transitions partially overlap. The zero-crossings are thus both sensitive to the parameters chosen and not trivially related to the atomic reference transitions. It is possible to produce a zero-crossing for this transition with a greater amplitude and steeper gradient by deliberately power-broadening the sub-Doppler features. Figure 7.8 shows a sample error signal produced by setting the pump (probe) power to 3.57 mW (134 μW). The magnetic field plays little role under these conditions. The resulting spectra appear very similar to power-broadened saturated absorption/hyperfine pumping spectra of the same transition, which can also be used in a 'side of peak' locking technique.

For the ^{87}Rb $F = 1 \rightarrow F'$ transitions, the hyperfine splitting is larger, and we can see from Figure 7.9 that the sub-Doppler features are more distinct. However, the fraction of light absorbed in a 7 cm vapour cell for this transition is less than 10% at room temperature, and the amplitude of the largest crossover feature is approximately five times smaller than the ^{85}Rb $F = 3 \rightarrow F' = 3, 4$ and ^{87}Rb $F = 2 \rightarrow F' = 2, 3$ features. Ohmic heating from a specially-designed solenoid has been used to increase absorption and improve

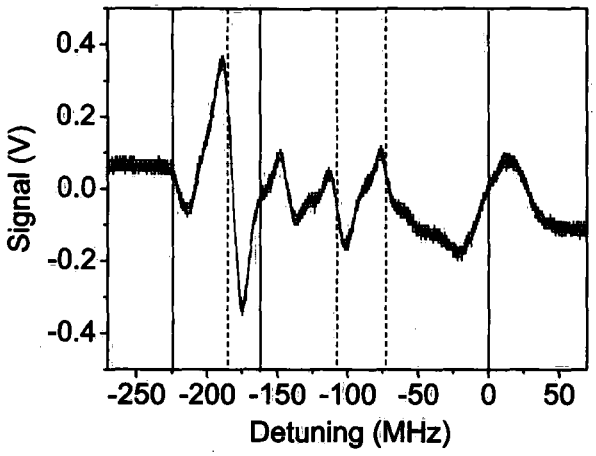

Figure 7.9: Sub-Doppler DAVLL spectra for the ^{87}Rb $F = 1 \rightarrow F'$ transitions. The amplitude of the largest crossover is five times smaller than the ^{85}Rb $F = 3 \rightarrow F' = 3, 4$ resonance at the same pump power and magnetic field. The amplitude of the signal could be improved by heating the vapour cell.

the conventional DAVLL signal for this transition [197]. This technique could be extended to sub-Doppler DAVLL by using a double solenoid, in which opposing currents generate a net magnetic field of 10 G along the axis of the vapour cell whilst also heating it to > 50 °C.

7.3.4 Dependence of lineshapes on polarisation purity

Changing the angle of the quarter wave plate influences the shape of both the conventional DAVLL background and the sub-Doppler DAVLL signals. For all spectra presented here, the wave plate angle was chosen such that the signal is zero far from resonance. In a system where the pump and probe beams are exactly linearly polarised and all polarisation optics are perfect, such 'zero-crossing angles' will be observed whenever one of the axes of the quarter wave plate is aligned at an angle of 45° relative to the probe beam's polarisation angle (horizontal). Rotating the quarter wave plate through 360° will therefore produce four zero-crossing angles located 90° apart. The sub-Doppler DAVLL spectra obtained at successive zero-crossing angles will be identical except for a sign change, and equally well-suited for laser locking.

The optical setup shown in Figure 7.1 was designed to produce polarisation purities of better than 300:1 in both beams. We have found that whenever PBSs are used in conjunction with half wave plates to produce a low-power beam, *e.g.* for spectroscopy, the polarisation purity of the weaker output beam is compromised. This is because a PBS typically allows 1-3% of input light with the wrong polarisation to 'leak' into each arm of the beamsplitter. If the power in the weaker output beam is comparable to this 'leaked' power, the polarisation of the beam will be highly elliptical (impure). To improve the polarisation purity of the spectroscopy beams, additional PBSs and half wave plates (not shown in diagram) were inserted in the pump and probe beams after the beams are separated. This method is very effective at 'cleaning up' the polarisation of the light transmitted through the PBSs; the polarisation purity of the pump and probe beams was $> 350:1$ at the cell compared to 70:1 immediately after the separating PBS.

Ultimately, however, the behaviour of the sub-Doppler DAVLL signal is strongly affected by the PBS used as an analyser. The fractional leakage noted above is slightly higher for the PBS's rejected arm, and this small anisotropy affects both the number of zero-crossing angles and the interval between them. To understand this behaviour, we modelled the PBS and quarter wave plate using a Jones matrix approach [196]. The light incident on the PBS has a polarisation defined by

$$L_{\text{in}} = \begin{bmatrix} \cos\phi \\ \sin\phi \end{bmatrix}, \tag{7.1}$$

where ϕ is the angle of the input polarisation relative to the PBS. The matrix for a quarter wave plate set at an angle θ with respect to the PBS with a phase shift of $\alpha \approx 90°$ is

$$M_{\lambda/4} = \begin{bmatrix} \cos\theta & -\sin\theta \\ \sin\theta & \cos\theta \end{bmatrix} \begin{bmatrix} 1 & 0 \\ 0 & e^{i\alpha} \end{bmatrix} \begin{bmatrix} \cos\theta & \sin\theta \\ -\sin\theta & \cos\theta \end{bmatrix}. \tag{7.2}$$

Hence our output matrix is

$$L_{\text{out}} = M_{\lambda/4} L_{\text{in}} \equiv \begin{bmatrix} V \\ H \end{bmatrix}, \tag{7.3}$$

where V and H represent vertically and horizontally polarised components of the light.

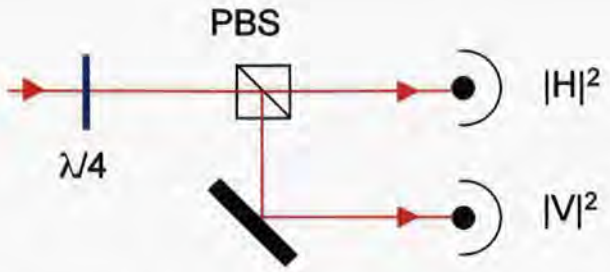

Figure 7.10: Illustration of the Jones matrix-derived signal. Light is incident on a quarter wave plate before hitting the PBS. For the 'perfect' PBS shown here, the light incident on the top (bottom) photodetector is entirely horizontally (vertically) polarised, and the signal recorded is $S = |V|^2 - |H|^2$.

For the perfect PBS cube represented in Figure 7.10, the signal S recorded by the photodiode circuit would be

$$S = |V|^2 - |H|^2. \tag{7.4}$$

However, as has been noted previously, the PBS is by no means perfect. Small amounts of light with the 'wrong' polarisation leak into each of the PBS' output arms. We therefore need to modify Eq. 7.4 to reflect this:

$$S = \left(v_{\mathrm{tr}}|V|^2 - h_{\mathrm{tr}}|H|^2\right) - \left(v_{\mathrm{ref}}|V|^2 - h_{\mathrm{ref}}|H|^2\right). \tag{7.5}$$

The subscripts 'tr' and 'ref' refer to transmitted and reflected light. Hence, coefficients like v_{tr} refer to the fraction of incident light of a given polarisation (H or V) found in the transmitted or reflected arms of the PBS cube. As Table 7.1 shows, to a first approximation the PBS transmits (reflects) horizontally (vertically) polarised light. This approximation is not good enough to account for the observed behaviour of zero-crossings. This is illustrated in Figure 7.11, which contains two plots of S as a function of the quarter wave plate angle θ. Figure 7.11 (a) shows S for a PBS which transmits 100% of incident horizontally polarised light and reflects 100% of incident vertically polarised light. Figure 7.11 (b) plots S again, this time using the measured values of v_{trans} *etc.* for the Casix PBS cubes used in this work.

Based on the measured amounts of vertically and horizontally polarised light in each arm of the analyser, we can see from Figure 7.11 (b) that we

	Transmitted	Reflected
Vertically polarised	0.01	0.99
Horizontally polarised	0.97	0.03

Table 7.1: Characterisation of Casix polarising beamsplitter cubes.

should expect *pairs* of zero-crossing angles separated by $(10 \pm 2)°$, centred at 45°. Experimentally, we observed zero-crossing angles whenever an axis of the quarter wave plate was aligned at 40 or 50° relative to the probe beam polarisation angle, in excellent agreement with the model. Figure 7.12 (a) shows the sub-Doppler DAVLL spectra obtained for two such zero-crossing angles. The sub-Doppler features are nearly identical, but the peaks in the Doppler background (inset) are separated by $\sim$ 200 MHz. This leads to a difference of (1.7 ± 0.1) MHz between the two angles in the frequency of the zero-crossing associated with the $F = 2 \rightarrow F' = 2, 3$ crossover feature.

The magnitude of these shifts and the separation between each zero crossing angle in a pair (ideally zero) are measures of polarisation quality. Figure 7.12 (b) shows sub-Doppler spectra obtained when the polarisation purity of the probe and pump beams was deliberately reduced to 145:1. With the polarisation purity halved, the separation of the zero-crossing angles increased to 18 degrees. Although the sub-Doppler spectra appear qualitatively similar for the two angles, the peaks of the Doppler background are now $\sim$ 250 MHz apart. This shifts the zero-crossing frequency of the $F = 2 \rightarrow F' = 2, 3$ crossover feature by (4.4 ± 0.1) MHz. Further reductions in polarisation purity produce increasingly different spectra at successive zero-crossing angles due to the complex interplay between sub-Doppler features and the Doppler background. For very poor polarisation purity ($\sim 15 : 1$), the sub-Doppler features are both qualitatively different in their lineshapes and located in different regions of the Doppler background, *e.g.* near the minimum as opposed to halfway up the side of the Doppler-broadened peak.

This behaviour has clear implications for laser locking. The error signals generated by such poorly linearly polarised beams will be more sensitive to small changes in polarisation due to *e.g.* changes in temperature. The magnetic field dependence of the error signal's zero-crossing will also differ

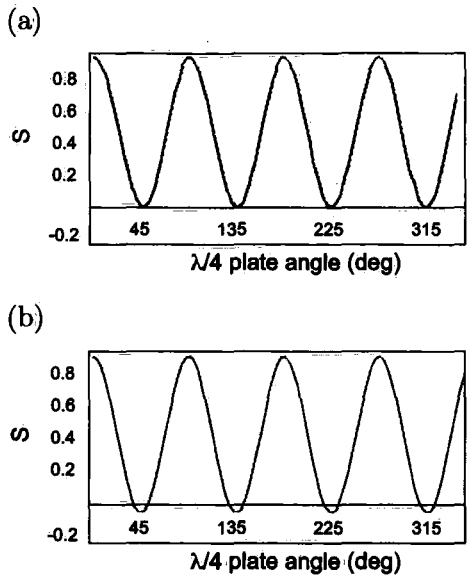

Figure 7.11: Signal recorded by the photodiode pair as a function of quarter wave plate angle for (a) 'perfect' optics and (b) a quarter wave plate with a phase shift of 89° and a PBS with the specifications given in Table 7.1. Zero-crossing angles occur whenever $S = 0$. This happens every 90° for the perfect optics. In (b), the model predicts *pairs* of zero-crossing angles separated by about 10 degrees.

between zero-crossing angles, as some sub-Doppler features may be located in a flat region of the Doppler background, and others on a slope. Polarisation spectra are also sensitive to impurities in polarisation, although this aspect was not studied in detail. It is therefore advisable to make the polarisation purity of the system as high as is practical. Note, however, that very good purity can be achieved without recourse to (expensive) specialised optics, and improvements in polarisation purity above 300-400:1 will yield diminishing returns as other factors (e.g. differences in the responsivity of the two photodiodes) can also produce a separation in zero-crossing angles.

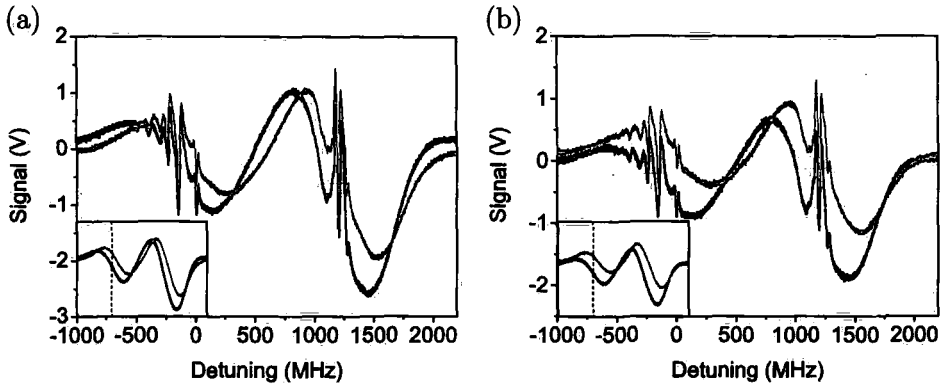

Figure 7.12: Sub-Doppler DAVLL spectra of the $F = 2 \rightarrow F'$ ($F = 3 \rightarrow F'$) transitions in ^{87}Rb (^{85}Rb). Spectra from successive zero-crossing angles are indicated with grey and black lines. Insets show the background DAVLL signal obtained with the pump beam blocked. A dashed line indicates the location of the crossover feature studied in Section 4.1. (a) Spectra obtained with a polarisation purity of $> 350 : 1$ in the pump and probe beams. Small changes in the position of the sub-Doppler features relative to the Doppler background have little effect on their suitability for use in laser locking. (b) Reducing the polarisation purity to 145:1 produces larger offsets, increasing the sensitivity of the error signal to changes in polarisation or magnetic field.

7.4 Conclusions

In summary, we have studied sub-Doppler DAVLL spectra for the Rb $D2$ transitions. The importance of polarisation purity in generating the spectra was discussed, and a simple model of the PBS analyser and quarter wave plate using Jones matrices was constructed to explain the presence of additional zero-crossing angles. The dependence of the amplitude and gradient of the error signals produced were characterised as a function of magnetic field and pump power. We suggest using a pump power of 150-300 μW and a magnetic field of $\sim$ 10 G to maximise the signal gradient and amplitude for the ^{87}Rb $F = 2 \rightarrow F' = 3, 2$ crossover transition. A comparison with polarisation spectroscopy showed similar amplitudes and gradients for the largest features of each scheme.

In this work, we have now examined three different locking methods, each of

which have some points in their favour. The magnetic field which maximises error signal amplitude and gradient for sub-Doppler DAVLL is an order of magnitude smaller than the optimum field for conventional DAVLL. The gradients of the error signals produced by sub-Doppler DAVLL are up to two orders of magnitude larger. Polarisation spectroscopy requires essentially no magnetic field at all, and produces signals with a similar amplitude and gradient for the same probe and pump powers. The capture range for these methods is, however, much reduced compared to conventional DAVLL, typically 10's rather than 100's of MHz. Finally, all three methods have important systematic effects involving temperature and polarisation purity/stability.

Whither, then, for laser locking? Both polarisation spectroscopy and DAVLL have been used to lock lasers in the Durham group, and both have the imprimatur of Nobel laureates behind them. Sub-Doppler DAVLL is newer, but also appears eminently suitable as a locking method. Very recently, other members of the Durham group have also investigated yet another method, modulation transfer spectroscopy, which holds considerable promise and may be used in the next-generation Rb-Cs experiment [191]. This experiment, and other plans for the future, are the subject of the final chapter of this thesis.

Part IV

Atom trek: the next generation

Chapter 8

Conclusions

8.1 Conclusions

In this work, we have described a new apparatus designed to study cold and ultracold mixtures of rubidium and caesium atoms. Results obtained from experiments on the magneto-optically trapped mixture were presented. Initial observations of the two-species science MOT showed greatly enhanced loss and diminished loading capability for both species when the other species was present. This qualitative picture of MOT performance was enhanced by quantitative studied of loss in single-species and two-species MOTs. We measured values for interspecies loss rate coefficients in the Rb-Cs MOT which were an order of magnitude higher than the corresponding factors for Rb or Cs single-species MOTs.

Spatially separating the MOTs during loading greatly reduces the loss due to heteronuclear inelastic collisions. We have developed a technique in which a beam of resonant light is used to shift the position of the Rb MOT during the loading phase of our experiment. Unlike previous techniques used for spatially separating mixture components in a MOT [40], our method does not require additional traps or magnetic fields to separate Rb and Cs atoms. Using this method, we can load 50-50 mixtures of Rb and Cs atoms into the magnetic trap at close to their respective maximum single-species atom numbers; alternatively, we can load primarily one species with arbitrarily small amounts of the other. The displaced MOT is thus an excellent starting point for ongoing and future studies on magnetically trapped mixtures, including

sympathetic cooling and investigations of interspecies Feshbach resonances.

Other work presented here has focused on spectroscopic techniques used for laser frequency stabilisation. Studies of polarisation spectroscopy, DAVLL and sub-Doppler DAVLL have enhanced our understanding of atom-light interactions in spectroscopic systems and how locking signals can be optimised for use in cold atom experiments like the Rb-Cs mixture project and its successors.

8.2 Future work

The next step for the Rb-Cs mixture project after the magnetic trap studies described in Ref. [84] are complete is to implement optical trapping. This section begins by describing optical trapping experiments which are planned for the near future, and concludes with a more speculative discussion of studies which could be contemplated in the longer term.

8.2.1 Optical 'dimple' trap

A logical first step for optical trapping in the mixture experiment would be to superimpose the potential generated by a single, focused, red-detuned laser beam on the magnetic potential of the baseball trap. As noted in Chapter 3, this configuration is the simplest way of realising the intensity gradient required for optical confinement of atoms. More importantly, combining an optical 'dimple' with a magnetic 'reservoir' potential represents a possible alternative route to BEC in caesium. Such a system would be simpler than the multiple optical traps which were used to condense Cs for the first time [69], and avoids the need for the crossed-beam CO_2 trap used both then and in a more recent experiment [226]. Implementing optical trapping would also allow us to study mixtures of the high-field-seeking $|F = 3, m_F = +3\rangle$ and $|F = 1, m_F = +1\rangle$ states of Cs and Rb, for which two-body inelastic collisions are forbidden and interspecies Feshbach resonances have recently been observed [83]. The principal challenges will be to

- Select appropriate parameters for the trap

- Implement stabilisation and control of the optical trapping laser's intensity
- Design a trap for which the components (*e.g.* lenses and beam blocks) do not interfere with existing equipment and diagnostics.

The solution to the first challenge lies in understanding the meaning of 'appropriate.' We saw in Chapter 3 that the depth of the trapping potential depends on the power, detuning, and waist of the focused beam. The *volume* of the trap is also important, because the number of atoms in the 'dimple' potential must be smaller than the number in the reservoir. Also, the two populations must remain in thermal contact for the 'dimple trick' of increased phase-space density at constant temperature to work [106]. Further studies are needed to determine which trapping parameters (optical and magnetic) will best fulfill these criteria, and how cold the mixture becomes after evaporation in the magnetic trap.

Intensity fluctuations are a well-known problem in optical traps [227]. A common technique for minimising them (in addition to selecting a well-behaved, stable laser at the outset!) is to monitor the trapping light after it has passed through an acousto-optic or electro-optic modulator by diverting a small fraction of the light onto a photodiode. The photodiode signal is then used as an input for servo electronics which regulate the voltage applied to the AOM/EOM to compensate for fluctuations in the laser's output intensity, producing a stable beam in the trapping region. The same AOM/EOM system can also be used for fast switching of the trapping potential and for producing smooth intensity ramps, *e.g.* for evaporative cooling in the dimple trap.

The final challenge is both the most mundane and arguably the most difficult to overcome in the current mixture apparatus. The apparatus was designed to maximise optical access to the 'science cell' region. However, other factors also had to be considered. For example, when constructing a magnetic trap, it is generally desirable to minimise the current and cooling requriements for the coils. The simplest way to do this is to place the trapping coils as close to the atoms as possible. This inevitably restricts optical access to the trapping region. The MOT beams and optics also occupy crit-

ical space near the experimental chamber. Although implementing a single focused-beam trap or 1D lattice created by two counterpropagating beams should present few major difficulties, the large number of beams needed to create and probe the two-species science MOT makes it difficult to investigate more elaborate trapping geometries using the current setup.

8.2.2 Magnetic transport

One way around this problem in a next-generation experiment would be to spatially separate the magnetic trapping/MOT and optical trapping regions of the apparatus, and transport the atoms between the two regions using magnetic fields. Two different magnetic transport techniques have been developed. The fixed-coils method demonstrated by Greiner *et al.* in Munich [228] employs several partially-overlapping anti-Helmholtz coil pairs aligned along a transfer path between different regions of the experimental apparatus. To move atoms along the coils, current is run through different coil pairs in a sequence described in the reference. Another method, developed at JILA and described in Ref. [229], uses a single pair of quadrupole coils which are mounted on a motorised translation stage which moves along a set of fixed rails.

The advantage of the fixed-coils method is that atoms can be transported with relative ease around corners or along some other non-linear path. The disadvantage is that it is more complex to set up than the moving-coils system, which has fewer components, many of which are available commercially. Hybrid systems have been used which combine some aspects of both techniques, *e.g.* a few fixed coils to maneouvre atoms around a barrier followed by a moving coil pair to complete the transport process [50]. In Durham, plans are being developed to use one or both types of magnetic transport on the ^{85}Rb solitons/evanescent wave experiment as well as the next-generation mixture apparatus. Figure 8.1 shows one possible configuration for a magnetic transport experiment. The figure is based on a prototype apparatus which has actually been constructed; the design is currently being modified to further improve optical access to the science cell.

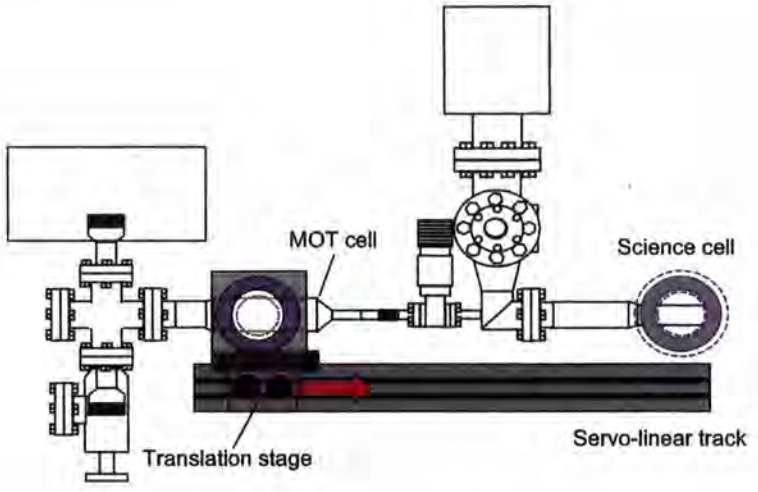

Figure 8.1: Schematic diagram of magnetic transport apparatus. Atoms are transported from the MOT cell into a UHV science cell using a single translation stage.

8.2.3 Optical lattices

Optical lattices have been used to explore a range of interesting phenomena in cold and ultracold systems, including atomic clocks [230] and quantum phase transitions [231]. They also hold great promise for neutral atom quantum computing; see *e.g.* Ref. [232] and references therein. These last two subjects are of particular interest for mixtures. In Chapter 2 we discussed the criteria for forming a quantum degenerate mixture in which the two components are miscible. Applying the Mott insulator transition to a miscible quantum degenerate mixture in a lattice, as was done for a sample of Bose-condensed Rb atoms by Greiner *et al.* [231], will produce a lattice with exactly one atom of each species per lattice site (Figure 8.2). Photoassociation or Feshbach resonances could then be used to form ultracold molecules, which after transfer into deeply bound vibrational states would also be highly polar (Chapter 1). This method for producing ultracold polar molecules was suggested by Jaksch *et al.* in 2002 [233]. The resulting lattice of RbCs dimers would fulfill the criteria for the quantum computing scheme proposed by DeMille in the same year [25].

Another promising application of optical trapping in mixtures are *species-*

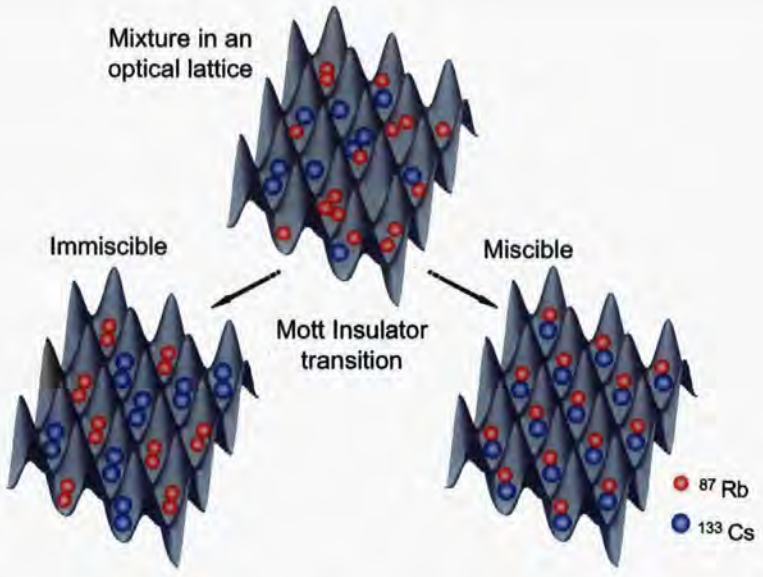

Figure 8.2: Illustration of molecule production scheme using Rb and Cs atoms in an optical lattice. Applying the Mott insulator transition to a miscible mixture produces a lattice containing one atom of each species per lattice site. For an immiscible mixture, the same phase transition will produce sites containing homonuclear atom pairs.

specific lattices [234]. Such lattices are formed when the wavelength of the laser beam is either tuned close to resonance with the 'target' species, or at a 'magic' wavelength [230] where the light shift of ground and excited states precisely cancels for the 'spectator' species. One possible use of this technique would be to improve sympathetic cooling in the cold mixture. Other applications include changing the effective mass of one species, which would provide an alternative to Feshbach resonances as a means of tuning interaction strengths in the mixture.

8.3 Outlook

Cold, ultracold and quantum degenerate mixtures of two or more atomic species hold great promise for the future of atomic physics research. The combination of rubidium and caesium atoms is of particular interest due to

the complementary scattering properties of the two species. Also, the near-identical magnetic moment-to-mass ratio of Cs and Rb in the $|F=3, m_F=\pm 3\rangle$ and $|F=1, m_F=\pm 1\rangle$ states (respectively) allows the two species to remain in close thermal contact in a magnetic trap even at low temperatures due to their near-identical gravitational sag. Future work on this mixture will explore different regimes of mixture interactions, and may eventually allow quantum computations to be performed with ultracold, polar RbCs molecules.

Part V

Appendices

Appendix A

Matlab image analysis programme

The Matlab image analysis programme used to process absorption images is substantially based on a code developed by Gerald Hechenblaikner at Oxford, with modifications for two-species imaging. The programme contains a number of subroutines, the majority of which perform routine file-control operations such as displaying the images or saving them to a new location, and are of little physical interest. It is however instructive to compare the actual analysis process, performed by the subroutine ana.m, with the general description of absorption imaging provided in Chapter 4.

The analysis subroutine turns the atoms, probe-only, and background images into three arrays A, B and C. Each element in the arrays represents the intensity (in counts) recorded by a single camera pixel. It then performs the following steps to generate x- and z-axis fits of the atomic cloud:

1. Subtracts the background from A and B
2. Resets any zero or negative intensities to the minimum nonzero intensity value in A or B
3. Redefines A as $\log\left(\frac{B}{A}\right)$, so that A is now an array of optical depths
4. Creates an x-axis row vector I_1 containing the sums of all the columns of A (Figure A.1). This is equivalent to integrating the optical depth over all values of z

5. Passes I_1 into the subroutine findsta.m, which generates a vector of initial-guess coefficients c(i) for a gaussian function R_1 of the form

$$R_1 = c(1) + c(2)\exp\left(\frac{(x - c(3))^2}{c(4)^2}\right). \tag{A.1}$$

6. Passes I_1 and the coefficient vector c into the subroutine fitfun.m, which returns the sum of $(R_1 - I_1)^2$. This function is a measure of the accuracy of the initial guess

7. Determines the best x-axis fit by using the built-in function fminsearch to find the coefficient vector cx which minimises the sum. The result is a new R_1 of the form

$$R_1 = cx(1) + cx(2)\exp\left(\frac{(x - cx(3))^2}{cx(4)^2}\right). \tag{A.2}$$

8. Repeats the fitting process for the z-axis, producing a z-axis fit R_2 from a transposed row vector I_2 and coefficient vector cz.

The physical significance of the four fitting coefficients is readily apparent from Equation A.2. The peak optical depth for a cross-section along a given value of x is cx(1)+cx(2), with cx(1) representing a background offset and cx(2) the 'real' optical depth. The centre of the cross-section is at cx(3) and cx(4) is the width.

To find the global peak optical depths, ana.m generates two new row vectors crossx and crossz, which are cross sections in x and z centred at the points cz(3) and cx(3), respectively (Figure A.2). Fits are found for crossx and crossz by the process described above, and the calculated peak optical depth along the x-axis is crossxfit(1)+crossxfit(2).

The last line of ana.m calls a new subroutine, datadisp.m, which calculates physical cloud parameters and displays them in the graphical interface. To do this, it reads in the fitting parameters found by ana.m; obtains the trap frequencies, magnification, binning, time of flight, and I/I_{sat} from the programme's graphical user interface; and defines the mass, wavelength, and total scattering cross section σ_0 of the atomic species.

In terms of these variables, the axial atom number N_a is

$$N_a = 8 * 10^{-6}\frac{(\mathrm{sum(I1)} - \mathrm{cx(1)} * \mathrm{length(I1)})\,\mathrm{xbin} * \mathrm{ybin}}{\mathrm{magnification}^2 * \sigma_{\mathrm{tot}}}, \tag{A.3}$$

where xbin and ybin represent the binning of the image. The equation for radial atom number N_r is similar, but with I_2 and cz(1) substituted for their axial counterparts. Both expressions may be made more transparent by noting that each pixel on the Andor iXon camera has an area of 8 μm^2, the sum of all elements in I_1 (or I_2) is the total optical depth of all pixels, and the length of I_1 (I_2) is the number of columns (rows). Hence the quantity cx(1)*length(I1) is the 'background' axial optical depth. Rewriting, we find

$$N_a = \frac{OD_x * \text{pixel area}}{\sigma_{tot}} \frac{\text{binning}}{\text{magnification}^2}, \tag{A.4}$$

where we have used OD_x to signify the optical depth along the x-axis. This result has the same form as the analytical result for N derived from peak optical depth as in Eq. 4.13 in Chapter 4, *i.e.*

$$N_{fit} = \frac{2\pi OD_{\text{pk}}\sigma_x\sigma_z}{\sigma_0}. \tag{A.5}$$

A similar analysis of the results for temperature and density shows that in terms of the Matlab programme variables, the radial temperature is

$$T_r = \frac{8\pi^2 m f_r^2 * \text{cz}(4)^2 * \text{ybin}^2/\text{mag}^2 * 8 * 10^{-6}}{2k_B} \tag{A.6}$$

Another 'translation' shows that this is equivalent to

$$T_r = \frac{m\omega_r^2\sigma_r^2}{k_B}. \tag{A.7}$$

The subroutine datadisp.m also calculates the density of the atom cloud both in the trap and after expansion (labelled 'densityTOF' in the programme):

$$n_{trap} = \frac{OD_z * \text{pixel area} * \text{binning}}{\text{magnification}^2 * \sigma_{\text{tot}}} \times \frac{\left(1 + 4\pi^2 f_x^2 * \text{TOF}^2 * 10^{-6}\right)^{1/2} \left(1 + 4\pi^2 f_z^2 * \text{TOF}^2 * 10^{-6}\right)^2}{\sigma_x \sigma_z^2 \pi^{3/2}} \tag{A.8}$$

$$n_{TOF} = \frac{OD_z * \text{pixel area} * \text{binning}}{\text{magnification}^2 * \sigma_{\text{tot}}} \left(\frac{1}{\sigma_x \sigma_z^2 \pi^{3/2}}\right). \tag{A.9}$$

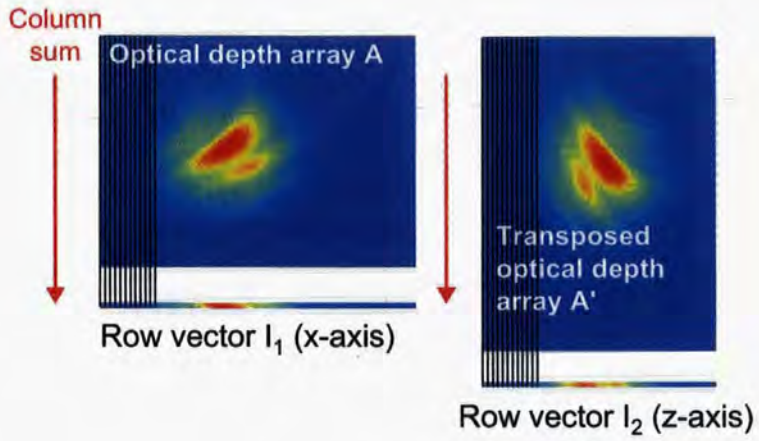

Figure A.1: Generating row vectors from the optical depth array. For the row vector along the z-axis, the array is transposed before the columns are summed.

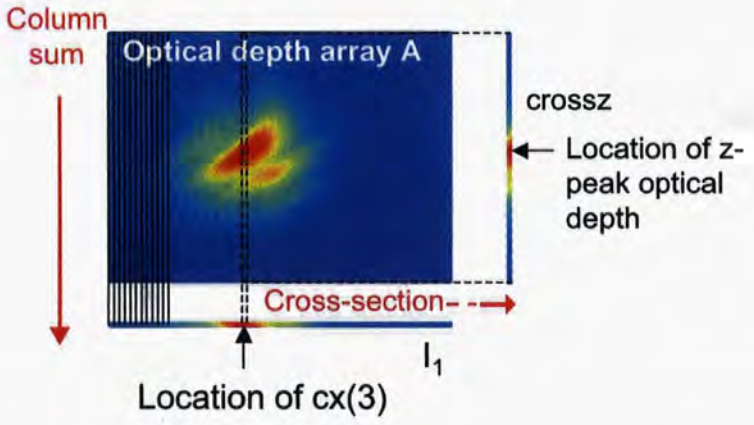

Figure A.2: The fitted centre of I_1, cx(3), determines which z-axis cross-section of the optical depth array should be fit to find the z-peak optical depth.

Appendix B

Camera routines

This appendix contains details of the sequence of events needed to record a series of images using the Andor iXon camera on the mixture experiment.

B.1 Single-species imaging

The steps for imaging a single species are listed here and illustrated in Figure B.1.

1. Set up the acquisition in the SOLIS software to take a single image in bulb mode. This is done by selecting the 'Setup acquisition' option under the Acquisition menu.

2. Run the programme called 'ImageOneSpeciXon.pgm' by selecting the 'Run program by filename' option under the File menu, then typing in or selecting this programme.

3. The programme then asks the user to select which species is being imaged - '0' for Cs, '1' for Rb. It also asks for a number to use for saving and indexing the acquired data. For example, if this is the first image being taken today, enter '1'.

After this user-controlled sequence has finished, the camera software executes the following steps:

1. The Andor code tells the camera to run.

2. After 190±2 ms, the camera is ready to acquire an image.

3. At any time afterwards, Labview can send a TTL pulse to the Ext Trigger input on the camera, and the camera will record an image. In bulb mode, the exposure time is the same as the length of the TTL pulse, as discussed in Chapter 4.

4. The acquisition is complete after 143 ± 2 ms. The Andor code then tells the computer to start saving the acquired data to the temporary .sif files used for displaying images within the SOLIS software.

5. After 20-50 ms the data is finished saving.

6. There is a 50 ms delay built into the Andor code which is used to give the computer time to draw the windows needed to display the data.

7. The Andor code outputs a 'finished' TTL pulse by setting the AUX-OUT 1 port to 'high' for 3 ms.

8. The TTL signal is sent to port DIO4 on the digital input-output boards. When the Labview subroutine waittrig.vi receives the signal, it exits its While loop.

9. Waittrig.vi tells Labview to wait an additional 200 ms before moving on to the next subroutine. During this time, the Andor code tells the camera to run again (Step 1) and by the time waittrig.vi is finished, the camera is ready to acquire another image (Step 2).

10. The Andor code repeats steps 1-9 until all three images (atoms, probe, background) have been acquired.

Once the three images have been acquired, the following steps complete the imaging sequence:

1. The Andor code exits its inner while loop.

2. If the user instructed the programme to save the data, the programme saves the images in .sif and .asc format, increments the index by one, and tells the user the data were saved. If the data are not being saved, the user is asked to continue, quit, or perform an emergency save. The

```
cls()
MoveWindow(output,0,500,880,300)
Print("SINGLE SPECIES ABSORPTION IMAGING.")

Input("Please select a species: Cs(0) or Rb(1)",s)
        if s==0 then
                Print("You are imaging Cs.")
        else
Step 1.3 if s==1 then
                Print("You are imaging Rb.")
        else
                Print("Invalid selection. Cs imaging will be assumed.")
        endif
        endif

Input("Please enter a start number for saving:",n)
        if n==0 then
                Print("The data are not being saved!")
        endif
        if n>0 then
                Print("The next acquisition set will be number ";n)
        endif
```

```
k=0

while(k<>'q')                   :rem routine loops until user hits 'q' to quit

        auxout(1,0)             :rem set aux out 1 low (0)

        counter=1

        while counter<4         :rem data acquisition loop (counter<4 takes three images)
Step 2.1 ------> run()          :rem then run the acquisition sequence as setup in Andor software
Step 2.4 ------> #counter=#0    :rem save the acquisition in the data set/window: counter
                 counter=counter+1
Step 2.6 ------> delay(50)      :rem delay to let drawing of the new window

                 auxout(1,1)    :rem set aux out high to signify end of the scan sequence
                 delay(20)      :rem 3ms pulse
Step 2.7 ------> auxout(1,0)    :rem set aux out low
                                :rem Print("the counter is now at ";counter)
```

```
Step 3.1 ----> wend

        MoveWindow(#1,0,0,440,500)
        MoveWindow(#2,440,0,440,500)        :rem arrange windows
        MoveWindow(#3,880,0,265,350)
        MinimizeWindow(#0)
Step 3.2 // Programme saves data, increments counter, and runs subroutine to turn
        numbers into dates

Step 3.3 wend
```

Figure B.1: Single-species camera code. Labels refer to the three enumerated lists in Section B.1.

last option allows the user to save data even if the code was not initially set up for saving.

3. The Andor code repeats all the steps in this section and the previous section until the user tells it to quit.

B.2 Two-species imaging

The code for two-species imaging is similar in many respects to single-species imaging.

To set up the acquisition for two-species imaging, follow these steps:

1. Set up the acquisition in the SOLIS software to take a two image sequence in fast kinetics mode, using fast external trigger mode. This is done by selecting the 'Setup acquisition' option under the Acquisition menu.

2. Run the programme called 'ImageTwoSpeciXon.pgm' by selecting the 'Run program by filename' option under the File menu, then typing in or selecting this programme.

The remainder of the code operates in much the same way as it does in the single-species case, with two exceptions. One is that the time between images in a pair (*e.g.* atom images for Rb and Cs) is less than 2 ms, as discussed in Chapter 4. The other difference is in the structure of the code which displays images within the SOLIS software. In the two-species version, windows 1, 2 and 3 display images of Cs atoms, Cs probe light, and the Cs background shot, respectively. Windows 4-6 contain the equivalent images for Rb.

B.3 Data saving

If the Andor code has been configured to save the data, images 1-3 (in the single species case) or images 1-6 (two species imaging) are saved in two formats. First, they are saved as .sif files, using the indexing numbers set by the user. This is the format recognised by the Andor software. They are

also saved as .asc (ASCII) files for processing in Matlab. The .asc filenames have the format data00n.asc, where n=1-3 for Cs, 4-6 for Rb; this is true for both single-species and two-species imaging.

Appendix C

Polarisation spectroscopy code

This appendix contains the Mathematica code for generating model polarisation spectra on the $F = 2 \rightarrow F'$ transitions in ^{87}Rb. To modify the code for other species, one must change the

- lifetime of the excited state
- atomic mass
- *values only* (NOT names) for hyperfine structure and fine structure splittings (E32 etc)
- variables used in calculating line strengths

and also the numerical values (NOT names) used for indexing which $|F, m_F\rangle$ sublevel is being considered in the calculations. These may be found in the first line of the code. For example, to use this code to generate model spectra for the ^{87}Rb $F = 3 \rightarrow F'$ transitions, one must set $F_2 = 3$, $F_1 = 2$, $F_3' = 4$, $F_2' = 3$, $F_1' = 2$, and $F_0' = 1$. The code will appear less intuitive once this is done, but this method is far easier and less error-prone than combing through the code to change the labels in every instance.

Defining variables

```
F2 = 2; F1 = 1; F3' = 3; F2' = 2; F1' = 1; F0' = 0; i = 3/2; Asat = 1; Clear[A, Asat, a]
```

```
{F2, F1, F3', F2', F1', F0'}
```

```
{2, 1, 3, 2, 1, 0}
```

```
L = 0; l' = 1; S = 1/2; s' = 1/2; J = 1/2; j' = 3/2;
```

```
τ = 27 * 10^-9
```

$$\frac{27}{1\,000\,000\,000}$$

```
Γ = 1/τ; Δ=. (*Δ=-2π (0)*10^8*)
```

The hyperfine splittings of the excited states and the fine structure splitting of the ground state are defined.

```
E32 = 267; E21 = 157; E10 = 72; Eg = 6835;
```

```
{E32, E21, E10, Eg}
```

```
{267, 157, 72, 6835}
```

Setting boundary conditions

We start with the population evenly distributed throughout all 8 mF levels of the ground state:

```
Grnd1Bcond = Table[ρF1,MF[0] = 1/((2 J + 1) (2 i + 1)), {MF, -F1, F1}]
```

$$\left\{\frac{1}{8}, \frac{1}{8}, \frac{1}{8}\right\}$$

```
Grnd2Bcond = Table[ρF2,MF[0] = 1/((2 J + 1) (2 i + 1)), {MF, -F2, F2}]
```

$$\left\{\frac{1}{8}, \frac{1}{8}, \frac{1}{8}, \frac{1}{8}, \frac{1}{8}\right\}$$

```
GrndBcond = Join[Grnd1Bcond, Grnd2Bcond]
```

$$\left\{\frac{1}{8}, \frac{1}{8}, \frac{1}{8}, \frac{1}{8}, \frac{1}{8}, \frac{1}{8}, \frac{1}{8}, \frac{1}{8}\right\}$$

There are (2J+1)(2I+1) initial states, 5 states with F=2 and 3 with F =1. There is no population in the excited state.

```
ExcitedBcond = Table[ρF,MF[0] = 0, {MF, 1, 2 F3' + 1 + 2 F2' + 1 + 2 F1' + 1 + 2 F0' + 1)]
```

```
{0, 0, 0, 0, 0, 0, 0, 0, 0, 0, 0, 0, 0, 0, 0, 0}
```

```
bcond = Join[GrndBcond, ExcitedBcond]
```

$$\left\{\frac{1}{8}, \frac{1}{8}, \frac{1}{8}, \frac{1}{8}, \frac{1}{8}, \frac{1}{8}, \frac{1}{8}, \frac{1}{8}, 0, 0, 0, 0, 0, 0, 0, 0, 0, 0, 0, 0, 0, 0, 0, 0\right\}$$

```
gnd = Join[Table[ρF1 g,MF, {MF, -F1, F1}], Table[ρF2 g,MF, {MF, -F2, F2}]];
excited = Join[Table[ρF0',MF, {MF, -F0', F0'}], Table[ρF1',MF, {MF, -F1', F1'}],
  Table[ρF2',MF, {MF, -F2', F2'}], Table[ρF3',MF, {MF, -F3', F3'}]];
ρ[t] = Join[gnd, excited]
```

$$\{\rho_{g,-1}, \rho_{g,0}, \rho_{g,1}, \rho_{2\,g,-2}, \rho_{2\,g,-1}, \rho_{2\,g,0}, \rho_{2\,g,1}, \rho_{2\,g,2}, \rho_{0,0}, \rho_{1,-1}, \rho_{1,0},$$
$$\rho_{1,1}, \rho_{2,-2}, \rho_{2,-1}, \rho_{2,0}, \rho_{2,1}, \rho_{2,2}, \rho_{3,-3}, \rho_{3,-2}, \rho_{3,-1}, \rho_{3,0}, \rho_{3,1}, \rho_{3,2}, \rho_{3,3}\}$$

The above just illustrates the form that the solution takes i.e. $\rho' = M\rho$, and the first element in the vector is the F = 1, M_F = -1 state

Calculating the line strengths

```
G = 2; g' = 3; MF' = 2; q = MF' - (MF' + δ); δ =.

(* for some reason if MF=G then mathematica makes MF :F' *)
(*so use lower/caps for the excited/ground state quantum numbers*)

{L, 1', S, s', J, j', i, G, g', MF', q}

{0, 1, 1/2, 1/2, 1/2, 3/2, 3/2, 2, 3, 2, -δ}

v = 0; w = 0; x = 0; y = 0; z = 0;


Do[
 Do[
  Do[
   Table[kw,w+x,y = 0, {y, -2 (F1 + F2 + F0' + F1' + F2' + F3' + 3), 2 (F1 + F2 + F0' + F1' + F2' + F3' + 3)};
    , {w, -2 (F1 + F2 + F0' + F1' + F2' + F3' + 3), 2 (F1 + F2 + F0' + F1' + F2' + F3' + 3)}]
   , {x, F0', F3'}]
  , {v, F0', F3'}]


Do[
 Do[
  Do[

   Table[
    kg',MF'→G,MF'+δ =
     3 * Γ
      ((-1)^(1+1'+S+J+j'+i-MF') Sqrt[(2 J + 1) (2 j' + 1) (2 G + 1) (2 g' + 1)] SixJSymbol[{1', j', S}, {J, L, 1}]
        SixJSymbol[{j', g', i}, {G, J, 1}] ThreeJSymbol[{G, MF' + δ}, {1, q}, {g', -MF'}])^2,
     {MF', -g', g'}]
    , {δ, -1, 1}]
   , {g', G - 1, G + 1}]
  , {G, F1, F2}]
```

- **Calculating the ground state matrix**

```
Mx1 =
  Table[

 -(kF2',MF-F1+1→F1,MF-F1 1/(1 + 4 ((Δ+(E32+Eg)×10^6 2π)/Γ)^2) + kF1',MF-F1+1→F1,MF-F1 1/(1 + 4 ((Δ+(E32+E21+Eg)×10^6 2π)/Γ)^2) +
     kF0',MF-F1+1→F1,MF-F1 1/(1 + 4 ((Δ+(E32+E21+E10+Eg)×10^6 2π)/Γ)^2)) a/Asat KroneckerDelta[MF, j] +
 kF2',MF-F1+1→F1,MF-F1 (a/Asat 1/(1 + 4 ((Δ+(E32+Eg)×10^6 2π)/Γ)^2) + 1)
  KroneckerDelta[MF, j - (2 F1 + 1 + 2 F2 + 1 + 2 F0' + 1 + 2 F1' + 1 + 2)]
 + kF2',MF-F1→F1,MF-F1 KroneckerDelta[MF, j - (2 F1 + 1 + 2 F2 + 1 + 2 F0' + 1 + 2 F1' + 1 + 1)] +
 kF2',MF-F1-1→F1,MF-F1 KroneckerDelta[MF, j - (2 F1 + 1 + 2 F2 + 1 + 2 F0' + 1 + 2 F1' + 1 + 0)] +
```

```
k_{F1',M_F-F1+1→F1,M_F-F1} ( a/A_sat 1/(1+4((Δ+(E32+E21+Eg)×10^6 2π)/Γ)^2) +1)
 KroneckerDelta[M_F, j-(2F1+1+2F2+1+2F0'+1+1)] +
k_{F1',M_F-F1→F1,M_F-F1} KroneckerDelta[M_F, j-(2F1+1+2F2+1+2F0'+1+0)] +
k_{F1',M_F-F1-1→F1,M_F-F1} KroneckerDelta[M_F, j-(2F1+1+2F2+1+2F0'+1-1)] +

k_{F0',M_F-F1+1→F1,M_F-F1} ( a/A_sat 1/(1+4((Δ+(E32+E21+E10+Eg)×10^6 2π)/Γ)^2) +1)
 KroneckerDelta[M_F, j-(2F1+1+2F2+1+0)] +
k_{F0',M_F-F1→F1,M_F-F1} KroneckerDelta[M_F, j-(2F1+1+2F2+1-1)] +
k_{F0',M_F-F1-1→F1,M_F-F1} KroneckerDelta[M_F, j-(2F1+1+2F2+1-2)] -

( k_{F3',M_F-(2F1+1+F2)+1→F2,M_F-(2F1+1+F2)} 1/(1+4(Δ/Γ)^2) + k_{F2',M_F-(2F1+1+F2)+1→F2,M_F-(2F1+1+F2)} 1/(1+4((Δ+E32×10^6 2π)/Γ)^2) +
  k_{F1',M_F-(2F1+1+F2)+1→F2,M_F-(2F1+1+F2)} 1/(1+4((Δ+(E32+E21)×10^6 2π)/Γ)^2) ) a/A_sat KroneckerDelta[M_F, j] +

k_{F3',M_F+1-(2F1+1+F2)→F2,M_F-(2F1+1+F2)} ( a/A_sat 1/(1+4(Δ/Γ)^2) +1)
 KroneckerDelta[M_F, j-(2F2+1+2F0'+1+2F1'+1+2F2'+1+2)] +
k_{F3',M_F-(2F1+1+F2)→F2,M_F-(2F1+1+F2)} KroneckerDelta[M_F, j-(2F2+1+2F0'+1+2F1'+1+2F2'+1+1)] +
k_{F3',M_F-1-(2F1+1+F2)→F2,M_F-(2F1+1+F2)} KroneckerDelta[M_F, j-(2F2+1+2F0'+1+2F1'+1+2F2'+1+0)] +

k_{F2',M_F+1-(2F1+1+F2)→F2,M_F-(2F1+1+F2)} ( a/A_sat 1/(1+4((Δ+E32×10^6 2π)/Γ)^2) +1)
 KroneckerDelta[M_F, j-(2F2+1+2F0'+1+2F1'+1+1)] +
k_{F2',M_F-(2F1+1+F2)→F2,M_F-(2F1+1+F2)} KroneckerDelta[M_F, j-(2F2+1+2F0'+1+2F1'+1+0)] +
k_{F2',M_F-(2F1+1+F2)-1→F2,M_F-(2F1+1+F2)} KroneckerDelta[M_F, j-(2F2+1+2F0'+1+2F1'+1-1)] +

k_{F1',M_F+1-(2F1+1+F2)→F2,M_F-(2F1+1+F2)} ( a/A_sat 1/(1+4((Δ+(E32+E21)×10^6 2π)/Γ)^2) +1)
 KroneckerDelta[M_F, j-(2F2+1+2F0'+1+0)] +
k_{F1',M_F-(2F1+1+F2)→F2,M_F-(2F1+1+F2)} KroneckerDelta[M_F, j-(2F2+1+2F0'+1-1)] +
k_{F1',M_F-1-(2F1+1+F2)→F2,M_F-(2F1+1+F2)} KroneckerDelta[M_F, j-(2F2+1+2F0'+1-2)],
{M_F, 0, 2F1+1+2F2+1+2F0'+1+2F1'+1+2F2'+1+2F3'},
{j, 0, 2F1+1+2F2+1+2F0'+1+2F1'+1+2F2'+1+2F3'}];
```

- **Calculating the excited state matrix**

```
Mx2 = Table[

 -(k_{F0', M_F-(2 F1+1+2 F2+1+F0')→F1, M_F-(2 F1+1+2 F2+1+F0')-1
      (1 + a/A_sat 1/(1 + 4 (1/Γ (Δ + (E32 + E21 + E10 + Eg) * 10^6 2 π))^2)) +
    k_{F0', M_F-(2 F1+1+2 F2+1+F0')→F1, M_F-(2 F1+1+2 F2+1+F0') + k_{F0', M_F-(2 F1+1+2 F2+1+F0')→F1, M_F-(2 F1+1+2 F2+1+F0')+1)
  KroneckerDelta[M_F, j]
 + k_{F0', M_F-(2 F1+1+2 F2+1+F0')→F1, M_F-(2 F1+1+2 F2+1+F0')-1  a/A_sat
  1/(1 + 4 (1/Γ (Δ + (E32 + E21 + E10 + Eg) * 10^6 2 π))^2) KroneckerDelta[M_F - (2 F1 + 1 + 2 F2 + 1), j] -
 (k_{F1', M_F-(2 F1+1+2 F2+1+2 F0'+1+F1')→F2, M_F-(2 F1+1+2 F2+1+2 F0'+1+F1')-1
      (1 + a/A_sat 1/(1 + 4 (1/Γ (Δ + (E32 + E21) * 10^6 2 π))^2)) +
    k_{F1', M_F-(2 F1+1+2 F2+1+2 F0'+1+F1')→F2, M_F-(2 F1+1+2 F2+1+2 F0'+1+F1') +
    k_{F1', M_F-(2 F1+1+2 F2+1+2 F0'+1+F1')→F2, M_F-(2 F1+1+2 F2+1+2 F0'+1+F1')+1 +
    k_{F1', M_F-(2 F1+1+2 F2+1+2 F0'+1+F1')→F1, M_F-(2 F1+1+2 F2+1+2 F0'+1+F1')-1
      (1 + a/A_sat 1/(1 + 4 (1/Γ (Δ + (E32 + E21 + Eg) * 10^6 2 π))^2)) +
    k_{F1', M_F-(2 F1+1+2 F2+1+2 F0'+1+F1')→F1, M_F-(2 F1+1+2 F2+1+2 F0'+1+F1') +
    k_{F1', M_F-(2 F1+1+2 F2+1+2 F0'+1+F1')→F1, M_F-(2 F1+1+2 F2+1+2 F0'+1+F1')+1) KroneckerDelta[M_F, j]
 + k_{F1', M_F-(2 F1+1+2 F2+1+2 F0'+1+F1')→F2, M_F-(2 F1+1+2 F2+1+2 F0'+1+F1')-1  a/A_sat
  1/(1 + 4 (1/Γ (Δ + (E32 + E21) * 10^6 2 π))^2) KroneckerDelta[M_F - (2 F2 + 1 + 2 F0' + 1), j] +
 k_{F1', M_F-(2 F1+1+2 F2+1+2 F0'+1+F1')→F1, M_F-(2 F1+1+2 F2+1+2 F0'+1+F1')-1  a/A_sat
  1/(1 + 4 (1/Γ (Δ + (E32 + E21 + Eg) * 10^6 2 π))^2) KroneckerDelta[M_F - (2 F1 + 1 + 2 F2 + 1 + 2 F0' + 1 + 1), j] -
 (k_{F2', M_F-(2 F1+1+2 F2+1+2 F0'+1+2 F1'+1+F2')→F2, M_F-(2 F1+1+2 F2+1+2 F0'+1+2 F1'+1+F2')-1
      (1 + a/A_sat 1/(1 + 4 (1/Γ (Δ + E32 * 10^6 2 π))^2)) +
    k_{F2', M_F-(2 F1+1+2 F2+1+2 F0'+1+2 F1'+1+F2')→F2, M_F-(2 F1+1+2 F2+1+2 F0'+1+2 F1'+1+F2') +
    k_{F2', M_F-(2 F1+1+2 F2+1+2 F0'+1+2 F1'+1+F2')→F2, M_F-(2 F1+1+2 F2+1+2 F0'+1+2 F1'+1+F2')+1 +
    k_{F2', M_F-(2 F1+1+2 F2+1+2 F0'+1+2 F1'+1+F2')→F1, M_F-(2 F1+1+2 F2+1+2 F0'+1+2 F1'+1+F2')-1
      (1 + a/A_sat 1/(1 + 4 (1/Γ (Δ + (E32 + Eg) * 10^6 2 π))^2)) +
    k_{F2', M_F-(2 F1+1+2 F2+1+2 F0'+1+2 F1'+1+F2')→F1, M_F-(2 F1+1+2 F2+1+2 F0'+1+2 F1'+1+F2') +
    k_{F2', M_F-(2 F1+1+2 F2+1+2 F0'+1+2 F1'+1+F2')→F1, M_F-(2 F1+1+2 F2+1+2 F0'+1+2 F1'+1+F2')+1) KroneckerDelta[M_F, j]
 + k_{F2', M_F-(2 F1+1+2 F2+1+2 F0'+1+2 F1'+1+F2')→F2, M_F-1-(2 F1+1+2 F2+1+2 F0'+1+2 F1'+1+F2')  a/A_sat
  1/(1 + 4 (1/Γ (Δ + E32 * 10^6 2 π))^2) KroneckerDelta[M_F - (2 F2 + 1 + 2 F0' + 1 + 2 F1' + 1 + 1), j]
 + k_{F2', M_F-(2 F1+1+2 F2+1+2 F0'+1+2 F1'+1+F2')→F1, M_F-1-(2 F1+1+2 F2+1+2 F0'+1+2 F1'+1+F2')  a/A_sat
  1/(1 + 4 (1/Γ (Δ + (E32 + Eg) * 10^6 2 π))^2)
```

```
KroneckerDelta[Mp - (2 F1 + 1 + 2 F2 + 1 + 2 F0' + 1 + 2 F1' + 1 + 2), j] -
 (k[F3', Mp-(2 F1+1+2 F2+1+2 F0'+1+2 F1'+1+2 F2'+1+F3')->F2, Mp-(2 F1+1+2 F2+1+2 F0'+1+2 F1'+1+2 F2'+1+F3') - 1
    (1 + a/Asat 1/(1 + 4 (Δ/Γ)^2))
  + k[F3', Mp-(2 F1+1+2 F2+1+2 F0'+1+2 F1'+1+2 F2'+1+F3')->F2, Mp-(2 F1+1+2 F2+1+2 F0'+1+2 F1'+1+2 F2'+1+F3') +
   k[F3', Mp-(2 F1+1+2 F2+1+2 F0'+1+2 F1'+1+2 F2'+1+F3')->F2, Mp-(2 F1+1+2 F2+1+2 F0'+1+2 F1'+1+2 F2'+1+F3')+1])
 KroneckerDelta[Mp, j] +
 k[F3', Mp-(2 F1+1+2 F2+1+2 F0'+1+2 F1'+1+2 F2'+1+F3')->F2, Mp-(2 F1+1+2 F2+1+2 F0'+1+2 F1'+1+2 F2'+1+F3')-1
  a/Asat 1/(1 + 4 (Δ/Γ)^2) KroneckerDelta[Mp - (2 F2 + 1 + 2 F0' + 1 + 2 F1' + 1 + 2 F2' + 1 + 2), j],

{Mp, 0, 2 F1 + 1 + 2 F2 + 1 + 2 F0' + 1 + 2 F1' + 1 + 2 F2' + 1 + 2 F3'},
{j, 0, 2 F1 + 1 + 2 F2 + 1 + 2 F0' + 1 + 2 F1' + 1 + 2 F2' + 1 + 2 F3')];
```

■ Calculating the matrix

```
Mx = Mx1 + Mx2;
```

Checking the matrix

A good check to make sure everything is in the right place is the columns should sum to zero, as checked below

```
Do[Print[Sum[Transpose[Mx][[i, j]], {j, 1, 2 (F1 + F2 + F0' + F1' + F2' + F3' + 3)}] // Simplify],
  {i, 1, 2 (F1 + F2 + F0' + F1' + F2' + F3' + 3)}] // Chop
```

NDSolve

```
<< Graphics`Graphics`

<< Graphics`Legend`

<< Graphics`MultipleListPlot`
```

Defining variables and setting boundary conditions

There is some duplication here from the Matrix section of the code, but it is often useful to check to make sure Mathematica has not reassigned values at some point.

```
{F1, F2, F0', F1', F2', F3'}
```

```
{1, 2, 0, 1, 2, 3}
```

```
{E32, E21, E10}
```

```
{267, 157, 72}
```

```
E31 = E32 + E21
```

```
424
```

```
n = 2 F1 + 1 + 2 F2 + 1 + 2 F0' + 1 + 2 F1' + 1 + 2 F2' + 1 + 2 F3' + 1
```

```
24
```

```
animax = (-kF3',F2-1→F2,F2 + kF3',F2+1→F2,F2) * (2 F2 + 1) / (2 F1 + 1 + 2 F2 + 1)
```

$$\frac{1\,750\,000\,000}{81}$$

```
bcond
```

$$\left\{\frac{1}{8}, \frac{1}{8}, \frac{1}{8}, \frac{1}{8}, \frac{1}{8}, \frac{1}{8}, \frac{1}{8}, \frac{1}{8}, 0, 0, 0, 0, 0, 0, 0, 0, 0, 0, 0, 0, 0, 0, 0, 0, 0\right\}$$

At t=0, the population of the F=2, mF=-2 state is 1/8 of the total.

```
ρF2,-F2[0]
```

$$\frac{1}{8}$$

The following steps get the matrix and boundary conditions into a format where the matrix equation can be solved.

```
Do[ρF2,MF[0] = 0, {MF, -F2, F2}]; Do[ρF2,MF[0] =., {MF, -F2, F2}]; Do[ρF1,MF[0] = 0, {MF, -F1, F1}];
Do[ρF1,MF[0] =., {MF, -F1, F1}]
```

```
gnd = Join[Table[ρF1,MF,g[0], {MF, -F1, F1}], Table[ρF2,MF,g[0], {MF, -F2, F2}]];
excited = Join[Table[ρF0',MF[0], {MF, -F0', F0'}], Table[ρF1',MF[0], {MF, -F1', F1'}],
  Table[ρF2',MF[0], {MF, -F2', F2'}], Table[ρF3',MF[0], {MF, -F3', F3'}]];
formbcond = Join[gnd, excited];
```

```
boundary = Table[formbcond[[i]] = bcond[[i]], {i, 1, n}];
```

```
gnd = Join[Table[ρF1,MF,g[t], {MF, -F1, F1}], Table[ρF2,MF,g[t], {MF, -F2, F2}]];
excited = Join[Table[ρF0',MF[t], {MF, -F0', F0'}], Table[ρF1',MF[t], {MF, -F1', F1'}],
  Table[ρF2',MF[t], {MF, -F2', F2'}], Table[ρF3',MF[t], {MF, -F3', F3'}]];
ρ[t] = Join[gnd, excited];
```

```
eqns = Mx.ρ[t];
```

```
equations = Table[∂t ρ[t][[i]] == eqns[[i]], {i, 1, n}];
```

```
{a = 0.01, Δ = -E32 * 10^6 * 2 π}
```

```
{0.01 , -534000.000  π}
```

```
Timing[sol0 = NDSolve[Join[equations, boundary], ρ[t], {t, 0, 2 * 10^2}];]
```

```
{0.133328  Second , Null }
```

```
a =.
```

```
Δ =.
```

This is just the number of states.

```
Length[ρ[t]]
```

```
24
```

Anisotropy calculation

Tabulating/checking line strengths

```
Table[k_{F3',mF+1→F2,mF} /. mF → i, {i, -4, 4}]
```

$$\left\{0, 0, \frac{200\,000\,000}{81}, \frac{200\,000\,000}{27}, \frac{400\,000\,000}{27}, \frac{2\,000\,000\,000}{81}, \frac{1\,000\,000\,000}{27}, 0, 0\right\}$$

```
Table[k_{F2',mF+1→F2,mF} /. mF → i, {i, -3, 3}]
```

$$\left\{0, \frac{500\,000\,000}{81}, \frac{250\,000\,000}{27}, \frac{250\,000\,000}{27}, \frac{500\,000\,000}{81}, 0, 0\right\}$$

```
Table[k_{F1',mF+1→F2,mF} /. mF → i, {i, -3, 3}]
```

$$\left\{0, \frac{100\,000\,000}{27}, \frac{50\,000\,000}{27}, \frac{50\,000\,000}{81}, 0, 0, 0\right\}$$

```
Table[k_{F3',mF-1→F2,mF} /. mF → i, {i, -4, 4}]
```

$$\left\{0, 0, \frac{1\,000\,000\,000}{27}, \frac{2\,000\,000\,000}{81}, \frac{400\,000\,000}{27}, \frac{200\,000\,000}{27}, \frac{200\,000\,000}{81}, 0, 0\right\}$$

```
Table[k_{F2',mF-1→F2,mF} /. mF → i, {i, -3, 3}]
```

$$\left\{0, 0, \frac{500\,000\,000}{81}, \frac{250\,000\,000}{27}, \frac{250\,000\,000}{27}, \frac{500\,000\,000}{81}, 0\right\}$$

```
Table[k_{F1',mF-1→F2,mF} /. mF → i, {i, -3, 3}]
```

$$\left\{0, 0, 0, \frac{50\,000\,000}{81}, \frac{50\,000\,000}{27}, \frac{100\,000\,000}{27}, 0\right\}$$

▪ Anisotropy

```
ani0 =
  Sum_{mF=-F2}^{F2} ( k_{F3', mF+1->F2, mF}
      (ρ[t][[mF + F2 + 1 + 2 F1 + 1]] -
        ρ[t][[(mF + 1) + F2 + 1 + 2 F1 + 1 + 2 F2 + 1 + 2 F0' + 1 + 2 F1' + 1 + 2 F2' + 1 + 1]]) -
     k_{F3', mF-1->F2, mF}
      (ρ[t][[mF + F2 + 1 + 2 F1 + 1]] -
        ρ[t][[(mF - 1) + F2 + 1 + 2 F1 + 1 + 2 F2 + 1 + 2 F0' + 1 + 2 F1' + 1 + 2 F2' + 1 + 1]]) );

ani-E32 =
  Sum_{mF=-F2}^{F2} ( k_{F2', mF+1->F2, mF}
      (ρ[t][[mF + F2 + 1 + 2 F1 + 1]] - ρ[t][[(mF + 1) + F2 + 1 + 2 F1 + 1 + 2 F2 + 1 + 2 F0' + 1 + 2 F1' + 1]]) -
     k_{F2', mF-1->F2, mF}
      (ρ[t][[mF + F2 + 1 + 2 F1 + 1]] - ρ[t][[(mF - 1) + F2 + 1 + 2 F1 + 1 + 2 F2 + 1 + 2 F0' + 1 + 2 F1' + 1]]) );

ani-E31 =
  Sum_{mF=-F2}^{F2} ( k_{F1', mF+1->F2, mF} (ρ[t][[mF + F2 + 1 + 2 F1 + 1]] - ρ[t][[(mF + 1) + F2 + 1 + 2 F1 + 1 + 2 F2 + 1 + 2 F0' + 1 - 1]]) -
     k_{F1', mF-1->F2, mF} (ρ[t][[mF + F2 + 1 + 2 F1 + 1]] - ρ[t][[(mF - 1) + F2 + 1 + 2 F1 + 1 + 2 F2 + 1 + 2 F0' + 1 - 1]]) );

a =.
```

<ani> vs I/Isat

This section calculates the anisotropy which builds up over time as a function of the laser intensity (relative to Isat). The calculation is repeated for three laser detunings, i.e. tuned to F=2 -> F'=3 (Δ=0), F=2 -> F'=2 (Δ=E32), and F=2 -> F'=1 (Δ=E31).

```
{amin, amax, astep} = {0, 50, 1}
```

```
{0, 50, 1}
```

```
{amin2, amax2, astep2} = {0.05, 0.95, 0.05}
```

```
{0.05, 0.95, 0.05}
```

▪ Δ=0

```
Δ = 0; Block[{$MaxExtraPrecision = Infinity}, Do[
      sol0a = NDSolve[Join[equations, boundary], ρ[t], {t, 0, 3000 * 10^-6}];
      ani0,a = ani0 /. sol0a;
  , {a, amin, amax, astep}]];
Block[{$MaxExtraPrecision = Infinity}, Do[
      sol0a = NDSolve[Join[equations, boundary], ρ[t], {t, 0, 3000 * 10^-6}];
      ani0,a = ani0 /. sol0a;
  , {a, amin2, amax2, astep2}]];
a = 0.01;
sol0a = NDSolve[Join[equations, boundary], ρ[t], {t, 0, 3000 * 10^-6}];
ani0,a = ani0 /. sol0a;
a = 0.1;
sol0a = NDSolve[Join[equations, boundary], ρ[t], {t, 0, 3000 * 10^-6}];
ani0,a = ani0 /. sol0a;
```

■ **Δ=-E32MHz**

```
Δ = -E32 * 10^6 * 2 π; Block[{$MaxExtraPrecision = Infinity}, Do[
      solE32_a = NDSolve[Join[equations, boundary], ρ[t], {t, 0, 300 * 10^-6}];
      ani-E32,a = ani-E32 /. solE32_a;
  , {a, amin, amax, astep}]];
Block[{$MaxExtraPrecision = Infinity}, Do[
       solE32_a = NDSolve[Join[equations, boundary], ρ[t], {t, 0, 300 * 10^-6}];
       ani-E32,a = ani-E32 /. solE32_a;
   , {a, amin2, amax2, astep2}]];
a = 0.01;
solE32_a = NDSolve[Join[equations, boundary], ρ[t], {t, 0, 300 * 10^-6}];
ani-E32,a = ani-E32 /. solE32_a;
a = 0.1;
solE32_a = NDSolve[Join[equations, boundary], ρ[t], {t, 0, 300 * 10^-6}];
ani-E32,a = ani-E32 /. solE32_a;
```

■ **Δ=-E31MHz**

```
Δ = -E31 * 10^6 * 2 π; Block[{$MaxExtraPrecision = Infinity}, Do[
      solE31_a = NDSolve[Join[equations, boundary], ρ[t], {t, 0, 300 * 10^-6}];
      ani-E31,a = ani-E31 /. solE31_a;
  , {a, amin, amax, astep}]];
Block[{$MaxExtraPrecision = Infinity}, Do[
       solE31_a = NDSolve[Join[equations, boundary], ρ[t], {t, 0, 300 * 10^-6}];
       ani-E31,a = ani-E31 /. solE31_a;
   , {a, amin2, amax2, astep2}]];
a = 0.01;
solE31_a = NDSolve[Join[equations, boundary], ρ[t], {t, 0, 300 * 10^-6}];
ani-E31,a = ani-E31 /. solE31_a;
a = 0.1;
solE31_a = NDSolve[Join[equations, boundary], ρ[t], {t, 0, 300 * 10^-6}];
ani-E31,a = ani-E31 /. solE31_a;
```

Analysis and Graphs

This section calculates the population of different sublevels for the laser detuning given below, as a function of time.

```
Δ = -E32 * 10^6 * 2 π
```

```
-534 000 000  π
```

```
pop8_0 = ρ[t][8]
pop7_0 = ρ[t][7]
pop6_0 = ρ[t][6]
pop5_0 = ρ[t][5]
pop4_0 = ρ[t][4]
pop3_0 = ρ[t][3]
pop2_0 = ρ[t][2]
pop1_0 = ρ[t][1]
```

```
Block[{$MaxExtraPrecision = Infinity},
  Do[population7_a = NDSolve[Join[equations, boundary], ρ[t], {t, 0, 3000 * 10^-5}];
   pop7_0,a = pop7_0 /. population7_a;, {a, amin, amax, astep}]];

Block[{$MaxExtraPrecision = Infinity},
  Do[population8_a = NDSolve[Join[equations, boundary], ρ[t], {t, 0, 3000 * 10^-5}];
   pop8_0,a = pop8_0 /. population8_a;, {a, amin, amax, astep}]];

Block[{$MaxExtraPrecision = Infinity},
  Do[population6_a = NDSolve[Join[equations, boundary], ρ[t], {t, 0, 3000 * 10^-5}];
   pop6_0,a = pop6_0 /. population6_a;, {a, amin, amax, astep}]];

Block[{$MaxExtraPrecision = Infinity},
  Do[population5_a = NDSolve[Join[equations, boundary], ρ[t], {t, 0, 3000 * 10^-5}];
   pop5_0,a = pop5_0 /. population5_a;, {a, amin, amax, astep}]];
Block[{$MaxExtraPrecision = Infinity},
  Do[population4_a = NDSolve[Join[equations, boundary], ρ[t], {t, 0, 3000 * 10^-5}];
   pop4_0,a = pop4_0 /. population4_a;, {a, amin, amax, astep}]];
Block[{$MaxExtraPrecision = Infinity},
  Do[population3_a = NDSolve[Join[equations, boundary], ρ[t], {t, 0, 3000 * 10^-5}];
   pop3_0,a = pop3_0 /. population3_a;, {a, amin, amax, astep}]];

Block[{$MaxExtraPrecision = Infinity},
  Do[population2_a = NDSolve[Join[equations, boundary], ρ[t], {t, 0, 3000 * 10^-5}];
   pop2_0,a = pop2_0 /. population2_a;, {a, amin, amax, astep}]];
Block[{$MaxExtraPrecision = Infinity},
  Do[population1_a = NDSolve[Join[equations, boundary], ρ[t], {t, 0, 3000 * 10^-5}];
   pop1_0,a = pop1_0 /. population1_a;, {a, amin, amax, astep}]];
```

```
Block[{$MaxExtraPrecision = Infinity},
  Do[population6a = NDSolve[Join[equations, boundary], ρ[t], {t, 0, 3000*10^-5}];
   pop60,a = pop60 /. population6a;, {a, amin2, amax2, astep2}]];
Block[{$MaxExtraPrecision = Infinity},
  Do[population5a = NDSolve[Join[equations, boundary], ρ[t], {t, 0, 3000*10^-5}];

   pop50,a = pop50 /. population5a;, {a, amin2, amax2, astep2}]];
Block[{$MaxExtraPrecision = Infinity},
  Do[population4a = NDSolve[Join[equations, boundary], ρ[t], {t, 0, 3000*10^-5}];
   pop40,a = pop40 /. population4a;, {a, amin2, amax2, astep2}]];
Block[{$MaxExtraPrecision = Infinity},
  Do[population3a = NDSolve[Join[equations, boundary], ρ[t], {t, 0, 3000*10^-5}];
   pop30,a = pop30 /. population3a;, {a, amin2, amax2, astep2}]];
Block[{$MaxExtraPrecision = Infinity},
  Do[population2a = NDSolve[Join[equations, boundary], ρ[t], {t, 0, 3000*10^-5}];
   pop20,a = pop20 /. population2a;, {a, amin2, amax2, astep2}]];
Block[{$MaxExtraPrecision = Infinity},
  Do[population1a = NDSolve[Join[equations, boundary], ρ[t], {t, 0, 3000*10^-5}];
   pop10,a = pop10 /. population1a;, {a, amin2, amax2, astep2}]];


Block[{$MaxExtraPrecision = Infinity},
  Do[population7a = NDSolve[Join[equations, boundary], ρ[t], {t, 0, 3000*10^-5}];
   pop70,a = pop70 /. population7a;, {a, amin2, amax2, astep2}]];

Block[{$MaxExtraPrecision = Infinity},
  Do[population8a = NDSolve[Join[equations, boundary], ρ[t], {t, 0, 3000*10^-5}];
   pop80,a = pop80 /. population8a;, {a, amin2, amax2, astep2}]];

population7a = NDSolve[Join[equations, boundary], ρ[t], {t, 0, 3000*10^-5}];
population8a = NDSolve[Join[equations, boundary], ρ[t], {t, 0, 3000*10^-5}];
population6a = NDSolve[Join[equations, boundary], ρ[t], {t, 0, 3000*10^-5}];
population5a = NDSolve[Join[equations, boundary], ρ[t], {t, 0, 3000*10^-5}];
population4a = NDSolve[Join[equations, boundary], ρ[t], {t, 0, 3000*10^-5}];
population3a = NDSolve[Join[equations, boundary], ρ[t], {t, 0, 3000*10^-5}];
population2a = NDSolve[Join[equations, boundary], ρ[t], {t, 0, 3000*10^-5}];
population1a = NDSolve[Join[equations, boundary], ρ[t], {t, 0, 3000*10^-5}];
```

Normalisation:

```
pop7_0,a = pop7_0 /. population7_a;
pop8_0,a = pop8_0 /. population8_a;
pop6_0,a = pop6_0 /. population6_a;
pop5_0,a = pop5_0 /. population5_a;
pop4_0,a = pop4_0 /. population4_a;
pop3_0,a = pop3_0 /. population3_a;
pop2_0,a = pop2_0 /. population2_a;
pop1_0,a = pop1_0 /. population1_a;
```

Sample graph:

```
Plot[Evaluate[{pop8_0,.1, pop7_0,.1, pop6_0,.1, pop5_0,.1, pop4_0,.1 , pop3_0,.1, pop2_0,.1, pop1_0,.1}],
 {t, 0, 10*10^(-6)},
 PlotStyle→{Hue[0.8], Hue[0.7], Hue[0.6], Hue[0.5], Hue[0.4], Hue[0.3], Hue[0.2], Hue[0.1]}]
```

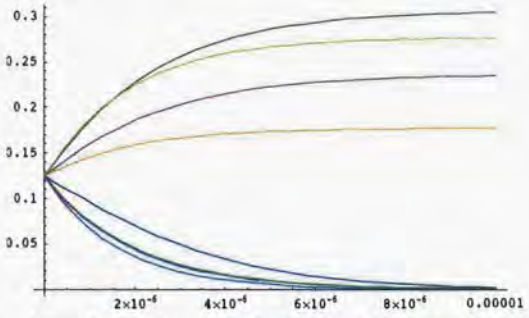

The population of the various sublevels of the excited state is put in tabular format for export into data files.

```
Pop22 = Table[{t, pop8_0,.1}, {t, 0, 10*10^(-6), 10.0*10^(-8)}];
Pop21 = Table[{t, pop7_0,.1}, {t, 0, 10*10^(-6), 10.0*10^(-8)}];
Pop20 = Table[{t, pop6_0,.1}, {t, 0, 10*10^(-6), 10.0*10^(-8)}];
Pop2minus1 = Table[{t, pop5_0,.1}, {t, 0, 10*10^(-6), 10.0*10^(-8)}];
Pop2minus2 = Table[{t, pop4_0,.1}, {t, 0, 10*10^(-6), 10.0*10^(-8)}];
Pop11 = Table[{t, pop3_0,.1}, {t, 0, 10*10^(-6), 10.0*10^(-8)}];
Pop10 = Table[{t, pop2_0,.1}, {t, 0, 10*10^(-6), 10.0*10^(-8)}];
Pop1minus1 = Table[{t, pop1_0,.1}, {t, 0, 10*10^(-6), 10.0*10^(-8)}];
```

These commands all export the data to files. The location for export should be modified by future users of this code.

```
SetDirectory["/export/home/dph3mh"]
FileOut[answers_] := OpenWrite[answers]
"/export/home/dph3mh"
Export["Rb8722Delta31.CSV", Pop22];

datafile = FileOut["Rb8722Delta31.txt"];
Do[Print[TableForm[Pop22]]];
WriteString[datafile, Pop22]
Close[datafile];

SetDirectory["/export/home/dph3mh"]
FileOut[answers_] := OpenWrite[answers]
"/export/home/dph3mh"
Export["Rb8721Delta31.CSV", Pop21];

datafile = FileOut["Rb8721Delta31.txt"];
Do[Print[TableForm[Pop21]]];
WriteString[datafile, Pop21]
Close[datafile];

SetDirectory["/export/home/dph3mh"]
FileOut[answers_] := OpenWrite[answers]
"/export/home/dph3mh"
Export["Rb8720Delta31.CSV", Pop20];

datafile = FileOut["Rb8720Delta31.txt"];
Do[Print[TableForm[Pop20]]];
WriteString[datafile, Pop20]
Close[datafile];

SetDirectory["/export/home/dph3mh"]
FileOut[answers_] := OpenWrite[answers]
"/export/home/dph3mh"
Export["Rb872-1Delta31.CSV", Pop2minus1];

datafile = FileOut["Rb872-1Delta31.txt"];
Do[Print[TableForm[Pop2minus1]]];
WriteString[datafile, Pop2minus1]
Close[datafile];
```

```
SetDirectory["/export/home/dph3mh"]
FileOut[answers_] := OpenWrite[answers]
"/export/home/dph3mh"
Export["Rb872-2Delta31.CSV", Pop2minus2];

datafile = FileOut["Rb872-2Delta31.txt"];
Do[Print[TableForm[Pop2minus2]]];
WriteString[datafile, Pop2minus2]
Close[datafile];
SetDirectory["/export/home/dph3mh"]
FileOut[answers_] := OpenWrite[answers]
"/export/home/dph3mh" .
Export["Rb8711Delta32.CSV", Pop11];

datafile = FileOut["Rb8711Delta32.txt"];
Do[Print[TableForm[Pop11]]];
WriteString[datafile, Pop11]
Close[datafile];


SetDirectory["/export/home/dph3mh"]
FileOut[answers_] := OpenWrite[answers]
"/export/home/dph3mh"
Export["Rb8710Delta32.CSV", Pop10];

datafile = FileOut["Rb8710Delta32.txt"];
Do[Print[TableForm[Pop10]]];
WriteString[datafile, Pop10]
Close[datafile];

SetDirectory["/export/home/dph3mh"]
FileOut[answers_] := OpenWrite[answers]
"/export/home/dph3mh"
Export["Rb871-1Delta32.CSV", Pop1minus1];

datafile = FileOut["Rb871-1Delta32.txt"];
Do[Print[TableForm[Pop1minus1]]];
WriteString[datafile, Pop1minus1]
Close[datafile];
```

▪ Plot Ani vs Time

```
Plot[Evaluate[1/animax {ani0,0.35, ani-E32,0.35, ani-E31,0.35, ani0,1, ani-E32,1, ani-E31,1}],
  {t, 0, 3*10^-6}, PlotRange→{-0.2, 0.5},
  PlotStyle→{{Hue[0.1], Dashing[{0.02, 0.02}]}, {Hue[0.6], Dashing[{0.02, 0.02}]},
    {Hue[0.9], Dashing[{0.02, 0.02}]}, Hue[0.1], Hue[0.6], Hue[0.9]},
  PlotLegend→{"Δ=0,I/Isat=0.35", "Δ=-267,I/Isat=0.35", "Δ=-424,I/Isat=0.35",
    "Δ=0,I/Isat=1", "Δ=-267,I/Isat=1", "Δ=-424,I/Isat=1"}, LegendPosition→{1.1, -.4},
  LegendSize→{0.82, 0.5}, LegendShadow→{0, 0}, AxesLabel→{"Time/s", "Ani(t)"}];
```

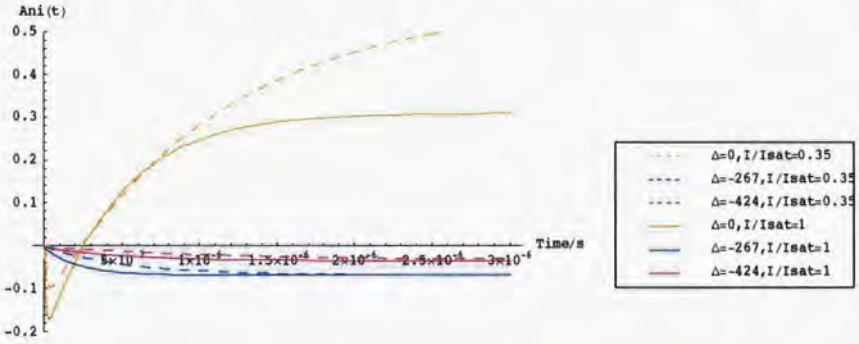

▪ Data

```
data0 = Table[Flatten[{a, ani0,a /. t→3*10^-6}], {a, amin, amax, astep}];
data267 = Table[Flatten[{a, ani-E32,a /. t→3*10^-6}], {a, amin, amax, astep}];
data424 = Table[Flatten[{a, ani-E31,a /. t→3*10^-6}], {a, amin, amax, astep}];
data0Fine = Table[Flatten[{a, ani0,a /. t→3*10^-6}], {a, amin2, amax2, astep2}];
data267Fine = Table[Flatten[{a, ani-E32,a /. t→3*10^-6}], {a, amin2, amax2, astep2}];
data424Fine = Table[Flatten[{a, ani-E31,a /. t→3*10^-6}], {a, amin2, amax2, astep2}];
```

▪ Plot Final Anisitropy vs I/Isat

```
MultipleListPlot[{data0, data267, data424}, PlotJoined → {True, True, True},
  SymbolShape → {PlotSymbol[Triangle], PlotSymbol[Star], PlotSymbol[Triangle]},
  PlotStyle → {Hue[0.2], Hue[0.6], Hue[0.9]}, PlotRange → {1.1 Min[data267], 1.1 Max[data0]},
  AxesLabel -> {"I/Isat", "Final Anisotropy"}, PlotLegend → {"Δ=0", "Δ=-267", "Δ=-424"},
  LegendPosition → {.5, .15}, LegendSize → {0.3, 0.3}];
```

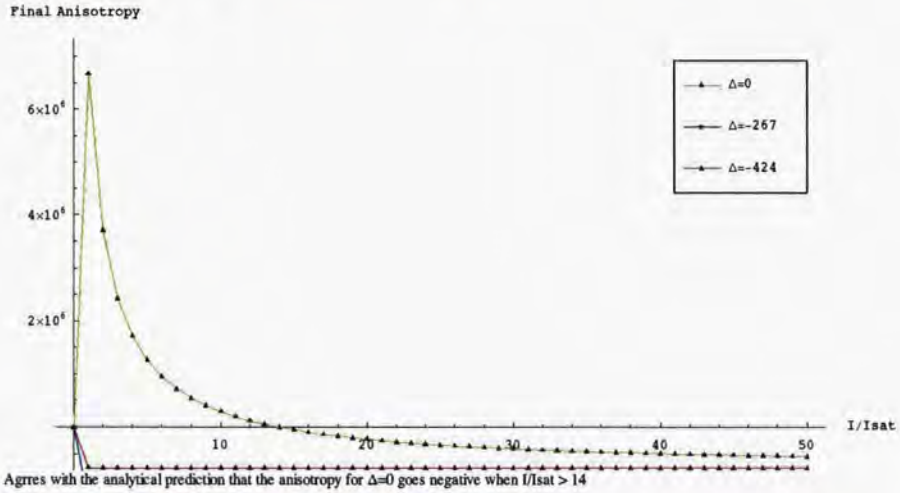

Agrres with the analytical prediction that the anisotropy for Δ=0 goes negative when I/Isat > 14

```
MultipleListPlot[{data0Fine, data267Fine, data424Fine}, PlotJoined → {True, True, True},
  SymbolShape → {PlotSymbol[Triangle], PlotSymbol[Star], PlotSymbol[Triangle]},
  PlotStyle → {Hue[0.2], Hue[0.6], Hue[0.9]}, PlotRange → {1.1 Min[data267Fine], 1.1 Max[data0Fine]},
  AxesLabel -> {"I/Isat", "Final Anisotropy"}, PlotLegend → {"Δ=0", "Δ=-267", "Δ=-424"},
  LegendPosition → {.6, .25}, LegendSize → {0.3, 0.3}];
```

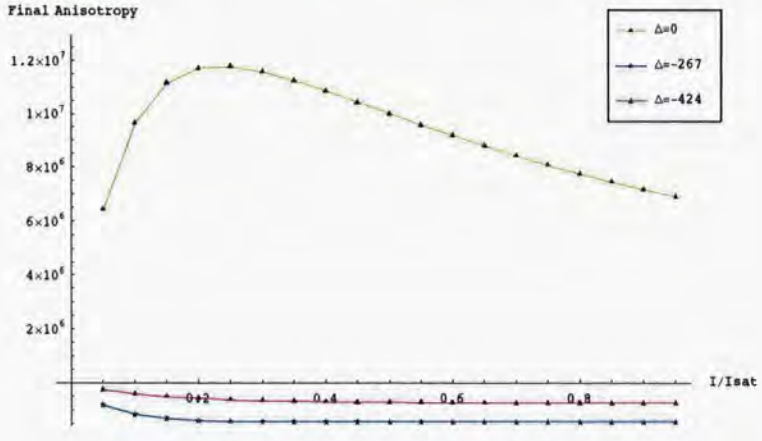

H(t)

Introduction

```
Clear[r, m, T, t]; kB =.
```

H(t) = G(t)×F(l) where $G(t) = \frac{m\,l^2}{k_B\,T\,t^3}\,\text{Exp}\left[-\frac{m\,l^2}{2\,k_B\,T\,t^2}\right]$ and $F(l) = \frac{1}{\pi\,(16\,r^2-4\,l^2)^{1/2}}$

Enter constants like mass, temperature, beam radius

```
m = 85 * 1.67 * 10^-27; T = 293; kB = 1.38 * 10^-23; r = .5 * 10^-3;
```

$$H = \text{Function}\left[t,\ \frac{-4\,t + \frac{e^{-\frac{2\,m\,r^2}{t^2\,T\,k_B}}\,\sqrt{2\,\pi}\,\text{Erfi}\left[\frac{\sqrt{2}\,\sqrt{m}\,r}{t\,\sqrt{T}\,\sqrt{k_B}}\right]\,(4\,m\,r^2+t^2\,T\,k_B)}{\sqrt{m}\,r\,\sqrt{T}\,\sqrt{k_B}}}{4\,t^2}\right];$$

Plots the time-of-flight weighting function for different beam radii.

```
r =.; Plot[{H[t] /. r → .5 * 10^-3, H[t] /. r → 1 * 10^-3, H[t] /. r → 0.25 * 10^-3}, {t, 10^-9, 10 * 10^-6}];
r = .5 * 10^-3;
```

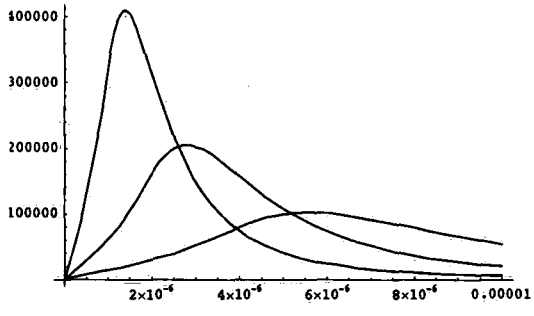

Now need to calulate product of H(t) and Anisotropy(t)

```
Plot[Evaluate[{ani0,1 * H[t]}], {t, 2 * 10^-9, 30 * 10^-6}]
```

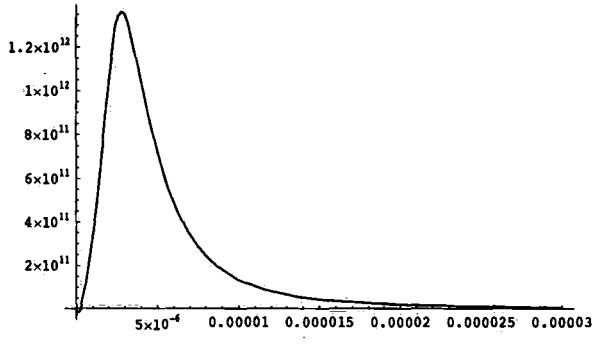

- Graphics -

<ani> vs I/Isat

We now look at the "average" anisotropy as a function of saturation.

```
avrg0 = Table[Flatten[{a, 1/animax NIntegrate[Evaluate[ani0,a H[t]], {t, 2*10^-9, tmax}]}],
    {a, amin, amax, astep}]; // Timing
avrg0fine = Table[Flatten[{a, 1/animax NIntegrate[Evaluate[ani0,a H[t]], {t, 2*10^-9, tmax}]}],
    {a, amin2, amax2, astep2}]; // Timing
```

```
{14.7994 Second , Null }
```

```
avrgE32 = Table[Flatten[{a, 1/animax NIntegrate[Evaluate[ani-E32,a H[t]], {t, 2*10^-9, tmax}]}],
    {a, amin, amax, astep}]; // Timing
avrgE32fine = Table[Flatten[{a, 1/animax NIntegrate[Evaluate[ani-E32,a H[t]], {t, 2*10^-9, tmax}]}],
    {a, amin2, amax2, astep2}]; // Timing
```

```
{4.44982 Second , Null }
```

```
avrgE31 = Table[Flatten[{a, 1/animax NIntegrate[Evaluate[ani-E31,a H[t]], {t, 2*10^-9, tmax}]}],
    {a, amin, amax, astep}]; // Timing
avrgE31fine = Table[Flatten[{a, 1/animax NIntegrate[Evaluate[ani-E31,a H[t]], {t, 2*10^-9, tmax}]}],
    {a, amin2, amax2, astep2}]; // Timing
```

```
{4.2165 Second , Null }
```

```
MultipleListPlot[{avrg0, avrgE32, avrgE31}, PlotJoined → {True, True, True},
  PlotLegend → {"Δ=0", "Δ=-E32", "Δ=-E31"}, AxesLabel → {"I/Isat", "<Ani>"},
  PlotStyle → {Hue[0.2], Hue[0.6], Hue[0.9]},
  SymbolShape → {PlotSymbol[Star], PlotSymbol[Star], PlotSymbol[Triangle]}];
```

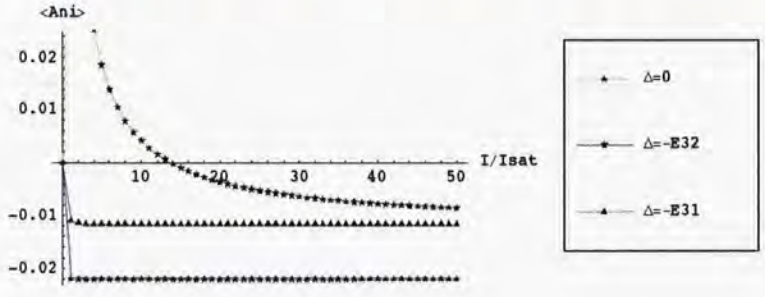

Dispersion Curve

- **Inputs**

```
x = Function[Δ, 2 Δ/Γ];
x
Function[Δ, 2 Δ/Γ]
Γ = Γ/(2 π 10^6) // N
5.89463
y = Function[Δ, 2 Δ/γ];
y
Function[Δ, 2 Δ/γ]
Plot[x[Δ]/(1 + x[Δ]^2), {Δ, -500, 100}]
```

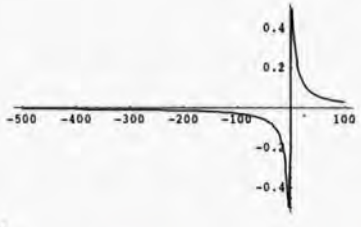


```
Δ =.;
Disp[a_] := (avrg0[[(a + 1), 2]] x[Δ]/(1 + x[Δ]^2) + avrgE32[[(a + 1), 2]] x[Δ + E32]/(1 + (x[Δ + E32])^2) +
  avrgE31[[(a + 1), 2]] x[Δ + E31]/(1 + (x[Δ + E31])^2) +
  (avrg0[[(a + 1), 2]] + avrgE32[[(a + 1), 2]]) 1/2 x[Δ + E32 * 0.5]/(1 + (x[Δ + E32 * 0.5])^2) +
  (avrgE32[[(a + 1), 2]] + avrgE31[[(a + 1), 2]]) 1/2 x[Δ + (E32 + E21 * 0.5)]/(1 + (x[Δ + (E32 + E21 * 0.5)])^2) +
  (avrg0[[(a + 1), 2]] + avrgE31[[(a + 1), 2]]) 1/2 x[Δ + (E31 * 0.5)]/(1 + (x[Δ + (E31 * 0.5)])^2));
```

```
DispBroad[a_] :=
 (avrg0[[(a + 1), 2]] y[Δ]/(1 + y[Δ]^2) + avrgE32[[(a + 1), 2]] y[Δ + E32]/(1 + (y[Δ + E32])^2) +
  avrgE31[[(a + 1), 2]] y[Δ + E31]/(1 + (y[Δ + E31])^2) +
  (avrg0[[(a + 1), 2]] + avrgE32[[(a + 1), 2]]) 1/2 y[Δ + E32 * 0.5]/(1 + (y[Δ + E32 * 0.5])^2) +
  (avrgE32[[(a + 1), 2]] + avrgE31[[(a + 1), 2]]) 1/2 y[Δ + (E32 + E21 * 0.5)]/(1 + (y[Δ + (E32 + E21 * 0.5)])^2) +
  (avrg0[[(a + 1), 2]] + avrgE31[[(a + 1), 2]]) 1/2 y[Δ + (E31 * 0.5)]/(1 + (y[Δ + (E31 * 0.5)])^2));

DispFine[a_] :=
 (avrg0fine[[(a/0.05), 2]] x[Δ]/(1 + x[Δ]^2) + avrgE32fine[[(a/0.05), 2]] x[Δ + E32]/(1 + (x[Δ + E32])^2) +
  avrgE31fine[[(a/0.05), 2]] x[Δ + E31]/(1 + (x[Δ + E31])^2) +
  (avrg0fine[[(a/0.05), 2]] + avrgE32fine[[(a/0.05), 2]]) 1/2 x[Δ + E32 * 0.5]/(1 + (x[Δ + E32 * 0.5])^2) +
  (avrgE32fine[[(a/0.05), 2]] + avrgE31fine[[(a/0.05), 2]]) 1/2 x[Δ + (E32 + E21 * 0.5)]/(1 + (x[Δ + (E32 + E21 * 0.5)])^2) +
  (avrg0fine[[(a/0.05), 2]] + avrgE31fine[[(a/0.05), 2]]) 1/2 x[Δ + (E31 * 0.5)]/(1 + (x[Δ + (E31 * 0.5)])^2));

DispBroadFine[a_] :=
 (avrg0fine[[(a/0.05), 2]] y[Δ]/(1 + y[Δ]^2) + avrgE32fine[[(a/0.05), 2]] y[Δ + E32]/(1 + (y[Δ + E32])^2) +
  avrgE31fine[[(a/0.05), 2]] y[Δ + E31]/(1 + (y[Δ + E31])^2) +
  (avrg0fine[[(a/0.05), 2]] + avrgE32fine[[(a/0.05), 2]]) 1/2 y[Δ + E32 * 0.5]/(1 + (y[Δ + E32 * 0.5])^2) +
  (avrgE32fine[[(a/0.05), 2]] + avrgE31fine[[(a/0.05), 2]]) 1/2 y[Δ + (E32 + E21 * 0.5)]/(1 + (y[Δ + (E32 + E21 * 0.5)])^2) +
  (avrg0fine[[(a/0.05), 2]] + avrgE31fine[[(a/0.05), 2]]) 1/2 y[Δ + (E31 * 0.5)]/(1 + (y[Δ + (E31 * 0.5)])^2));
```

■ **Graphics**

```
Plot[{Disp[1], Disp[2], Disp[3], Disp[4], Disp[5], Disp[6]}, {Δ, -500, 100},
 AxesLabel → {"Δ/2π.MHz", "<A> x[Δ]/(1+x[Δ]^2)"}, PlotRange → {-0.04, 0.04},
 PlotLegend → {"I/I_sat=1", "I/I_sat=2", "I/I_sat=3", "I/I_sat=4", "I/I_sat=5", "I/I_sat=6"},
 PlotStyle → {Hue[0.9], Hue[0.8], Hue[0.7], Hue[0.6], Hue[0.5], Hue[0.4]},
 LegendPosition → {1.1, -0.4}, LegendShadow → {0, 0}, PlotLabel → "87Rb F=2 → F'"]
```

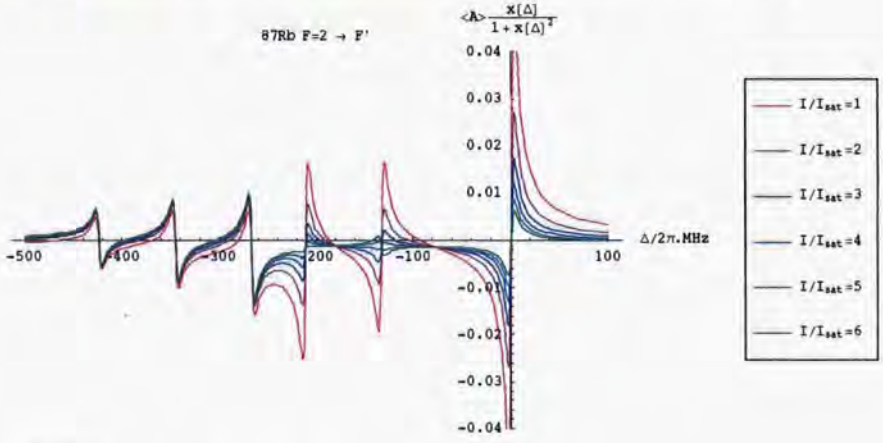

- Graphics -

```
Plot[Disp[30], {Δ, -500, 100}, AxesLabel → {"Δ/2π.MHz", "<A> x[Δ]/(1+x[Δ]^2)"}]
```

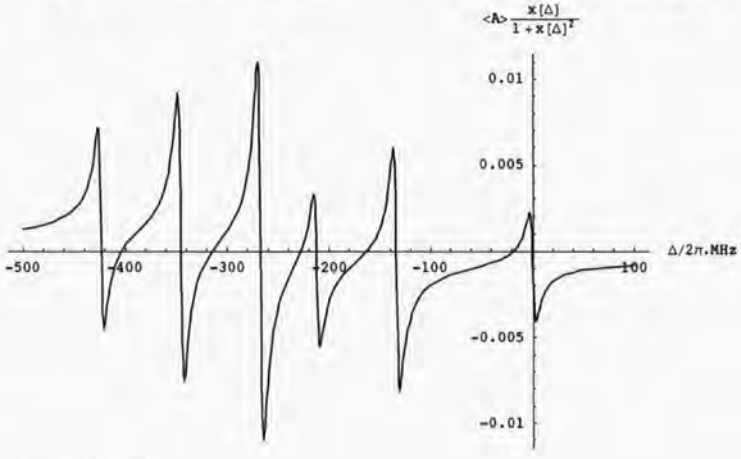

- Graphics -

```
Plot[DispFine[0.75], {Δ, -500, 100}, AxesLabel → {"Δ/2π.MHz", "<A> x[Δ]/(1+x[Δ]^2) "},
 PlotLabel → "87Rb F=2 → F'"]
```

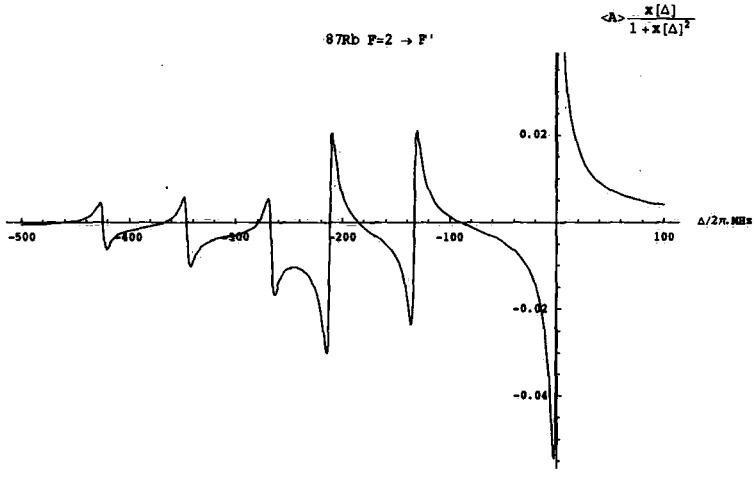


```
γ = 10;
Plot[DispBroadFine[0.75], {Δ, -500, 100}, AxesLabel → {"Δ/2π.MHz", "<A> x[Δ]/(1+x[Δ]^2) "},
 PlotLabel → "Broadened 87Rb F=2 → F'"]
```

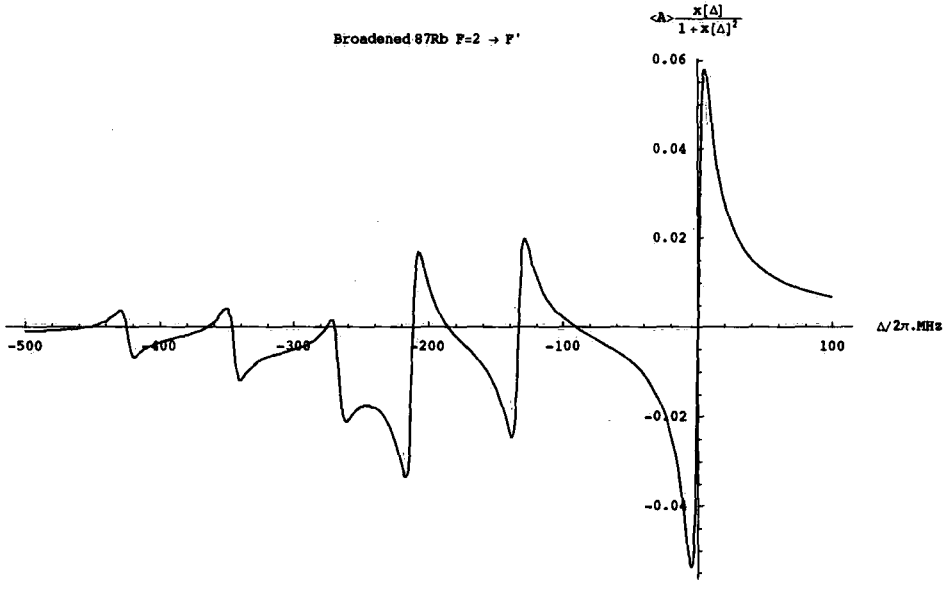

Line Broadening Mechanisms

This section illustrates the effects of different broadening mechanisms on the spectra.

Lorentzian Broadening

```
γ = 10;

Plot[{DispFine[0.75], DispBroadFine[0.75]}, {Δ, -500, 100},
 AxesLabel → {"Δ/2π.MHz", "<A> x[Δ]/(1+x[Δ]^2)"}, PlotStyle → {Hue[0.9], Hue[0.7]},
 PlotLegend → {"b=0", "b=4"}, LegendPosition → {1.1, -0.2}, LegendShadow → {0, 0},
 LegendSize → {0.4, 0.4}]
```

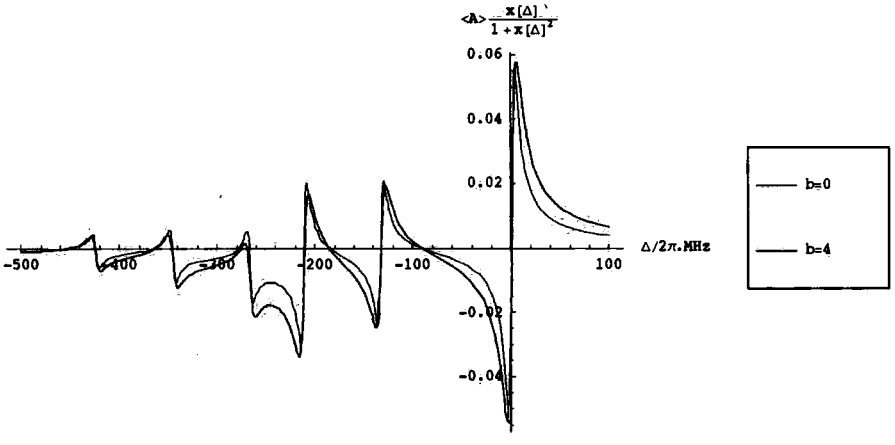

■ **Gaussian Broadening**

```
Gaussian[G_] := Table[Exp[-4 Log[2] (n / G)^2], {n, -10, 10}];

data = Table[DispFine[0.75], {Δ, - 500, 100}];

dataBroad = Table[DispFine[0.75], {Δ, - 490, 110}];

MultipleListPlot[
 {Max[ListConvolve[Gaussian[25], data, {-1, 1}]]/
   Max[ListConvolve[Gaussian[1], data, {-1, 1}]] ListConvolve[Gaussian[1], data, {-1, 1}],
  Max[ListConvolve[Gaussian[25], data, {-1, 1}]]/
   Max[ListConvolve[Gaussian[5], data, {-1, 1}]] ListConvolve[Gaussian[5], data, {-1, 1}],
  ListConvolve[Gaussian[25], data, {-1, 1}]}, PlotJoined → True,
 PlotRange → {1.1 Min[ListConvolve[Gaussian[25], data, {-1, 1}]],
   1.1 Max[ListConvolve[Gaussian[25], data, {-1, 1}]]}, SymbolShape → {None, None, None},
 PlotStyle → {Hue[0.9], Hue[0.7], Hue[0.5]},
 PlotLabel → "Dispersion curve after convolution with Gaussian of width G",
 PlotLegend → {"G = 1", "G = 5", "G = 25", "Lorentzian b=4"}, LegendShadow → {0, 0},
 LegendPosition → {1.1, -0.2}, LegendSize → {0.4, 0.4}];
```

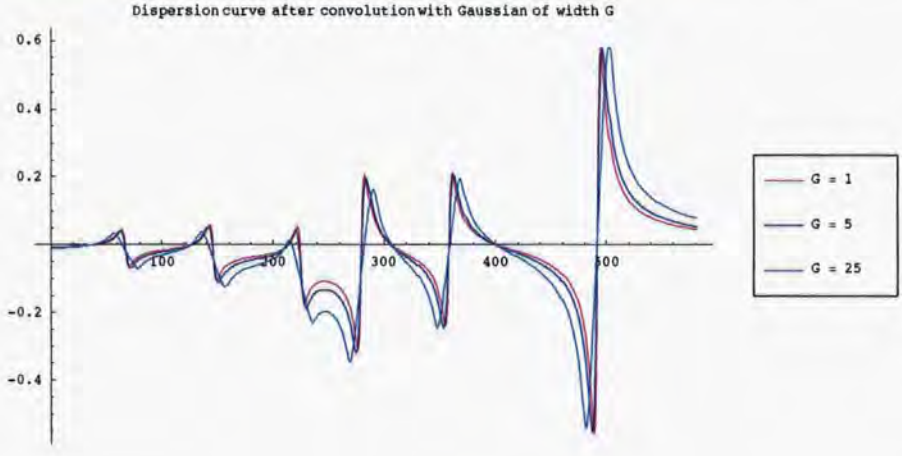

▪ Combination

```
γ = 12; dataBroad = Table[DispBroadFine[0.1], {Δ, - 490, 210}];
Broadened = ListConvolve[Gaussian[0.86], dataBroad, {-1, 1}];
ListPlot[Broadened, PlotJoined → True, PlotRange → {1.1 Min[Broadened], 1.1 Max[Broadened]}]
```

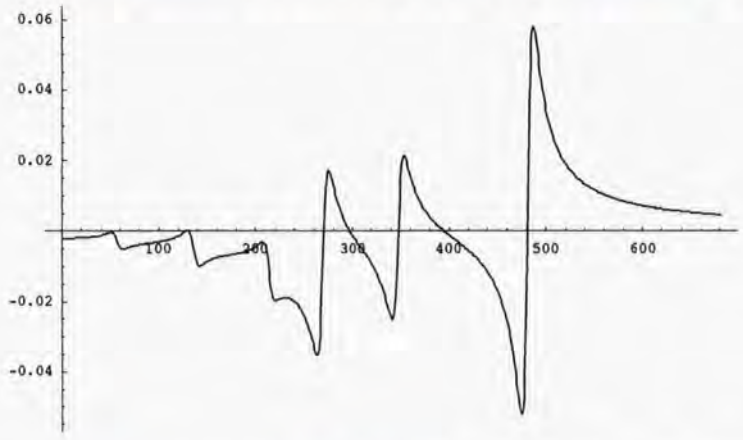


```
Theory = Table[{Δ, Broadened[[Δ + 480]]}, {Δ, -479, 200}];
```

Exports the theoretical plots to files.

```
SetDirectory["/export/home/dph3mh"]
FileOut[answers_] := OpenWrite[answers]
```

```
/export /home /dph3mh
```

```
Export["Rb87Cooltheory.CSV", Theory];
```

```
datafile = FileOut["Rb87Cooltheory.txt"];
Do[Print[TableForm[Theory]]];
WriteString[datafile, Theory]
Close[datafile];
```

Appendix D

Optical layout

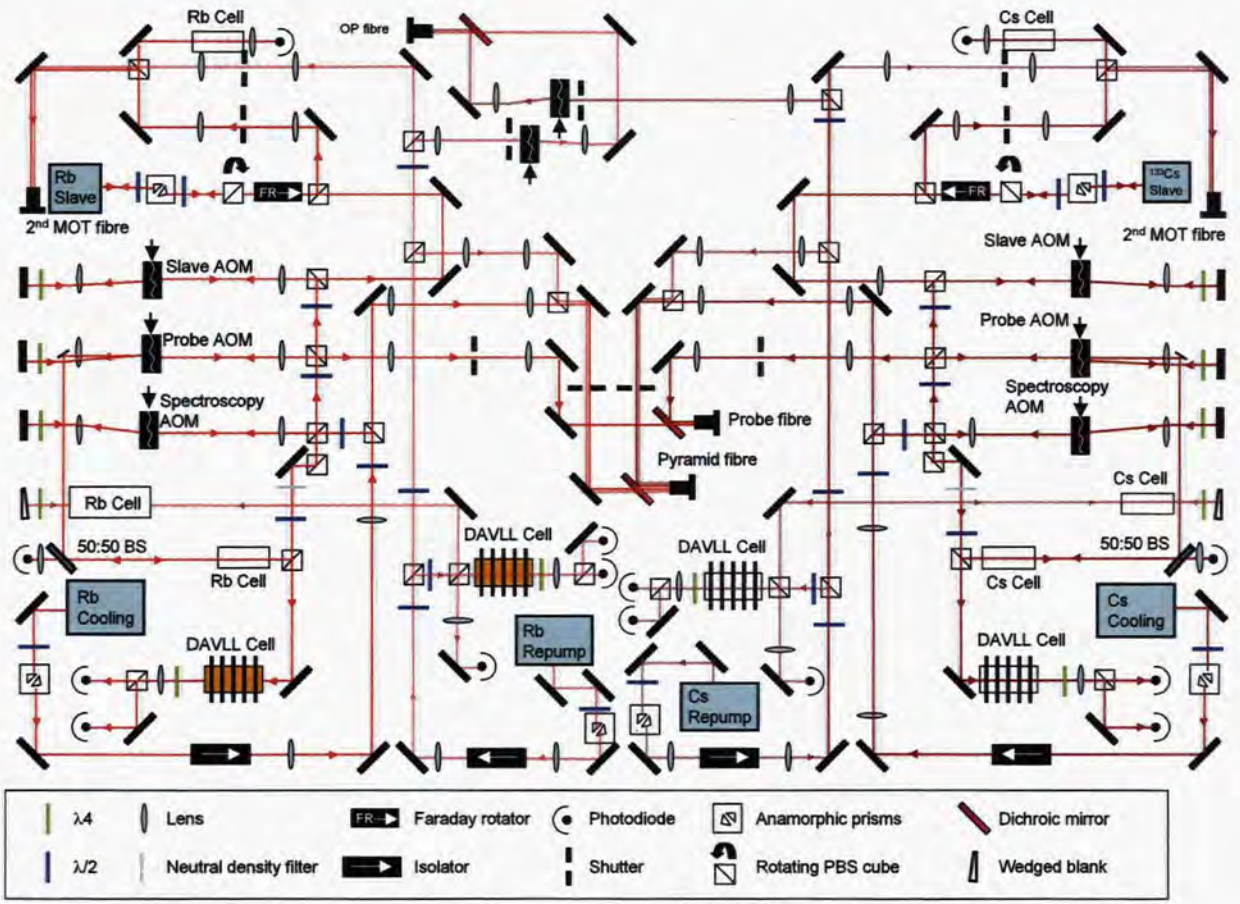

Figure D.1: Optical layout for Rb-Cs mixture experiment.

Bibliography

[1] K. B. Davis, M.-O. Mewes, M. R. Andrews, N. J. van Druten, D. S. Durfee, D. M. Kurn, and W. Ketterle, *Bose-Einstein Condensation in a Gas of Sodium Atoms*, Phys. Rev. Lett. **75**, 3969 (1995).

[2] M. R. Anderson, J. R. Ensher, M. R. Matthews, C. E. Wieman, and E. A. Cornell, *Observation of Bose-Einstein Condensation in a Dilute Atomic Vapor*, Science **269**, 198 (1995).

[3] B. DeMarco and D. S. Jin, *Onset of Fermi Degeneracy in a Trapped Atomic Gas*, Science **285**, 1703 (1999).

[4] C. C. Bradley, C. A. Sackett, J. J. Tollett, and R. G. Hulet, *Evidence of Bose-Einstein Condensation in an Atomic Gas with Attractive Interactions*, Phys. Rev. Lett. **75**, 1687 (1995).

[5] G. Roati, F. Riboli, G. Modugno, and M. Inguscio, *Fermi-Bose Quantum Degenerate ^{40}K-^{87}Rb Mixture with Attractive Interaction*, Phys. Rev. Lett. **89**, 150403 (2002).

[6] G. Modugno, M. Modugno, F. Riboli, G. Roati, and M. Inguscio, *Two Atomic Species Superfluid*, Phys. Rev. Lett. **89**, 190404 (2002).

[7] G. Roati, M. Zaccanti, C. D'Errico, J. Catani, M. Modugno, A. Simoni, M. Inguscio, and G. Modugno, *^{39}K Bose-Einstein Condensate with Tunable Interactions*, Phys. Rev. Lett. **99**, 010403 (2007).

[8] D. G. Fried, T. C. Killian, L. Willmann, D. Landuis, S. C. Moss, D. Kleppner, and T. J. Greytak, *Bose-Einstein Condensation of Atomic Hydrogen*, Phys. Rev. Lett. **81**, 3811 (1998).

[9] A. Robert, O. Sirjean, A. Browaeys, J. Poupard, S. Nowak, D. Boiron, C. I. Westbrook, and A. Aspect, *A Bose-Einstein Condensate of Metastable Atoms*, Science **292**, 461 (2001).

[10] Y. Takasu, K. Maki, K. Komori, T. Takano, K. Honda, M. Kumakura, T. Yabuzaki, and Y. Takahashi, *Spin-Singlet Bose-Einstein Condensation of Two-Electron Atoms*, Phys. Rev. Lett. **91**, 040404 (2003).

[11] T. Fukuhara, Y. Takasu, M. Kumakura, and Y. Takahashi, *Degenerate Fermi Gases of Ytterbium*, Phys. Rev. Lett. **98**, 030401 (2007).

[12] A. Griesmaier, J. Werner, S. Hensler, J. Stuhler, and T. Pfau, *Bose-Einstein Condensation of Chromium*, Phys. Rev. Lett. **94**, 160401 (2005).

[13] M.-O. Mewes, M. R. Andrews, D. M. Kurn, D. S. Durfee, C. G. Townsend, and W. Ketterle, *Output Coupler for Bose-Einstein Condensed Atoms*, Phys. Rev. Lett. **78**, 582 (1997).

[14] N. R. Claussen, *Dynamics of Bose-Einstein condensates near a Feshbach resonance in ^{85}Rb*, PhD thesis, University of Colorado, 2003.

[15] R. Wynar, R. S. Freeland, D. J. Han, C. Ryu, and D. J. Heinzen, *Molecules in a Bose-Einstein condensate*, Science **2000**, 1016 (2000).

[16] E. A. Donley, N. R. Claussen, S. T. Thompson, and C. E. Wieman, *Atom-Molecule coherence in a Bose-Einstein condensate*, Nature **417**, 529 (2002).

[17] K. E. Strecker, G. B. Partridge, A. G. Truscott, and R. G. Hulet, *Formation and propagation of matter-wave soliton trains*, Nature **417**, 150 (2002).

[18] L. Khaykovich, F. Schreck, G. Ferrari, T. Bourdel, J. Cubizolles, L. D. Carr, Y. Castin, and C. Salomon, *Formation of a Matter-Wave Bright Soliton*, Science **296**, 1290 (2002).

[19] H. Pu and N. P. Bigelow, *Properties of Two-Species Bose Condensates*, Phys. Rev. Lett. **80**, 1130 (1998).

[20] G. Modugno, G. Roati, F. Riboli, F. Ferlaino, R. J. Brecha, and M. Inguscio, *Collapse of a Degenerate Fermi Gas*, Science **297**, 2240 (2002).

[21] M. Lewenstein, L. Santos, M. A. Baranov, and H. Fehrmann, *Atomic Bose-Fermi Mixtures in an Optical Lattice*, Phys. Rev. Lett. **92**, 050401 (2004).

[22] K. M. Jones, E. Tiesinga, P. D. Lett, and P. S. Julienne, *Ultracold photoassociation spectroscopy: Long-range molecules and atomic scattering*, Rev. Mod. Phys. **78**, 483 (2006).

[23] T. Köhler, K. Góral, and P. S. Julienne, *Production of cold molecules via magnetically tunable Feshbach resonances*, Rev. Mod. Phys. **78**, 1311 (2006).

[24] L. Santos, G. V. Shlyapnikov, P. Zoller, and M. Lewenstein, *Bose-Einstein Condensation in Trapped Dipolar Gases*, Phys. Rev. Lett. **85**, 1791 (2000).

[25] D. DeMille, *Quantum Computation with Trapped Polar Molecules*, Phys. Rev. Lett. **88**, 067901 (2002).

[26] I. Bloch, M. Greiner, O. Mandel, T. W. Hänsch, and T. Esslinger, *Sympathetic cooling of ^{85}Rb and ^{87}Rb*, Phys. Rev. A **64**, 021402R (2001).

[27] S. B. Papp and C. E. Wieman, *Observation of Heteronuclear Feshbach Molecules from a ^{85}Rb-^{87}Rb Gas*, Phys. Rev. Lett. **97**, 180404 (2006).

[28] M. Anderlini, E. Courtade, M. Cristiani, D. Cossart, D. Ciampini, C. Sias, O. Morsch, and E. Arimondo, *Sympathetic cooling and collisional properties of a Rb-Cs mixture*, Phys. Rev. A **71**, 061401R (2005).

[29] M. Haas, V. Leung, D. Frese, D. Haubrich, S. John, C. Weber, A. Rauschenbeutel, and D. Meschede, *Species-selective microwave cooling of a mixture of rubidium and caesium atoms*, New Journal of Physics **9**, 147 (2007).

[30] M. L. Harris, P. Tierney, and S. L. Cornish, *Magnetic trapping of a cold Rb-Cs atomic mixture*, J. Phys. B **41**, 035303 (2008).

[31] J. Catani, L. D. Sarlo, G. Barontini, F. Minardi, and M. Inguscio, *Degenerate Bose-Bose mixture in a 3D optical lattice*, Phys. Rev. A **77**, 011603R (2008).

[32] S. R. Granade, M. E. Gehm, K. M. O'Hara, and J. E. Thomas, *All-Optical Production of a Degenerate Fermi Gas*, Phys. Rev. Lett. **88**, 120405 (2002).

[33] A. G. Truscott, K. E. Strecker, W. I. McAlexander, G. B. Partridge, and R. G. Hulet, *Observation of Fermi Pressure in a Gas of Trapped Atoms*, Science **291**, 2570 (2001).

[34] F. Schreck, L. Khaykovich, K. L. Corwin, G. Ferrari, T. Bourdel, J. Cubizolles, and C. Salomon, *Quasipure Bose-Einstein Condensate Immersed in a Fermi Sea*, Phys. Rev. Lett. **87**, 080403 (2001).

[35] Z. Hadzibabic, C. A. Stan, K. Dieckmann, S. Gupta, M. W. Zwierlein, A. Görlitz, and W. Ketterle, *Two-Species Mixture of Quantum Degenerate Bose and Fermi Gases*, Phys. Rev. Lett. **88**, 160401 (2002).

[36] M. Taglieber, A.-C. Voigt, T. Aoki, T. W. Hänsch, and K. Dieckmann, *Quantum Degenerate Two-Species Fermi-Fermi Mixture Coexisting with a Bose-Einstein Condensate*, Phys. Rev. Lett. **100**, 010401 (2008).

[37] G. Modugno, G. Ferrari, G. Roati, R. J. Brecha, A. Simoni, and M. Inguscio, *Bose-Einstein Condensation of Potassium Atoms by Sympathetic Cooling*, Science **294**, 1320 (2001).

[38] S. B. Papp, J. M. Pino, and C. E. Wieman, *Studying a dual-species BEC with tunable interactions*, arXiv:0802.2591 (2008).

[39] L. D. Sarlo, P. Maioli, G. Barontini, J. Catani, F. Minardi, and M. Inguscio, *Collisional properties of sympathetically cooled* ^{39}K, Phys. Rev. A **75**, 022715 (2007).

[40] A. Mosk, S. Kraft, M. Mundrich, K. Singer, W. Wohlleben, R. Grimm, and M. Weidemüller, *Mixture of Ultracold Lithium and Cesium Atoms in an Optical Dipole Trap*, Applied Physics B **73**, 791 (2001).

[41] M. Anderlini, PhD thesis, University of Pisa, 2005.

[42] E. A. Donley, N. R. Claussen, S. L. Cornish, J. L. Roberts, E. A. Cornell, and C. E. Wieman, *Dynamics of collapsing and exploding Bose-Einstein condensates*, Nature **412**, 295 (2001).

[43] K. Molmer, *Bose Condensates and Fermi Gases at Zero Temperature*, Phys. Rev. Lett. **80**, 1804 (1998).

[44] F. Riboli and M. Modugno, *Topology of the ground state of two interacting Bose-Einstein condensates*, Phys. Rev. A **65**, 063614 (2002).

[45] D. M. Jezik and P. Capuzzi, *Interaction-driven effects on two-component Bose-Einstein condensates*, Phys. Rev. A **66**, 015602 (2002).

[46] S. Inouye, J. Goldwin, M. L. Olsen, C. Ticknor, J. L. Bohn, and D. S. Jin, *Observation of Heteronuclear Feshbach Resonances in a Mixture of Bosons and Fermions*, Phys. Rev. Lett. **93**, 183201 (2004).

[47] C. A. Stan, M. W. Zwierlein, C. H. Schunck, S. M. F. Raupach, and W. Ketterle, *Observation of Feshbach Resonances between Two Different Atomic Species*, Phys. Rev. Lett. **93**, 143001 (2004).

[48] F. Ferlaino, C. D'Errico, G. Roati, M. Zaccanti, M. Inguscio, and G. Modugno, *Feshbach spectroscopy of a K-Rb atomic mixture*, Phys. Rev. A **73**, 040702(R) (2006).

[49] B. Deh, C. Marzok, C. Zimmerman, and P. W. Courteille, *Feshbach resonances in mixtures of ultracold ^6Li and ^{87}Rb gases*, Phys. Rev. A **77**, 010701(R) (2008).

[50] S. B. Papp, *Experiments with a two-species Bose-Einstein condensate using widely tunable interparticle interactions*, PhD thesis, University of Colorado, 2007.

[51] S. Kotochigova, P. S. Julienne, and E. Tiesinga, *Ab initio calculation of the KRb dipole moments*, Phys. Rev. A **68**, 022501 (2003).

[52] T. Mukaiyama, J. R. Abo-Shaeer, K. Xu, J. K. Chin, and W. Ketterle, *Dissociation and Decay of Ultracold Sodium Molecules*, Phys. Rev. Lett. **92**, 180402 (2004).

[53] C. Ospelkaus, S. Ospelkaus, L. Humbert, P. Ernst, K. Sengstock, and K. Bongs, *Ultracold Heteronuclear Molecules in a 3D Optical Lattice*, Phys. Rev. Lett. **97**, 120402 (2006).

[54] T. Volz, N. Syassen, D. M. Bauer, E. Hansis, S. Dürr, and G. Rempe, *Preparation of a quantum state with one molecule at each site of an optical lattice*, Nature Physics **2**, 692 (2006).

[55] S. D. Kraft, P. Staanum, J. Lange, L. Vogel, R. Wester, and M. Weidemüller, *Formation of ultracold LiCs molecules*, J. Phys. B **39**, S993 (2006).

[56] J. Sage, S. Sainis, T. Bergeman, and D. DeMille, *Optical production of ultracold polar molecules*, Phys. Rev. Lett. **94**, 203001 (2005).

[57] B. L. Brown, A. J. Dicks, and I. A. Walmsley, *Coherent Control of Ultracold Molecule Dynamics in a Magneto-Optical Trap by Use of Chirped Femtosecond Laser Pulses*, Phys. Rev. Lett. **96**, 173002 (2006).

[58] M. Mackie, R. Kowalski, and J. Javanainen, *Bose-Stimulated Raman Adiabatic Passage in Photoassociation*, Phys. Rev. Lett. **84**, 3803 (2000).

[59] L.-H. Lu and Y.-Q. Li, *Conversion of ^{40}K-^{87}Rb mixtures into stable molecules*, Phys. Rev. A **76**, 053608 (2007).

[60] J. M. Hutson and P. Soldán, *Molecule formation in ultracold atomic gases*, Int. Rev. Phys. Chem. **25**, 497 (2006).

[61] A. J. Kerman, J. M. Sage, S. Sainis, T. Bergeman, and D. DeMille, *Production of Ultracold, Polar RbCs* Molecules via Photoassociation*, Phys. Rev. Lett. **92**, 033004 (2004).

[62] M. Baranov, L. Dobrek, K. Góral, L. Santos, and M. Lewenstein, *Ultracold Dipolar Gases - a Challenge for Experiments and Theory*, Phys. Scr. **T102**, 74 (2002).

[63] C. J. Myatt, E. A. Burt, R. W. Ghrist, E. A. Cornell, and C. E. Wieman, *Production of Two Overlapping Bose-Einstein Condensates by Sympathetic Cooling*, Phys. Rev. Lett. **78**, 586 (1997).

[64] J. Stenger, S. Inouye, D. M. Stamper-Kurn, H.-J. Miesner, A. P. Chikkatur, and W. Ketterle, *Spin domains in ground-state Bose-Einstein condensates*, Nature **396**, 345 (1999).

[65] M. W. Mancini, A. R. L. Caires, G. D. Telles, V. S. Bagnato, and L. G. Marcassa, *Trap loss rate for heteronuclear cold collisions in two species magneto-optical trap*, Eur. Phys. J. D **30**, 105 (2004).

[66] S. Hensler, A. Griesmaier, J. Werner, A. Görlitz, and T. Pfau, *A two species trap for chromium and rubidium atoms*, J. Mod. Opt. **51**, 1807 (2004).

[67] D. Guéry-Odelin, D. Söding, P. Desbiolles, and J. Dalibard, *Is Bose-Einstein condensation of atomic cesium possible?*, Europhys. Lett. **44**, 25 (1998).

[68] Z.-Y. Ma, A. M. Thomas, C. J. Foot, and S. L. Cornish, *The Evaporative Cooling of a Gas of Caesium Atoms in the Hydrodynamic Regime*, J. Phys. B **36**, 3533 (2003).

[69] T. Weber, J. Herbig, M. Mark, H.-C. Nägerl, and R. Grimm, *Bose-Einstein Condensation of Cesium*, Science **299**, 232 (2003).

[70] A. Marte, T. Volz, J. Schuster, S. Dürr, G. Rempe, E. G. M. van Kempen, and B. J. Verhaar, *Feshbach Resonances in Rubidium 87: Precision Measurement and Analysis*, Phys. Rev. Lett. **89**, 283202 (2002).

[71] J. Herbig, T. Kraemer, M. Mark, T. Weber, C. Chin, H.-C. Nägerl, and R. Grimm, *Preparation of a Pure Molecular Quantum Gas*, Science **301**, 1510 (2003).

[72] T. Kraemer, M. Mark, P. Waldburger, J. G. Danzl, C. Chin, B. Engeser, A. D. Lange, K. Pilch, A. Jaakkola, H.-C. Nägerl, and R. Grimm,

Evidence for Efimov quantum states in an ultracold gas of caesium atoms, Nature **440**, 315 (2006).

[73] M. Gustavsson, E. Haller, M. J. Mark, J. G. Danzl, G. Rojas-Kopeinig, and H.-C. Nägerl, *Control of Interaction-Induced Dephasing of Bloch Oscillations*, Phys. Rev. Lett **100**, 080404 (2008).

[74] P. J. Leo, C. J. Williams, and P. S. Julienne, *Collision Properties of Ultracold ^{133}Cs Atoms*, Phys. Rev. Lett. **85**, 2721 (2000).

[75] U. Schlöder, H. Engler, U. Schünemann, R. Grimm, and M. Weidemüller, *Cold inelastic collisions between lithium and cesium in a two-species magneto-optical trap*, Eur. Phys. J. D **7**, 331 (1999).

[76] Z.-Y. Ma, 2005, Unpublished data.

[77] D. M. Stamper-Kurn, H.-J. Meisner, A. P. Chikkatur, S. Inouye, J. Stenger, and W. Ketterle, *Reversible Formation of a Bose-Einstein Condensate*, Phys. Rev. Lett. **81**, 2194 (1998).

[78] M. J. Jamieson, H. Sarbazi-Azad, H. Ouerdane, G.-H. Jeung, Y. S. Lee, and W. C. Lee, *Elastic scattering of cold caesium and rubidium atoms*, J. Phys. B **36**, 1085 (2003).

[79] M. Anderlini, D. Ciampini, D. Cossart, E. Courtade, M. Cristiani, C. Sias, O. Morsch, and E. Arimondo, *Model for collisions in ultracold-atom mixtures*, Phys. Rev. A **72**, 033408 (2005).

[80] M. Anderlini and D. Guéry-Odelin, *Thermalization in mixtures of ultracold gases*, Phys. Rev. A **73**, 032706 (2006).

[81] V. Vuletić, C. Chin, A. J. Kerman, and S. Chu, *Degenerate Raman Sideband Cooling of Trapped Cesium Atoms at Very High Atomic Densities*, Phys. Rev. Lett. **81**, 5768 (1998).

[82] R. Grimm, 2007, Private communication.

[83] H.-C. Nägerl, 2008, Private communication.

[84] P. Tierney, PhD thesis, Durham University, 2008.

[85] M. L. Harris, C. S. Adams, S. L. Cornish, I. C. McLeod, E. Tarleton, and I. G. Hughes, *Polarization Spectroscopy in Rubidium and Cesium*, Phys. Rev. A **73**, 062509 (2006).

[86] M. L. Harris, S. L. Cornish, A. Tripathi, and I. G. Hughes, *Optimization of sub-Doppler DAVLL on the rubidium D2 line*, J. Phys. B **41**, 085401 (2008).

[87] W. Ketterle, *When atoms behave as waves: Bose-Einstein condensation and the atom laser*, Rev. Mod. Phys **74**, 1131 (2002).

[88] M. R. Matthews, B. P. Anderson, P. C. Haljan, D. S. Hall, C. E. Wieman, and E. A. Cornell, *Vortices in a Bose-Einstein Condensate*, Phys. Rev. Lett. **83**, 2498 (1999).

[89] F. Dalfovo, S. Giorgini, L. P. Pitaevskii, and S. Stringari, *Theory of Bose-Einstein condensation in trapped gases*, Rev. Mod. Phys. **71**, 463 (1999).

[90] J. R. Abo-Shaeer, C. Raman, J. M. Vogels, and W. Ketterle, *Observation of Vortex Lattices in Bose-Einstein Condensates*, Science **292**, 476 (2001).

[91] W. Ketterle, D. S. Durfee, and D. M. Stamper-Kurn, *Making, probing and understanding Bose-Einstein condensates*, in *Proceedings of the International School of Physics - Enrico Fermi*, edited by M. Inguscio, S. Stringari, and C. E. Wieman, volume 67, 1999.

[92] C. J. Pethick and H. Smith, *Bose-Einstein Condensation in Dilute Gases* (Cambridge University Press, 2002).

[93] ed. A. Griffin, D. W. Snoke, and S. Stringari, *Bose-Einstein Condensation* (Cambridge University Press, 1995).

[94] C. J. Joachain, *Quantum Collision Theory* (North-Holland, 1983).

[95] J. J. Sakurai, *Modern Quantum Mechanics, 2nd ed.* (Addison Wesley, 1993).

[96] J. Weiner, *Cold and Ultracold Collisions in Quantum Microscopic and Mesoscopic Systems* (Cambridge University Press, 2003).

[97] C. J. Foot, *Atomic Physics* (Oxford University Press, 2005).

[98] C. Chin, *Cooling, Collisions and Coherence of Cold Cesium Atoms in a Trap*, PhD thesis, Stanford University, 2001.

[99] J. L. Roberts, *Bose-Einstein Condensates with Tunable Atom-atom Interactions*, PhD thesis, University of Colorado, 2001.

[100] J. P. Burke, *Theoretical Investigation of Cold Alkali Atom Collisions*, PhD thesis, University of Colorado, 1999.

[101] A. M. Thomas, *Ultra-cold collisions and evaporative cooling of caesium in a magnetic trap*, PhD thesis, University of Oxford, 2004.

[102] J. Dalibard, *Collisional dynamics of ultra-cold atomic gases*, Proceedings of the International School of Physics - Enrico Fermi **321** (1999).

[103] L. S. Butcher, D. N. Stacey, C. J. Foot, and K. Burnett, *Ultracold collisions for Bose-Einstein condensation*, Phil. Trans. R. Soc. Lond. A **357**, 1421 (1999).

[104] A. Derevianko, W. R. Johnson, M. S. Safronova, and J. F. Babb, *High-Precision Calculations of Dispersion Coefficients, Static Dipole Polarizabilities, and Atom-Wall Interaction Constants for Alkali-Metal Atoms*, Phys. Rev. Lett. **82**, 3589 (1999).

[105] M. Marinescu and H. R. Sadeghpour, *Long-range potentials for two-species alkali-metal atoms*, Phys. Rev. A **59**, 390 (1999).

[106] J. Herbig, *Quantum-Degenerate Cesium: Atoms and Molecules*, PhD thesis, University of Innsbruck, 2005.

[107] C. Regal, *Experimental realization of BCS-BEC crossover physics with a Fermi gas of atoms*, PhD thesis, University of Colorado, 2006.

[108] J. M. Kinast, *Thermodynamics and superfluidity of a strongly interacting Fermi gas*, PhD thesis, Duke University, 2006.

[109] Y. Ohashi and A. Griffin, *BCS-BEC Crossover in a Gas of Fermi Atoms with a Feshbach Resonance*, Phys. Rev. Lett. **89**, 130402 (2002).

[110] M. Randeria, ed. A. Griffin, D. W. Snoke, and S. Stringari, *Bose-Einstein Condensation* (Cambridge University Press, 1996), .

[111] E. Tiesinga, B. J. Verhaar, and H. T. C. Stoof, *Threshold and resonance phenomena in ultracold ground-state collisions*, Phys. Rev. A **47**, 4114 (1993).

[112] E. Timmermans, P. Tommasini, M. Hussein, and A. Kerman, *Feshbach resonances in atomic Bose-Einstein condensates*, Phys. Rep. **315**, 199 (1999).

[113] F. H. Mies, E. Tiesinga, and P. S. Julienne, *Manipulation of Feshbach resonances in ultracold atomic collisions using time-dependent magnetic fields*, Phys. Rev. A **61**, 022721 (2000).

[114] B. D. Esry, C. H. Greene, J. P. Burke, and J. L. Bohn, *Hartree-Fock Theory for Double Condensates*, Phys. Rev. Lett. **78**, 3594 (1997).

[115] T.-L. Ho and V. B. Shenoy, *Binary Mixtures of Bose Condensates of Alkali Atoms*, Phys. Rev. Lett. **77**, 3276 (1996).

[116] G. Roati, *Quantum Degenerate Potassium-Rubidium Mixtures*, PhD thesis, Università Degli Studi di Trento (Florence), 2003.

[117] S. Chu, *Nobel Lecture: The Manipulation of Neutral Particles*, Rev. Mod. Phys **70**, 685 (1998).

[118] C. Cohen-Tannoudji, *Nobel Lecture: Manipulating Atoms with Photons*, Rev. Mod. Phys **70**, 707 (1998).

[119] W. D. Phillips, *Nobel Lecture: Laser Cooling and Trapping of Neutral Atoms*, Rev. Mod. Phys **70**, 721 (1998).

[120] E. A. Cornell and C. E. Wieman, *Nobel Lecture: Bose-Einstein condensation in a dilute gas, the first 70 years and some recent experiments*, Rev. Mod. Phys **74**, 875 (2002).

[121] E. Raab, M. Prentiss, A. Cable, S. Chu, and D. Prichard, *Trapping of Neutral Sodium Atoms with Radiation Pressure*, Phys. Rev. Lett. **59**, 2631 (1987).

[122] M. Kasevich, E. Riis, S. Chu, and R. DeVoe, *rf spectroscopy in an atomic fountain*, Phys. Rev. Lett. **63**, 612 (1989).

[123] S. Stenholm, *Semiclassical theory of laser cooling*, Rev. Mod. Phys. **58**, 699 (1986).

[124] C. S. Adams and E. Riis, *Laser Cooling and Trapping of Neutral Atoms*, Prog. Quant. Electron. **21**, 1 (1997).

[125] H. J. Metcalf and P. van der Straten, *Laser Cooling and Trapping* (Springer, 1999).

[126] R. Frisch, Z. Phys. **86**, 42 (1933).

[127] S. Chu, L. Hollberg, J. E. Bjorkholm, A. Cable, and A. Ashkin, *Three-Dimensional Viscous Confinement and Cooling of Atoms by Resonance Radiation Pressure*, Phys. Rev. Lett. **55**, 48 (1985).

[128] P. D. Lett, R. Watts, C. Westbrook, W. Phillips, P. Gould, and H. Metcalf, *Observation of atoms laser cooled below the Doppler limit*, Phys. Rev. Lett. **61**, 169 (1988).

[129] J. Dalibard and C. Cohen-Tannoudji, *Laser cooling below the Doppler limit by polarization gradients: simple theoretical models*, J. Opt. Soc. Am. B **6**, 2023 (1989).

[130] C. N. Cohen-Tannoudji and W. D. Phillips, *New Mechanisms for Laser Cooling*, Physics Today , 33 (1990).

[131] G. K. Woodgate, *Elementary atomic structure* (Oxford University Press, 1983).

[132] K. Lee, J. Kim, H. Noh, and W. Jhe, *Single-Beam Atom Trap in a Pyramidal and Conical Hollow Mirror*, Opt. Lett. **21**, 1177 (1996).

[133] J. Arlt, O. Maragò, S. Webster, S. Hopkins, and C. Foot, *A Pyramidal Magneto-Optical Trap as a Source of Slow Atoms*, Opt. Comm. **157**, 303 (1998).

[134] A. M. Steane and C. J. Foot, *Laser Cooling below the Doppler Limit in a Magneto-Optical Trap*, Europhys. Lett.. **14**, 231 (1991).

[135] P. D. Lett, W. D. Phillips, S. L. Rolston, C. E. Tanner, R. N. Watts, and C. I. Westbrook, *Optical molasses*, J. Opt. Soc. Am. B **6**, 2084 (1989).

[136] C. G. Townsend, N. H. Edwards, C. J. Cooper, K. P. Zetie, C. J. Foot, A. M. Steane, P. Szriftgiser, H. Perrin, and J. Dalibard, *Phase-space Density in the Magneto-Optical Trap*, Phys. Rev. A. **52**, 1423 (1995).

[137] D. W. Sesko, T. G. Walker, and C. E. Wieman, *Behavior of neutral atoms in a spontaneous force trap*, J. Opt. Soc. Am. B **8**, 946 (1991).

[138] A. S. Arnold and P. J. Manson, *Atomic density and temperature distributions in magneto-optical traps*, J. Opt. Soc. Am. B **17**, 497 (2000).

[139] A. M. Steane, M. Chowdhury, and C. J. Foot, *Radiation Force in the Magneto-optical Trap*, J. Opt. Soc. Am. B. **9**, 2142 (1992).

[140] W. Petrich, M. Anderson, J. Ensher, and E. Cornell, *Behaviour of Atoms in a Compressed Magneto-Optical Trap*, J. Opt. Soc. Am. B. **1**, 1332 (1994).

[141] J. Weiner, V. S. Bagnato, S. Zilio, and P. S. Julienne, *Experiments and theory in cold and ultracold collisions*, Rev. Mod. Phys. **71**, 1 (1999).

[142] D. Steck, *Alkali D line data*, Website, 2008, `http://steck.us/alkalidata/`.

[143] J. P. Shaffer, W. Chalupczak, and N. P. Bigelow, *Trap loss in a two-species Na-Cs magneto-optical trap: intramultiplet mixing in heteronuclear ultracold collisions*, Phys. Rev. A **60**, R3365 (1999).

[144] G. D. Telles, L. S. Aguiar, L. G. Marcassa, and V. S. Bagnato, *Evidence of a two-color trap-loss channel*, Phys. Rev. A **66**, 025403 (2002).

[145] M. Mudrich, S. Kraft, J. Lange, A. Mosk, and M. Weidemüller, *Hyperfine-changing collisions in an optically trapped gas of ultracold cesium and lithium*, Phys. Rev. A **70**, 062712 (2004).

[146] G. D. Telles, V. S. Bagnato, and L. G. Marcassa, *Alternative to the Hyperfine-Change-Collision Interpretation for the Behavior of Magneto-optical-Trap Losses at Low Light Intensity*, Phys. Rev. Lett. **86**, 4496 (2001).

[147] B. Ueberholz, S. Kuhr, D. Frese, V. Gomer, and D. Meschede, *Cold collisions in a high-gradient magneto-optical trap*, J. Phys. B **35**, 4899 (2002).

[148] A. R. Allouche, M. Korek, K. Fakherddin, A. Chaalan, M. Dagher, F. Taher, and M. Aubert-Frécon, *Theoretical electronic structure of RbCs revisited*, J. Phys. B **33**, 2307 (2000).

[149] A. L. Migdall, J. V. Prodan, W. D. Phillips, T. H. Bergeman, and H. J. Metcalf, *First observation of magnetically trapped neutral atoms*, Phys. Rev. Lett. **54**, 2596 (1985).

[150] W. Petrich, M. H. Anderson, J. R. Ensher, and E. A. Cornell, *Stable, Tightly Confining Magnetic Trap for Evaporative Cooling of Neutral Atoms*, Phys. Rev. Lett. **74**, 3352 (1995).

[151] V. S. Bagnato, G. Lafyatis, A. G. Martin, E. L. Raab, R. N. Ahmad-Bitar, and D. E. Pritchard, *Continuous Stopping and Trapping of Neutral Atoms*, Phys. Rev. Lett. **58**, 2194 (1987).

[152] C. R. Monroe, *Experiments with optically and magnetically trapped cesium atoms*, PhD thesis, University of Colorado, 1992.

[153] T. Bergeman, G. Eretz, and H. Metcalf, *Magnetostatic trapping fields for neutral atoms*, Phys. Rev. A **35**, 1535 (1987).

[154] P. F. Griffin, *Laser Cooling and Loading of Rb into a Large Period, Quasi-Electrostatic, Optical Lattice*, PhD thesis, Durham University, 2005.

[155] K. J. Weatherill, *A CO2 Laser Lattice Experiment for Cold Atoms*, PhD thesis, Durham University, 2007.

[156] R. Grimm, M. Weidemüller, and Y. B. Ovchinnikov, *Optical Dipole Traps for Neutral Atoms*, Adv. Atom. Mol. Opt. Phys **42**, 95 (2000).

[157] A. Ashkin, *Acceleration and Trapping of Particles by Radiation Pressure*, Phys. Rev. Lett. **24**, 156 (1970).

[158] S. Chu, J. E. Bjorkholm, A. Ashkin, and A. Cable, *Experimental Observation of Optically Trapped Atoms*, Phys. Rev. Lett. **57**, 314 (1986).

[159] V. S. Lethokov, *Narrowing of the Doppler Width in a Standing Light Wave*, JETP Lett. **7**, 272 (1968).

[160] C. Salomon, J. Dalibard, A. Aspect, H. Metcalf, and C. Cohen-Tannoudji, *Channeling Atoms in a Laser Standing Wave*, Phys. Rev. Lett. **59**, 1659 (1987).

[161] C. S. Adams, H. Lee, N. Davidson, M. Kasevich, and S. Chu, *Evaporative Cooling in a Crossed Dipole Trap*, Phys. Rev. Lett. **74**, 3577 (1995).

[162] B. P. Anderson, T. L. Gustavson, and M. A. Kasevich, *Atom trapping in nondissipative optical lattices*, Phys. Rev. A **53**, R3727 (1996).

[163] C. A. Sackett, C. C. Bradley, M. Welling, and R. G. Hulet, *Bose-Einstein condensation of lithium*, Appl. Phys. B **65**, 433 (1997).

[164] K. B. Davis, M.-O. Mewes, M. A. Joffe, M. R. Andrews, and W. Ketterle, *Evaporative Cooling of Sodium Atoms*, Phys. Rev. Lett. **74**, 5202 (1995).

[165] M. Barrett, J. Sauer, and M. Chapman, *All-Optical Formation of an Atomic Bose-Einstein Condensate*, Phys. Rev. Lett. **87**, 010404 (2001).

[166] T. Weber, *Bose-Einstein Condensation of Cesium*, PhD thesis, University of Innsbruck, 2003.

[167] A. S. Arnold, J. S. Wilson, and M. G. Boshier, *A Simple Extended-Cavity Diode Laser*, Rev. Sci. Inst. **69**, 1236 (1998).

[168] D. A. Smith, *Single-Impulse Magnetic Focusing of Launched Cold Atoms*, PhD thesis, Durham University, 2005.

[169] M. J. Pritchard, *Manipulation of Ultracold Atoms using Magnetic and Optical Fields*, PhD thesis, Durham University, 2006.

[170] S. Lasertechnik, *Spectroscopy with Diode Lasers*, Website, 2008, `http://data.sacher-laser.com/lynx/lynx2005.pdf`.

[171] S. Cornish, *Gaussian Beams and the Knife-Edge Measurement*, Website, 2006, `http://massey.dur.ac.uk/resources/grad_skills/KnifeEdge.pdf`.

[172] G. D. Rovera, G. Santarelli, and A. Clairon, *A laser diode system stabilized on the Caesium D2 line*, Rev. Sci. Instrum. **65**, 1502 (1994).

[173] N. P. Robins, B. J. J. Slagmolen, D. A. Shaddock, J. D. Close, and M. B. Gray, *Interferometric, modulation-free laser stabilization*, Opt. Lett. **27**, 1905 (2002).

[174] G. Jundt, G. T. Purves, C. S. Adams, and I. G. Hughes, *Non-linear Sagnac interferometry for pump-probe dispersion spectroscopy*, Eur. Phys. J. D **27**, 273 (2002).

[175] H. Gilles, B. Cheron, and J. Hamel, *Dispersive effects in optically pumped ($2\,^3S_1$) ^4He atomic vapor measured by using a geometrical optics technique*, Opt. Comm. **190**, 179 (2001).

[176] G. T. Purves, G. Jundt, C. S. Adams, and I. G. Hughes, *Refractive index measurements by probe-beam deflection*, Eur. Phys. J. D **29**, 433 (2004).

[177] C. I. Sukenik, H. C. Busch, and M. Shiddiq, *Modulation-free laser frequency stabilization and detuning*, Opt. Comm. **203**, 133 (2002).

[178] E. D. van Ooijen, G. Katgert, and P. van der Straten, *Laser frequency stabilization using Doppler-free bichromatic spectroscopy*, Appl. Phys. B **79**, 57 (2004).

[179] J. A. Kerckhoff, C. D. Bruzewicz, R. Uhl, and P. K. Majumder, *A frequency stabilization method for diode lasers utilizing low-field Faraday polarimetry*, Rev. Sci. Instrum. **76**, 093108 (2005).

[180] S. E. Park, H. S. Lee, T. Y. Kwon, and H. Cho, *Dispersion-like signals in velocity-selective saturated-absorption spectroscopy*, Opt. Comm. **192**, 49 (2001).

[181] V. B. Tiwari, S. Singh, S. R. Mishra, H. S. Rawat, and S. C. Mehendale, *Laser frequency stabilization using Doppler-free bi-polarization spectroscopy*, Opt. Comm. **263**, 249 (2006).

[182] V. B. Tiwari, S. Singh, S. R. Mishra, H. S. Rawat, and S. C. Mehendale, *Laser frequency stabilization using a balanced bi-polarimeter*, Appl. Phys. B **83**, 93 (2006).

[183] C. Wieman and T. W. Hänsch, *Doppler-Free Laser Polarization Spectroscopy*, Phys. Rev. Lett. **36**, 1170 (1976).

[184] C. P. Pearman, C. S. Adams, S. G. Cox, P. F. Griffin, D. A. Smith, and I. G. Hughes, *Polarization Spectroscopy of a Closed Atomic Transition: Applications to Laser Frequency Locking*, J. Phys. B. **35**, 5141 (2002).

[185] A. Ratnapala, C. J. Vale, A. G. White, M. D. Harvey, N. R. Heckenberg, and H. Rubinsztein-Dunlop, *Laser frequency locking by direct measurement of detuning*, Opt. Lett. **29**, 2704 (2004).

[186] B. Chéron, H. Gilles, J. Hamel, O. Moreau, and H. Sorel, *Laser frequency stabilization using Zeeman effect*, J. de Physique III **4**, 401 (1994).

[187] K. L. Corwin, Z.-T. Lu, C. F. Hand, R. J. Epstein, and C. E. Wieman, *Frequency-Stabilized Diode Laser with the Zeeman Shift in an Atomic Vapor*, Appl. Opt. **37**, 3295 (1998).

[188] T. Petelski, M. Fattori, G. Lamporesi, J. Stuhler, and G. M. Tino, *Doppler-free spectroscopy using magnetically induced dichroism of atomic vapor: a new scheme for laser frequency locking*, Eur. Phys. J. D **22**, 279 (2002).

[189] G. Wasik, W. Gawlik, J. Zachorowski, and W. Zawadzki, *Laser frequency stabilization by Doppler-free magnetic dichroism*, Appl. Phys. B **75**, 613 (2002).

[190] G. C. Bjorklund, *Frequency-modulation spectroscopy: a new method for measuring weak absorptions and dispersions*, Opt. Lett. **5**, 15 (1980).

[191] D. J. McCarron, S. A. King, and S. L. Cornish, *Modulation transfer spectroscopy in atomic rubidium*, arXiv:0805.2708 (2008).

[192] K. B. MacAdam, A. Steinbach, and C. Wieman, *A narrow-band tunable diode laser system with grating feedback, and a saturated absorption spectrometer for Cs and Rb*, Am. J. Phys. **60**, 1098 (1992).

[193] D. A. Smith and I. G. Hughes, *The Role of Hyperfine Pumping in Multilevel Systems Exhibiting Saturated Absorption*, Am. J. Phys **72**, 631 (2004).

[194] A. Millett-Sikking, I. G. Hughes, P. Tierney, and S. L. Cornish, *DAVLL lineshapes in atomic rubidium*, J. Phys. B **40**, 187 (2007).

[195] N. Beverini, E. Maccioni, P. Marsili, A. Ruffini, and F. Sorrentino, *Frequency stabilization of a diode laser on the Cs D2 resonance line by the Zeeman effect in a vapor cell*, Appl. Phys. B **73**, 133 (2001).

[196] J. M. Reeves, O. Garcia, and C. A. Sackett, *Temperature stability of a dichroic atomic vapor laser lock*, Applied Optics **45**, 372 (2006).

[197] D. J. McCarron, I. G. Hughes, P. Tierney, and S. L. Cornish, *A heated vapor cell unit for dichroic atomic vapor laser lock in atomic rubidium*, Rev. Sci. Instrum. **78**, 093106 (2007).

[198] V. V. Yashchuk, D. Budker, and J. R. Davis, *Laser frequency stabilization using linear magneto-optics*, Rev. Sci. Instrum. **71**, 341 (2000).

[199] D. Sarkisyan, A. Papoyan, T. Varzhapetyan, J. Alnis, K. Blush, and M. Auzinsh, *Sub-Doppler spectroscopy of Rb atoms in a sub-micron vapour cell in the presence of a magnetic field*, J. Opt. A: Pure Appl. Opt. **6**, S142 (2004).

[200] D. Meschede, *Optics, Lasers and Light* (Wiley-VCH, 2004).

[201] N. Lundblad, D. C. Aveline, R. J. Thompson, J. M. Kohel, J. Ramirez-Serrano, W. M. Klipstein, D. G. Enzer, N. Yu, and L. Maleki, *Two-species cold atomic beam*, J. Opt. Soc. Am. B **21**, 3 (2004).

[202] C. E. Wieman, D. E. Pritchard, and D. J. Wineland, *Atom cooling, trapping, and quantum manipulation*, Rev. Mod. Phys. **71**, S253 (1999).

[203] W. Süptitz, G. Wokurka, F. Strauch, P. Kohns, and W. Ertmer, *Simultaneous cooling and trapping of ^{85}Rb and ^{87}Rb in a magneto-optical trap*, Opt. Lett. **19**, 1571 (1994).

[204] C. I. Sukenik and H. C. Busch, *Simultaneous trapping of rubidium and metastable argon in a magneto-optical trap*, Phys. Rev. A **66**, 051492(R) (2002).

[205] M. Taglieber, A.-C. Voigt, F. Henkel, S. Fray, T. W. Hänsch, and K. Dieckmann, *Simultaneous magento-optical trapping of three atomic species*, Phys. Rev. A **73**, 011402(R) (2006).

[206] G. D. Telles, W. Garcia, L. G. Marcassa, V. S. Bagnato, D. Ciampini, M. Fazzi, J. H. Müller, D. Wilkowski, and E. Arimondo, *Trap loss in a two-species Rb-Cs magneto-optical trap*, Phys. Rev. A **63**, 033406 (2001).

[207] G. D. Telles, L. G. Marcassa, S. R. Muniz, S. G. Miranda, A. Antunes, C. Westbrook, and V. S. Bagnato, *Inelastic cold collisions of a Na/Rb mixture in a magneto-optical trap*, Phys. Rev. A **59**, R23 (1999).

[208] J. P. Shaffer, W. Chalupczak, and N. P. Bigelow, *Photoassociative ionization of heteronuclear molecules in a novel two-species magneto-optical trap*, Phys. Rev. Lett. **82**, 1124 (1999).

[209] T. Walker, D. Sesko, and C. Wieman, *Collective behavior of optically trapped neutral atoms*, Phys. Rev. Lett. **64**, 408 (1990).

[210] S. D. Gensemer, V. Sanchez-Villicana, K. Y. N. Tan, T. T. Grove, and P. L. Gould, *Trap-loss collisions of ^{85}Rb and ^{87}Rb: Dependence on trap parameters*, Phys. Rev. A **56**, 4055 (1997).

[211] D. Sesko, T. Walker, C. Monroe, A. Gallagher, and C. Wieman, *Collisional losses from a light-force trap*, Phys. Rev. Lett. **63**, 961 (1989).

[212] E. Arimondo, M. Inguscio, and P. Violino, *Experimental determinations of hyperfine structure in alkali atoms*, Rev. Mod. Phys. **49**, 31 (1977).

[213] E. Tarleton, *Modeling pump-probe spectroscopy*, MSci report, Durham University, 2004.

[214] J. D.-R. C. Cohen-Tannoudji and G. Grynberg, *Atom-Photon Interactions* (Wiley, 1998).

[215] G. T. Purves, *Absorption and dispersion in atomic vapours: applications to interferometry*, PhD thesis, Durham University, 2006.

[216] N. Coppendale, MSci report, Durham University, 2005.

[217] U. Volz and H. Schmoranzer, *Precision lifetime measurements on alkali atoms and on helium by beam-gas-laser spectroscopy*, Phys. Scr. T **T65**, 48 (1996).

[218] R. J. Rafac, C. E. Tanner, A. E. Livingston, and H. G. Berry, *Fast-beam laser lifetime measurements of the cesium* $6p^2P_{1/2,3/2}$ *states*, Phys. Rev. A **60**, 3648 (1999).

[219] A. R. Edmonds, *Angular Momentum in Quantum Mechanics* (Princeton University Press, 1960).

[220] Y. Yoshikawa, T. Umeki, T. Mukae, Y. Torii, and T. Kuga, *Frequency Stabilization of a Laser Diode with Use of Light-Induced Birefringence in an Atomic Vapor*, Applied Optics **42**, 6645 (2003).

[221] J. Walewski, C. F. Kaminski, S. F. Hanna, and R. P. Lucht, *Dependence of partially saturated polarization spectroscopy signals on pump intensity and collision rate*, Phys. Rev. A **64**, 063816 (2001).

[222] H. D. Do, G. Moon, and H.-R. Noh, *Polarization spectroscopy of rubidium atoms: Theory and experiment*, Phys. Rev. A **77**, 032513 (2008).

[223] P. Siddons, C. S. Adams, C. Ge, and I. G. Hughes, *Absolute absorption on the rubidium D lines: comparison between theory and experiment*, arXiv:0805.1139 (2008).

[224] P. Tremblay, A. Michaud, M. Levesque, S. Thériault, M. Breton, and J. Beaubien, *Absorption profiles of alkali-metal D lines in the presence of a static magnetic field*, Phys. Rev. A. **42**, 2766 (1990).

[225] L. P. Maguire, R. M. W. van Bijnen, E. Mese, and R. E. Scholten, *Theoretical calculation of saturated absorption spectra for multi-level atoms*, J. Phys. B **39**, 2709 (2006).

[226] C.-L. Hung, X. Zhang, N. Gemelke, and C. Chin, *Fast, Runaway Evaporative Cooling to Bose-Einstein Condensation in Optical Traps*, arXiv:0804.0060 (2008).

[227] M. E. Gehm, K. M. OHara, T. A. Savard, and J. E. Thomas, *Dynamics of Noise-Induced Heating in Atom Traps*, Phys. Rev. A **58**, 3914 (1998).

[228] M. Greiner, I. Bloch, T. W. Hänsch, and T. Esslinger, *Magnetic transport of trapped cold atoms over a large distance*, Phys. Rev. A **63**, 031401 (2001).

[229] H. J. Lewandowski, D. M. Harber, D. L. Whitaker, and E. A. Cornell, *Simplified System for Creating a Bose-Einstein Condensate*, Journal of Low Temperature Physics **132**, 309 (2003).

[230] M. Takamoto, F.-L. Hong, R. Higashi, and H. Katori, *An optical lattice clock*, Nature **435**, 321 (2005).

[231] M. Greiner, O. Mandel, T. Esslinger, T. W. Hänsch, and I. Bloch, *Quantum phase transition from a superfluid to a Mott insulator in a gas of ultracold atoms*, Nature **415**, 39 (2002).

[232] C. S. Adams, *Neutral atom quantum computing in optical lattices: far red or far blue?*, Website, 2004, `http://massey.dur.ac.uk/research/co2/co2.html`.

[233] D. Jaksch, V. Venturi, J. I. Cirac, C. J. Williams, and P. Zoller, *Creation of a Molecular Condensate by Dynamically Melting a Mott Insulator*, Phys. Rev. Lett. **89**, 040402 (2002).

[234] L. J. LeBlanc and J. H. Thywissen, *Species-specific optical lattices*, Phys. Rev. A **75**, 053612 (2007).